The Regulation of *Arabidopsis thaliana* Stem Development by IQ67-Domain Proteins

A thesis submitted to the University of East Anglia for the degree of Doctor of Philosophy

Bryony Yates

Registration Number: 100348260

08/02/2026

ABSTRACT

Early plant anatomists noted that different plant tissues exhibit contrasting patterns of cell division, often juxtaposed against each other (Sachs 2011 [1875]). In some regions of the shoot apical meristem (SAM), for example, the angles of new cell walls are highly variable, while other regions have regimented cell wall orientation (Bencivenga et al. 2016). The tight regulation of these cell division patterns implies that cell wall orientation is important for plant morphogenesis. However, the relationship between division orientation and morphogenesis is poorly understood, because many mutants with wall orientation defects have either remarkably normal growth or complex pleiotropic phenotypes (Spinner et al. 2013; Kirik et al. 2012; Schaefer et al. 2017). Furthermore, we have an incomplete understanding of how division orientation is regulated: many signals that direct cell wall orientation have been identified, but the mechanisms and molecular components that perceive and translate them into robust cell wall positioning are not well-characterised.

The plant-specific IQ67-domain (IQD) genes encode a large family of calmodulin-binding proteins that are implicated in the regulation of morphogenesis. At the cellular level, IQDs regulate microtubule organisation and are proposed to act as scaffolds for intracellular signalling (Abel et al. 2013; Bürstenbinder, Mitra, et al. 2017). Here I report that members of the 1A subfamily of *Arabidopsis* IQDs localise to mitotic structures, including the preprophase band (PPB), cortical division zone (CDZ), and cell plate. Loss of function of the entire 1A subfamily (6 genes) impairs the orientation of new cell walls specifically in the pith-producing region of the SAM and increases the thickness of the plant stem. I propose that, in wild type plants, 1A IQDs are recruited to the PPB/ CDZ to ensure robust division plane positioning, while misoriented divisions in loss-of-function mutants drive radial stem growth by increasing the number of pith cell files. These results highlight how changes to cell division orientation can drive differential organ growth and identify novel molecular regulators of cell division orientation.

ACKNOWLEDGEMENTS

I would like to thank my supervisors Robert Sablowski and Richard Smith for their support and guidance throughout my PhD. Our many thought-provoking discussions have shaped how I think about and approach scientific questions and made me into the scientist I am today. I would also like to thank all the members of the Sablowski and Smith groups who have supported me over the past four years. I would particularly like to thank Boris Stojikolvic for supporting me with the protein-protein interaction part of the project, Max Bush for providing guidance on many aspects of lab work, and Nicole Mol for continuing were I have left off and helping me to plug the remaining gaps in the 1A IQD story. I would like to thank the many technical support staff at JIC – Horticultural Services, Lab Support, Light Microscopy – for providing training and technical services that have supported this work in countless ways. I am grateful to the UKRI Biotechnology and Biological Sciences Research Council for funding my PhD through the Norwich Research Park Doctoral Training Partnership (grant number BB/T008717/1). I would like to thank all the staff working for the NRPDTP programme and Graduate Schools Office whose behind-the-scenes support has made my PhD possible.

I want to thank the members of the UEA Quiz Society, who have been a source of fun and laughter that has helped to sustain me through some of the more stressful moments of my PhD. And finally, I could not have done any of it without the unwavering love and support of my parents, my sister, Abigail, and my fiancé Henry.

TABLE OF CONTENTS

TABLE OF FIGURES

ABBREVIATIONS

AI	Artificial Intelligence
AUR1	AURORA1
CaM/CAM	Calmodulin
CDS	Coding Sequence
CDZ	Cortical Division Zone
ChIP-seq	Chromatin Immunoprecipitation sequencing
CI	Confidence Interval
CLV3	CLAVATA 3
CML	Calmodulin-like
cMT	Cortical Microtubule
Col-0	Columbia 0
dCAPS	Derived Cleaved Amplified Polymorphic Sequences
ER	Endoplasmic Reticulum
GFP	Green Fluorescent Protein
GO	Gene Ontology
GTPase	guanosine triphosphatase
GUS	β-glucuronidase
IQD	IQ67 Domain
IQR	Inter-quartile range
ipTM	interface predicted Template Modelling (score)
KLCR	KINESIN LIGHT CHAIN-RELATED
KTN1	KATANIN1
MAP	Microtubule-Associated Protein
MAP4-MBD	Microtubule binding domain of Microtubule-Associated Protein 4
MPK6	MITOGEN-ACTIVATED PROTEIN KINASE 6
mPS-PI	Modified Pseudo-Schiff-propidium iodide
MT	Microtubule
PAE	Predicted Aligned Error
PHGAP	PLECKSTRIN HOMOLOGY GTPase ACTIVATING PROTEIN
PI	Propidium iodide
POK	PHRAGMOPLAST ORIENTING KINESINS
pLDDT	predicted Local Distance Difference Test
PM	Plasma membrane

PP2A	Protein phosphatase 2A
pTM	predicted Template Modelling (score)
RFP	Red Fluorescent Protein
ROP	Rho of Plants (family of GTPases)
RPL	REPLUMLESS
RZ	Rib zone
SAM	Shoot apical meristem
TON1	TONNEAU1
TRM	TON1 RECRUITING MOTIF
TTP	TON1, TRM, and PP2A complex
UTR	Untranslated region
WUS	WUSCHEL
YFP	Yellow fluorescent protein

1 INTRODUCTION

1.1 MORPHOGENESIS – IT'S COMPLICATED!

Morphogenesis is the process by which biological tissues and organs grow and acquire shapes. It is taking place every single moment in every living plant and gives rise to the dazzling diversity of plant forms that populate our planet. While morphogenesis is simple conceptually, its biological underpinnings are highly complex. The genome does not provide a straightforward blueprint for the size and shape of a multicellular organism. Nor are they the sum of that organism's independent constituent parts - namely, its numerous cells, with their many different specialised properties. Rather, morphogenesis is an emergent property of multiple integrated processes (gene expression, cell division, cell growth, hormone levels, biomechanics) operating across different levels of biological organisation (cells, tissues, and organs). These processes interact and overlap, making their contributions difficult to disentangle. Elevated hormone levels might regulate gene expression, which affects cell wall composition, which affects cell mechanics, which affects cell growth, which affects cell division, which affects tissue mechanics, which affects gene expression, which affects hormones…etc. Making sense of this complicated web is key to understanding the basis of earth's biological diversity.

Plant morphogenesis is distinct from that of other multicellular eukaryotes (animals, fungi), for three many reasons:

(1) Morphogenesis in plants is largely post-embryonic. Unlike animals, which either maintain the same body plan from birth or undergo one or more discrete metamorphoses, plants modify their bodies throughout life. Plants change the number, size and positioning of organs depending on factors like life-stage, nutritional status and the environment. This is a key evolutionary adaptation to a life fixed in one place, forced to weather any and all environmental changes in order to survive.

(2) Plant cells are bound by cellulose cell walls. Thus, like the larger plant body, the plant cells are also immobile. This means that morphology necessarily derives solely from the magnitude and orientation of cell growth and proliferation. Furthermore, mechanical forces are transmitted through connected cell walls, allowing coordination of growth at the organ scale (Coen and Cosgrove 2023; Verger et al. 2018).

(3) The green plant lineage evolved multicellularity independently of animals and fungi. While some conserved regulators and pathways were recruited convergently during the separate origins of multicellularity, the mechanisms and molecular machinery that underpin plant multicellularity are largely plant-specific (Leyser 2011; Jarvis et al. 2003; Harashima et al. 2013)

Over the last few decades, several key players in plant morphogenesis have been identified. Fundamentally, organ size and shape are controlled by the rate, duration and direction of cell proliferation and cell enlargement. Both are regulated by phytohormones, including auxin, gibberellins, brassinosteroids and cytokinins, and there is frequently crosstalk between different hormone signalling pathways (Vanstraelen and Benková 2012). Hormones primarily regulate gene expression, modulating the level of cell-cycle regulators, cell wall loosening enzymes, microtubule (MT)-associated proteins (MAPs) and other regulators of cell growth and division (Wang et al. 2018). Microtubular arrays affect the orientation of cell division, cell expansion, cell wall mechanics and orchestrate many aspects of the cell cycle (Müller 2019; Dixit and Cyr 2004). Mechanical forces, at the cell and tissue levels, are also highly influential, since plant cells are pressurised and immobile, and cell growth is a turgor-driven process (Coen and Cosgrove 2023).

These three components – hormones, cytoskeleton and mechanics – are closely coupled and the interactions between them largely coordinate development (Sampathkumar et al. 2014). It is these interactions, and the factors and mechanisms that mediate and tune them, that are the focus of much ongoing research. One family of proteins that are proposed to play a role in this are the IQ67-domain (IQD) proteins (Dahiya and Bürstenbinder 2023; Bürstenbinder, Mitra, et al. 2017). This thesis investigates how members of the IQD protein family tune plant morphogenesis, using the *Arabidopsis thaliana* stem as a model system.

1.2 The Plant Stem

When compared to complex leaf shapes, fractal root networks and showy flowers, the stem appears somewhat simple and perhaps uninteresting. However, the stem is fundamental to plant growth and adaptation. The backbone of the plant, the stem supports the photosynthetic and reproductive organs and thereby determines how successfully the plant can feed itself and reproduce. It follows that alterations to stem size, shape and architecture (introduced via selective breeding) underpin many of our

most agronomically-important crop varieties (Hedden 2003; Liu et al. 2020; Ferrero-Serrano et al. 2019; Wang et al. 2018)

Far from a uniform cylinder, the stem contains multiple tissue types. The *Arabidopsis* stem is formed of four concentric tissue layers: pith, vascular bundles, cortex and epidermis (**fig. 1**). The epidermis acts as a barrier to water loss and pathogens, and is hypothesised to mechanically constrain growth (Kutschera and Niklas 2007); the vascular tissue contains different specialised cell types that transport of water and carbohydrates throughout the plant and provide structural support for the stem; the cortex and pith comprise thin-walled parenchyma cells. Stem tissue is generated by cell division in the rib zone (RZ), a region of the shoot apical meristem (SAM) that sits below the central zone (Serrano-Mislata and Sablowski 2018).

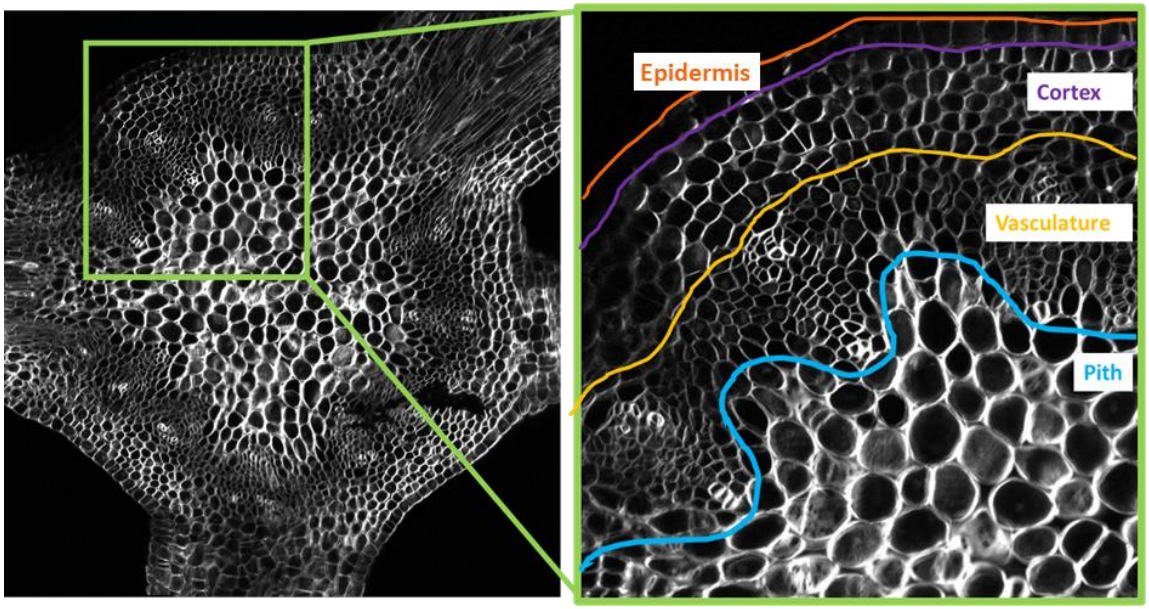

Figure 1: The layered organisation of the *Arabidopsis* inflorescence stem. Calcofluor white-stained transverse section of plant stem, taken approx. 200 µm from stem tip.

Key regulators of stem growth include gibberellin signalling and organ boundary genes, but few targets of these pathways have been characterised (Serrano-Mislata and Sablowski 2018). Chromatin immunoprecipitation sequencing (ChIP-seq) was performed to identify targets of two key stem development regulators, REPLUMLESS (RPL) (which regulates the expression of organ boundary genes) and REPRESSOR OF GA (RGA) (Serrano-Mislata et al. 2017; Bencivenga et al. 2016). These data identified that several members of the IQD family might be transcriptionally regulated by these genes, pointing to possible roles in stem development.

1.3 THE IQD FAMILY

The members of the IQD protein family are united by the presence of a plant-specific IQ67 domain. This 67-amino acid domain combines three types of predicted calmodulin (CaM)-binding motifs – IQ (IQxxxRGxxxR; Pfam 00612), 1-5-10, and 1-8-14 motifs – each present in 1-4 copies (Rhoads and Friedberg 1997; Abel et al. 2005). IQD genes have been found in all major clades of land plants and in some species of charophyte algae, but are not found outside of the Viridiplantae (Dahiya et al. 2023; Abel et al. 2005). In the angiosperm lineage, these genes have multiplied and diversified several times over: of the angiosperm species characterised, most have around 30 *IQD* genes (although bread wheat has more than 100), comprising up to five subfamilies (1, 2, 3, 4 and 5) (Feng et al. 2014; Wu et al. 2016; Abel et al. 2005; Mei et al. 2021; Ke et al. 2022). Phylogenetic analysis has partitioned the *IQD* subfamilies further into subclasses (clade 1A, 1B, 1C, 1D, 2A, 2B, 3A, 3B) (Abel et al. 2005). The subfamilies contain closely related orthologues from diverse angiosperm species, indicating that the major *IQD* lineages already existed when monocots and eudicots diverged (Abel et al. 2005). Separate phylogenetic analyses have identified slightly different arrangements of subfamilies, but point to an even more ancient origin for some *IQD* subfamilies, in the last common ancestor of all land plants (Dahiya et al. 2023). More recent expansion and diversification of the *IQD* family in angiosperms is the consequence of whole genome duplications (Abel et al. 2005).

The presence of several CaM-recruitment motifs in IQD proteins strongly points towards a role in CaM-mediated intracellular signalling. CaMs and CaM-like (CML) proteins are key intermediaries in many signalling pathways, since they bind the Ca^{2+} (a ubiquitous secondary messenger) to trigger a wide array of downstream processes. Binding of CaMs and CMLs has been verified for several AtIQD proteins (Levy et al. 2005; Mitra et al. 2019; Wendrich et al. 2018; Bürstenbinder, Möller, et al. 2017). Binding of some CaMs to IQDs is enhanced by Ca^{2+}, but others bind more strongly in low Ca^{2+} conditions (Wendrich et al. 2018), suggesting that IQDs may be able to finely modulate cellular responses to Ca^{2+}. IQD proteins share additional conserved amino acid motifs located N- and C-terminally of the IQ67 domain, the occurrence and spacing of which varies between family members (Abel et al. 2005). These additional motifs are important for binding other interacting partners (Kumari et al. 2021) and may dictate functional specialisation. Indeed, IQDs are predicted to operate as signal-integrating scaffolds, recruiting CaMs and other proteins to specific intracellular sites and mediating regulation by Ca^{2+} (Bürstenbinder, Mitra, et al. 2017; Mitra et al. 2019; Kölling et al. 2019). The fact that IQDs are also regulated by several

phytohormones, including auxin and gibberellins, provides further opportunity for signal integration (Möller et al. 2017; Bi et al. 2018; Rashotte et al. 2003; Zentella et al. 2007).

IQDs play roles in diverse biological processes, including cell and organ morphogenesis (Feng et al. 2023; Bürstenbinder, Möller, et al. 2017; Yuanfeng Li et al. 2021), metabolism (Levy et al. 2005; Zhao et al. 2025) and response to stressors such as cold, drought, herbivory and hypoxia (Zhao et al. 2025; Yuan et al. 2019; Levy et al. 2005; Zhang et al. 2024). It follows that overexpression of IQDs can confer many agronomically desirable traits, including improved tolerance of drought and hypoxia, herbivore deterrence and enhanced photosynthesis (Matthes et al. 2022; Yuan et al. 2019; Zhao et al. 2025; Levy et al. 2005; Yuan et al. 2022). IQDs hold significant, untapped potential for crop improvement, and many IQD family members have been identified in important crop species including bread wheat (Ke et al. 2022), rice (Abel et al. 2005), apple (Zhang et al. 2024), watermelon (Dou et al. 2022), cotton (Rehman et al. 2021), potato (Mei et al. 2021), soy bean (Wu et al. 2016), tomato (Bao et al. 2023) and Chinese cabbage (Yuan et al. 2019). Because the IQD families in different crop species are typically large, the individual genes are likely to have highly specialised functions. This makes them promising targets for the modification of specific plant traits, as they are less likely to generate unwanted pleiotropic effects.

A role for IQDs in the regulation of crop morphogenesis is already well-established. Some of the earliest links between IQDs and organ morphology were uncovered through quantitative trait locus mapping of fruit shape. The *sun* locus in tomato explains 58 % of the variation between an elongated-fruit variety of *Solanum lycopersicum* and its round-fruited wild relative *Solanum pimpinellifolium* (Xiao et al. 2008). The *SUN* gene encodes an IQD protein that, in the elongated variety, is translocated to a different genomic location and consequently expressed at a higher level. Similar observations of IQDs differentiating fruit morphologies have been made in watermelon (Dou et al. 2018), pepper (Wang et al. 2024) and cucumber (Pan et al. 2017), and organ elongation or shortening is also a consequence of IQD over-expression in model plant systems (Yuanfeng Li et al. 2021; Li et al. 2023; Bürstenbinder, Möller, et al. 2017). Other developmental phenotypes generated by ectopic IQD expression include helical growth (Wu et al. 2011; Bürstenbinder, Möller, et al. 2017; Wendrich et al. 2018), altered leaf serrations and venation (Mckechnie-Welsh 2021; Wu et al. 2011), reduced root meristem length (Wendrich et al. 2017) and cell shape changes (Liang et al. 2018; Mitra et al. 2019). Morphogenetic phenotypes in *iqd* loss of function mutants have been less frequently reported, likely due to genetic redundancy

between different members of the IQD family. However, skewed root angle and altered leaf pavement cell morphology have been reported for some *iqd* single gene mutants (Feng et al. 2023; Liang et al. 2018; Zang et al. 2021).

1.3.1 The 1A IQD subfamily

The 1A subfamily of *AtIQD* genes has 6 members, *AtIQD22* to *AtIQD27* (hereafter all references to specific *IQD* genes/ proteins refer to *A. thaliana* unless otherwise specified). Although there is some discrepancy between separate phylogenetic analyses of the *Arabidopsis* IQDs, *IQDs 22-27* consistently form a monophyletic subclade within the wider IQD family (Abel et al. 2005; Dahiya et al. 2023; Wendrich et al. 2018). Most of these genes have received little research attention, although clues to a possible role in morphogenesis have emerged from large-scale datasets. In seedlings, *IQD22* expression is negatively regulated by gibberellins (Zentella et al. 2007), while *IQD23, IQD26* and *IQD27* are >=1.5-fold downregulated in embryos with reduced auxin response (Möller et al. 2017; Wendrich et al. 2018). ChIP-seq data indicates that RPL binds DNA sequences near five of the six 1A IQDs (*IQD22, IQD23, IQD24*, *IQD26* and *IQD27*) (Bencivenga et al. 2016; Mckechnie-Welsh 2021). This suggests that these genes might be transcriptionally regulated by RPL, which is expressed in the centre of the RZ and required for normal RZ patterning and stem growth (Bencivenga et al. 2016).

Individual *iqd* loss-of-function mutants frequently lack conspicuous morphological phenotypes, with more severe phenotypes emerging when multiple mutations are combined (Sugiyama et al. 2017; Kumari et al. 2021; Bürstenbinder, Möller, et al. 2017; Yang et al. 2021) and IQDs from the same subclade often share similar transcriptional regulation, subcellular localisation and function (Kumari et al. 2021; Vaddepalli et al. 2021; Wendrich et al. 2018). Therefore, to investigate the functions of 1A IQDs, a sextuple mutant with loss-of-function alleles for every member of the *IQD* 1A subfamily was generated (*iqd22 iqd23 iqd24 iqd25 iqd26 iqd27,* hereafter referred to a *1aiqd*) (Mckechnie-Welsh 2021). The most pronounced phenotype of *1aiqd* plants is a thicker stem, deriving from a large increase in the number of pith cells (Mckechnie-Welsh 2021). Otherwise, the stem and its constituent layers are morphologically normal. Stem growth phenotypes have been reported in other IQD studies, but they have been little explored (Badmi et al. 2018; Wu et al. 2016). As well as having a thicker stem, the *1aiqd* mutant has defects in cell division orientation in the central region of the RZ, where pith tissue is generated (Mckechnie-Welsh 2021). However, this previous work did not elucidate how or why mutating the *1A IQDs* caused this cellular phenotype or confirm how it is connected

to the increase in stem thickness. Additional phenotypes of *1aiqd* plants include broader, flatter leaves with more frequent and deeper serrations, more branching, and more spherical seed shape. *1aiqd* plants also have a weakly penetrant phyllotactic phenotype: 4-6% of rosettes have bijugate phyllotaxis, switching to opposite branch pairing at the floral transition (Mckechnie-Welsh 2021).

1.4 RESEARCH AIMS

The overarching aim of this thesis is to determine how subfamily 1A *IQDs* regulate stem morphology in *Arabidopsis* at the molecular, cellular and organ levels. In doing so, it aims to reveal the biological functions of an understudied group of genes and uncover developmental mechanisms that may be applied to plant growth in general. The following chapters start at the largest scale, exploring the regulation of stem growth, and successively scale down, so that by chapter 4, the molecular components that underpin organ-scale changes are the focus.

Chapter 2 provides a detailed characterisation of stem growth and meristem anatomy of a *1aiqd* mutant to determine if and how changes in oriented cell divisions generate the thick stem phenotype. Chapter 3 investigates the expression and subcellular localisation of 1A IQDs, to gain insight into how they regulate cell division orientation. Chapter 4 explores the molecular mechanism by which IQDs regulate cell division and works towards identifying molecular interactors of 1A IQDs.

2 ISOLATION AND PHENOTYPIC ANALYSIS OF A SUBFAMILY 1A IQD MUTANT

2.1 INTRODUCTION

Almost all plant organs derive from populations of dividing stem cells situated inside a meristem (Aichinger et al. 2012). Located at the root tips, stem apices and in the vasculature, they modulate growth, initiate new organs, and govern tissue maintenance and repair. Meristems underpin much of what makes plant development unique, allowing plants to regenerate organs after damage, and modify growth and organ production according to their environment and nutritional status.

Plant meristems are organised into spatially distinct regions that give rise to specific tissues or cell layers (Aichinger et al. 2012). This spatial organisation is tightly controlled by complex regulatory networks such that changes to the size of meristem regions or disruption of the boundaries between them can significantly impact morphogenesis (Schoof et al. 2000; Bencivenga et al. 2016). The *Arabidopsis* SAM comprises three zones: the central zone (CZ), which houses slowly dividing stem cells; the surrounding peripheral zone (PZ), where cells divide more rapidly and new organs initiate; and the underlying rib zone (RZ), which produces new stem tissue. The RZ is further subdivided into a central rib meristem, in which cells divide transversely to produce parallel files of pith cells; and the peripheral region, which is continuous with the overlying PZ and generates the outer stem tissues (epidermis, cortex and vascular bundles) (Sachs 1965; Serrano-Mislata and Sablowski 2018). The SAM also has a layered structure: the outermost epidermal layer (L1) and the subepidermal layer (L2) divide anticlinally, producing clonally separate cell monolayers; the underlying body of the meristem belongs to the L3 layer, and houses cells that divide in all different planes (Fletcher 2002).

The CZ and PZ have been intensely studied, revealing much about how meristematic stem cell populations are maintained and how new leaves and flowers are initiated (Barton 2010). The L1 layer has proved an invaluable model for understanding how cell growth and division regulate organ shape (Kierzkowski et al. 2012; Louveaux et al. 2016; Serrano-Mislata et al. 2015). In contrast, relatively little is known about the growth of the RZ or its role in regulating stem development. This is not because the RZ or stem lack real-world relevance; on the contrary, modified stem development underpins major yield increases

in cereal crops (Hedden 2003). However, the technical challenges of studying the relatively inaccessible, 3-dimensional RZ have made it an unattractive research subject.

Nonetheless, there is a growing body of work on stem development, which highlights the particular importance of the cell division regulation in the RZ. Cells divide most actively in the top 0.5-2 mm of the stem (Davière et al. 2014) and then rapidly expand until ceasing growth a few cm below the apex (Hall and Ellis 2012; Bencivenga et al. 2016). In *Arabidopsis*, activation of cell divisions in the RZ is necessary for the rapid stem elongation that accompanies the transition to flowering, and can similarly drive a switch from rosette to caulescent growth in *Arabidopsis* (Ejaz et al. 2021). Furthermore, inhibiting gibberellin signalling in just the top 2 mm of the stem potently represses stem elongation, underlining the importance of the actively dividing region (Serrano-Mislata et al. 2017).

3D imaging techniques that, in the absence of live cell tracking, can reconstruct growth and cell division patterns, have shed light on oriented growth in the RZ (Bencivenga et al. 2016; Serrano-Mislata et al. 2017). Cells in the rib meristem consistently divide transversely and growth in this region is largely parallel to the main stem axis (Bencivenga et al. 2016). Peripheral to the rib meristem, cell division orientation is more variable and radial, which correlates with a more radial growth direction (Bencivenga et al. 2016). In *rpl* mutants, ectopic expression of organ boundary genes makes cell division orientation in the rib meristem more similar to the RZ periphery (i.e. more variable and radial) (Bencivenga et al. 2016). This change is associated with impaired stem elongation, suggesting that growth and cell division orientation in the RZ might have significant impacts on stem growth. RZ activity can also affect the properties of the SAM independently of stem growth: regulation of cell proliferation in the RZ via gibberellin signalling and the cell-cycle regulator KRP2, regulates overall meristem size but not stem elongation (Serrano-Mislata et al. 2017).

The *1aiqd* mutant has a unique combination of RZ and stem growth phenotypes (Mckechnie-Welsh 2021). *1aiqd* plants have thicker stems, with mean cross-sectional area up to 88% larger than wild type plants. The increase in stem radius derives entirely from an increase in the number of pith cell files, ruling out increased secondary growth (which occurs in the cambium) as a contributing factor. Associations between altered cell number/morphology and organ shape have been reported for other lines with altered *IQD* activity. For example, the elongated fruit shapes of tomatoes overexpressing *SlIQD21a* or *SUN* are associated with directional changes in cell shape and/or number (Bao et al. 2023; Wu et al. 2011). Since pith cells derive from the rib meristem, it is plausible that the

increase in cell number derives from changes in the RZ. Close inspection of *1aiqd* rib meristems revealed that most new cell walls are oriented transversally (generating vertically stacked daughters), but cell division orientation is overall more variable than in wild type plants (Mckechnie-Welsh 2021). Moreover, small numbers of rib meristem cells divide radially (the new cell walls running longitudinally from the top to the bottom of the cell) in *1aiqd* mutants, which is very rarely observed in wild type plants. This produces horizontally adjacent daughter cells, which could explain the increased number of pith cell files.

The increase in misoriented cell divisions offers a plausible mechanism to explain the increase in pith cell number and stem thickness: radial cell divisions insert new files of pith cells and the larger number of radially expanding cells drives increased radial growth of the stem. However, drawing a direct line from cell division orientation to growth is not trivial. Firstly, cell division orientation responds to cues that coordinate organ-scale growth, including mechanical stress and hormone signalling (Mirabet et al. 2018; Hoermayer et al. 2024; Yoshida et al. 2014; Louveaux et al. 2016). Therefore, misoriented cell divisions could be an output of organ-level changes in oriented growth rather than a driver. Furthermore, the placement of a new cell wall does not in itself drive growth – it merely subdivides an already-growing entity (a cell), leading some to argue that cell division overall contributes little to organ morphogenesis (Burda et al. 2024). The *1aiqd* mutant offers an opportunity to test how cell division in the RZ might influence radial stem growth.

2.1.1 Chapter aims

In this chapter I further characterise the growth and cellular phenotypes of the *1aiqd* mutant. I firstly describe the generation of a modified *1a iqd* sextuple loss-of-function line, designed to overcome transgene silencing issues that plagued the original *1aiqd* mutant line (Mckechnie-Welsh 2021). After confirming that the new line (referred to as *1aiqd-2*) has the same phenotypes as the original, I characterise vertical and radial growth over time and at different levels of spatial and temporal resolution. I then focus on the rib meristem, providing a detailed characterisation of the changes in cell geometry, number and growth within this region.

2.2 RESULTS

2.2.1 Constructing the *1aiqd-2* mutant

The sextuple mutant *1aiqd* was previously generated by combining one loss-of-function CRISPR-Cas9-induced mutation in the *IQD24* gene with T-DNA insertions mutations for the remaining five 1A *IQD* genes (Mckechnie-Welsh 2021). However, work to express fluorescent reporters in this genetic background failed. Introduction of several different

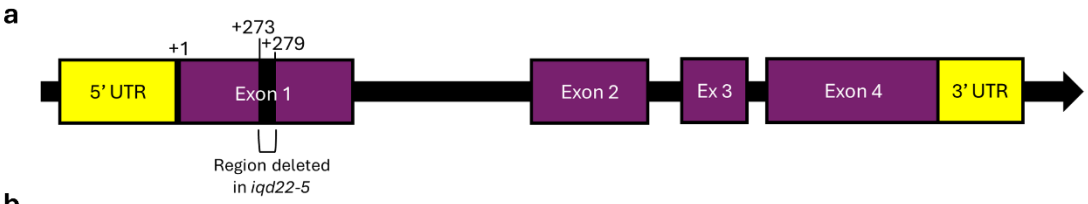

b

IQD22

MGKASRWFRSLFGVKKPDPGYPDLSVETPSRSTSSNLKRRWSFVKSKREKESTPINQVPHTPSLPNSTPPPPSHHQSSPRRRRKQKPMWED
EGSEDSDKHAIAVAAATAAVAEAAVAAANAAAAVVRLTSTSGRSTRSPVKARFSDGFDDVVAHGSKFYGHGRDSCELAVIKIQSIFRGYLAKRA
LRALKGLVRLQAIVRGHIERKRMSVHLRRMHALVRAQARVRATRVIVTPESSSSQSNNTKSSHFQNPGPPTPEKLEHSISSRSSKLAHSHLFKR
NGSKASDNNRLYPAHRETFSATDEEEKILQIDRKHISSYTRRNRPDMFYSSHLILDNAGLSEPVFATPFSPSSSHEEITSQFCTAENSPQLYSATS
RSKRSAFTASSIAPSDCTKSCCDGDHPSYMACTESSRAKARSASAPKSRPQLFYERPSSKRFGFVDLPYCGDTKSGPQKGSALHTSFMNKAY
PGSGRLDRLGMPIGYRY*

iqd22-5

MGKASRWFRSLFGVKKPDPGYPDLSVETPSRSTSSNLKRRWSFVKSKREKESTPINQVPHTPSLPNSTPPPPSHHQSSPRRRRKQKPMWE***E***
VKIRTSMLLRWLPRLLRLLKLQSPPLMLLLRSSG*

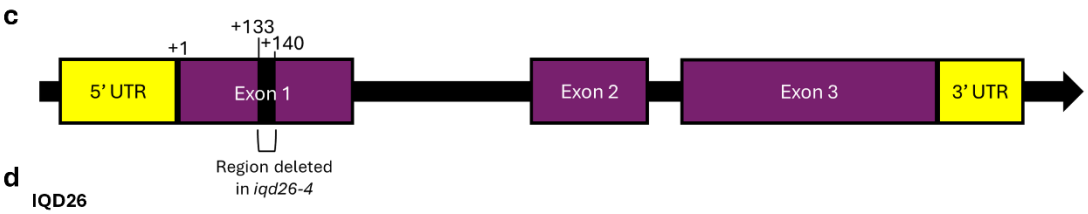

d

IQD26

MGRAARWFKGIFGMKKSKEKENCVSGDVGGEAGGSNIHRKVLQADSVWLRTYLAETDKEQNKHAIAVAAATAAAADAAVAAAQAAVAVVRL
TSNGRSGGYSGNAMERWAAVKIQSVFKGYLARKALRALKGLVKLQALVRGYLVRKRAAETLHSMQALIRAQTSVRSQRINRNNMFHPRHSLE
RLDDSRSEIHSKRISISVEKQSNHNNNAYDETSPKIVEIDTYKTKSRSKRMNVAVSECGDDFIYQAKDFEWSFPGEKCKFPTAQNTPRFSSSMA
NNNYYYTPPSPAKSVCRDACFRPSYPGLMTPSYMANTQSFKAKVRSHSAPRQRPDRKRLSLDEIMAARSSVSGVRMVQPQPQPQTQTQQQ
KRSPCSYDHQFRQNETDFRFYN*

iqd26-4

MGRAARWFKGIFGMKKSKEKENCVSGDVGGEAGGSNIHRKVLQA***LAQNLPCGNRQRTEQTRDCGCCCYSRGC****

Figure 2: CRISPR-Cas9 induced mutations in *IQD22* and *IQD26* are predicted to disrupt and truncate translated protein sequences. (a) Diagram showing the location of the 7 bp region of the *IQD22* genomic sequence deleted in the *iqd22-5* mutant allele in the. **(b)** Wild type amino acid sequence of IQD22, compared with the predicted amino acid sequence that would be translated from the *iqd22-5* allele. **(c)** Diagram showing the location of the 8 bp region of the *IQD26* genomic sequence deleted in the *iqd26-4* mutant allele. **(d)** Wild type amino acid sequence of *IQD26*, compared with the predicted amino acid sequence that would be translated from the *iqd26-4* allele. Bold italics indicate regions of predicted amino acid sequence that differ from the wild type allele, due to frame shift. * indicates a stop codon.

reporters into this background, by crossing or transformation, resulted in total or chimeric silencing of the reporters (Mckechnie-Welsh 2021). Successive outcrossing determined that silencing was associated with the presence of the *iqd22-1* and *iqd26-3* T-DNA insertion alleles. The *iqd22-1* and *iqd26-3* derive from the SALK and GABI collections, respectively. T-DNA insertion mutants from these collections have previously been shown

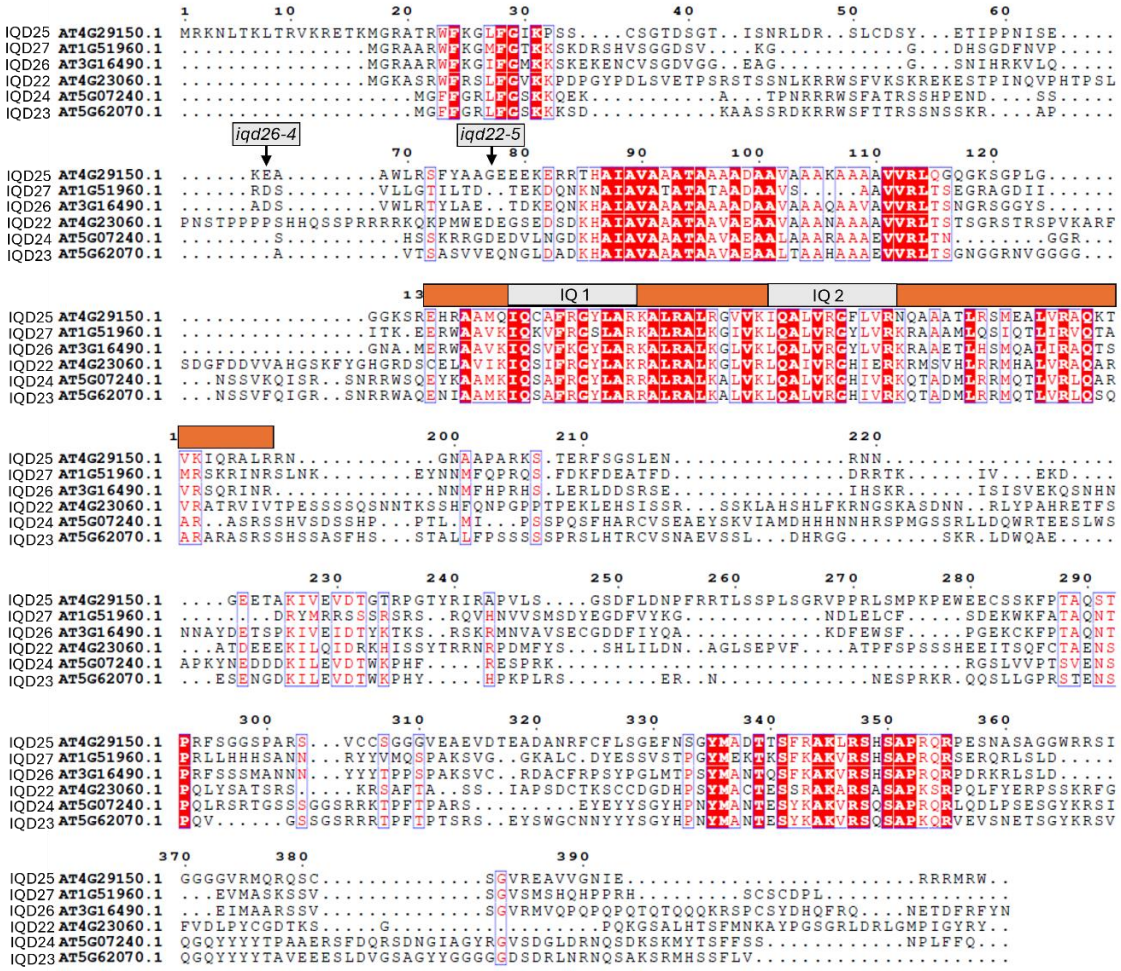

Figure 3: *iqd22-5* and *iqd26-4* mutations are predicted to disrupt the most conserved protein sequences. Multiple sequence alignment between the protein sequences of the 1A IQD subfamily. The position of the first amino acids disrupted by the *iqd22-5* and *iqd26-4* mutations, and the location of the IQ67 domain (orange bar), IQ1 and IQ2 motifs are indicated. Residues with a high % of equivalence across sequences (based on identity and shared physico-chemical properties) are coloured. Letters representing residues that are identical in all sequences are coloured white with a red background. Letters representing residues that differ between sequences but share physicochemical properties are coloured red. Colour-coding was generated using ESPript version 3.0 https://espript.ibcp.fr/ESPript/cgi-bin/ESPript.cgi (Robert and Gouet, 2014)

to induce transgene silencing, and different individual T-DNA insertion lines vary in their propensity to induce silencing (Daxinger et al. 2008; Mlotshwa et al. 2010). The observed transgene silencing was therefore likely to be induced by the presence of the *iqd22-1* and *iqd26-3* alleles, and it was determined that these should be substituted with novel CRISPR-Cas9-induced alleles.

Constructs designed to induce CRISRP-Cas9 mutagenesis in *IQD22* and *IQD26* were introduced into a genetic background containing *iqd23-2*, *iqd24*, and *iqd27-2*. Several mutations were induced at both loci, and one allele from each – hereafter referred to as *iqd22-5* and *iqd26-4* – were selected. A line containing all five mutations was crossed back to the original *1aiqd* mutant to introduce the *iqd25-1* allele into the same background. Successive rounds of crossing and selfing generated the new sextuple *1aiqd* mutant, hereafter referred to as *1aiqd-2* to differentiate it from the original version of the line.

iqd22-5 and *iqd26-4* are predicted to be loss of function mutations. The *iqd22-5* and *iqd26-4* alleles both contain short (7 bp and 8 bp, respectively) deletions in the first exons of their respective proteins. Both deletions generate a frame shift and premature stop codon in the protein coding sequence (**fig. 2**). Multiple sequence alignment of the 1A IQD subfamily reveals two regions that are highly conserved across the subfamily – the IQ67 domain, containing the IQ1 and IQ2 motifs (Abel et al. 2005), and a region rich in hydrophobic residues, situated N-terminally relative to the IQ67 domain (**fig. 3**). The high level of amino acid sequence conservation suggests that these regions are important for protein function. The *iqd22-5* and *iqd26-4* are situated N-terminally to these regions (**fig. 3**) and are therefore completely disrupt them.

I have successfully transformed several different transgenes in this line (see Section 2.2.7 and Chapter 3), indicating that the *1aiqd-2* line is not as prone to transgene silencing as the original *1aiqd* line.

2.2.2 Phenotypes of the *1aiqd-2* mutant

To determine whether the *1aiqd-2* line could replicate the organ phenotypes of the *1aiqd* mutant, *1aiqd-2* plants were grown alongside wild type col-0 plants and stem diameter was measured on the day when the first floral abscission was observed. Diameter was measured at three positions on the stem: near the top of the stem at an ink mark approx. 2 mm from the meristem; where the first silique pedicel meets the stem; at the base of the stem (**fig. 4a**). At all positions, the *1aiqd-2* mutant had significantly larger stem diameter

(**fig. 4a-d**). The *1aiqd-2* diameter was on average 12% larger near the stem apex, 18% larger at the first silique, and 21% at the stem base. *1aiqd-2* mutants were also significantly shorter (17% short on average) than the wild type at this stage (**fig. 4e**). This is

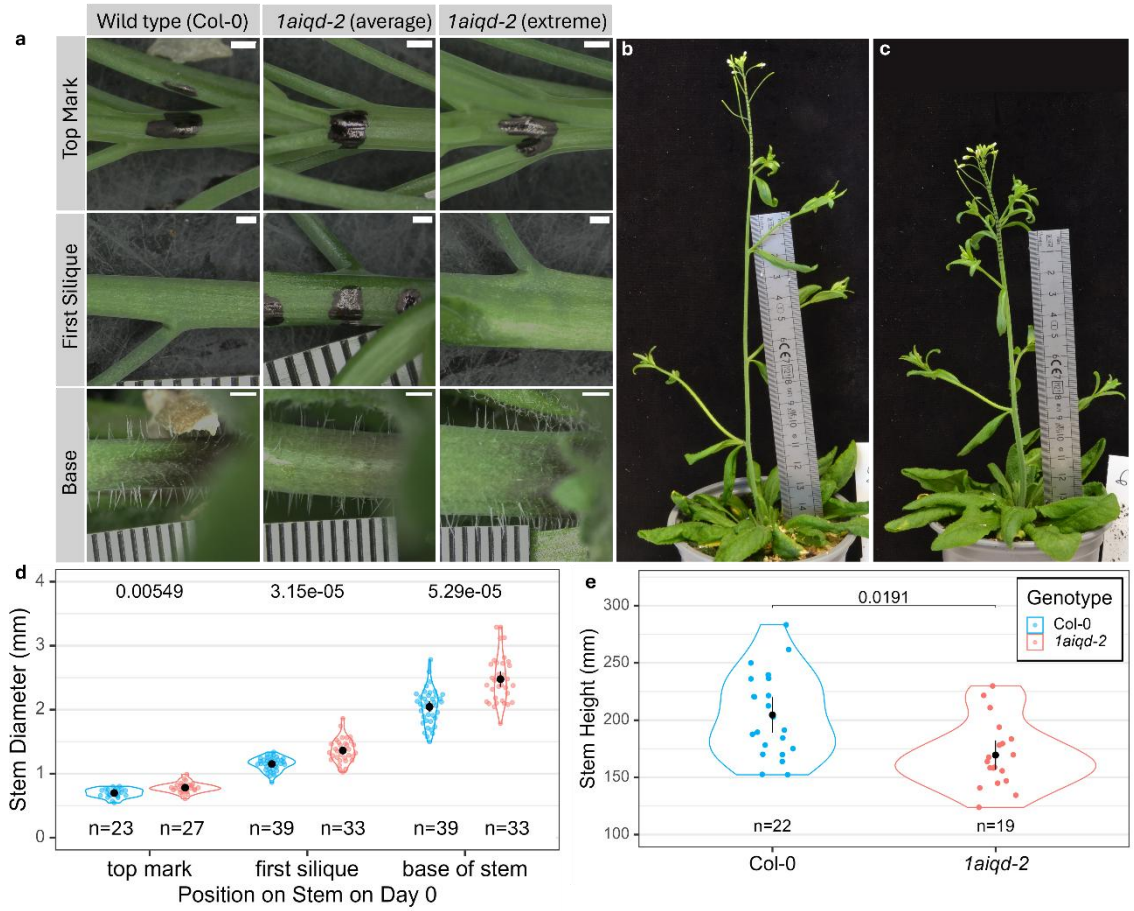

Figure 4: *1aiqd-2* stems are significantly thicker and shorter than the wild type at the time of first floral organ abscission. (a) Stereomicrographs of three plants stems at the base, at the position where the pedicel of the first silique attaches to the stem and at a pen ink landmark drawn approx. 2 mm from the meristem. Stems shown in the left and middle columns of panels have similar dimensions to the mean values for their respective genotypes. The stem shown in the right 3 panels is a *1aiqd-2* mutant with dimensions near the maximum values recorded for the genotype. **(b,c)** Photographs showing wild-type (b) and *1aiqd-2* (c) plants on day 0, the day when the first abscission of floral organs was observed. **(d)** Stem diameters, measured on day 0 at the positions shown in (a). **(e)** Stem heights, measured on day 0. Black dots and whiskers show mean and 95% confidence interval (CI) of the mean. p values were calculated using the Mann Whitney U test. Scale bar: 0.5 mm (top and middle panels of (a)), 1 mm (bottom panels of (a)).

similar to *1aiqd* plants – wild type and *1aiqd* plants were measured when they had four elongated siliques and *1aiqd* was found to be significantly shorter (Mckechnie-Welsh 2021). The difference may derive from the two lines reaching first floral organ abscission at different ages: *1aiqd-2* were measured for the first time significantly earlier than wild type plants (Mann Whitney U test, $U = 280$, $p = 3.4 \times 10^{-5}$). The median age at first measurement for *1aiqd-2* plants was 34 days, whereas for wild type plants it was 37 days.

The original *1aiqd* mutant also displayed a prominent rosette leaf phenotype (Mckechnie-Welsh 2021), that was reproduced by the *1aiqd-2* mutant. The rosette leaves of the *1aiqd-2* mutant appear broader and flatter and this was visibly apparent after at least 2.5 weeks of growth **(fig. 5).** Superficially, this is similar to the phenotype of plants of expressing IQD22 translationally fused to mCherry, under the control of its native promoter

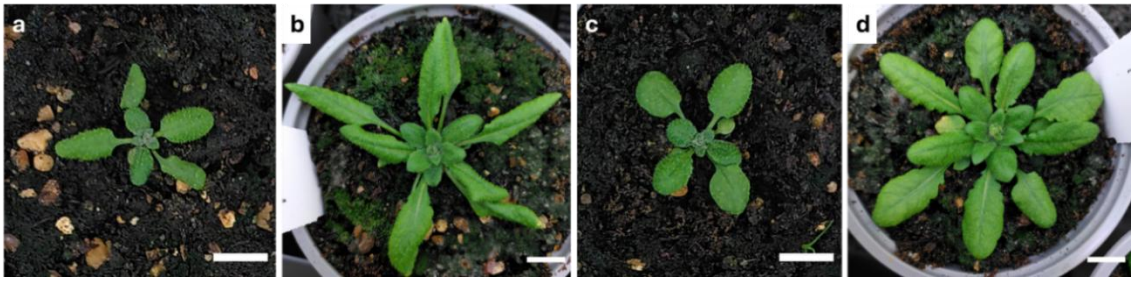

Figure 5: *1aiqd-2* plants have flatter, rounder-looking looking leaves compared to wild type. Photographs of wild type (a,b) and *1aiqd-2* (c,d) rosettes. (a,c) 2.5-week-old plants. (b,d) 4-week-old plants. Scale bar: 1 cm

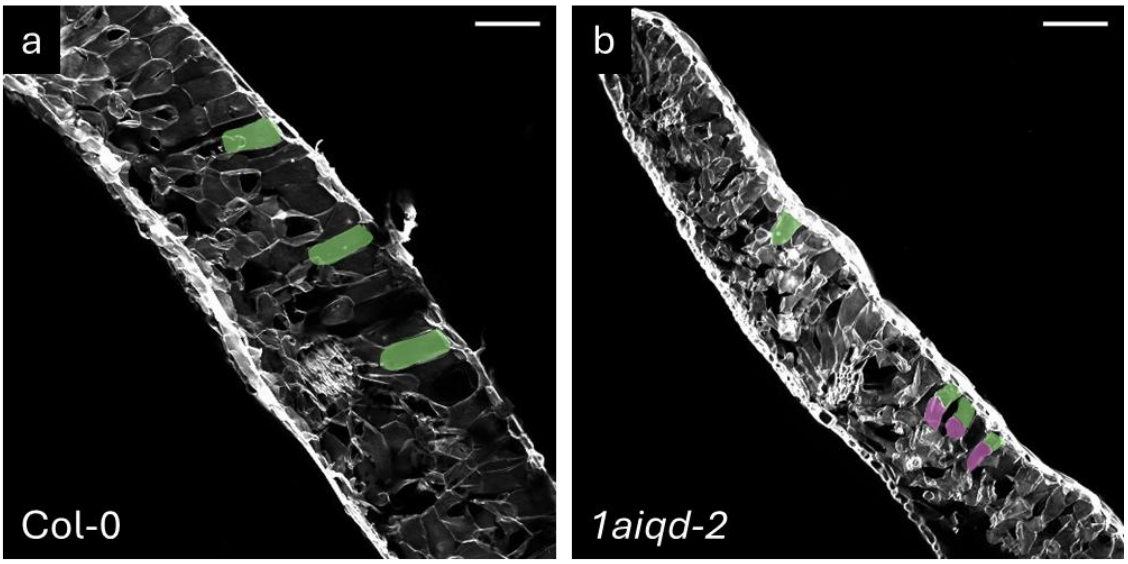

Figure 6: Preliminary indications of a palisade cell division phenotype in the *1aiqd-2* mutant. Maximum intensity Z-projections of leaf cross-sections. Fully expanded rosette

leaves were sectioned by hand and stained with calcofluor white. Selected palisade cells are highlighted in green. Where palisade cells have undergone a periclinal division, the two sister cells are highlighted in green and pink.

(*proIQD22::IQD22-mCherry)* (Matthes et al. 2022). In leaves, *IQD22* expression is specific to palisade cells (Matthes et al. 2022; Procko et al. 2022). The leaves of *proIQD22:IQD22-mCherry* plants are rounder and thicker than their wild type counterparts and microscopic examination revealed that these leaves have an increased number of palisade cell layers , which is an anatomical characteristic of "sun" leaves (Matthes et al. 2022; Boardman 1977). A preliminary inspection of *1aiqd-2* rosette leaves revealed that some palisade cells had periclinal cell divisions, which are rarely observed in the wild type **(fig 6)**. Typically palisade cells divide anticlinally, to maintain a growing single layer of cells, and only undergo periclinal conditions when plants are grown under high light conditions (Weston et al. 2000). A quantification of leaf thickness and palisade cell layers would be necessary to confirm whether the *1aiqd-2* mutant does indeed have a "sun" leaf phenotype, like *proIQD22:IQD22-mCherry*, but this was beyond the scope of this project. If the *1aiqd-2* leaf phenotype does indeed share an anatomical basis with the *proIQD22:IQD22-mCherry* line, this would raise the question of why expressing *IQD22* and mutating it (alongside the other 5 1A *IQDs*) would yield a similar outcome. It might reflect antagonistic interactions among the 1A *IQDs*. Alternatively, the *proIQD22:IQD22-mCherry* might be an *IQD22* loss-of-function line arising from to transgene-induced silencing or dominant negative effects of the IQD22 protein fusion. Functionality of the *IQD22* protein in this line was not confirmed by mutant complementation, nor was the expression of the native *IQD22* confirmed by RT-PCR (Matthes et al. 2022).

2.2.3 Growth dynamics of the *1aiqd-2* mutant post-flowering

The increase in thickness of *1aiqd-2* stems relative to the wild type implies that the *1aiqd-2* mutant has a faster radial growth rate. To test this hypothesis, I measured *1aiqd-2* and wild type stems two time points: the day when first floral organ abscission was observed (day 0) and four days later (day 4). After four days, the increase in stem diameter in *1aiqd-2* plants was not significantly different from wild type plants, whether measured in absolute or relative terms **(fig 7a, c)**.

Since an increase in growth in one direction might induce a compensatory but inverse growth effect in the perpendicular direction, I also measured vertical growth. On each plant I drew 24 ink marks at 2 mm intervals, starting 2 mm from the meristem. This divided the plant into 25 segments, where segment one was between the meristem and the first

mark, and segment 25 was between the lowest mark and the base of the stem. I measured the length of each segment on day 0 and day 4, and calculated the difference to determine vertical growth. The absolute amount of stem elongation was not significantly

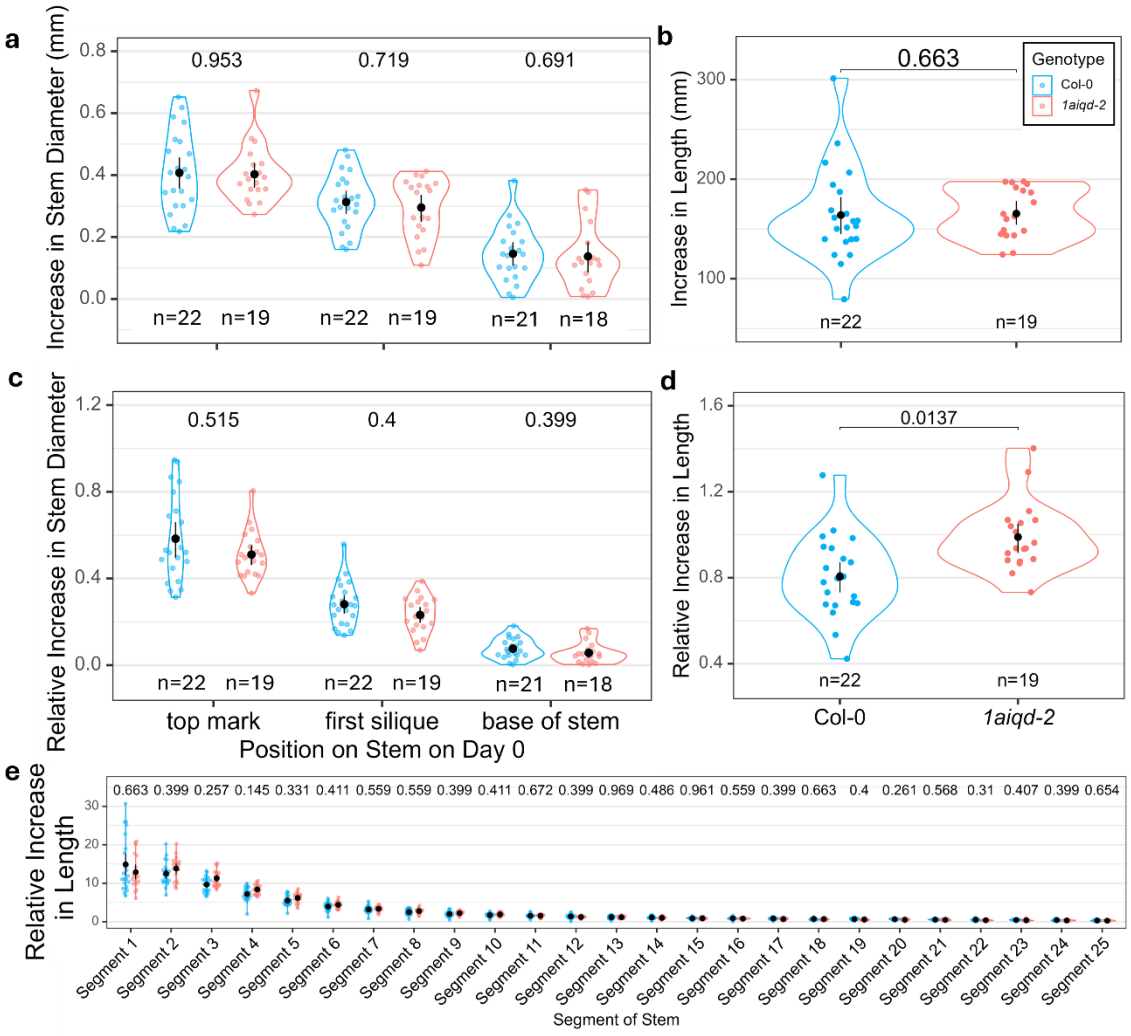

Figure 7: Wild type and *1aiqd-2* plants grow by a similar amount over four days after flower abscission. **(a)** Absolute increase in stem diameter after four days, measured at three positions on the stem: the top mark on the stem (approx. 2 mm from the meristem), where the first silique is attached to the stem, and the base of the stem. **(b)** Absolute increase in stem height after four days. **(c, d)** The same data as presented in (a) and (b) but expressed as a proportion of the measurement on day 0. **(e)** Relative increase in the length of 2 mm-long stem segments over four days, where segment 1 is the most apical segment. Adjusted p values for pairwise comparisons are shown. Initial p values were calculated using the Mann Whitney U test. The p values for the whole dataset were than adjusted using the Benjamini-Hochberg method. Black dots and whiskers show mean and 95% confidence interval of the mean.

different between the wild type and mutant (**fig. 7b**). When stem elongation is expressed relative to the starting height, the *1aiqd-2* mutant grew significantly more (**fig. 7d**). However, this result is uninformative because the *1aiqd-2* plants were shorter to begin with (**fig. 4e**) and starting height is unlikely to be important to growth rate, since for both lines most vertical growth occurred in only the top 1.4 cm of the stem (segments 1 to 7) (**fig. 7e**). The observation that most elongation occurred in the top 1.4 cm is consistent with previous findings (Bencivenga et al. 2016). There was also no difference in elongation at the level of individual stem segments (**fig. 7e**). Therefore, the *1aiqd-2* mutant has a comparable rate of stem elongation to the wild type. The same observation has been made of the original *1aiqd* mutant (Mckechnie-Welsh 2021).

In summary, the stems of *1aiqd-2* mutants are typically thicker than those of wild type plants along the whole length of the stem. However, radial growth during this stage (post first floral organ abscission) occurs at a similar rate.

Based on these findings, there are three possible mechanisms that give *1aiqd-2* mutants a thicker stem:

1. *1aiqd-2* stems exhibit more rapid radial growth than the wild type but only within the top 2 mm of the meristem. Therefore, all the difference in stem thickness between wild type and mutant stems is established in this region and maintained as the stems proceed to grow at a similar rate. This seems reasonable when considering a significant difference in stem thickness was observed only 2 mm from the meristem in these mature plants.
2. *1aiqd-2* stems exhibit more rapid radial growth over a larger region than the top 2 mm, but the difference is too small to detect in older stems. The diameter of new stem tissue decreases as the stem grows – i.e. the diameter at the base of a 1 cm stem is much greater than the diameter 1 cm from the top of a 15 cm stem. If the difference in growth rate between *1aiqd-2* and wild type is proportional to the size of the stem, the absolute difference would be greater in smaller plants, and therefore easier to detect.
3. The *1aiqd-2* stems do not exhibit more rapid radial growth than wild type plants. Instead, *1aiqd-2* stems are thicker from the outset because the mutant has a larger SAM.

2.2.4 Growth dynamics of the *1aiqd-2* mutant pre-flowering

To determine whether *1aiqd-2* plants grow more than wild type plants at an earlier stage of development, I performed another growth-tracking experiment. I first measured plants when their stems were approx. 6.5 mm tall and tracked their growth over four days, with measurements taken at two-day intervals (**fig. 8**). Although the actual stem heights on day 0 ranged between 4 and 9 mm, the distributions of heights were statistically similar

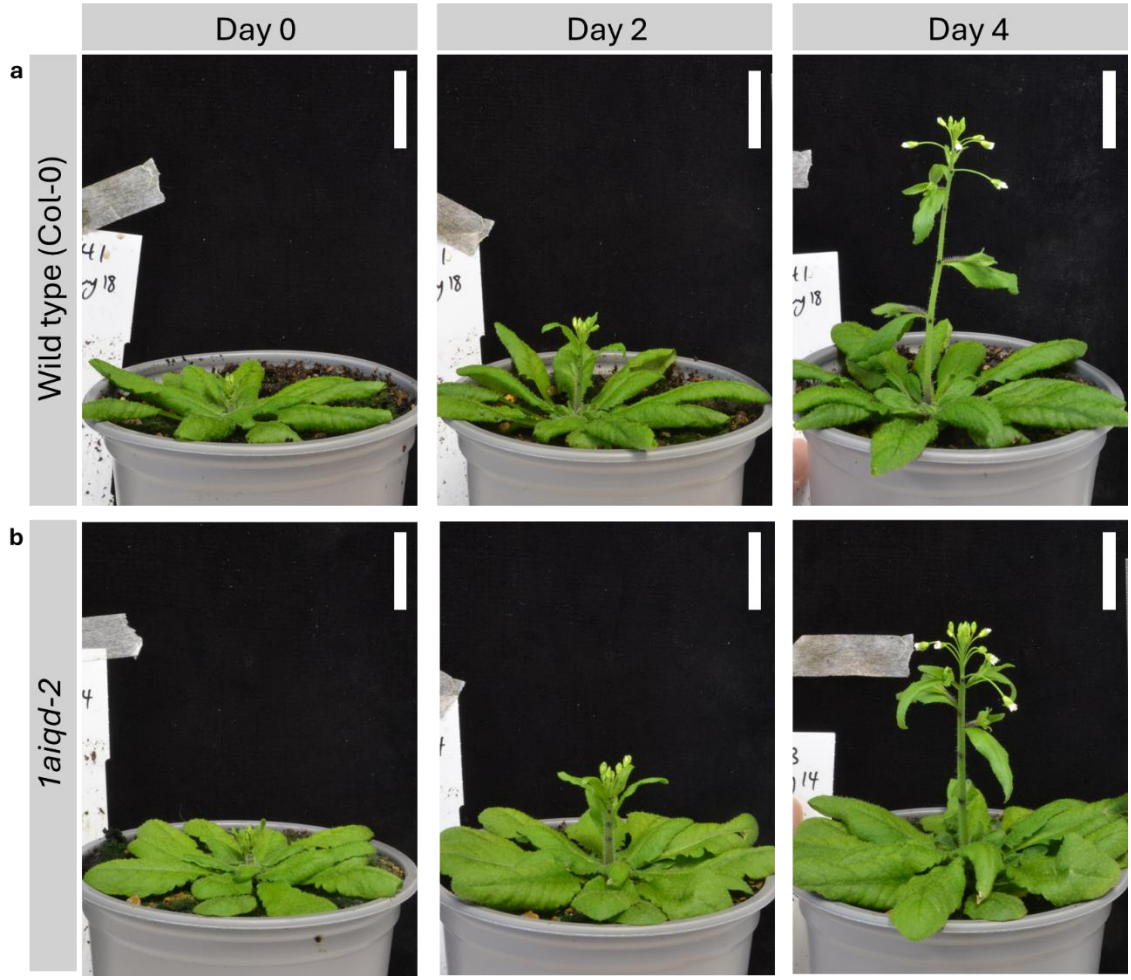

Figure 8: Experimental set up for measuring plant growth prior to flowering. Photographs of the same wild type **(a)** and *1aiqd-2* **(b)** plants on day 0, 2 and 4. Scale bar: 2 mm. On day 0, plants approx. 6.5 mm tall were marked with ink dots at approximately 1 mm, 2 mm, 3 mm and 4 mm from the SAM. The same plants were imaged for measurement 2 and 4 days later. At each time point, a portion of the plants were dissected, fixed in EtOH and retained for microscopic analysis.

between genotypes, indicating no bias in the sampling (**fig. 9a**). On day 0, the stems were marked with ink dots at approximately 1 mm, 2 mm, 3 mm and 4 mm from the stem apex. On days 0, 2, and 4, the stem diameter was measured at the position of each mark. The

marks divided the plant into five segments, where segment one is between the stem apex and the 1 mm mark, and segment five is between the 4 mm mark and the stem base. The length of these segments was also measured on days 0, 2 and 4. At each time point, I dissected a portion of the plants, fixed them in EtOH and retained them for microscopic analysis. For these plants, I also measured the diameter at the base of the stem.

On day 0, the diameter of *1aiqd-2* plants at all 4 marked positions was significantly larger than the wild type (**fig. 9b-d**). The relative difference in diameter was similar across all 4 of the marked positions, being 22-24% greater than the wild type. Even at 1 mm from the stem apex, *1aiqd-2* stem diameters were on average 0.16 mm (95% CI: 0.1-0.23) or 24% larger than the wild type. The differences in stem diameter remained broadly consistent over four days: at position 3 (marked approx. 3 mm from the stem apex on day 0), *1aiqd-2* stem diameters were on average 0.24 mm (95% CI: 0.20-0.28) or 24% larger on day 0, 0.29 mm (95% CI: 0.24-0.35) or 23.3% larger on day 2 and were 0.29mm (95% CI: 0.21-0.37) or 19.2% larger on day 4 (**fig. 9d,e**).

Between day 0 and day 2, the *1aiqd-2* plants exhibited slightly more absolute radial growth than the wild type at position 3: wild type plants grew 0.23 mm (95% CI: 0.22-0.25), while *1aiqd-2* plants grew 0.29 mm (95% CI: 0.27-0.32) (**fig. 10a**). A small, although not statistically significant, difference was also observed at position 4 – the wild type plants grew 0.24 mm (95% CI: 0.22-0.27) and *1aiqd-2* plants grew 0.29 mm (95% CI 0.26 – 0.32). However, the two genotypes showed no significant differences in growth at these positions when measured over the whole 4-day period (**fig. 10c**). Since there was no significant difference in growth at these positions between days 2 and 4 (i.e. the wild type did not grow more in this period to "catch up" with the mutant, **fig. 10b**), this implies that any statistically detectable differences established after the first two days were abolished by the increased variability in growth over the following two-day period.

There was no significant difference in stem elongation between the genotypes, either over the total length of the stem or within individual segments (**fig. 11**). Since the plants were the same height to begin with and subsequently elongated at the same rate, this implies that the difference in height observed at the stage of first floral organ abscission (**fig. 4e**) derive from *1aiqd-2* plants reaching this developmental stage slightly earlier.

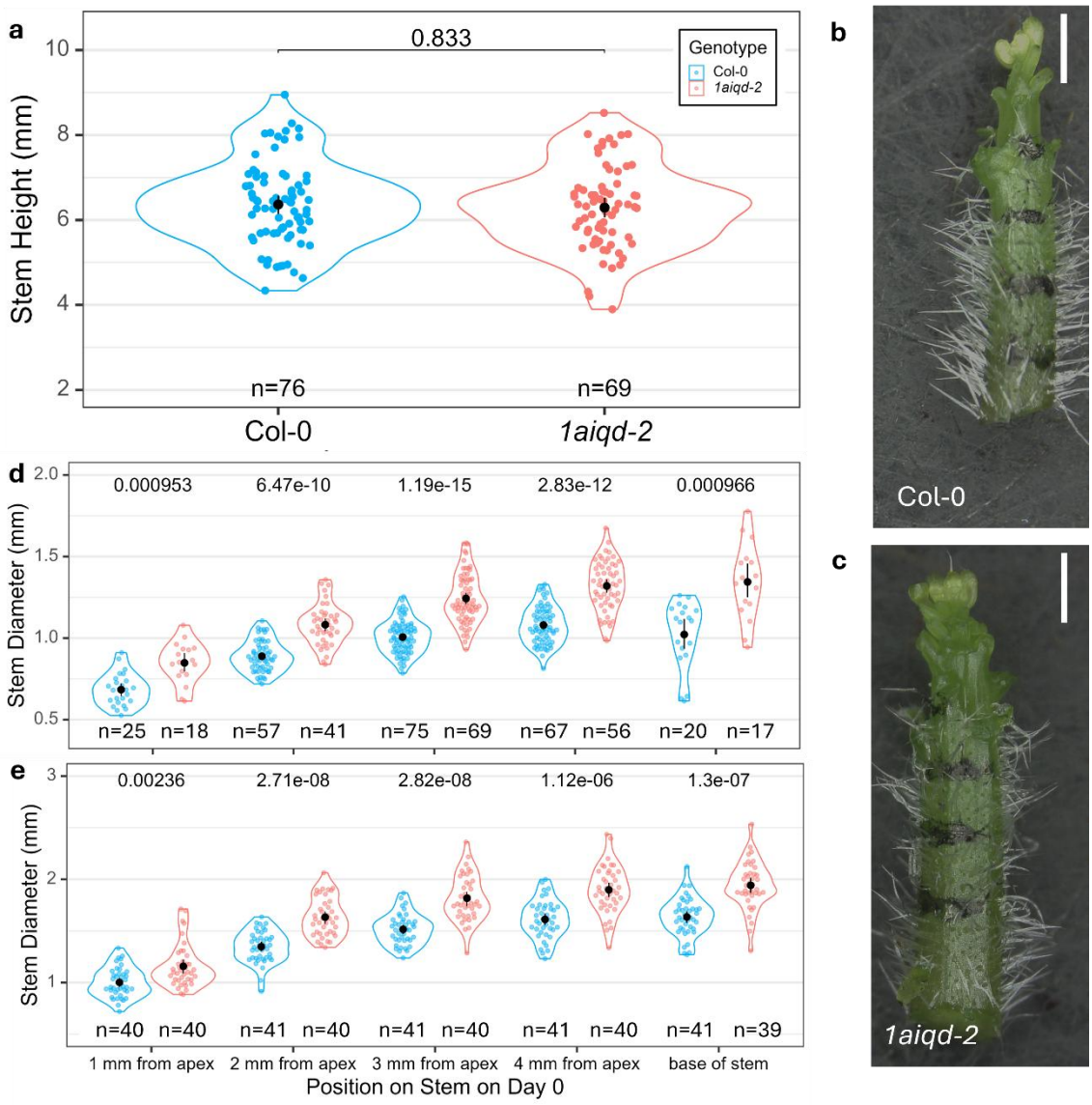

Figure 9: The *1aiqd-2* thick stem phenotype is evident in the early stages of stem growth. **(a)** The height of *1aiqd-2* and wild type stems on the first day of measurement (day 0). **(b)** A wild type and **(c)** *1aiqd-2* stem, harvested on day 0. Both have stem radii similar to the average for the genotype. **(d)** Stem diameter at ink landmarks drawn approx. 1 mm, 2 mm, 3 mm and 4 mm from the stem apex (see b and c), and at the base of the stem. Sample sizes differ between positions, because accurate stem diameters could not be accurately measured for all positions on all plants because they were partially obscured by leaves or branches. **(e)** Stem diameter at the same landmarks, after four days of growth. Note that sample sizes are smaller than in (d), because some plants were harvested on day 0 and day 2. Adjusted p values for pairwise comparisons are shown. Initial p values were calculated using the Mann Whitney U test. The p values for the whole dataset were then adjusted using the Benjamini-Hochberg method. Black dots and whiskers show mean and 95% CI of the mean. Scale bar: 1 mm

Notably, while the amount of radial growth was similar at all positions measured – after four days, the increase in diameter was 0.5-0.6mm, or 40-50% – elongation varied substantially between segments – segment 3 grew by 1100-1200% over four days,

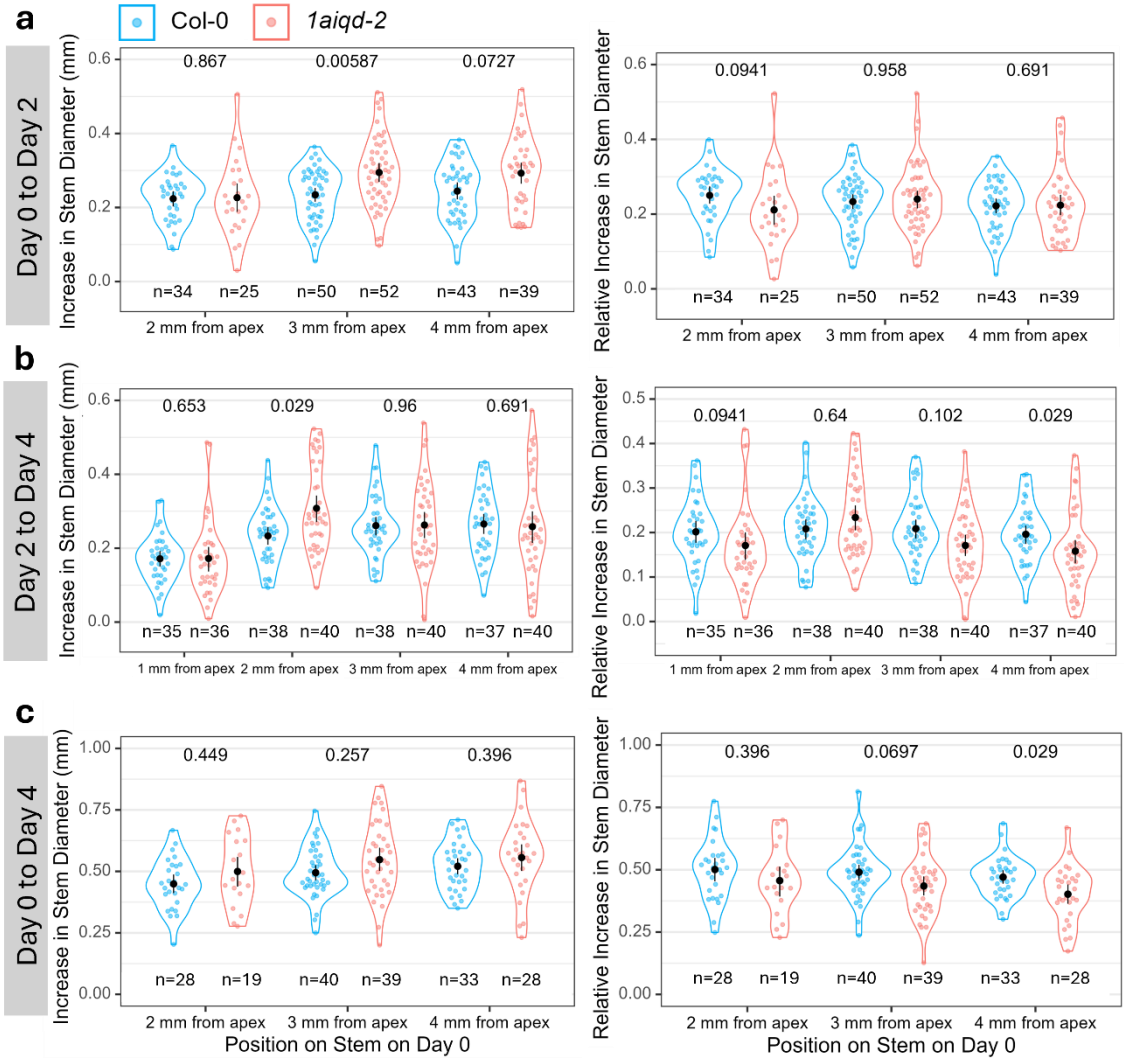

Figure 10: Wild type and *1aiqd-2* plants grow by a similar amount over two days and four days. Change in stem diameter from day 0 to day 2 **(a)**, day 2 to day 4 **(b)** and day 0 to day 4 **(c)** expressed in mm (left panels), and as a proportion of the initial diameter on day 0 (right panels). Stem diameter was measured at ink landmarks drawn approx. 2 mm, 3 mm and 4 mm from the stem apex (see fig. 9b,c), and at the base of the stem. There was insufficient data for the landmark 1 mm from the stem because in most plants that were retained for growth measurements, the stem diameter at this position was obscured by branches on day 0. Adjusted p values for pairwise comparisons are shown. Initial p values were calculated using the Mann Whitney U test. The p values for the whole dataset were then adjusted using the Benjamini-Hochberg method. Black dots and whiskers show mean and 95% CI of the mean.

whereas segment 1 grew by only ~450% (**fig. 11b**). Thus, rapid elongation in a particular stem region did not influence its radial expansion rate and so radial and vertical growth were not closely coupled. This might explain why the increased thickness of *1aiqd-2* stems did not induce a compensatory reduction in height/ elongation rate.

These data indicate that the stem thickness phenotype of *1aiqd-2* mutants is established early in two senses: the phenotype is already established in stems that have very recently

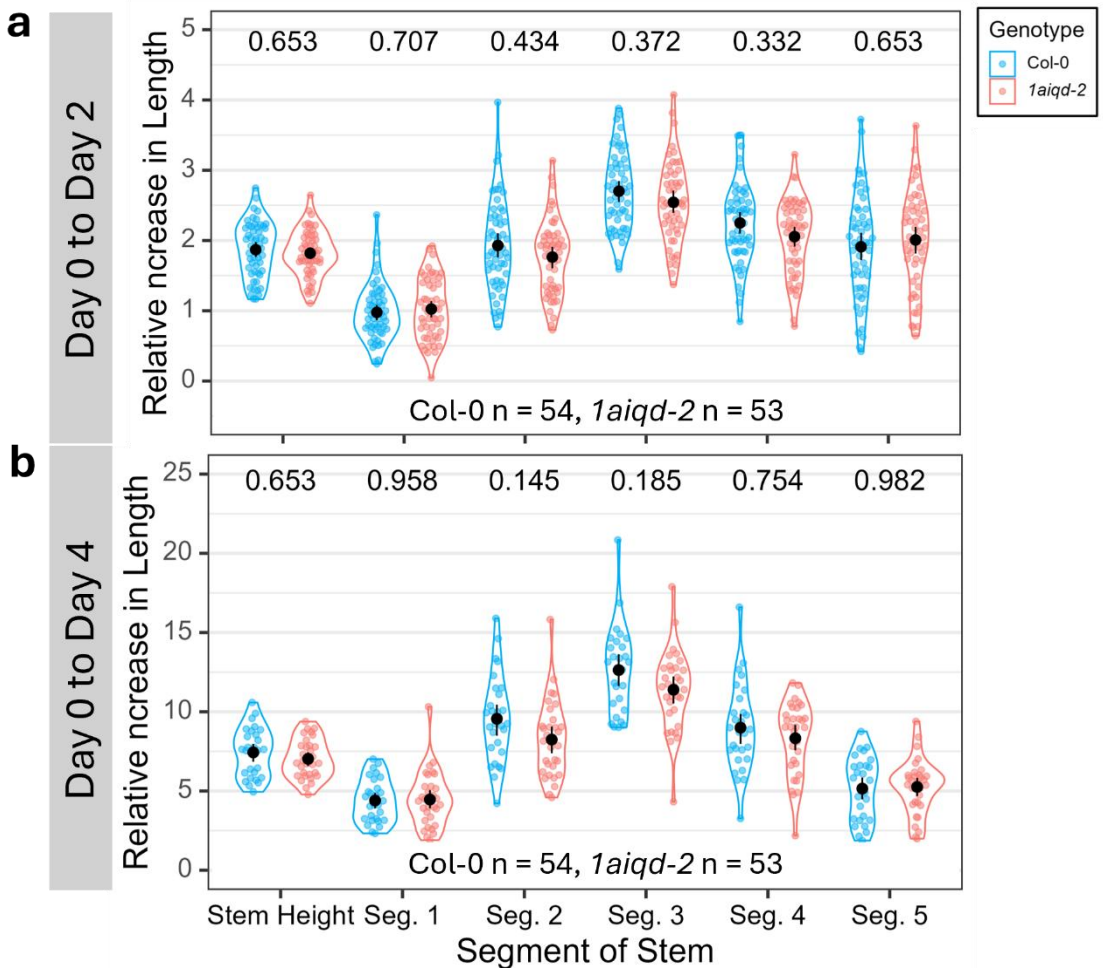

Figure 11: *1aiqd-2* and wild type stems elongate by a similar amount over two and four days. Increase in the length of stem segments and the height of the stem after two **(a)** and four **(b)** days, relative to the length on day 0. The segments are the distance between ink landmarks as shown in fig. 9b,c . Segment (Seg.) 1 is the region between the uppermost landmark and the apex of the stem, seg. 2 is between the first and second landmarks and so on. Adjusted p values for pairwise comparisons are shown. Initial p values were calculated using the Mann Whitney U test. The p values for the whole dataset were then adjusted using the Benjamini-Hochberg method. Black dots and whiskers show mean and 95% CI of the mean.

bolted, and the differences are established within ~1 mm of the meristem. Although *1aiqd-2* plants may exhibit slightly more radial growth in stem regions > 2 mm from the apex, this contributes little to the overall difference between genotypes. These findings disprove the hypothesis that *1aiqd-2* stems are thicker because they exhibit more rapid radial growth over a larger region than the top 2 mm of stem. The two remaining hypotheses – (1) *1aiqd-2* stems exhibit more rapid radial growth than wild type but only

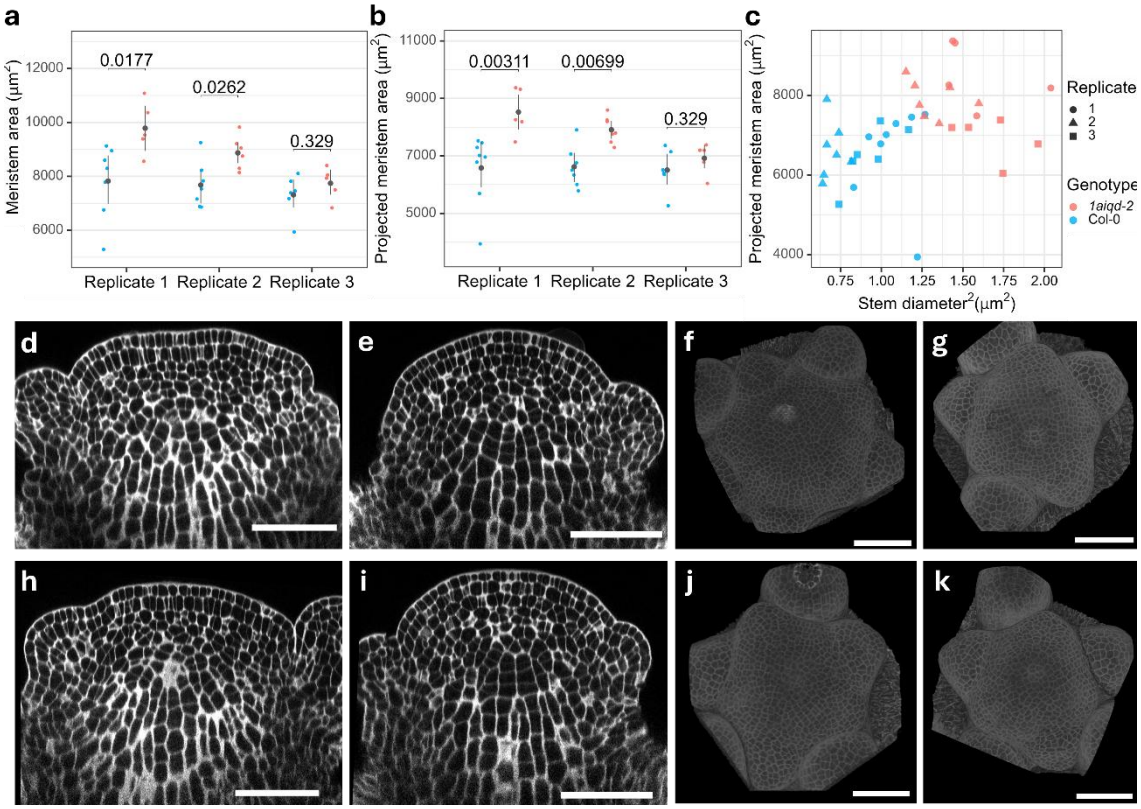

Figure 12: Loss of 1A *IQD* genes affects meristem size and morphology. (a, b) Quantification of meristem area **(a)** and projected area **(b)** of col-0 and *1aiqd-2* meristems across three separate experiments. Area is the total surface area of the meristem; projected area is the area of the 2D shape generated by projecting the meristem surface onto the plane perpendicular to the stem's vertical axis. **(c)** Projected meristem area plotted against the square of stem diameter, measured 3 mm from the meristem. **(d,e h,i)** Longitudinal optical sections of propidium iodide (PI)-stained *1aiqd-2* (d, h) and wild type col-0 (e,i) meristems. (d,e) are representative of experimental replicate 1 and (h,i) of replicate 3. **(f,g,j,k)** 3D volumetric projections of the same meristems: (d, f), (e,g), (h,j), (i,k). Points and whiskers indicate bootstrapped mean and 95% CI of the mean. Mann Whitney U tests were used to calculate significance. All plants analysed were approx. five weeks old and 6 (+/- 2) mm tall. A minimum of five meristems were analysed per genotype per replicate experiment. Scale bars: 50 µm

within the top 2 mm of the meristem; (3) *1aiqd-2* stems are thicker from the outset because the mutant has a larger meristem size – still require testing.

2.2.5 Meristem morphology of the *1aiqd-2* mutant

To determine whether differences in meristem size could explain the thick stem, meristems from ~6 mm tall plants (as shown in 9b, c) were imaged. *1aiqd-2* meristems were typically larger, measured by both surface area and projected area (the 2D footprint made by the meristem) (**fig. 12a,b**). However, this finding was not consistent across three replicate experiments, even though the *1aiqd*-2 stem diameters were consistently larger (**fig. 12c,** x axis). Furthermore, there was no apparent genotype-independent correlation between meristem size and stem diameter (**fig. 12c**). This suggests that the increased meristem size is not the cause of the thick stem phenotype. A more consistent phenotype of *1aiqd-2* meristems was a flatter, less domed shape, in comparison to wild type meristems (**fig. 12d-k**). This was independent of size, as it was observed even when the *1aiqd-2* meristem was of comparable size to wild type meristems (**fig. 12h-k**).

2.2.6 The effects of *1aiqd-2* on cell division orientation and rib meristem morphology

The original *1aiqd* mutant displayed a disruption of division plane orientation in the rib meristem (Mckechnie-Welsh 2021). To establish whether the *1aiqd-2* mutant reproduces this finding, and whether it could reasonably explain the thick stem phenotype, I quantified the orientation of recently placed cell walls in the rib meristems of wild type and *1aiqd-2* plants.

In the rib meristem, new cell walls are typically inserted transversally to the main axis of the stem (which is also the main direction of growth), and this generates parallel files of cells. In the *1aiqd-2* mutant, the majority of cells did indeed divide transversally (**fig. 13, 14**). However, a sizeable minority deviated significantly, with some new walls even running longitudinally from the top to the bottom of the cell (**fig. 13c, yellow arrows**). In the wild type, no such extreme wall orientation was observed. One possible explanation for *1aiqd-2* plants having extreme wall angles is that these are low probability events, and *1aiqd-2* plants might have more of them if they have more cell divisions in total. Therefore, the density of different wall angles was plotted, and clearly illustrates that extreme wall angles make up a larger proportion of wall angles in the mutant (**fig. 14b**). To statistically compare the data, the proportion of wall angles > 45° degrees were considered (since this reflects wall that are closer to vertical than horizontal) and this was significantly higher in the *1aiqd-2* mutant (**fig. 14c**).

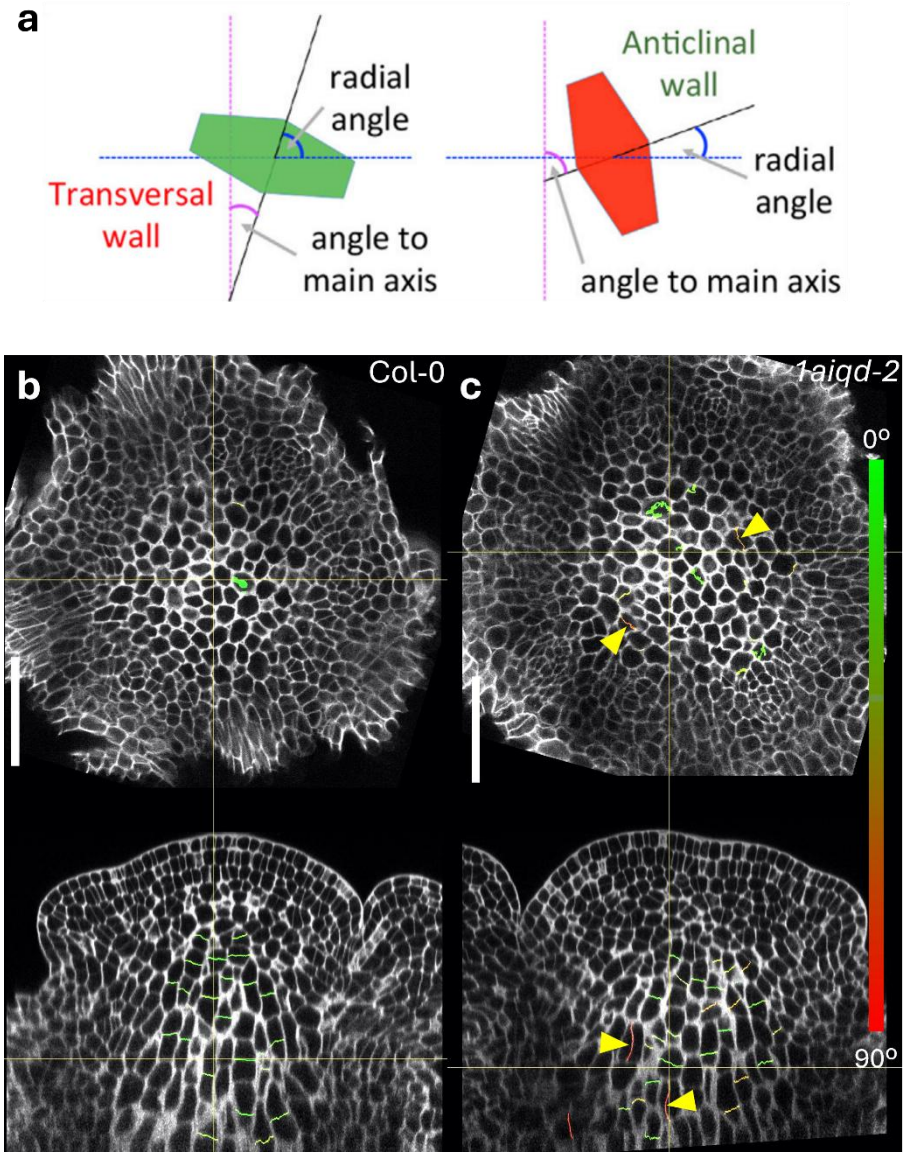

Figure 13: *1aiqd-2* plants have misoriented cell divisions in the rib meristem. (a) Diagrammatic representation of how wall orientation is calculated. First, a 2D plane is fitted to the cell wall. The angle between the vector orthogonal to that plane, and the vector for the main vertical axis of the meristem is calculated. For transversal walls (typical orientation), this angle will be near 0°. As wall orientation increasingly diverges from transversal, the angle increases. **(b,c)** Single optical sections of fixed PI-stained SAMs from wild type Col-0 (a), *1aiqd-2* (b) plants. Meristems were harvested from 5-week-old plants, at the stage "day 0" shown in fig. 8. Transverse sections approx. 100 µm from the meristem apex (upper panels) and longitudinal sections through the centre of the meristem (lower panels) are shown. Recently formed cell walls in the rib meristem are coloured on a scale of green to red. See fig. 14 for quantification. Yellow triangles indicate non-transversal cell walls. Scale bars: 50 µm

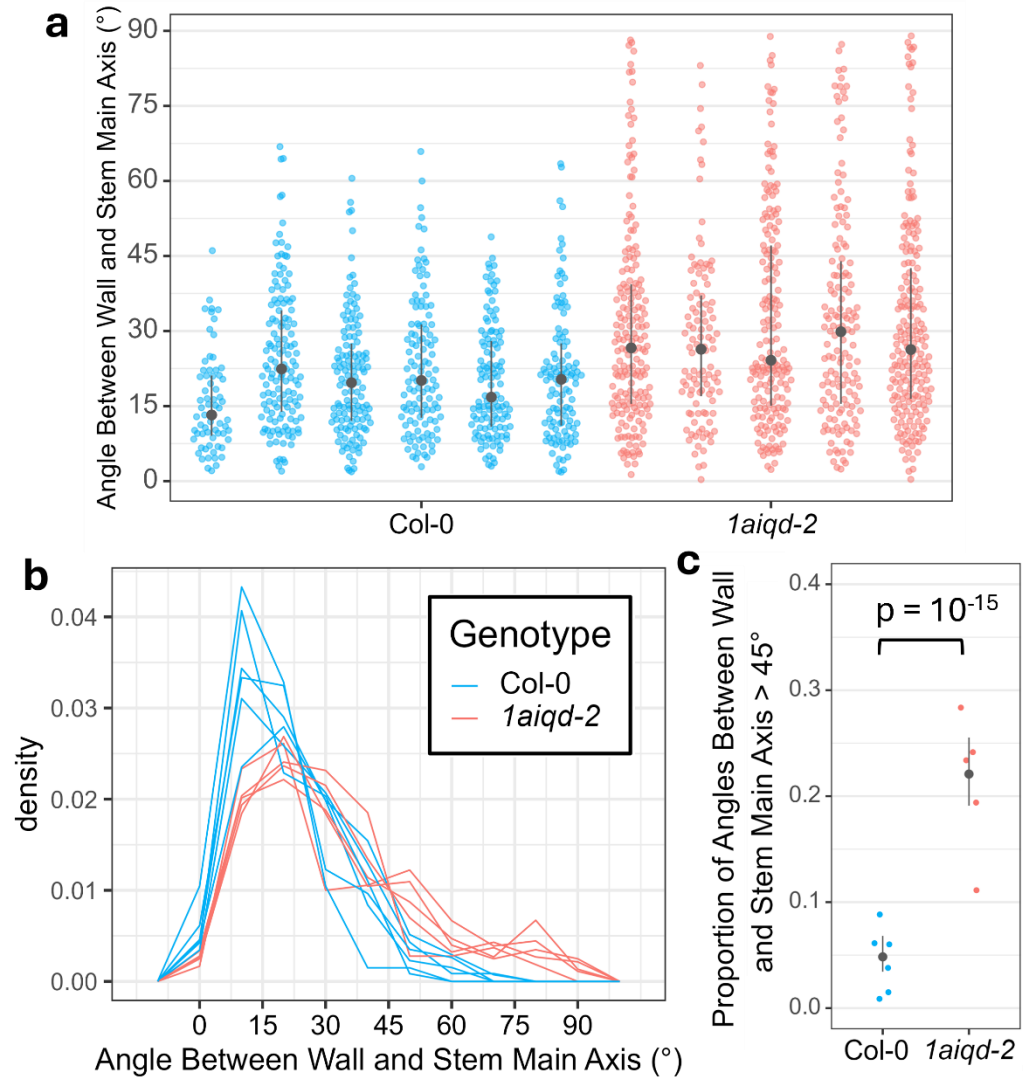

Figure 14: *1aiqd-2* plants have an increased frequency of misoriented cell divisions in the rib meristem. Quantification of new cell wall orientation in the rib meristem as measured in fixed PI-stained SAMs from wild type Col-0 and *1aiqd-2* plants. Meristems were harvested from 5-week-old plants, at the stage "day 0" shown in fig. 8. Five or six meristems were analysed per genotype. **(a)** Angle between wall and main axis (where values closer to zero indicate more transversely oriented walls, (see fig 13 for details)). Each point represents the angle of an individual wall and each set of points represents the walls of an individual meristem. Black dots and whiskers show median and IQR. **(b)** Density plot of the same data shown in (a). Each line represents an individual meristem. (**c**) The proportion of wall angles > 45° in each meristem. Data were analysed using a Poisson model. Black dots and whiskers show back-transformed estimates for the rates and asymptotic upper and lower confidence levels (conceptually equivalent to mean and 95% CI).

To determine how changes in cell division relate to growth, rib meristem area and cell number were quantified at two positions: 60 µm and 100 µm vertical distance from the meristem apex. At 60 µm from the apex, 1aiqd-2 and wild type rib meristems occupied a similar area, although 1aiqd-2 plants had 21% more cells on average (fig. 15a,e). At 100µm from the meristem, 1aiqd-2 rib meristems were 40% larger than the wild type and had 57% more cells (fig. 15b,f). Both genotypes saw an increase in cell number and area from 60 µm to 100 µm. The rib meristem of wild type plants had a mean increase of 23.5 cells (35%) and 2200 µm2 (76%) area. For 1aiqd-2 plants, the increase was much larger - 60.5 cells (73%) and 4000 µm2 (131%) **(fig 15c,d,g,h).**

Differences in cell size cannot explain why the rib meristem area expands more across this distance in the *1aiqd-2* line. Cell cross-sectional area (measured in the plane orthogonal to the stem main axis (**fig. 16a**) and volume were very variable between plants of the same genotype (**fig. 17a, b**). This makes it difficult to discern genotype-level differences, but the data do not indicate that the *1aiqd-2* mutants overall had larger cells. This is consistent with data from more mature stem tissue, which showed that *1aiqd-2* pith cells are in fact smaller than the wild type (Mckechnie-Welsh 2021). Therefore, the greater expansion of rib meristem area seen in the *1aiqd-2* mutant derives from the greater increase in cell number.

Cell geometry is an important, and the default, determinant of cell division plane selection: the most likely division plane is the one with the smallest area that divides the cell equally in half (Smith 2001; Besson and Dumais 2011). Therefore, an alteration in division plane either arises from a change in cell geometry or the violation of the geometric rule. Notably, perturbation of IQD activity (either through mutation or ectopic expression) has been shown to modify cell geometry in certain organs and tissues (Feng et al. 2023; Liang et al. 2018; Mitra et al. 2019). However, visual inspection of cells with the largest deviation in cell division angle, revealed that the inferred shape of the parent cell was not conspicuously different from other cells in the tissue or wild type cells, either in transverse or longitudinal cross-sections (**fig. 13b,c**). Indeed, in the longitudinal cross-section, the new cell wall runs almost parallel to the long axis of the cell, and is therefore very different from the plane of minimum area (**fig. 13c, yellow arrows**). To quantitatively determine whether there were in fact any genotype-level changes in cell geometry that might explain the difference in cell division orientation, several cell geometric properties were also quantified **(fig. 16)**.

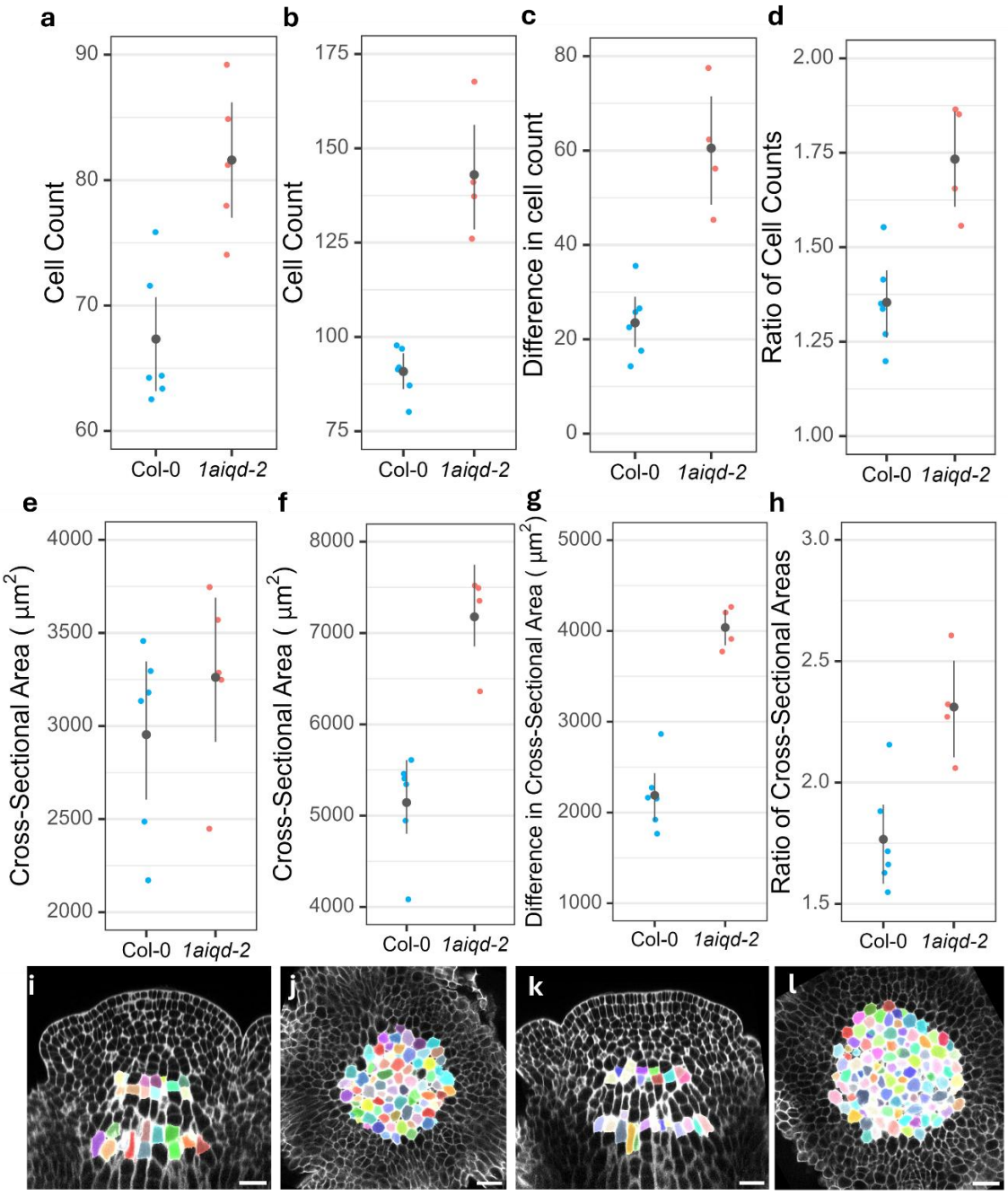

Figure 15 : The *1aiqd-2* mutant has increased radial growth of the rib meristem. Quantification of rib meristem cell number and cross-sectional area as measured in fixed PI-stained SAMs from wild type Col-0 and *1aiqd-2* plants. Meristems were harvested from 5-week-old plants, at the stage "day 0" shown in fig. 8. Four to six meristems were analysed per genotype. **(a, b)** The number of rib meristem cells in cross-sections 60 µm (a) and 100 µm (b) from the meristem apex. **(c,d)** Difference in cell number between the 100 µm and 60 µm cross-sections, expressed as an absolute difference (number of cells at 100 µm - number of cells at 60 µm) (c), and as a ratio (number of cells at 100 µm ÷ number of cells at 60 µm) (d). **(e, f)** Area occupied by the rib meristem in cross-sections 60 µm (e)

and 100 µm (f) from the meristem apex. **(g,h)** difference in area between the 100 µm and 60 µm cross-sections, expressed as an absolute difference (area at 100 µm - area at 60 µm) (g), and as a ratio (area at 100 µm ÷ area at 60 µm) (h). **(i-p)** single optical sections of PI-stained SAMs from Col-0 (i, j) and *1aiqd-2* (k,l) plants. Longitudinal sections from the centre of the meristem (I,k) and transversal sections 100 µm from the meristem apex (j,l) are shown. Cells in the rib meristem at 60 µm and 100 µm from the meristem apex are highlighted in colour. Scale bar: 20 µm. Black dots and whiskers show the bootstrapped mean and 95% CI.

Unlike the cell size metrics (**fig. 17a,b**), the distributions of the ratio of cell axes and the coefficient of variance (CV) of cell radii (both measures of cell shape) were fairly consistent between plants irrespective of genotype (**fig. 17c,d**). When the data for each genotype were pooled, the distributions of both metrics did not statistically differ between genotypes (Anderson-Darling T.AD = -0.62, p = 0.72 and T.AD = -0.71, p = 0.79, respectively) **(fig. 18a,b)**, which indicates that the *1aiqd-2* cells were no more or less elongated than the wild type. This shows that cell growth anisotropy was unchanged in *1aiqd-2* rib meristems and implies that the observed changes in cell division orientation did not derive from changes in cell shape.

There were some differences in the cell orientation, measured by calculating the angle between the cell's main axis and the main vertical axis of the stem (**fig. 16b**). At 60 µm from the apex, the cell orientation was highly variable (**fig. 17e**). This is because the cells have yet to acquire the characteristic elongated shape of pith cells (**fig. 15i,k**). This makes the cell axes more similar in length (this is reflected in the ratio of main and secondary axes being near 1 (**fig. 17c**)), meaning there is a lot of variation in which axis is the main axis. By 100 µm, more cells have an elongated shape, meaning the main axis is more clearly defined. In the wild type, most cells were oriented with their main axis at an angle of 0-40° relative to the vertical axis of the stem, with a median around 20°. Some more extreme angles were observed - these were likely the daughter cells of recent divisions, which have a more cubic shape. In the mutant, the distribution was similar in some plants, while a couple of plants had a distribution that was shifted to slightly higher values – with median values around 26° and a greater proportion of the distribution between 30° and 45° (**fig. 17e**). This could be explained by the increased radius of *1aiqd-2* plants – cells further from the centre of the stem tended to have a larger slope **(fig. 18c)**. There were no clear differences in the abundance of more extreme cell angles (> 60°). An increase in cell

orientations around 40°, could explain a subtle shift in the distribution of cell division angles, but cannot account for an increase of extremely non-transversal cell divisions

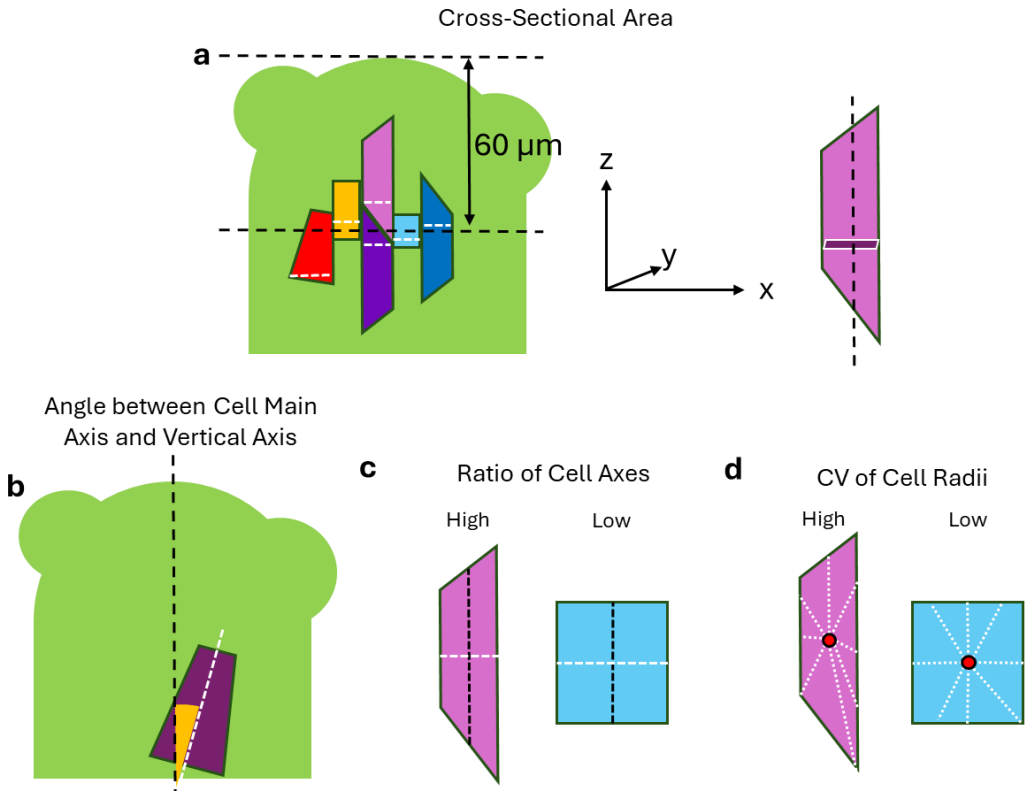

Figure 16: Cell geometry measurements quantified in fig 17. (a) Cell cross-sectional area. Cells are selected if they are situated a specified vertical distance from the meristem apex (60 µm in the diagram). A cell's cross-sectional area (measured in the XY plane, perpendicular to the meristem's vertical axis) at its widest point (represented by the white dashed lines) is measured. **(b)** Angle between cell main axis (white dashed line) and meristem vertical axis (black dashed line). This provides information about cell orientation. **(c)** Ratio of cell axes. The ratio between the length of the cell primary (black dashed line) and secondary axis. **(d)** Coefficient of variance (CV) of cell radii. The distance between the cell centroid and every voxel on the cell surface is measured. The CV of these values is calculated by dividing the stand deviation by the mean. This provides information about the sphericity of the cell.

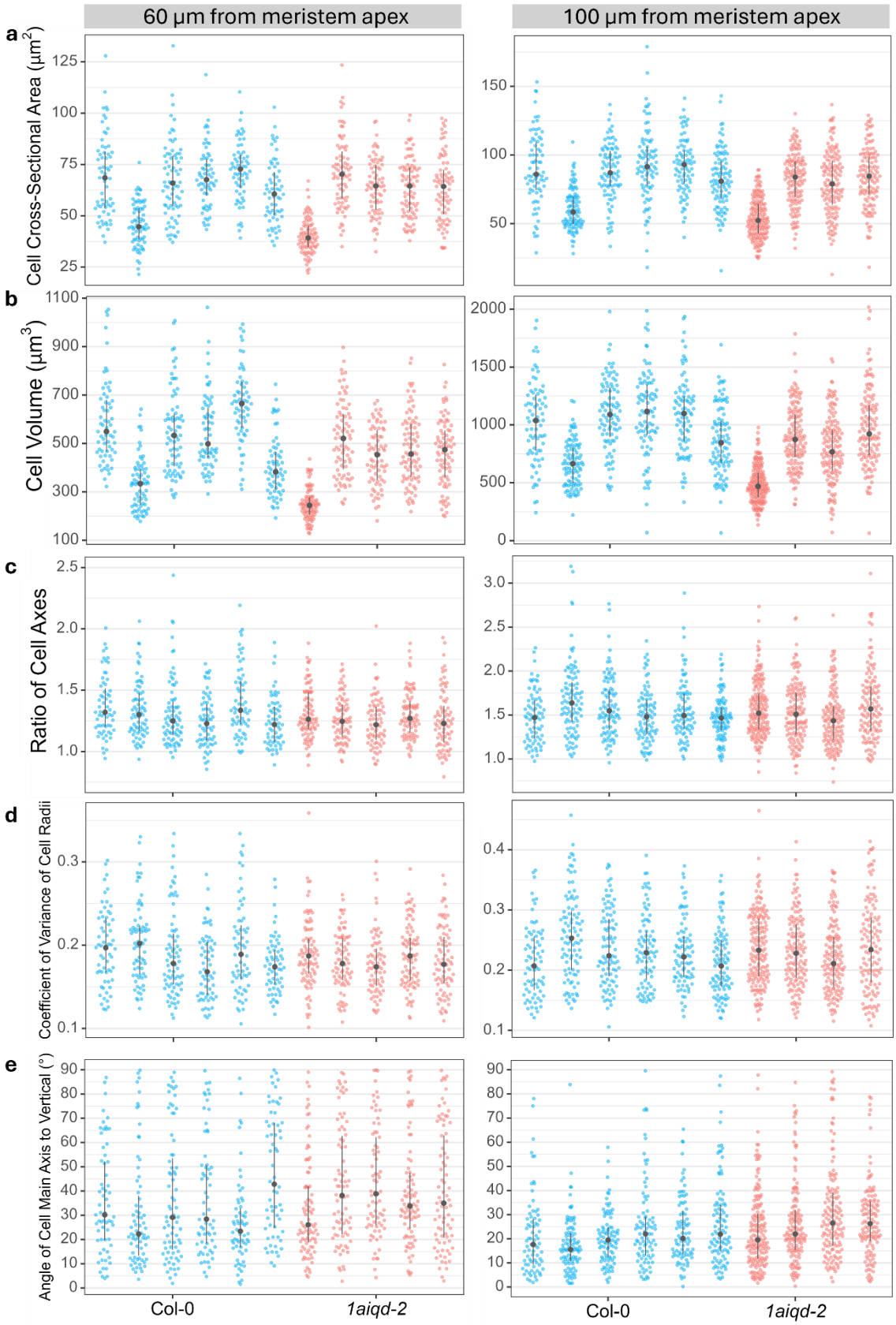
60 µm from meristem apex
100 µm from meristem apex
a
Cell Cross-Sectional Area (µm²)
b
Cell Volume (µm³)
c
Ratio of Cell Axes
d
Coefficient of Variance of Cell Radii
e
Angle of Cell Main Axis to Vertical (°)
Col-0
1aiqd-2
Col-0
1aiqd-2

Figure 17 (previous page): Loss of 1A *IQD* genes has little effect on cell geometry in the rib meristem. Quantification of rib meristem cell geometry: **(a)** cross-sectional area, **(b)** cell volume, **(c)** ratio of primary cell axis to secondary cell axis, **(d)** coefficient of variance of cell radii, **(e)** angle between cell main axis and vertical stem axis. Cells were measured from 3D confocal images stacks of fixed PI-stained SAMs from wild type Col-0 and *1aiqd-2* plants. Cells were measured if they were within 60 µm (left panels) or 100 µm (right panels) of the meristem apex. Each point represents the measurement for an individual cell and each set of points represents the cells of an individual meristem. Meristems were harvested from 5-week-old plants, at the stage "day 0" shown in fig. 8. Four to six meristems were analysed per genotype. Black dots and whiskers show median and IQR.

2.2.7 Clonal analysis of the *1aiqd-2* mutants

2.2.7.1 Construction of 1aiqd-2 *lines for clonal analysis*

For misoriented cell divisions to drive growth, a radial cell division must generate two parallel cell files that contribute more to radial growth than an individual cell file (**fig. 19**). It is not possible to track the growth of cells in the rib meristem by live imaging, because the cells are too deep inside the meristem and stem. Therefore, to determine how division orientation (and the*1aiqd-2* mutations more generally) contribute to the radial growth of the stem, I employed the Cre-*lox*P recombination system (Sieburth et al. 1998; Gallois et al. 2002; Bencivenga et al. 2016). This system marks individual cells and their descendants by inducing stable, heritable GFP expression. The system has two components: a heat shock-inducible Cre recombinase and an endoplasmic reticulum (ER)-tagged GFP reporter that is only expressed when *lox*P sites are recombined. Existing versions of the system carry the *lox*P:reporter and Cre recombinase components on separate T-DNAs (Gallois et al. 2002) and these are either crossed or transformed separately into the required lines and those lines are crossed together to generate the heat shock-inducible line. To speed up the generation of new plant lines I cloned both

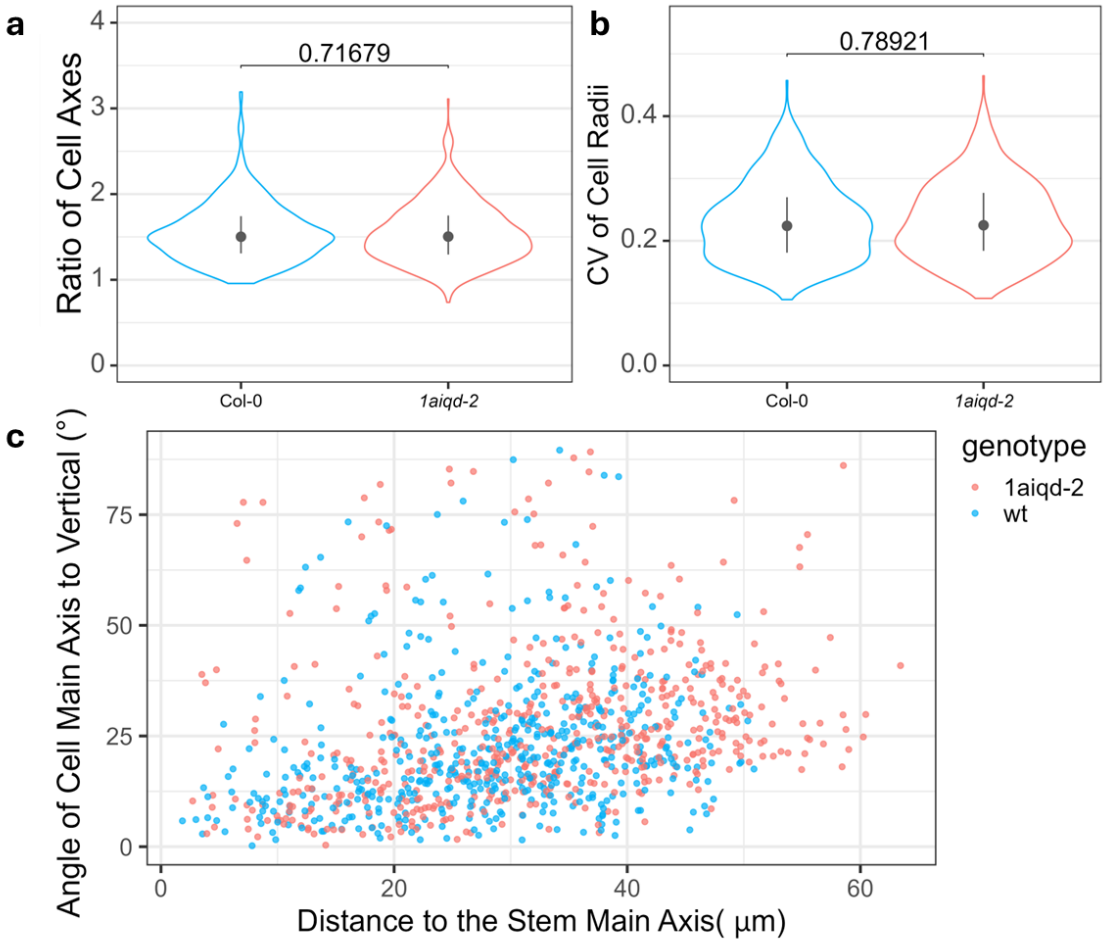

Figure 18. Loss of 1A *IQD* genes does not affect cell shape and is unlikely to directly affect cell orientation. Quantification of rib meristem cell geometry in cells situated 100 µm from the meristem apex. **(a)** Ratio of primary cell axis to secondary cell axis and **(b)** coefficient of variance of cell radii. Data from 4-6 meristems (shown separately in fig. 17c,d) per genotype were pooled together. p values were calculated using Anderson-Darling test to compare distributions. Black dots and whiskers show median and IQR. **(c)** The horizontal distance between the cell centroid and the main vertical axis of the stem plotted against the angle between the cell main axis and the vertical axis of the stem. Each point represents a single cell and the data were pooled from 4-6 meristems per genotype. Black dots and whiskers show median and IQR.

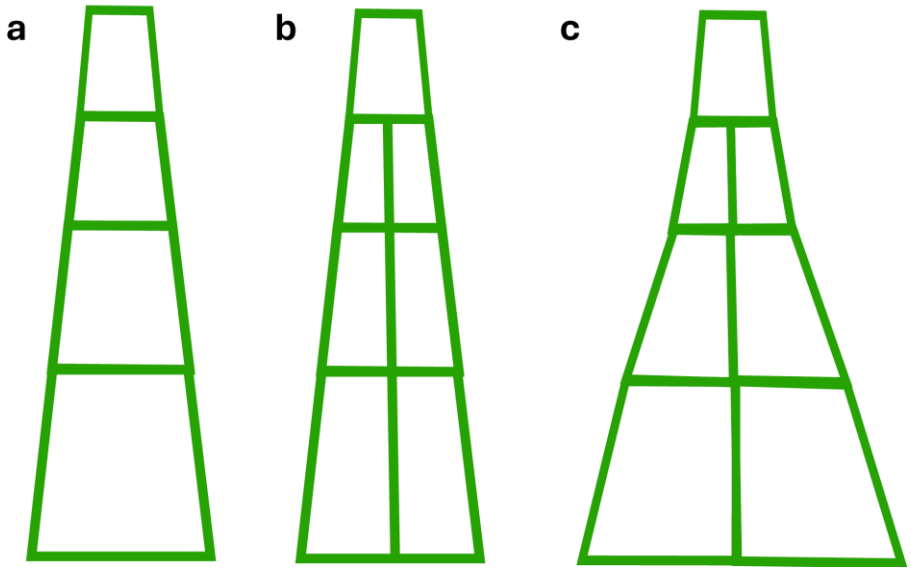

Figure 19: Different scenarios could follow a radial cell division. Diagrammatic representation of cell files in the rib meristem, showing the possible outcomes of a radial cell division. **(a)** A typical cell file, with exclusively transverse cell divisions. **(b)** One radial division has generated two adjacent cells that subsequently divided transversally to produce parallel cell files. The radial expansion of the cells in adjacent files is small, such that the two files are a similar width to the individual cell file in (a). **(c)** The same scenario as shown in (b), except, the cells undergo more radial expansion to be a similar size to the cells in the single cell file.

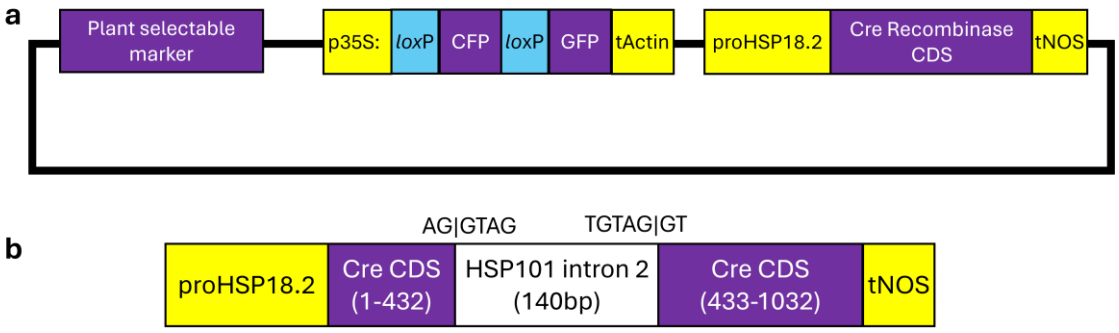

Figure 20: Construct design for heat shock-inducible cell lineage marking system. (a) Graphical representations of **(a)** the original plasmid design and **(b)** the redesigned Cre recombinase module, with the *AtHSP101* intron inserted into the *Cre* CDS (the sequences of the predicted 5' and 3' splice sites are annotated above). The *p35S:*lox*P:CFP-ER:*lox*P:GFP-ER:tActin* and proHSP18.2:Cre:tNOS modules were cloned from published constructs (Sieburth et al. 1998; Bencivega et al. 2016) and the *HSP101* intron was cloned from *Arabidopsis* gDNA.

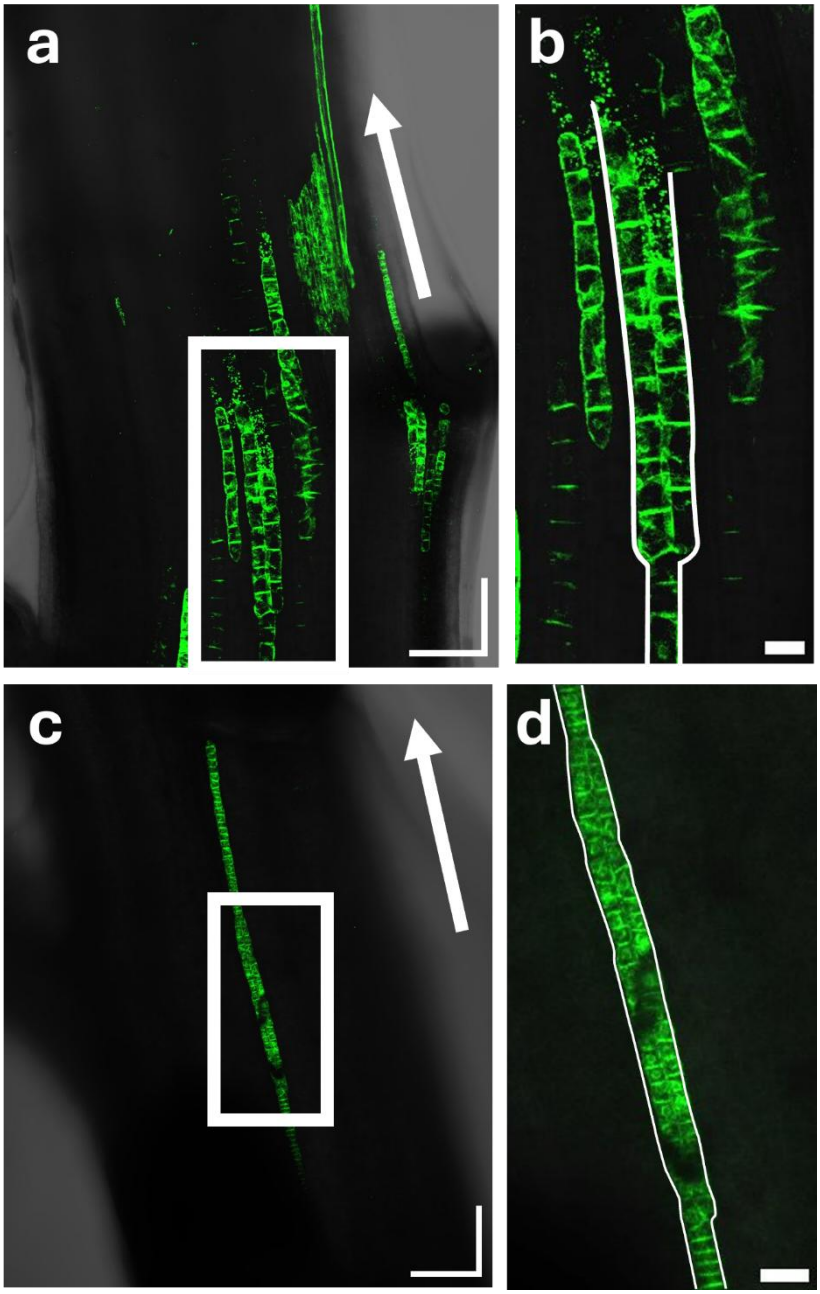

Figure 21: Clonal GFP sectors reveal the insertion of new pith cell files. Max intensity projections of confocal Z-stacks showing GFP-ER-marked clones (green) in the pith tissue of longitudinally bisected stem apices. Images were captured 10 days after Cre-catalysed *lox*P recombination. Images from plants with *1aiqd-2* **(a-b)** and wild type **(c-d)** backgrounds are shown. (b) and (d) are magnifications of the boxed regions in (a) and (c), respectively, highlighting bifurcating sectors. White lines in (b) and (d) mark the overall shape of the clones. Arrows point in the direction of the SAM. Scale bars: 100 µm (a,c) and 25 µm (b,d). GFP induction and imaging were performed by Nicole Mol, with guidance from Bryony Yates.

components onto a single T-DNA (**fig. 20a**) using Golden Gate cloning. During this process, I generated level 1 Golden Gate-compatible modules of the *proHSP:Cre* and *p35S:*lox*P:CFP-ER:*lox*P:GFP-ER*, so that they can be easily reused to clone different heat shock inducible constructs.

My initial attempts to clone the *lox*P:reporter and Cre recombinase components into the same binary vector failed because the plasmids I recovered had already undergone Cre-*lox* recombination. This pointed to leaky expression of the Cre recombinase in the host *E. coli*. As well as preventing recovery of the desired plasmid, Cre expression was likely toxic to the *E. coli*, because during the cloning process, I only recovered Cre-recombinase-containing plasmids at low yields.

I redesigned the plasmid by inserting an intron into the Cre recombinase coding sequence (CDS) to obstruct its expression in *E. coli*. Because heat shock can affect splicing, I sought an intron from a gene that is expressed (and thus successfully spliced) under heat shock conditions. I selected the 140 bp intron 2 from *AtHSP101* based on the following criteria: available data (Winter et al. 2007; Kilian et al. 2007) indicated high expression of the mRNA during heat shock; the length of the intron (140 bp) is not divisible by 3, and so will introduce a frame shift when inserted into the CDS. I amplified the intron from genomic DNA and inserted it into the Cre recombinase CDS between AG and GT residues, to generate the 5' and 3' splice sites (**fig. 20b**). Otherwise, the final construct design was unchanged. I successfully cloned this version and transformed it into Col-0 and *1aiqd-2* plants.

2.2.7.2 Inspection of Clonal Sectors

To inspect the geometry of clonal cell lineages in the pith tissue, plants were imaged 10 days after heat-shocking. Bifurcating sectors - where a single file becomes two parallel files - were frequently observed in *1aiqd-2* plants and at lower frequency in the wild type plants (**fig. 21**). In these bifurcating clones, the cells in the parallel files were a similar width to the cells in the single files immediately above or below them (**fig. 21b,d**). As a result, the total width of the parallel files was greater than the individual files (as in **fig. 19c**). This indicates that radial cell divisions do insert new cell files and that the resulting parallel cell files occupy more space than a single transversally dividing file.

2.3 DISCUSSION

2.3.1 The stem phenotype of the *1aiqd-2* mutants is established at or near the SAM

In this chapter I investigated the growth of the *1aiqd-2* mutant to identify the factors that underpin its large stem diameter. Contrary to my expectations, the *1aiqd-2* stems did not have a measurable increase in radial growth rate that would account for the thicker stems. Instead, the thicker stem of the mutant is already well-established when stems are very small and within a few mm of the stem apex, indicating that the phenotype is established at or near the SAM. Indeed, over a short vertical distance (this can be used as a proxy for time, since cells in the rib meristem get vertically displaced during growth) *1aiqd-2* rib meristems increase in area to a much greater extent than the wild type. This is associated with an increase in cell number, but not cell size, which is consistent with the hypothesis that misoriented cell divisions in the rib meristem drive radial growth by inserting new cell files (Mckechnie-Welsh 2021). Furthermore, the shape of Cre-*lox* GFP sectors in the pith showed that a change in the orientation of cell divisions is a plausible cause of increased radial growth of the stem. However, I cannot rule out the reverse causation - that changes to growth (driven by some third factor e.g. mechanics) drive the changes in cell division and rib meristem cell number in the *1aiqd-2* mutant. Discriminating between these two hypotheses – that changes in cell division drive growth or are a consequence of it - hinges on the mechanism by which 1A IQDs regulate cell division orientation. This is the focus of the following two chapters.

1aiqd-2 is one of very few mutants with reported defects in rib meristem organisation. One other that has been characterised in detail is *rpl,* which, like the *1aiqd-2* mutant, has misoriented cell divisions in the rib meristem (Bencivenga et al. 2016). However, *rpl* and *1aiqd-2* have very different growth phenotypes: *rpl* plants display reduced stem elongation and small-to-normal-sized rib meristems, whereas *1aiqd-2* plants elongate normally and have larger rib meristems (Bencivenga et al. 2016). This raises the question of why two plants with similar changes in cell division orientation have such different phenotypes. However, the discrepancy may derive from the different underlying mechanisms that drive the changes in cell division orientation. The altered cell division in *rpl* is caused by ectopic expression of the organ boundary gene *LIGHT SENSITIVE HYPOCOTYLS 4*, which either narrows the rib meristem or induces rib periphery identity in the central meristem (Bencivenga et al. 2016). Changes to organ identity can affect many different aspects of plant development, including the development of the vasculature and cambium, which, if disrupted can cause stem dwarfing (Bush et al. 2022). Indeed,

vascular anatomy is perturbed in *rpl* (Smith and Hake 2003). While the mechanism that underpins the *1aiqd-2/1aiqd* phenotype is unclear, it has normal stem elongation and vascular anatomy (Mckechnie-Welsh 2021), making it a better model for specifically investigating the effects of cell division orientation on growth dynamics and direction.

I also identified that *1aiqd-2* mutants have altered SAM geometry and, in some cases, larger SAMs. This phenotype is unlikely to drive the rib meristem/ stem phenotype because it is inconsistent and does not clearly correlate with stem diameter. However, it might be a secondary effect of the *1aiqd-2* mutation with inconsistent penetrance, possibly arising downstream of changes in the underlying RZ. Indeed, cell proliferation in the RZ has previously been shown to modulate overall SAM size by constraining the growth of the overlying cell layers (Serrano-Mislata et al. 2017). Meristem size is also regulated by a feedback loop involving CLAVATA3 (CLV3) and WUSCHEL (WUS), which restricts the domain of stem cell activity in the SAM (Yadav et al. 2011; Clark et al. 1995). Some regulatory relationship between the 1A IQDs and the CLV3-WUS pathway cannot be ruled out but given there is no relationship between stem diameter and meristem size in these data, the pathway would likely have little bearing on stem radial growth. Since meristem shape and size impact phyllotaxis (Reinhardt 2004), the sporadic occurrence of very large meristems could explain the low penetrance of phyllotactic defects that has been observed in the *1aiqd* mutant (Mckechnie-Welsh 2021). However, further work is required to establish a link between meristem morphology and phyllotaxis in these lines.

2.3.2 Generation of materials for studying plant development

Prior work on the developmental effects of the *1aiqd* mutant had been hampered by transgene silencing which was presumed to originate from the *iqd22-1* (SALK 103903.55.75.x) and *iqd26-3* (GK-728F02) alleles (Mckechnie-Welsh 2021). Using CRISPR-Cas9 mutagenesis I generated new alleles (named *iqd22-5* and *iqd26-4*), which are predicted to completely disrupt the IQD22 and IQD26 protein sequences, and I incorporated them into a new 1A IQD sextuple mutant line, *1aiqd-2*. Because this new line is not associated with frequent transgene silencing, transgenic tools can now be used to investigate the *1aiqd-2* mutant in much more detail.

Recent work has highlighted roles for *iqd22* specifically in leaf development and hypoxia sensing (Matthes et al. 2022; Zhao et al. 2025). Previously published *iqd22* mutants derive from either a single base substitution that does not affect most of the protein sequence (Zhao et al. 2025) or intronic T-DNA substitutions that do not fully knock-out protein expression (Matthes et al. 2022). The *iqd22-5* allele is a missense mutation that disrupts

almost the entire protein sequence, including the IQ67 domain. It therefore offers a useful tool to investigate the effects of full *iqd22* knock out on these published phenotypes, and any others that are yet to be discovered.

The Cre-*lox*P system is a powerful tool for studying plant development. By facilitating mosaic induction of specific genes it can reveal non-cell-autonomous effects of gene expression (Gallois et al. 2004; Sieburth et al. 1998), and reveal 3-dimensional growth patterns in inaccessible organs (Bencivenga et al. 2016). In this chapter I describe the construction of a new T-DNA architecture for the introduction of heat shock inducible transgenes into *A. thaliana*. This new architecture makes it much more straightforward to introduce the Cre-*lox*P system into different mutant lines, since only a single T-DNA locus needs to be introduced via crossing or transgenesis. This is particularly useful for genetic backgrounds carrying multiple mutations that make crossing difficult and time-consuming. Furthermore, by generating level 1 Golden Gate modules for the constituent parts of the Cre-*lox*P system, I have made it much easier to generate different variants of the Cre-*lox*P system, e.g. using different plant selectable markers or inducible transgenes.

3 EXPRESSION AND LOCALISATION OF 1A IQD PROTEINS

3.1 INTRODUCTION

The *1aiqd-2* mutations cause three phenotypic changes in the stem: disrupted division orientation in the rib meristem, increased pith cell number (in the transverse plane) and increased stem diameter. A plausible hypothesis links these phenotypes together in a causal chain: the disrupted division plane generates more cells in the radial direction, and this drives an increase in stem diameter. This hypothesis raises the additional question: how do 1A IQDs regulate division plane orientation? This is not a straightforward question to answer, for there are many different mechanisms that regulate division orientation and several mechanisms through which IQDs have already been shown, or proposed, to regulate cellular processes.

3.1.1 The regulation of cell division orientation in plants

The process of cytokinesis in plants is distinct from other eukaryotes, requiring plant-specific proteins and MT structures. For most of the plant cell cycle, the MTs form cortical arrays that lie close to the plasma membrane (PM). Towards the end of G2, the MTs (and some actin microfilaments) reorganise to form a narrow, cortical ring that encircles the cell – the preprophase band (PPB) (**fig. 22**). The position of the PPB reliably predicts the division site, where the new cell wall will ultimately fuse to the existing walls (Livanos and Müller 2019). This site is referred to as the cortical division zone (CDZ) and it persists until the end of cytokinesis, distinguished by the localised, yet dynamic, accumulation of specific proteins (Smertenko et al. 2017).

As the cell enters metaphase, the PPB disassembles and the cell's dominating microtubular structure becomes the mitotic spindle (**fig. 22**). After chromatid separation, the spindle MTs reorganise and form the phragmoplast (**fig. 22**). This is a structure of MTs and actin microfilaments, situated on opposite sides of, and oriented perpendicular to, the plane of the future cell wall. Vesicles, derived from the trans-Golgi network, traffic along the phragmoplast MTs to the midline of the phragmoplast. Here they fuse with other vesicles, delivering cell wall components to form the cell plate. The cell plate grows laterally outwards from the centre, via the fusion of new vesicles at its edges, until it fuses with the parent cell's PM at the division site (Smertenko et al. 2017).

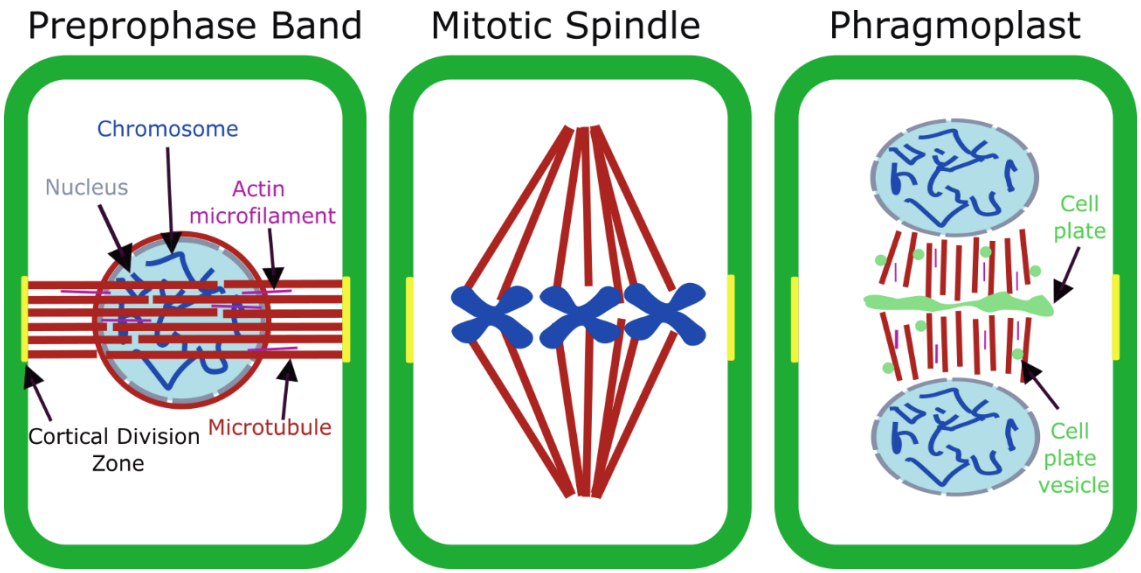

Figure 22: Microtubule structures during plant cell division.

As a default, plant cells divide symmetrically, partitioning the cell's cytoplasmic contents more-or-less equally between two daughter cells. A classic geometric rule, identified 150 years ago, can mostly explain the positioning of the division plane – out of all the planes that can generate equally-sized daughters, the selected plane is the one that minimises the area of the new cell wall (Smith 2001). This cell geometry-based selection is, however, a probabilistic phenomenon: the chance of the minimising division plane being selected decreases, when an alternative plane has a similar area (Besson and Dumais 2011). The cell geometries in the *1aiqd-2* mutant rib meristem are unchanged and misoriented cell walls diverge significantly from the smallest area rule (Chapter 2). Therefore, changes in cell geometry cannot explain the change in cell division orientation. However, the mutations could affect how the cell perceives or responds to geometric and other cues or how the initially selected division plane is "remembered" through subsequent stages of mitosis.

Although the precise nature of how cells sense their shape is unclear, a long-standing model centres the interactions between the nucleus and cell periphery. Cytoplasmic strands, which are associated with MTs and actin filaments, radiate from the nucleus to the cell cortex (Lloyd et al. 1992). Because these strands are under tension, they seek a force-minimising configuration. This corresponds to the shortest distance between the nucleus and the cell periphery, and is achieved by migrating the nucleus to the cell's centre (Lloyd 1991; Asada 2019). The PPB then forms in the region with the densest accumulation of cytoplasmic strands (Besson and Dumais 2011). The importance of this mechanism likely depends on cell type – in some cells nuclear positioning varies little and

the PPB is mostly assembled (and aligns with) interphasic cortical MT (cMT) arrays (Lloyd et al. 1992; Bouchez et al. 2024).

An alternative school of thought proposes that, rather than sensing geometry directly, cell division orientation is determined by mechanical stress (Louveaux et al. 2016). The mechanical and geometric models make the same division plane prediction for many cells (since geometry is often the main contributor to mechanical stress), while the mechanical model is better at predicting orientation in cells affected by significant tissue-level stress (Louveaux et al. 2016; Robinson 2021). In the stem epidermis, a cell's shape, specifically its aspect ratio, determines whether it divides according to the minimum area/ geometric rule or according to tissue-derived tensile stress (Melogno et al. 2024).

Whether geometry or mechanics is the ultimate driver of default division plane selection, the cell's cytoskeleton is the proximate determining factor. Modelling and experimental work on isolated cells have demonstrated that cell geometry modifies the organisation of the MT cytoskeleton and this can explain changes to division orientation (Chakrabortty et al. 2018; Mirabet et al. 2018; Durand-Smet et al. 2020). However, in the context of a growing, multicellular plant, other cues (even weak ones) can counteract or bias the effects of cell geometry on MT organisation (Mirabet et al. 2018). Light, hormones (auxin, gibberellins) and mechanical stress can modify the arrangement of cMTs (Sambade et al. 2012; Lindeboom et al. 2013; Vineyard et al. 2013; Robinson and Kuhlemeier 2018), and this is associated with the reorientation of cell divisions (Louveaux et al. 2016; Yoshida et al. 2014; Hoermayer et al. 2024). Thus, MTs are likely responsible for integrating intrinsic geometric/ mechanical information with external cues to regulate division orientation. This has been observed, for example, in *Arabidopsis* embryos, where auxin-dependent control of cell division orientation is mediated by the MT and actin cytoskeleton (Vaddepalli et al. 2021). Furthermore, a recently-discovered step in plant cell division might modulate how cells respond to these external cues (Melogno et al. 2024). Approximately 3 hours before cell division, the cMT arrays reorganise: they lose any directional alignment acquired during interphase and rearrange into a radial array. This "radial step" is unaffected by cell shape, auxin or mechanical perturbation and is proposed to confer insensitivity to these cues in the lead up to cell division, thereby make division plane positioning more robust (Melogno et al. 2024). There is also growing evidence that division plane specification depends on the duration of the cell cycle, or specific phases within it, via effects on cytoskeletal organisation (Bouchez et al. 2024).

Downstream of division plane determination, additional factors transmit the plane's position through subsequent stages of mitosis, ensuring the cell reliably divides along the specified division plane (Smertenko et al. 2017). The first visual marker of the division plane is the PPB, which forms towards the end of G2. Historically, the PPB was presumed essential for positioning the division plane, but mutants that lack PPBs have revealed that it merely adds stringency: in tissues with typically uniform cell division orientation, mutants with defective/ absent PPBs show increased variability in division plane selection rather than complete disruption (Schaefer et al. 2017; Kumari et al. 2021). Instead, the PPB supports robust division plane orientation by efficiently recruiting a specific set of proteins to the CDZ (Dahiya and Bürstenbinder 2023; Smertenko et al. 2017; Schaefer et al. 2017). The CDZ proteins remain in place after PPB disassembly, landmarking the position of the future division plane until cytokinesis is completed. Interactions among CDZ proteins are important for maintaining the CDZ, by recruiting and spatially confining its constituent proteins (Kumari et al. 2021; Walker et al. 2007; Mills et al. 2022). Loss of function of CDZ-associated proteins disrupts cell division orientation, with varying degrees of severity (Lipka et al. 2014; Walker et al. 2007; Mills et al. 2022; Stöckle et al. 2016). Some CDZ proteins function directly in downstream division plane positioning , for example in orienting and positioning the phragmoplast at the division site (Lipka et al. 2014; Walker et al. 2007). The PPB may also be important for positioning and orienting the spindle (Schaefer et al. 2017; Ambrose and Cyr 2008).

In summary, there are many different ways that 1A IQDs could be influencing cell division orientation in the stem. 1A IQDs might:

1. modify the cues that influence division plane positioning (e.g. cell mechanics, tissue mechanics, hormone signalling).
2. regulate the cell's ability to respond these cues, e.g. by influencing signal transduction or the ability of MTs to reorganise in response to signals or mechanical cues
3. regulate PPB formation and/ or positioning
4. regulate phragmoplast positioning, either directly or via the recruitment of specific regulators to the CDZ

Hypothesis (1) seems unlikely, since it would predict a general shift in average cell division orientation, rather than increased variability. However, it does raise the possibility that the *1aiqd-2* mutant phenotype acts in a non-cell autonomous manner - e.g. by altering the mechanical properties of the epidermis, it alters tissue mechanics, and

therefore division orientation, of the internal stem tissues. Hypotheses 2-4 seem more likely, since a modest impairment of any of these functions could reasonably yield the increase in the variability of cell division orientation that we see in the *1aiqd-2* mutant.

3.1.2 The many different functions of IQD proteins

IQDs are hypothesised to act as molecular scaffolds: they bind many different cellular components (e.g. cytosolic proteins, the PM, cytoskeleton, nucleus) and facilitate interactions between them (Bürstenbinder, Mitra, et al. 2017; Abel et al. 2013). Scaffold proteins are important signalling hubs, allowing multiple cellular processes to be precisely coordinated in space and time. This is a very broad remit, implying that IQDs could play a role in almost any cellular process. The IQD family is large and very few of its members have been studied in mechanistic detail. Nonetheless, research over the last decade has demonstrated at least four mechanisms by which IQDs regulate cellular processes: PPB/CDZ Establishment and Maintenance, cMT organisation, PM microdomain maintenance, and protein stabilisation (Yuanfeng Li et al. 2021; Kumari et al. 2021; Sugiyama et al. 2017; Zang et al. 2021; Zhao et al. 2025). Furthermore, each of these mechanisms has either already been shown to influence morphogenesis or feasibly could.

3.1.2.1 Regulation of PPB/CDZ establishment and maintenance

One group of IQDs plays a direct role in division plane orientation by regulating PPB-formation and promoting the recruitment of proteins to the CDZ. Mutating all three genes in the *IQD6-8* subclade generates cell division orientation defects in the embryo and root epidermis (Vaddepalli et al. 2021; Kumari et al. 2021). IQD6 and IQD8 localise to the CDZ and cell plate, and they directly interact with PHRAGMOPLAST ORIENTING KINESINS (POKS) and PLECKSTRIN HOMOLOGY GTPase ACTIVATING proteins (PHGAPs), which are core components of the CDZ (Kumari et al. 2021). In the *iqd678* mutant, PPBs are frequently tilted, sparse or absent and recruitment of POKs and PHGAPs to the CDZ is retarded. This disrupts phragmoplast orientation and subsequent cell wall placement (Kumari et al. 2021). Research into IQD orthologues from algae and bryophytes, suggests that this may be the ancestral role of IQDs, although it is probably not conserved in all extant IQD proteins (Dahiya et al. 2023).

The phenotypic similarities between the *iqd678* root cells and *1aiqd-2* rib meristem are striking – both show an increase in the variability of cell division orientation (Kumari et al. 2021). It is possible, therefore, that IQD6-8 and 1A IQDs regulate cell division orientation via similar mechanisms in the root and rib meristem, respectively. However, 1A IQDs are

not closely related to IQD6-8 within the AtIQD family and the members of the two subclades have few protein sequence motifs in common (Abel et al. 2005). Thus, even if they are involved in a similar mechanism, there may be substantial mechanistic differences.

3.1.2.2 Regulation of cMTs

External and internal cues dynamically modify the organisation of cMTs to regulate cell growth and division. Some IQDs impact the ability of MTs to dynamically reorganise, via regulation of MT stability, which has consequences for cell shape, growth anisotropy and division plane positioning (Yuanfeng Li et al. 2021; Bao et al. 2023; Liang et al. 2018; Feng et al. 2023; Hoermayer et al. 2024; Yang et al. 2021). This is because the cMTs that lie proximate to the PM surface guide the protein complexes that synthesise and deposit cell wall cellulose (Li et al. 2012; Paredez et al. 2006; Wilson et al. 2021). Thus, cMT organisation can affect the amount of cellulose deposition and the orientation of the microfibrils, thereby affecting the extensibility of the cell wall.

In *iqd5* and *iqd21* mutants, the cMTs are less stable and this is associated with more randomly oriented cMTs in puzzle-shaped cotyledon pavement cells (Liang et al. 2018; Feng et al. 2023). This is hypothesized to alter the pattern of cell wall cellulose deposition, altering localised growth anisotropy, and it likely explains the reduced lobe outgrowth in the cells (Feng et al. 2023; Liang et al. 2018). Conversely, cells that overexpress *IQD21* or *IQD16* have more ordered, directional cMT arrays, due to enhanced MT stability and bundling. This is associated with growth that is more anisotropic, likely due to the mechanical resistance imposed by directional cellulose deposition (Feng et al. 2023; Yuanfeng Li et al. 2021; Bürstenbinder, Möller, et al. 2017). This mechanism may underpin one of the earliest known phenotypes of IQD misregulation, that of altered tomato fruit shape. The elongated fruits of tomatoes overexpressing *SlIQD21* have more transversely orientated cMTs in the cells of the endocarp (Bao et al. 2023). This may derive from a MT-stabilising effect of *SlIQD21a* that perturbs dynamic MT rearrangement as the fruit develops.

It has been proposed that IQDs operate as signalling hubs that integrate various cues to direct MT reorganisation (Bürstenbinder, Mitra, et al. 2017; Vaddepalli et al. 2021). For some IQDs, this is mediated by the MT-severing enzyme KATANIN1 (KTN1), which is required for the reorganisation of MTs in response to both cell geometry and external cues (Durand-Smet et al. 2020; Uyttewaal et al. 2012; Yuanfeng Li et al. 2021; Feng et al. 2023). IQD21 and IQD16 directly interact with KTN1 and regulate its activity and thereby

modify cMT organisation (Feng et al. 2023; Yuanfeng Li et al. 2021). It is unknown whether the IQD-KTN1 interaction is more widespread in the IQD family.

3.1.2.3 Regulation of PM microdomains

Plant PMs comprise many diverse subdomains, differing in their size, position and composition (Jarsch et al. 2014). Polar domains are especially important for plant morphogenesis (Elliott and Kirchhelle 2020; Gorelova et al. 2021) and can regulate cell division orientation (Muroyama et al. 2020). Moreover, PM subdomains are important for establishing local mechanical properties. For example, specific, localised accumulation of the RAB-A5c GTPases at the geometric edges of cells maintains normal cell and organ geometry, likely by promoting wall-stiffening in these domains (Kirchhelle et al. 2016)

Some IQDs have important roles in the establishment and/ or maintenance of PM subdomains, and this hinges on the ability of IQDs to bridge the PM, MTs and other cellular components. IQD2 supports the maintenance of localised ER-PM contact sites (Zang et al. 2021). These sites influence the general organisation of the cortical ER and cytoskeleton, and also act as signalling hubs, which might regulate a diverse set of physiological and developmental processes (Bayer et al. 2017). IQD2 forms a trimeric complex with MT-binding KINESIN LIGHT CHAIN-RELATED (KLCR) proteins and actin-binding NETWORKED 3C, bridging actin, MTs and the ER at the PM (Zang et al. 2021). A similar mechanism could have relevance for cell division, since an ER ring associates with the PPB in some dividing plant cells (Giannoutsou et al. 2012; Zachariadis et al. 2001). However, it is not known what – if any – role this ER ring has in the regulation of cell division or even if there are direct ER-PM or ER-MT interactions at this site.

IQD13 has a highly specialised function: it regulates the shape of pits in the secondary cell walls of metaxylem vessels (Sugiyama et al. 2017). However, it could point to a more generalised mechanism of IQD function. IQD13 promotes the association between MTs and the PM, which spatially confines the domain of active RHO-RELATED PROTEIN FROM PLANTS 11 (ROP11) (Sugiyama et al. 2017). ROP11 is a Rho-type GTPase that initiates the formation of the cell wall pits (Oda and Fukuda 2012) . Concentrated domains of ROP activity underpin many different cellular processes in plants (Yang and Lavagi 2012) , including cell division orientation (Mulvey and Dolan 2023), cell growth (Hwang et al. 2010), leaf puzzle cell digitation (Fu et al. 2010), and auxin transport (Nagawa et al. 2012; Lin et al. 2012), so this mechanism may well be more widespread.

3.1.2.4 Stabilisation of non-MT proteins

More recently it has been shown that IQDs can regulate protein abundance by direct binding or binding their interactors. Under hypoxic conditions, a complex of IQD22 and CaM2 binds to and stabilises ALCOHOL DEHYDROGENASE 1 (ADH1), allowing a key component of the plant's metabolic hypoxia response to accumulate within cells (Zhao et al. 2025). IQD22 also stabilises the transcription factor RELATED TO AP2.12 (RAP2.12) by enhancing its interaction with calcium-dependent protein kinase 12 (CPK12). This leads to the upregulation of hypoxia-responsive genes (Zhao et al. 2025). So far, this is the only direct, mechanistic example of an IQD regulating gene expression, although separate instances of IQD knockdown/ mutation inducing transcriptional changes have been observed (Yuan et al. 2019; Levy et al. 2005). Since many aspects of morphogenesis are transcriptionally controlled, this mechanism opens up broad possibilities for IQD-mediated regulation of development. Division plane selection is affected by auxin signalling and specific transcription factors, and so IQD-mediated regulation of TFs could very plausibly play a role in the *1aiqd-2* phenotype (Yoshida et al. 2014; Ishikawa et al. 2023).

3.1.3 The expression of 1A IQDs

The first step in understanding how 1A IQDs regulate cell division and growth, is identifying where they are expressed at the organ and tissue levels. This will determine whether the IQDs are acting locally to regulate cell division or causing growth changes more broadly. As might be expected for such a gene large family, IQDs vary significantly in their expression patterns, suggesting that they have evolved specialised functions. Some IQDs have cell-cycle-dependent expression (Kumari et al. 2021) and some are regulated by hormones, including auxin (Möller et al. 2017; Wendrich et al. 2018) and gibberellins (Zentella et al. 2007). Several IQDs have tissue- or cell-type specific expression, for example in meristematic tissue (Kumari et al. 2021), leaf palisade cells (Matthes et al. 2022; Procko et al. 2022) or vasculature (Sugiyama et al. 2017). The expression of many IQDs is sensitive to environmental conditions, including hypoxia (Zhao et al. 2025), drought (Yuan et al. 2019), mechanical stimulation (Levy et al. 2005), temperature (Zhang et al. 2024), nutrient deprivation (Ke et al. 2022) and others (Mei et al. 2021).

The expression of 1A IQDs has not previously been explored, but there is some information available from large-scale screens. Three genes from the 1A IQD subfamily have auxin-sensitive gene expression (Möller et al. 2017; Wendrich et al. 2018). *IQD23, IQD26* and *IQD27* are >1.5-fold downregulated in embryos when the transcriptional auxin

response is repressed. Seven other *IQDs* show the same behaviour, including the regulators of cell division orientation, *IQD6, IQD7* and *IQD8* (Möller et al. 2017; Wendrich et al. 2018; Kumari et al. 2021; Vaddepalli et al. 2021). Additionally, *IQD22* is transcriptionally downregulated by gibberellin (GA) via the DELLA pathway (Zentella et al. 2007). However, this is the extent of existing knowledge and provides little insight into their possible functions of 1A IQDs.

3.1.4 IQD localisation

An IQD protein's subcellular localisation is integral to its function as a molecular scaffold. Not much is known about the subcellular localisation of 1A subfamily IQDs in Arabidopsis, however transient assays of 1A AtIQDs in *Nicotiana benthamiana* offer some clues (Bürstenbinder, Möller, et al. 2017). 1A AtIQDs (and indeed the whole AtIQD family) all showed slightly different localisation patterns. All localised to the PM, with IQD22, IQD24 and IQD25 localised to distinct and immobile plasma-membrane sub-domains. IQD22 colocalised with cMTs while IQD23 and IQD26 also showed filamentous localisation patterns, consistent with microtubular localisation. IQD23 additionally localised to the nucleolus and IQD24 to nuclear subdomains. However, these data provide a limited view of 1A IQD localisation, since the proteins were not expressed under their native promoters. Furthermore, these data offer only a static snapshot, and do not capture localisation dynamics. Indeed, many IQDs localise dynamically and in several cases their localisation is cell-cycle dependent (Kumari et al. 2021; Wendrich et al. 2018).

3.1.5 Chapter aims

In this chapter, I characterise the expression and subcellular localisation of 1A IQDs, to determine whether they directly regulate cell division orientation or cause broader growth effects that alter cell division as an indirect consequence. By probing the subcellular localisation in more detail, I further aim to shed light on *how* 1A IQDs regulate cell division orientation and pinpoint the specific stage(s) of cell division in which they operate.

3.2 RESULTS

3.2.1 Expression of 1A IQDs at the organ and tissue levels

Publicly available gene expression data (Schmid et al. 2005) indicate that *IQD22, IQD23, IQD24, IQD26* and *IQD27* (*IQD25* expression data were not available) are expressed at varying levels in different tissues (**fig. 23a**). *IQD22, IQD26* and *IQD27* are preferentially expressed in the shoot apex at all stages of development, but particularly during flowering and the floral transition. *IQD26* is additionally expressed in the vegetative rosette and root. *IQD24* is expressed in cotyledons, rosette and cauline leaves, while the relative expression of *IQD23* is similar across different organs. None of the five genes exhibit high levels of relative expression in the mature stem, either at the 1st node or second stem internode. A separate study, exploring differential genes expression in different cell types in mature stem (Shi et al. 2021), identified only two 1A *IQD*s to be differentially expressed in the pith relative to the vascular bundles (the control). *IQD24* expression was significantly downregulated in the pith relative to the vascular bundles, while *IQD26* was significantly upregulated (**fig. 23b**). These data suggest that *IQD22, IQD26* and *IQD27* may be the most important for regulating cell division orientation in the shoot apex. To characterise the expression patterns of 1A IQDs with greater spatial and tissue-level resolution, I generated *proIQD:GUS* reporter lines.

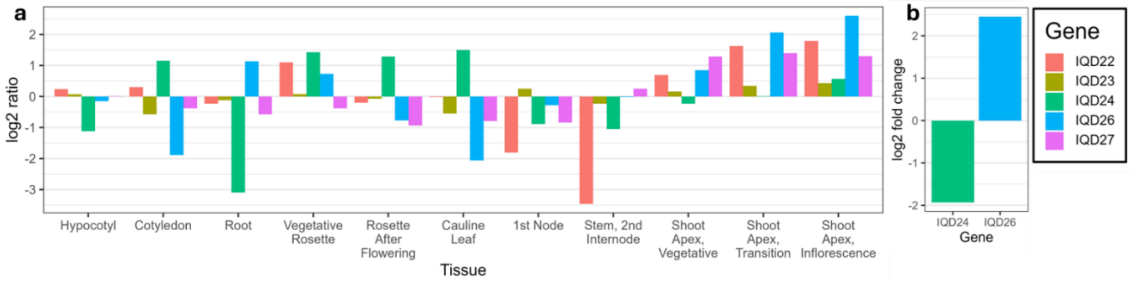

Figure 23: 1A *IQDs* have different organ-level gene expression. (a) Relative RNA expression values (log2 ratio relative to the median level) of *IQD22, IQD23, IQD24, IQD26* and *IQD27* in different *Arabidopsis* tissues. The publicly available microarray data (Schmid et al. 2005) were exported from Arabidopsis Electronic Fluorescent Pictograph (eFP) Browser (Winter et al. 2007). Data were not available for *IQD25*. **(b)** Differential expression (log2 fold change) of genes that are significantly differentially expressed in the pith relative to the vascular bundles in mature stem tissue (Shi et al. 2021).

In seedlings, *proIQD26:GUS* was highly expressed in the root meristem, lateral root primordia, developing leaves and SAM (**fig. 24a-f**). In 3-week-old vegetative rosettes,

expression was largely absent from mature rosette leaves, being strongest in the middle of the rosette (in the newest leaves) (**fig. 24g-i**). Here the staining was punctuated by darker speckles (**fig. 24i**). The speckles were limited to the newer leaves and the base

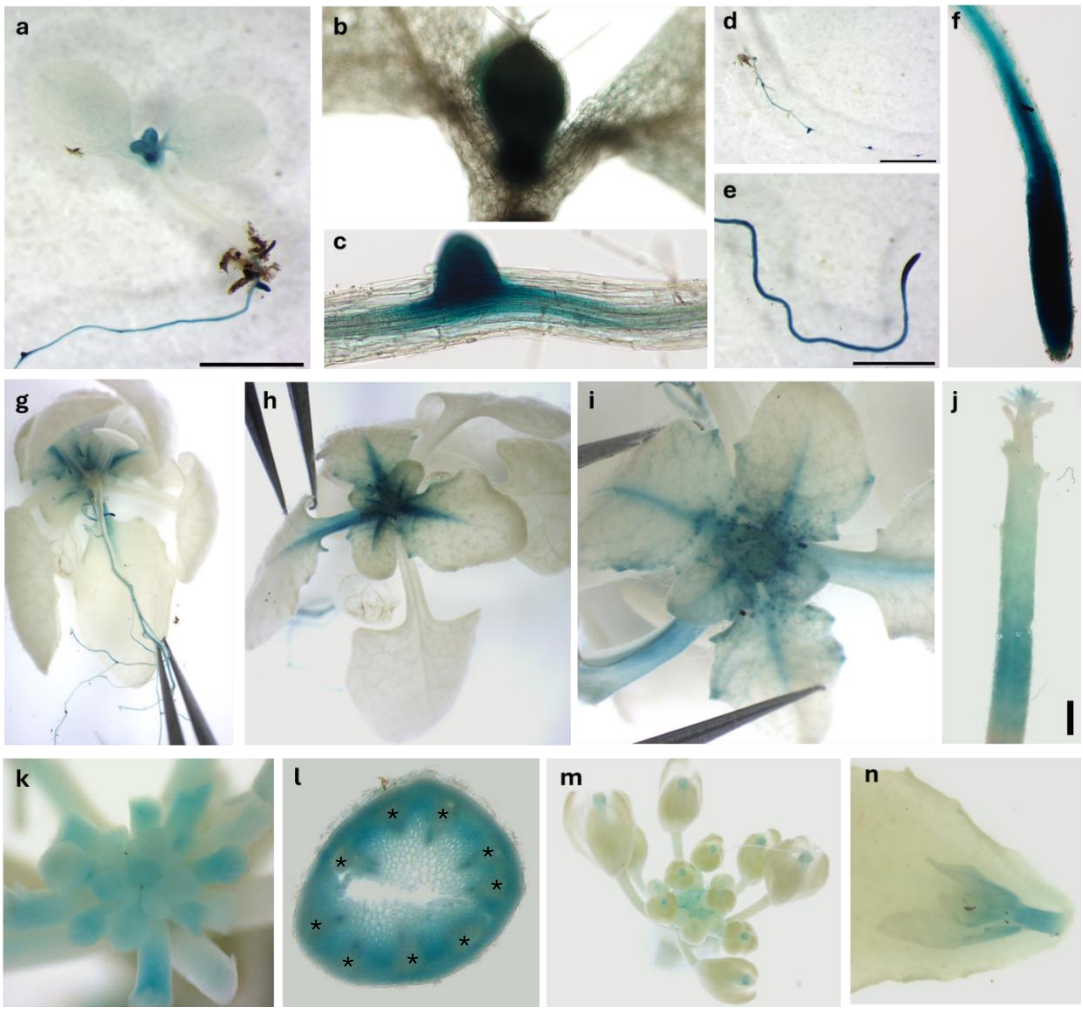

Figure 24: *proIQD26:GUS* is expressed in dividing tissues. Histochemical staining of 7-day-old seedlings (a-f), 3-week-old rosettes (g-i) and 6-week-old flowering stems (j-n) expressing *proIQD26:GUS*. Plants were stained intact and subsequently dissected for imaging. **(a)** Whole seedling, **(b)** apical meristem with developing leaves, **(c)** lateral root primordium, **(d)** root with multiple lateral root primordia, **(e)** root terminating in root meristem, **(f)** root meristem, **(g-i)** rosette leaves and roots, **(j)** flowering stem, with buds and branches removed, **(k)** SAM, **(l)** transversal stem section cut approx. 7 mm below the meristem, **(m)** flowering stem apex, **(n)** lateral branch. Asterisks indicate the vascular bundles. Results are representative of 3 independent transgenic lines. Scale bars: 1 mm

of slightly older leaves. Similarly spotty patterns of staining can be observed in reporters for cell cycle activity (Colón-Carmona et al. 1999) and so this pattern of staining may reflect cell-cycle linked expression. Expression was largely absent from mature rosette

leaves. In flowering stems, *proIQD26:GUS* was expressed in the shoot apical meristem, although absent from the region immediately below (**fig. 24j,k**). Where *proIQD26:GUS* was expressed further down the stem, all tissues bar the vasculature exhibited staining (contrast **fig. 24l** with **fig. 28g**). This is consistent with data showing that *IQD26* expression is upregulated in the pith relative to the vascular bundles (**fig. 23b,** (Shi et al. 2021)). *proIQD26:GUS* also expressed in the young side branches, floral buds and stigmas (**fig. 24m,n**). Notably, across different developmental stages, most tissues exhibiting high

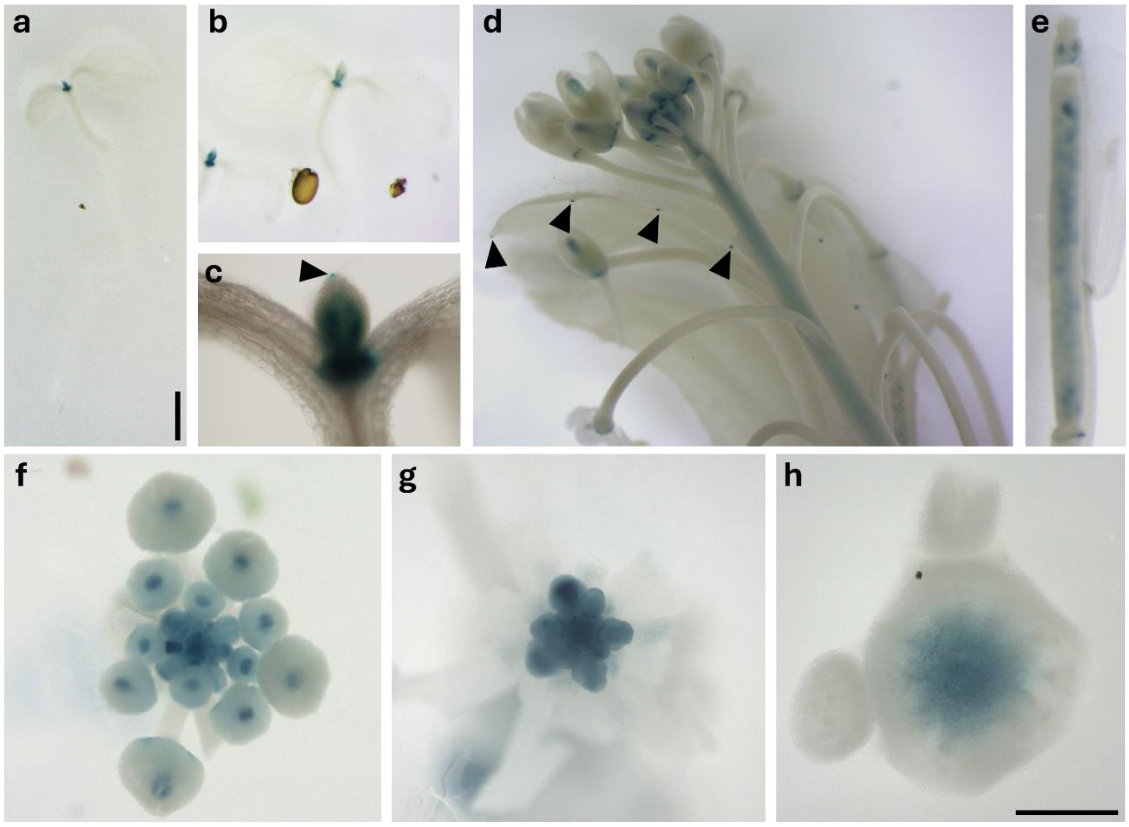

Figure 25: *proIQD27:GUS* is primarily expressed in internal tissues. Histochemical staining of 7-day-old seedlings (a-c) and 6-week-old flowering stems (d-h) expressing *proIQD27:GUS*. Plants were stained intact and subsequently dissected for imaging purposes. **(a,b)** Whole seedlings, **(c)** apical meristem with developing leaves, **(d)** flowering stem, **(e)** developing silique, **(f, g)** the same shoot apical meristem, before and after the outer buds have been removed, **(h)** transversal stem section cut approx. 1-2 mm below the meristem. Black arrowheads indicate leaf serration tips. Results are representative of 3 independent transgenic lines. Scale bars: (a) 1 mm, (h) 0.5 mm

proIQD26:GUS expression were meristematic or otherwise undergoing significant cell division/ growth: root meristems, apical meristems, young leaves and buds. This is a similar pattern of expression to *IQD8* (Kumari et al. 2021).

In seedlings, *proIQD27:GUS* was expressed only in the developing leaves, where it was absent from the leaf edges, and in the apical meristem (**fig. 25a-c**). GUS staining was absent from mature leaves, except for at the very tips of the leaf serrations (**fig. 25d**). In flowering stems, *proIQD27:GUS* was expressed in the stem, but its expression was confined to the pith tissue and the meristem (**fig. 25d-h**). The most striking observation was that, across different organs and developmental stages, *proIQD27* specifically expressed in the internal tissues. Furthermore, it is expressed most strongly in actively

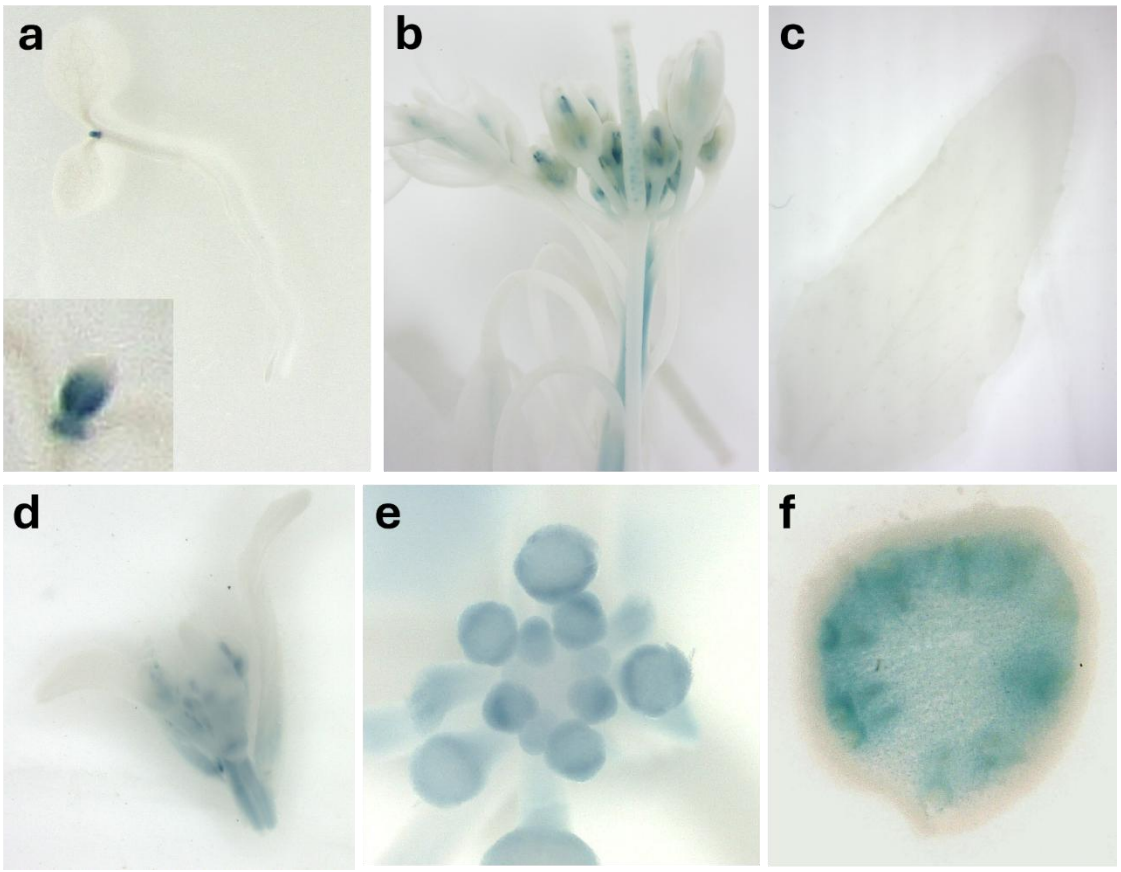

Figure 26: *proIQD25:GUS* is expressed in the stem interior, in developing leaves and floral buds. Histochemical staining of 7-day-old seedling (a) and 6-week-old flowering stems (b-f) expressing *proIQD25:GUS*. **(a)** Whole seedling with magnified view of a seedling apex inset, **(b)** flowering apex, **(c)** cauline leaf, **(d)** lateral branch, **(e)** SAM, **(f)** transverse stem section cut 1-2 cm below the stem apex. Results are representative of 3 independent transgenic lines.

growing tissues, including the developing leaves, the shoot apical meristem and the youngest floral buds. This makes *IQD27* a strong contender for direct regulation of rib meristem development.

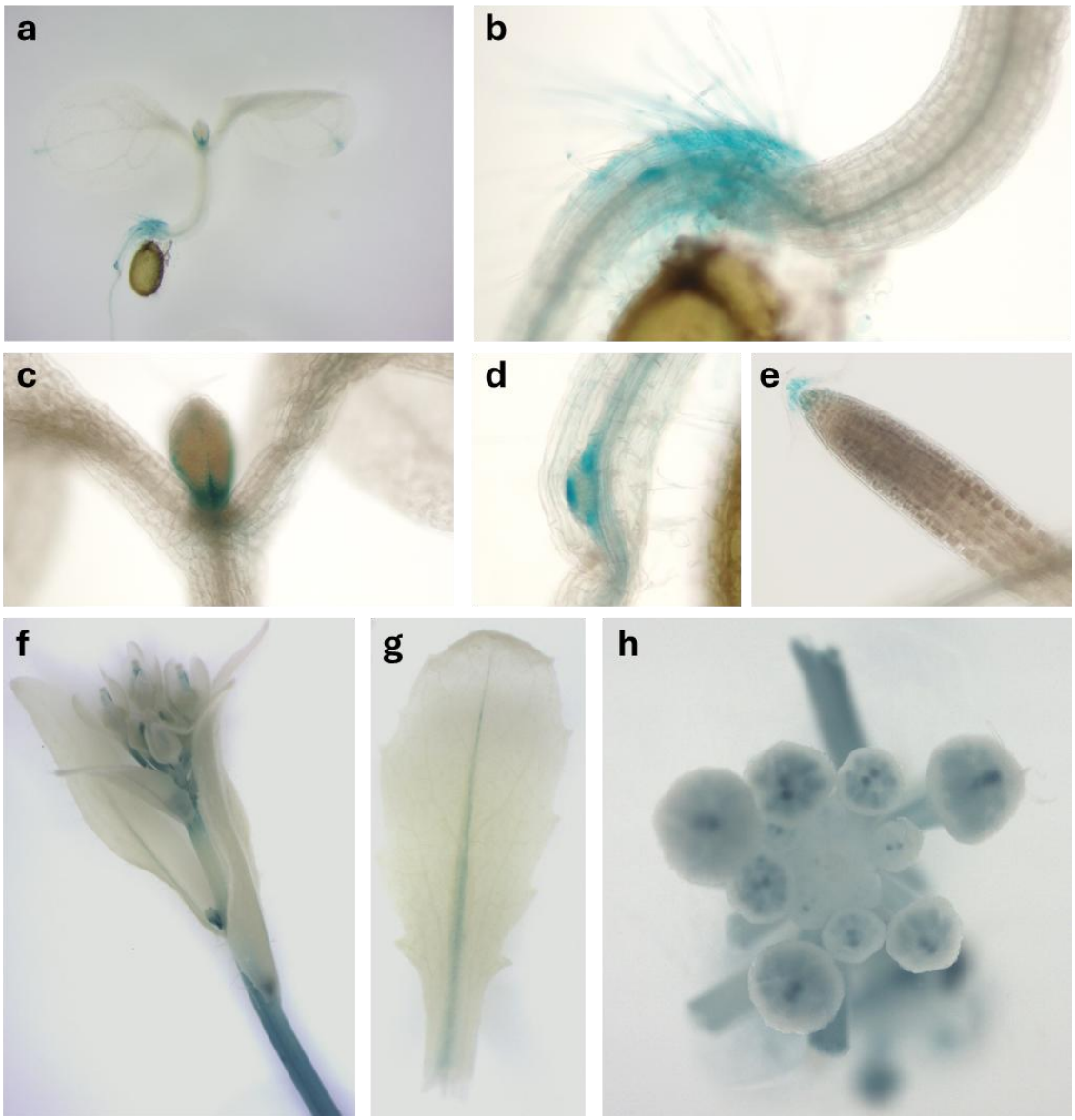

Figure 27: *proIQD23:GUS* is expressed in lateral root primordia and stems, but not in the shoot or root meristems. Histochemical staining of 7-day-old seedlings (a-e) and 6-week-old flowering stems (f-h) expressing *proIQD23:GUS*. **(a)** Whole seedling, **(b)** hypocotyl-root junction, **(c)** apical meristem with developing leaves, **(d)** lateral root primordium, **(e)** root apical meristem, **(f)** flowering stem, **(g)** cauline leaf, **(h)** SAM. Results are representative of 3 independent transgenic lines.

In seedlings, *proIQD25:GUS* was expressed only in the developing leaves and apical meristem, similar to *IQD27* (**fig. 26a**). It was not expressed in mature leaves or flowers, except in the gynoecium (**fig. 26b-c**). *proIQD25:GUS* was expressed in the stem and young lateral branches, although expression was absent from the epidermis and cortex (**fig. 26b,d,f**). This is a different stem expression pattern to *IQD27*, which was additionally absent from the vascular and interfascicular tissue (**fig. 25h**). *proIQD25:GUS* was strongly

expressed in developing floral buds, but weakly or not expressed in the shoot apical meristem itself. This pattern of *IQD25* expression shown here is similar to previously published results (Bürstenbinder, Möller, et al. 2017).

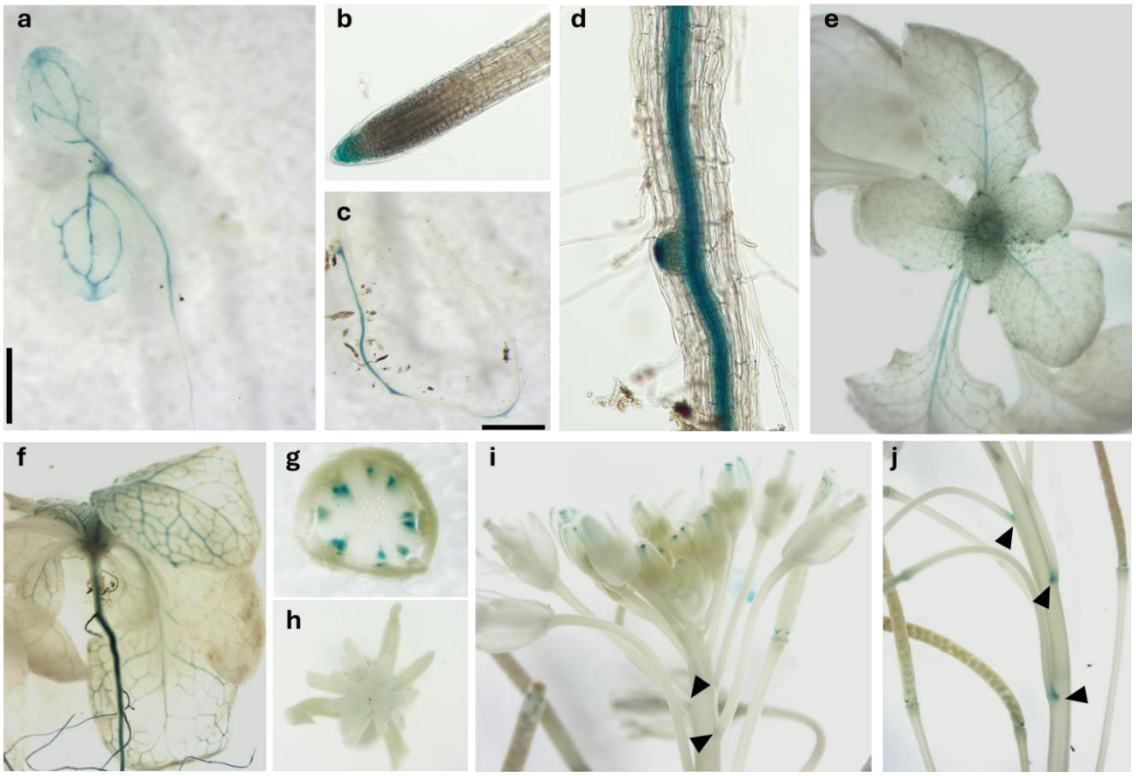

Figure 28: *proIQD24:GUS* is primarily expressed in the vasculature. Histochemical staining of 7-day-old seedlings (a-d), 3-week-old rosettes (e,f) and 6-week-old flowering plants (g-j) expressing *proIQD24:GUS*. Plants were stained intact and subsequently dissected for imaging purposes. **(a)** Whole seedling, **(b)** root meristem, **(c)** whole root, **(d)** lateral root primordium, **(e, f)** rosette leaves and roots, **(g)** transverse stem section, **(h)** SAM, **(i)** flowering apex, **(j)** stem with siliques. Black arrowheads indicate regions of intense GUS staining at the pedicel-stem junction. Results are representative of 3 independent transgenic lines. Scale bar: 0.5 mm

In seedlings, *proIQD23:GUS* was expressed in developing leaves, lateral root primordia, root cap and at the top of the root, where it meets the hypocotyl (**fig. 27a-e**). In flowering stems, it was expressed in the stem, pedicels, and gynoecia (**fig. 27f,h**). Expression was absent in the apical meristem of the hypocotyl and stem (**fig. 27c,h**), which contrasts with the *IQD26* and *IQD27* GUS reporters, but is consistent with RNA expression data (**fig. 23a**). It is therefore unlikely *IQD23* contributes to the regulation of division orientation in the stem apex in wild type plants.

proIQD24:GUS was expressed in the cotyledons and roots of seedlings, with a pattern of staining indicative of vascular expression (**fig. 28a-d**). Similarly, *proIQD24:GUS* was expressed in the vasculature of vegetative rosette leaves and stems (**fig. 28e-g**). This is consistent with data showing that *IQD24* expression is downregulated in the pith relative to the vascular bundles (**fig 23b,** (Shi et al. 2021))**.** Expression was absent from the stem apex (**fig. 28h**). Aside from the vasculature, *proIQD24:GUS* accumulated at the pedicel-stem junction. The expressions pattern of *IQD24* suggests that it does not play a significant role in regulating division orientation in the wild-type plants. Nonetheless, the vascular bundles support stem growth mechanically and nutritionally, and mutations in vasculature-expressed genes can cause defects in stem development (Bush et al. 2022).

A *proIQD22:GUS* reporter was not generated after repeated attempts to clone the *IQD22* promoter failed. This was likely due discrepancies between the *IQD22* promoter sequence in the TAIR sequence repository and in our gDNA template, a discrepancy which has been highlighted by other authors (Matthes et al. 2022). However, *proIQD22:GUS* has been generated by other authors, who report expression in many different plant organs, including seedlings (throughout), roots, stems, leaves, flowers and siliques (Zhao et al. 2025). It has also been reported that levels of native *IQD22* transcripts are lowest in the stem relative to all other tissues tested (Zhao et al. 2025). In leaves *IQD22* expression is specific to the palisade cell layer (Matthes et al. 2022; Procko et al. 2022), but whether expression is equally as cell-type/ cell-layer specific in other organs has not been determined.

3.2.2 Expression and localisation of 1A IQDs in the SAM

The GUS staining indicated that *IQD26* and *IQD27* are all expressed in the SAM. To determine more precise expression domains, and investigate subcellular protein localisation, I generated *proIQD:IQD-YFP* fusions. I transformed these into the *1aiqd-2* mutant background to generate lines that could be used both to determine protein localisation and test complementation of the mutant phenotype. For *proIQD23:IQD23-YFP and proIQD24:IQD24-YFP*, YFP signal was not detectable in the SAM, which is consistent with the expression of their respective GUS reporters. The remaining lines are described in the following sections.

3.2.2.1 Expression and localisation of IQD26-YFP

IQD26-YFP was expressed in all layers of the shoot apical meristem (although signal was weaker in the interior of the bud primordia) and localised near the plasma membranes (**fig. 29a**)**.** A distinctive pattern of subcellular localisation was observable, most clearly in

the L1 and L2 cell layers (**fig. 29b, d**). Some cells exhibited concentrations of IQD26-YFP signal near the middle of opposite cell walls (**fig. 29c,** white arrows), a distribution that resembles the position of MTs in the PPB. Other cells had an accumulation of IQD26-YFP signal on their newest cell wall (**fig. 29c,** yellow arrows). This pattern of localisation was less obvious in lower cell layers, possibly because the orientation of cell divisions in these layers is broadly parallel with the (transverse) imaging plane, and image resolution was poorer in the z plane.

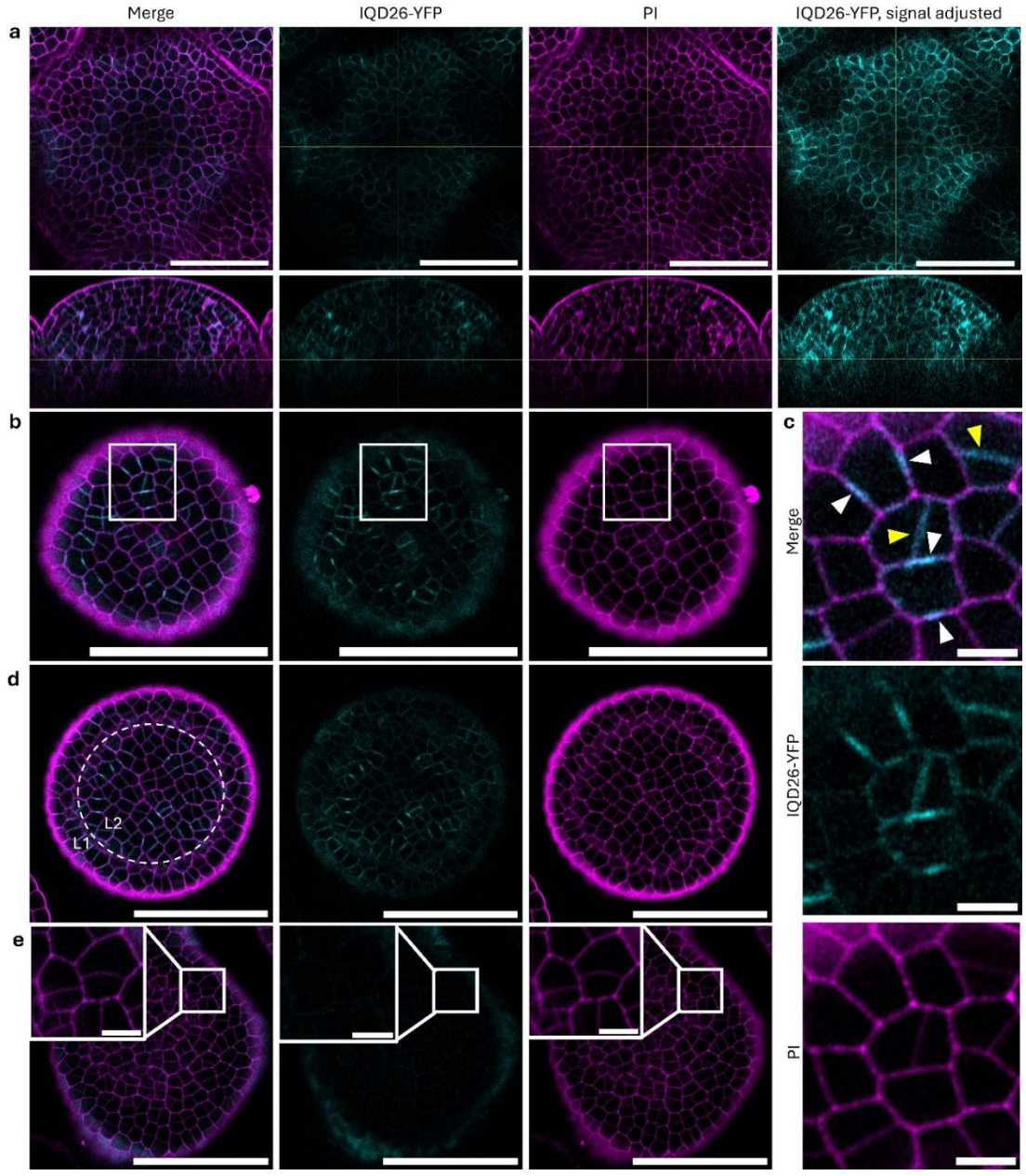

Figure 29: IQD26 is expressed throughout the SAM and has a distintive pattern of subcellular localisation. (a-d) Localisation of IQD26-YFP in the shoot apical meristem of a flowering *proIQD26:IQD26/1aiqd-2* plants. Single optical sections of IQD26-YFP (cyan),

PI-stained cell walls (magenta) and merged signal are shown. Identical acquisition settings and image adjustments were applied to the YFP (cyan) channel across figures 29, 30 and 31. The YFP (cyan) channel with additional brightness adjustment (for easier visualisation) is also shown in (a) (rightmost panels). Transverse sections approx. 45 µm (a), 5 µm (b) and 10 µm (d) from the meristem apex and longitudinal sections (a) are shown. **(c)** Magnification of the framed region in (b). White arrowheads indicate regions of cell walls where IQD26-YFP signal is stronger relative to the rest of the wall. Yellow arrows indicate recently formed cell walls (an assumption based on cell geometry and weak PI signal) that have strong IQD26-YFP signal. Cells inside the L1 and L2 layers are indicated in (d). Images are representative of three independent transgenic lines. **(e)** Single optical sections of a PI-stained meristem from the *1aiqd-2* line showing the level of background signal in the YFP (cyan) channel. PI (magenta) and YFP (cyan) channels were obtained with the same settings as the images in figures 29a-d, 30 and 31. A magnification of some epidermal cells is shown. Scale bars: (a,b, d, e) 50 µm, (c) 5 µm

3.2.2.2 Expression and localisation of IQD27-YFP

IQD27-YFP was only expressed in the interior of the SAM, being largely absent from the meristem L1 and L2 layers, except in the very early bud primordia (**fig. 30a,b**). This is similar to its expression in the mature stem, which was confined to the pith (**fig. 25h**). Where IQD27-YFP was expressed in the meristem, the signal was much stronger than IQD26-YFP and IQD25-YFP (compare **figs. 29a, 30a, 31a).** IQD27-YFP localised near to the plasma membranes but because it was mostly absent in the L1 and L2, a distinctive pattern of subcellular localisation like that of IQD26-YFP was less obvious. Nevertheless, in a small number of cells (mainly the bud primordium epidermis), similar localisation to *IQD26-YFP* could be observed – concentration of IQD27-YFP signal near the middle of opposite cell walls (**fig. 30c**). This suggests that IQD26-YFP and IQD27-YFP have similar subcellular localisation and may, therefore, have a similar function. This makes sense in light of their ancestry – IQD26 and IQD27 are a pair of paralogous sister genes, which probably arose as the result of a whole-genome duplication event around 75 million years ago (Abel et al. 2005). Furthermore, it is not uncommon for closely-related IQDs subclade share similar subcellular localisation (Wendrich et al. 2018; Vaddepalli et al. 2021; Kumari et al. 2021).

3.2.2.3 Expression and localisation of IQD25-YFP

IQD25-YFP was weakly expressed throughout the upper layers of the SAM, although signal was even weaker or completely absent in the L1 layer (**fig. 31a**). This is consistent with

proIQD25:GUS lines having little to no GUS staining in the SAM (**fig. 26e**). Further down the meristem, expression was strongest in the peripheral zone and absent from the outermost cell layers, similar to the expression of *proIQD25:GUS* in the mature stem (**fig. 26f**). Like IQD26-YFP and IQD27-YFP, IQD25-YFP localised near the cell membrane (consistent with previous observations (Bürstenbinder, Möller, et al. 2017)) but additionally formed bright puncta in the cytoplasm (**fig. 31c**). The plasma membrane-localised signal was

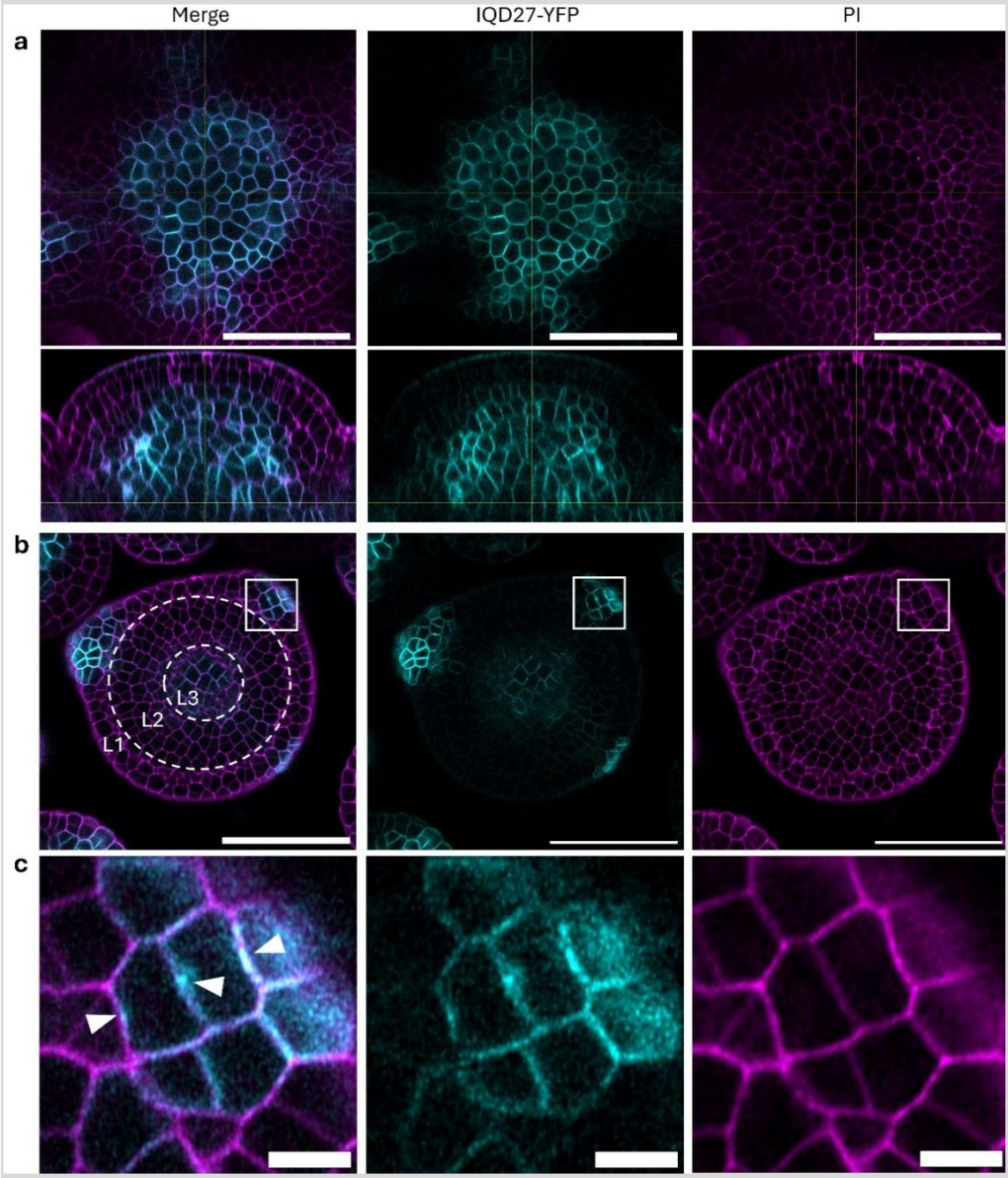

Figure 30 (previous page): IQD27 expression in the SAM is mostly restricted to the inner tissues. (a, b) Localisation of IQD27-YFP in shoot apical meristem of flowering

proIQD27:IQD27/1aiqd-2 plants. Single optical sections of IQD27-YFP (cyan, centre), PI-stained cell walls (magenta, right) and merged signal (left) are shown. Transverse sections approx. 60 µm (a) and 15 µm (b) from the meristem apex and longitudinal sections (a) are shown. Cells inside the L1, L2 and L3 layers are indicated in (b). **(c)** Magnification of the framed region in (b). Arrowheads indicate regions of cell walls where IQD27-YFP signal is stronger relative to the rest of the wall. Images are representative of three independent transgenic lines. Identical acquisition settings and image adjustments were applied to the YFP (cyan) channel across figures 29, 30 and 31. Scale bars: (a,b) 50 µm, (c) 5 µm

consistent within and between cells, lacking the distinctive pattern seen for IQD26-YFP and IQD27-YFP. This suggests that IQD25 may have a different function to IQD26 and IQD27.

3.2.3 Localisation of IQD26-YFP with respect to MTs

To determine whether IQD26-YFP accumulates at the PPB, as its localisation suggests, *proIQD26:IQD26-YFP* was transformed into a Col-0 line containing the *RFP-TUA5* reporter. In the SAM epidermis, IQD26-YFP colocalised with MTs at the PPB (**fig. 32a,b,c,f**). In cells at earlier stages of PPB formation – determined by the presence of a broad accumulation of microtubules at the CDZ and the absence of perinuclear microtubules – IQD26-YFP was barely present at the CDZ (**fig. 32b,d,f**). This suggests that IQD26-YFP is recruited to the CDZ after the PPB has started forming. IQD26-YFP also localised to the cell plate but did not localise along the length of the phragmoplast microtubules (**fig. 32e,f**). Phragmoplast MTs are typically oriented with their plus ends towards the phragmoplast midzone (Smertenko et al. 2017). It is therefore not clear whether IQD26-YFP is localising to the MT plus ends that are adjacent to the cell plate, the membranous structure of the cell plate itself or, possibly, acting as an interface between the two. An interfacing role is possible, since other IQDs function as bridges between MTs and membranous cell compartments (Zang et al. 2021; Sugiyama et al. 2017). As the cell plate expands, the phragmoplast becomes more ring-shaped, lacking MTs in its centre (Smertenko et al. 2017). IQD26-YFP still localised to the cell plate in the MT-depleted regions (**fig. 34d**), implying that, even if its initial localisation depends on the phragmoplast MTs, it is retained at the cell plate as the phragmoplast expands.

In cells that were not undergoing mitosis, IQD26-YFP localised uniformly around the cell, at or near to the plasma membranes. However, the strength of IQD26-YFP signal was variable between cells. Pairs of adjacent cells – likely sister cells, based on their geometry – had

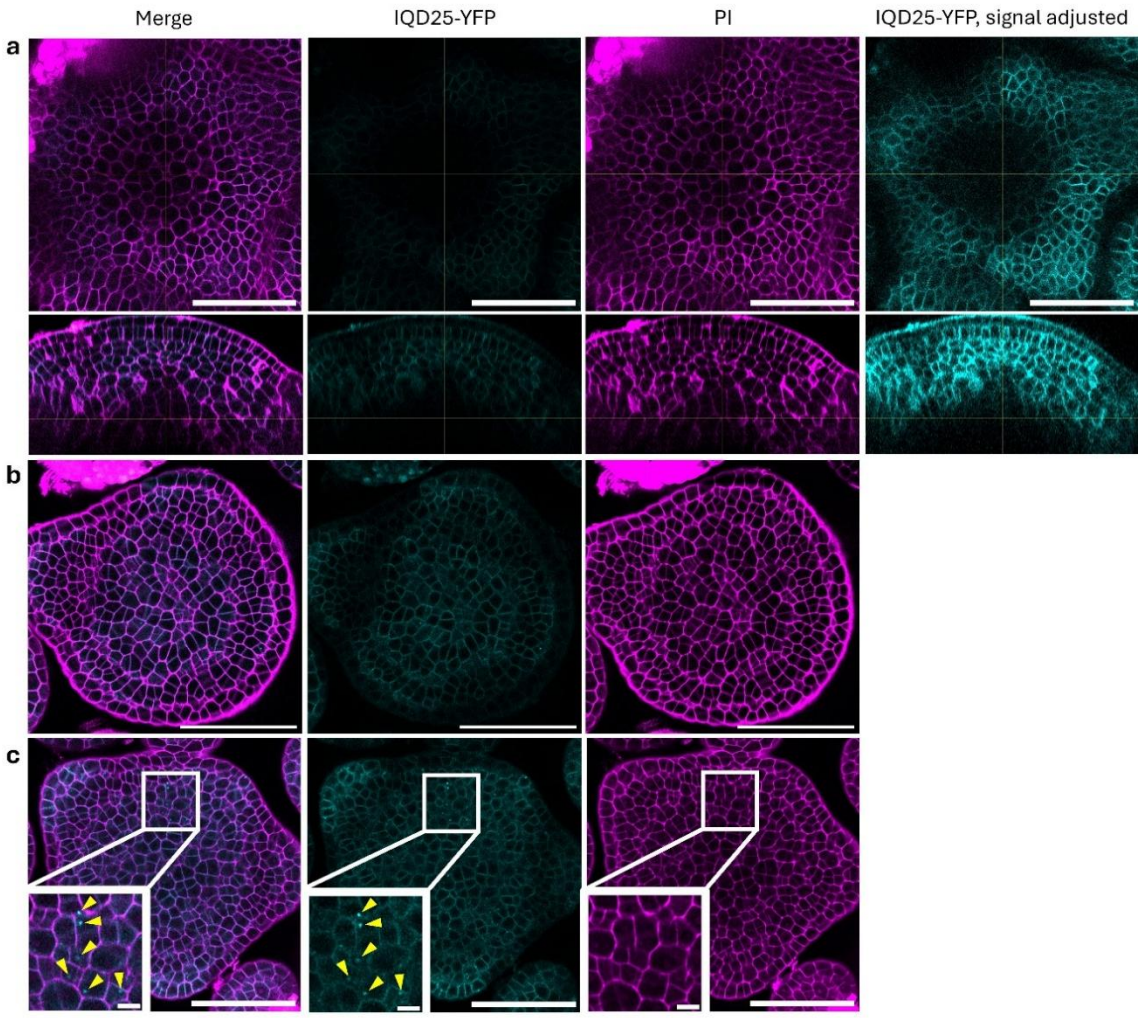

Figure 31: IQD25 is expressed throughout the shoot apical meristem. (a-c) Localisation of IQD25-YFP in the shoot apical meristem of flowering *proIQD25::IQD25/1aiqd-2* plants. **(a-c)** Single optical sections of IQD25-YFP (cyan), PI-stained cell walls (magenta) and merged signal are shown. Identical acquisition settings and image adjustments were applied to the YFP (cyan) channel across figures 29, 30 and 31. The YFP (cyan) channel with additional brightness adjustment is also shown in (a) (rightmost panels) for easier visualisation. Transverse sections approx. 50 µm (a), 17 µm (b) and 25 µm (c) from the meristem apex and longitudinal sections (a) are shown. Yellow arrowheads indicate point-like cytoplasmic accumulations of IQD25-YFP. Images are representative of three independent transgenic lines. Scale bars: (a,b, c main panels) 50 µm, (c inset) 5 µm

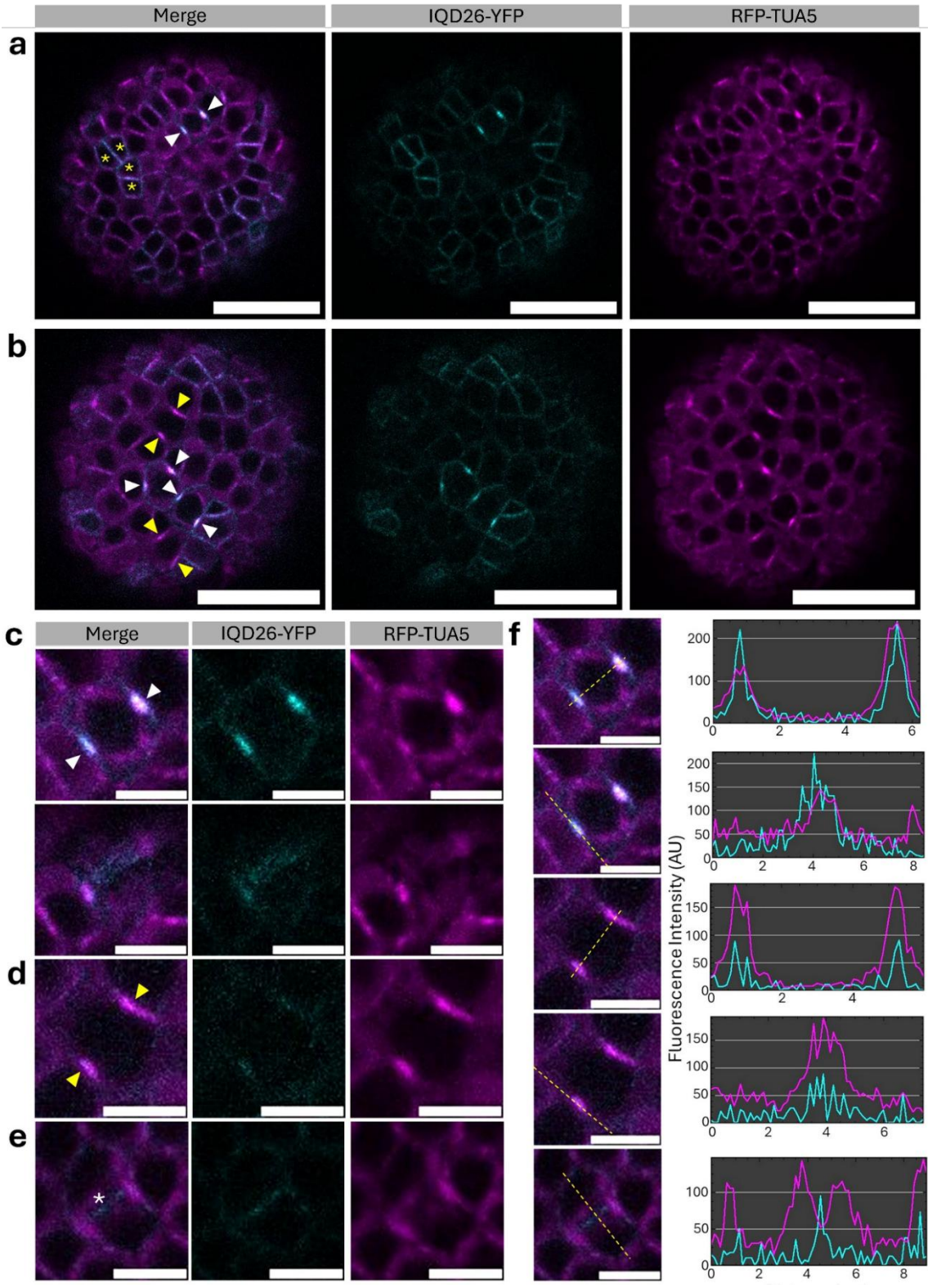

Figure 32 (previous page): IQD26-YFP localises to the PPB and cell plate in the SAM. **(a, b)** Localisation of IQD26-YFP and RFP-TUA5 in SAM epidermis. Single optical sections of IQD26-YFP (cyan, centre), RFP-TUA5 (magenta, right) and merged signal (left) are shown. Meristems shown in (a) and (b) derive from two independent transformations of *proIQD26:IQD26-YFP*. **(c)** Cross-section (top row) and surface (bottom row) of a cell at the

PPB stage. **(d)** A cell with PPB-like accumulation of MTs but little corresponding accumulation of IQD26-YFP. The cell lacks perinuclear MTs and the PPB is more diffuse, suggesting an earlier stage of prophase than (c). **(e)** Cell at the phragmoplast stage of cell division. **(f)** Fluorescence intensity profiles of RFP-TUA5 (magenta) and IQD26-YFP (cyan) in the cells shown in (d-e). Profiles were analysed along the yellow dashed lines. White arrows indicate PPBs with IQD26-YFP accumulation. Yellow arrows indicate early-stage PPBs with minimal/ no IQD26-YFP accumulation. Yellow asterisks indicate pairs of cells with brighter cell-membrane-localised IQD26-YFP signal than surrounding cells. White asterisk indicates the cell plate within the phragmoplast. Scale bar: (a,b) 20 µm, (c-f) 5 µm

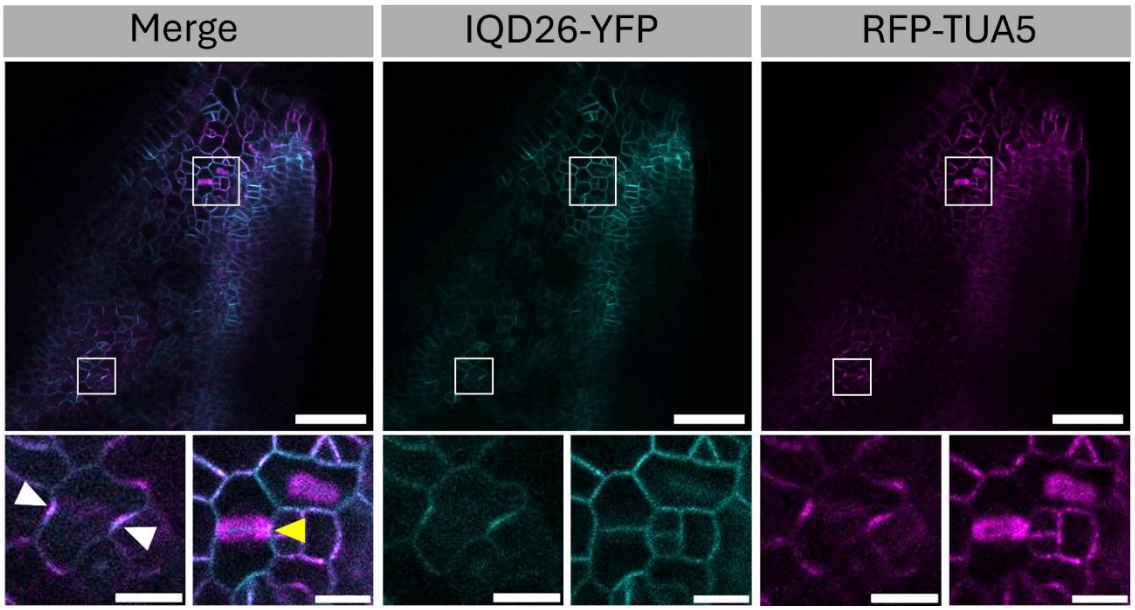

Figure 33: IQD26-YFP localises to the PPB and cell plate in leaf epidermis. (a, b) Localisation of IQD26-YFP and RFP-TUA5 in the leaf epidermis of a 10-day-old seedling. Single optical sections of IQD26-YFP (centre), RFP-TUA5 (right) and merged signal (left) are shown. Magnifications of the framed regions are shown, highlighting a cell at the PPB stage (left) and cells at the phragmoplast stage (right). White arrowheads indicate the PPB. Yellow arrowhead indicates the position of the cell plate within the phragmoplast. Scale bar: (upper panels) 50 µm, (lower panels) 10 µm

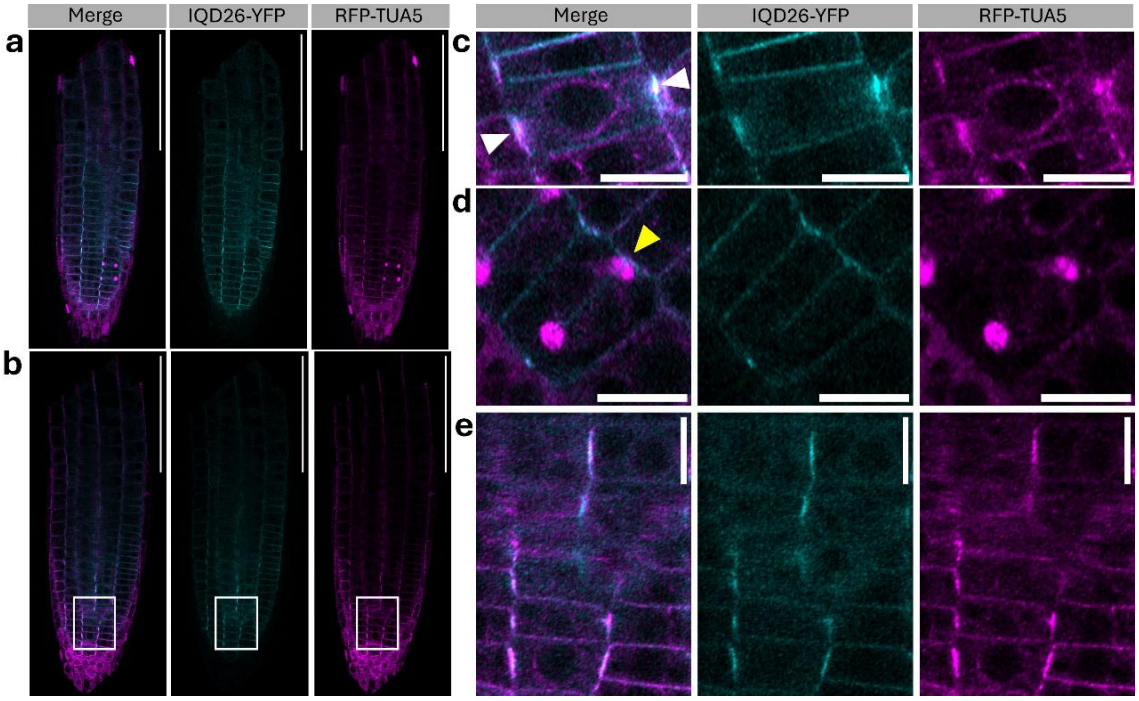

Figure 34: **IQD26-YFP localises to the PPB and cell plate in the root meristem. (a, b)** Localisation of IQD26-YFP and RFP-TUA5 in the root tip of 6-day-old seedlings. Single optical sections of IQD26-YFP (cyan, centre), RFP-TUA5 (magenta, right) and merged signal (left) are shown. (a) and (b) show different optical sections of the same root. **(c)** A cell at the PPB stage. **(d)** A cell at the phragmoplast stage of cell division. **(e)** Magnification of the framed region in (b). White arrowheads indicate the position of the PPB. Yellow arrowhead indicates the position of the cell plate within the phragmoplast. Scale bar: (a,b) 100 µm, (c-f) 10 µm

stronger cell-membrane IQD26-YFP than their neighbours (**fig. 32a, yellow asterisks**). If these are indeed recently divided sisters, this would suggest that IQD26-YFP accumulates during cell-division and lingers for some time after. The localisation of IQD26-YFP with respect to MTs was very similar in both the root tip and developing leaf (**fig. 33, 34**). In these tissues, *IQD26-YFP* localised to the PPB and cell plate in mitotic cells, and at the plasma membrane in the remaining cells. In the root, plasma membrane localisation was less uniform within a single cell – the IQD26-YFP signal was more concentrated at the longitudinal cell walls, particularly in cells near the root tip and in cell layers beneath the epidermis (**fig. 34b,e**) . This corresponds to the distribution of RFP-TUA5 signal in these cells, which localises along the cell's transversal cMT arrays. Overall, the subcellular localisation of IQD26-YFP is very similar to that reported for IQD8-GFP, suggesting that it may play a similar role in PPB formation and/or the recruitment of proteins to the CDZ (Kumari et al. 2021).

3.2.4 The dynamics of IQD26 localisation

To better understand how IQD26 localisation changes through the cell cycle, I performed an imaging time-course using the IQD26-YFP and RFP-TUA5 reporters. I first attempted to perform the time course in the SAM. However, the weak IQD26-YFP signal rapidly attenuated with repeated imaging, and no useful images could be obtained. Additionally, a time course was not attempted with IQD27-YFP, due to the technical challenges of performing a time course on the inner meristem tissues. Since IQD26 is highly expressed in the root meristem (**fig. 34**), and I have established that the localisation of IQD26 is similar across different organs (**figs. 32, 33, 34**), I performed the imaging on roots.

Several hours prior to cell division, IQD26-YFP and RFP-TUA5 accumulated at opposite cell walls that were longitudinal to the main axis of the root (**fig. 35a**). Over several hours, this became more concentrated around the midpoint of each wall, forming the PPB (**fig. 35a**, 5th panel). When the PPB broke down, the MTs migrated to form the spindle but IQD26-YFP did not colocalise with the spindle MTs. Instead, it stayed concentrated at the CDZ (**fig. 35a**, 6th panel) until phragmoplast formation, when it localised to the cell plate (**fig. 35a**, 7th panel). IQD26-YFP remained localised to the new cell wall immediately following cytokinesis – the wall had brighter IQD26-YFP signal than the transverse cell walls of neighbouring cells – but the signal faded over time, until it was consistent with its neighbours (**fig. 35a** 8th panel, **fig. 35c**). This dynamic pattern of IQD26 localisation is consistent with a role in PPB formation or later stages in CDZ maintenance and setup. This is strong evidence that IQD26 (and possibly other 1A IQDs) directly regulates cell division orientation in the rib meristem. Because IQD26 remained concentrated at the CDZ after PPB disassembly (much like IQD8 (Kumari et al. 2021)), a role in CDZ maintenance seems especially plausible.

3.2.5 Gene co-expression network of *IQD26*

In silico co-expression data (Zogopoulos et al. 2025) further support a role for *IQD26* in cell division. Among genes co-expressed with *IQD26, "*cell cycle*"* was the most statistically significantly enriched Gene Ontology (GO) Biological Process (adj. p = 1.5 x 10-75,), while the most enriched Molecular Function and Cellular Component were microtubule binding (adj. p = 3.0 x 10-20) and microtubule cytoskeleton (adj. p = 2.1 x 10-20), respectively (**fig. 36**). *IQD6* and *IQD8* are co-expressed with *IQD26* (Appendix 1, **Table 1**), further suggesting there may be functional similarities between these proteins.

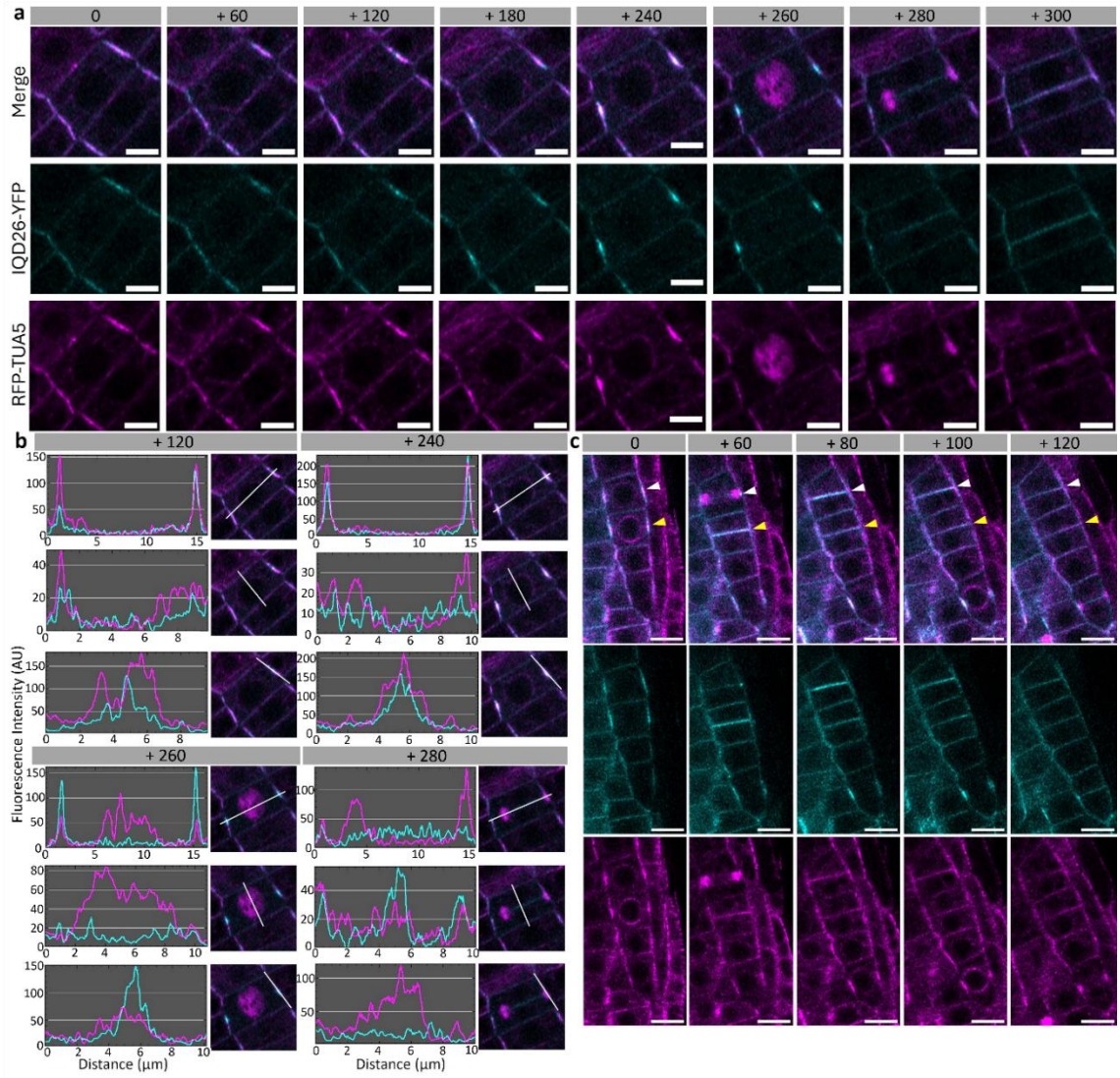

Figure 35: IQD26 localises dynamically during cell division. (a,c) Subcellular localisation of IQD26-YFP and RFP-TUA5 (a microtubule marker) in a root tip epidermal cells over the course of six (a) and two (c) hours. The roots of 6-day-old *proIQD26-IQD26-YFP RFP-TUA5* seedlings were imaged initially at approximately one-hour intervals for then at approximately 20 min intervals. For each time point, the time elapsed in minutes since the capture of the first (left-most) image is indicated. Single optical sections of YFP (cyan, middle panels), RFP (magenta, lower panels) and merged signal (top panels) are shown. In (c), arrowheads indicate the position of the division planes for cell divisions occurring between 0 and 60 minutes (yellow arrowheads), and between 60 and 80 minutes (white arrowheads). **(b)** Fluorescence intensity profiles of RFP-TUA5 (magenta) and IQD26-YFP (cyan) at selected time-points from (a). Profiles were analysed along the white lines. Scale bar: (a) 5 µm, (c) 10 µm

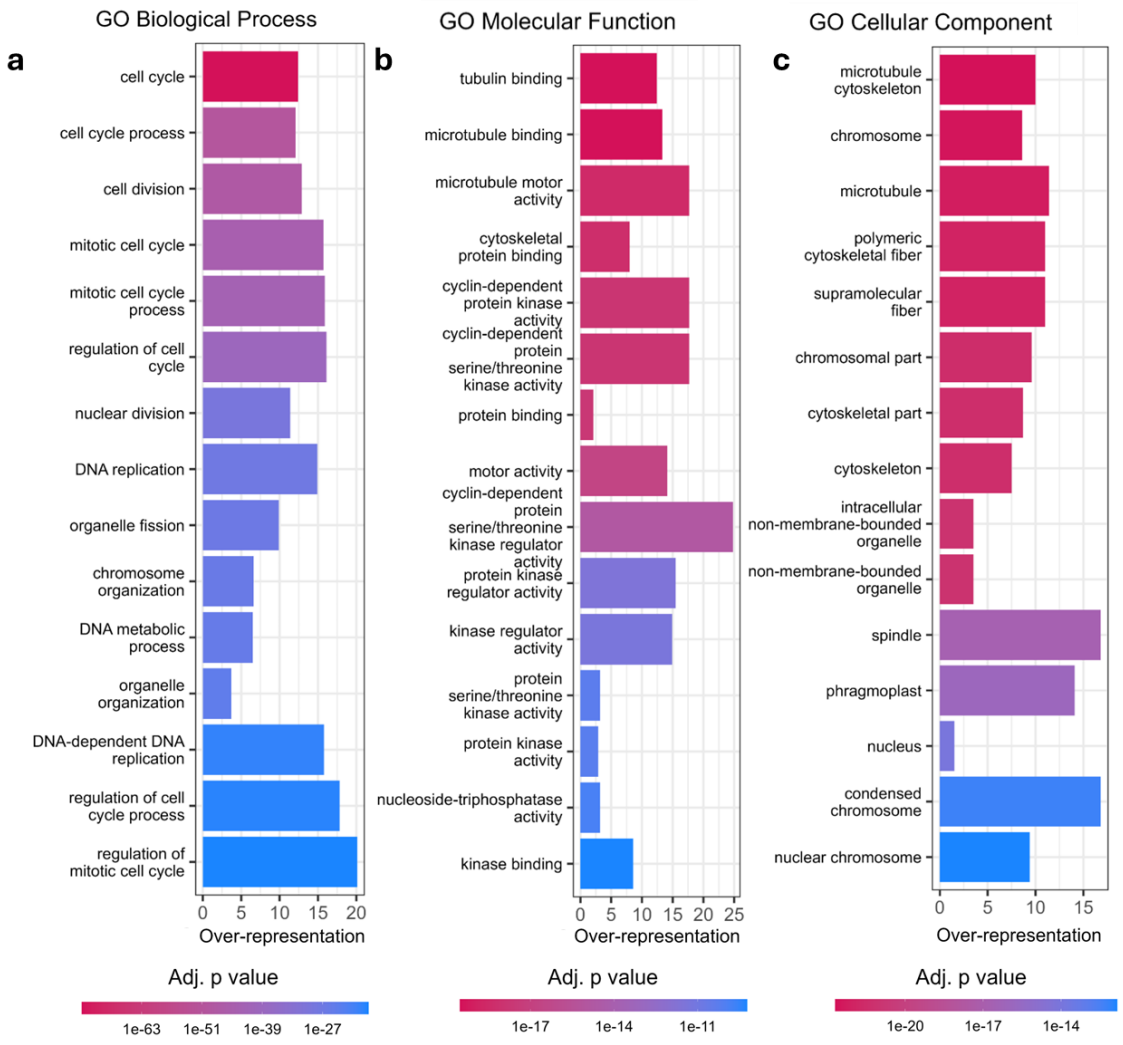

Figure 36: Cell cycle and microtubule-related genes are over-represented among *IQD26* co-expressed genes. (a-c) Bar plots showing the 15 most significantly enriched GO Biological Process (a), Molecular Function (b) and Cellular Component (c) terms among *IQD26*-co-expressed genes. A list of 343 genes (Appendix 1; **Table 1**) that are co-expressed with *IQD26* was generated using the Arabidopsis Coexpression Tool (ACT) Version 2.6 (https://www.michalopoulos.net/act2.6/ (Zogopoulos et al. 2025)) and GO-term enrichment analyses performed, also through ACT2.6.

3.2.6 Complementation of the *1aiqd-2* phenotype by *IQD26*

3.2.6.1 Macroscopic phenotypes

Since the expression and subcellular localisation are so variable amongst the members of the 1A IQD subfamily, I needed to determine whether the observed localisation of IQD26 is functionally relevant to the *1aiqd-2* stem phenotype. To this end, I tested whether endogenous and transgenic *IQD26* could complement the *1aiqd-2* mutant phenotypes.

For this, I generated a pentuple *1a iqd* mutant line by reintroducing the wild type *IQD26* allele into the *1aiqd-2* mutant. The resulting line – *iqd22iqd23iqd24iqd25iqd27* – is hereafter referred to as *iqd22.23.24.25.27*. Stem diameter was measured at two positions – 1 mm from the stem apex and 3 mm from the stem apex. At both positions wild type, *proIQD26:IQD26-YFP/1aiqd-2 #5,* and *iqd22.23.24.25.27* had narrower stems when compared *1aiqd-2* but were not significantly different from each other (**fig. 37b-d**). *proIQD26:IQD26-YFP/1aiqd-2 #46* had narrower stems than all other lines, with a mean diameter 20% smaller than the wild type Col-0.

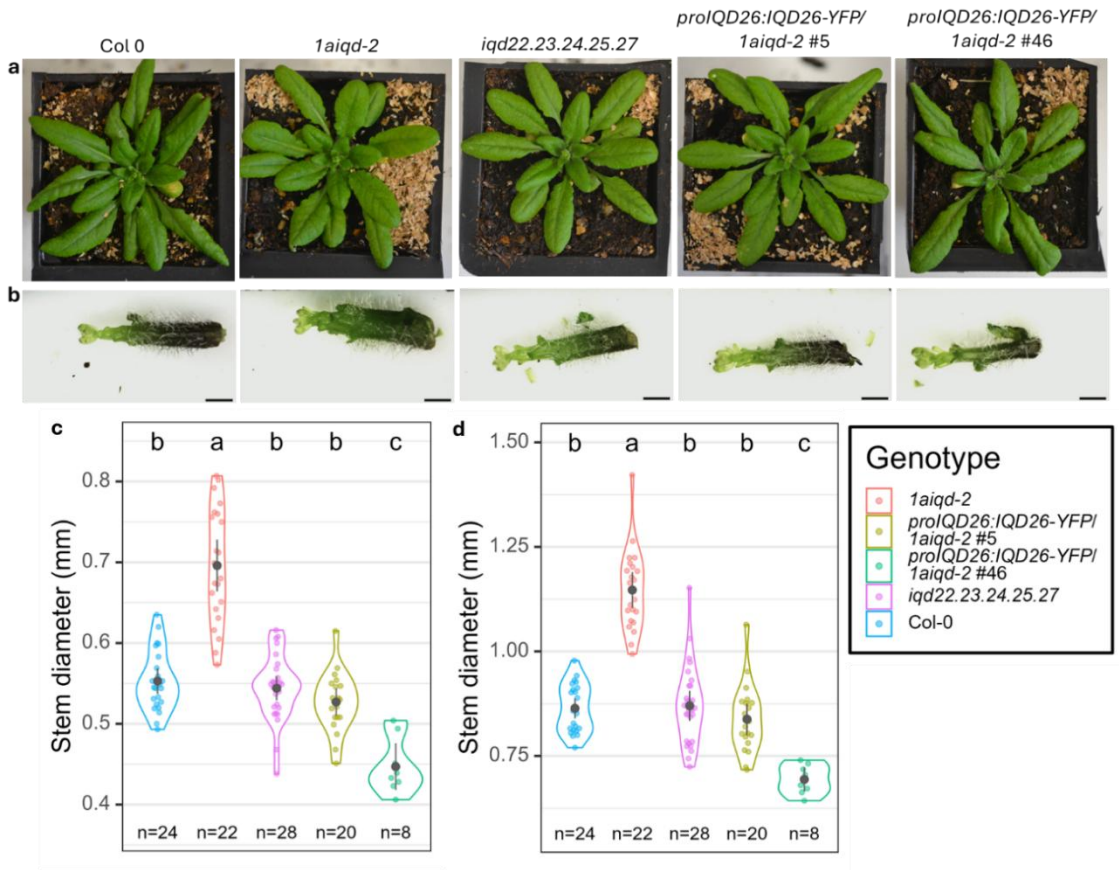

Figure 37: Native and transgenic *IQD26* fully complement the *1aiqd-2* stem phenotype. (a) Photographs showing rosettes of approx. 5-week-old plants. Left to right: wild type Col-0, *1aiqd-2*, *iqd 22.23.24.25.27,* two independent lines of *proIQD26:IQD26-YFP/1aiqd-2*. **(b)** Stereomicrographs showing ~5 mm tall stems, of the same genotypes as (a). **(c,d)** Stem diameters measured 1mm (c) and 3 mm (d) from the stem apex. Statistical significance was determined by Welch's ANOVA. Pairwise comparisons were computed using the Games Howell test, using a significance level of 0.05. Different letters indicate groups with significantly different means. Grey dots and whiskers indicate mean and 95% CI of the mean. Scale bar: 1 mm.

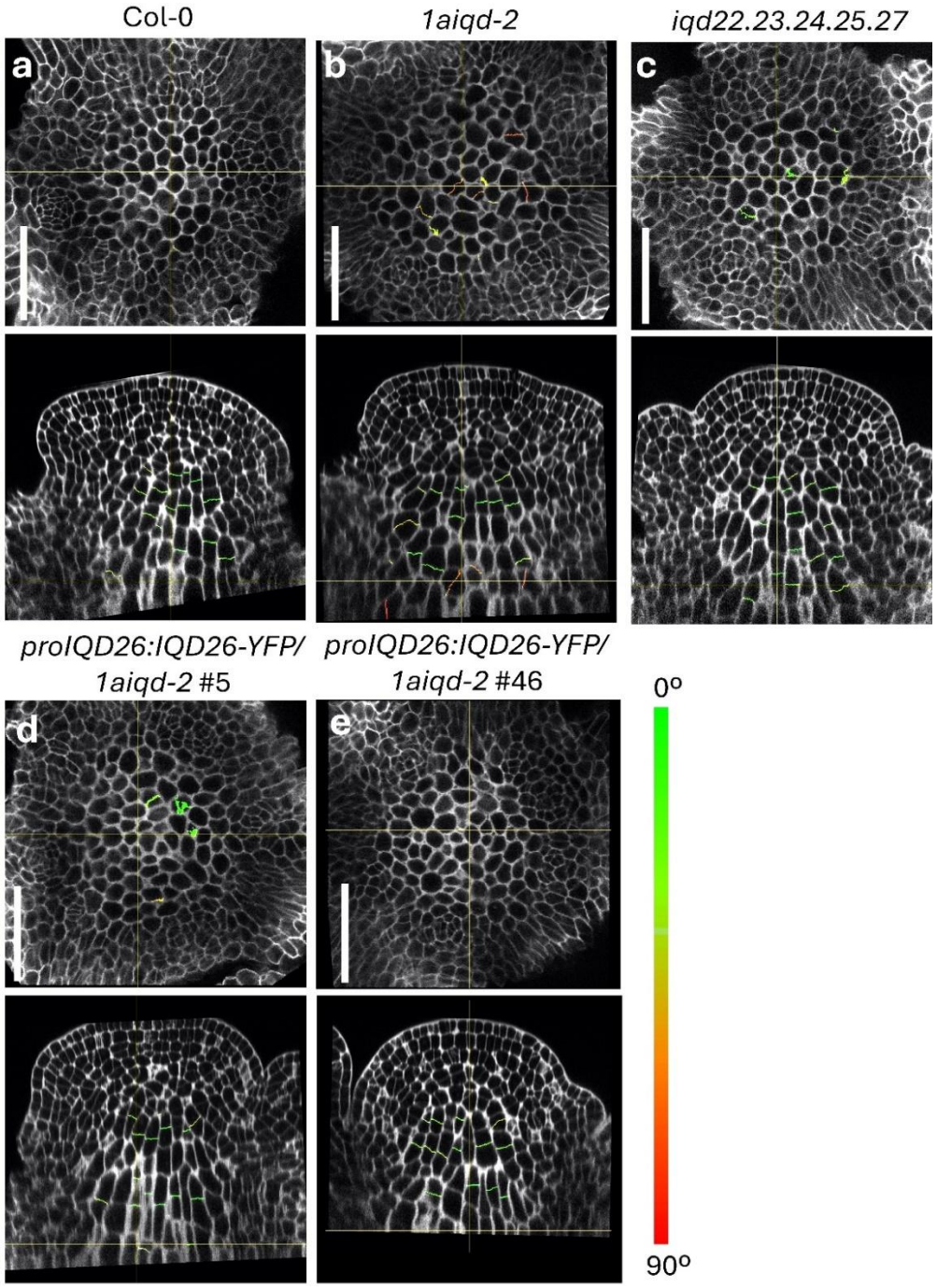

Figure 38: Native and transgenic *IQD26* restore wild type cell division orientation in the rib meristem. (a-e) Single optical sections of fixed PI-stained SAMs from wild type Col-0 (a), *1aiqd-2* (b), *iqd 22.23.24.25.27* (c) and *proIQD26:IQD26-YFP/1aiqd-2* (d,e) plants. Meristems were harvested from 5-week-old plants, at the stage shown in fig. 37a,b. Transverse sections approx. 110 µm from the meristem apex (upper panels) and longitudinal sections through the centre of the meristem (lower panels) are shown. Recently formed cell walls in the rib meristem are coloured on a scale of green to red where green walls are more transversely oriented and red wall are more longitudinal (see Chapter 2, fig. 13). See fig. 39 for quantification. Scale bars: 50 µm

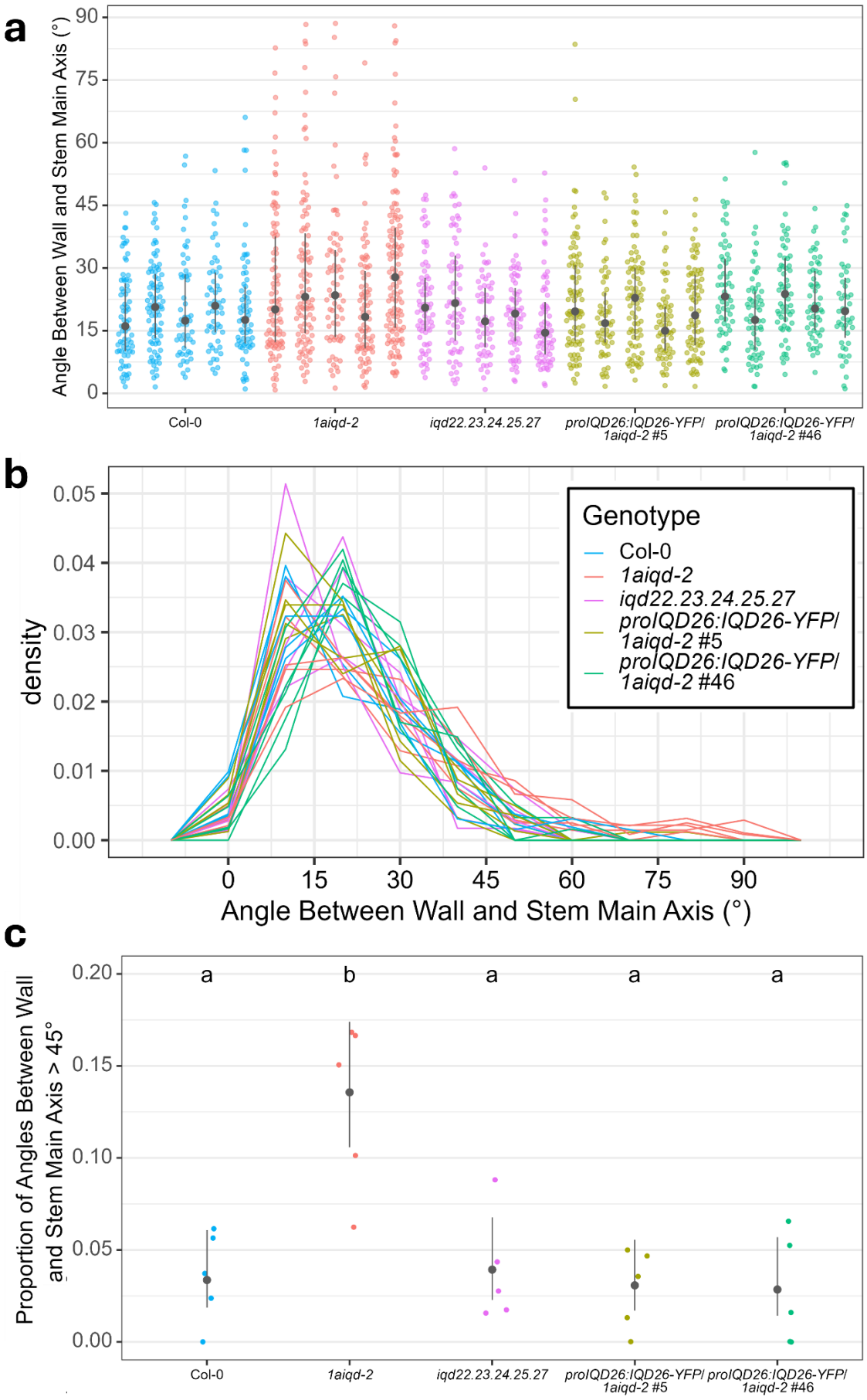
a
Angle Between Wall and Stem Main Axis (°)
0
15
30
45
60
75
90
Col-0
1aiqd-2
iqd22.23.24.25.27
proIQD26:IQD26-YFP/ 1aiqd-2 #5
proIQD26:IQD26-YFP/ 1aiqd-2 #46
b
density
0.00
0.01
0.02
0.03
0.04
0.05
Genotype
Col-0
1aiqd-2
iqd22.23.24.25.27
proIQD26:IQD26-YFP/ 1aiqd-2 #5
proIQD26:IQD26-YFP/ 1aiqd-2 #46
0
15
30
45
60
75
90
Angle Between Wall and Stem Main Axis (°)
c
Proportion of Angles Between Wall and Stem Main Axis > 45°
0.00
0.05
0.10
0.15
0.20
a
b
a
a
a
Col-0
1aiqd-2
iqd22.23.24.25.27
proIQD26:IQD26-YFP/ 1aiqd-2 #5
proIQD26:IQD26-YFP/ 1aiqd-2 #46

Figure 39 (previous page): Native and transgenic *IQD26* restore wild type cell division orientation in the rib meristem. Quantification of new cell wall orientation in the rib meristem as measured in fixed PI-stained SAMs from wild type Col-0, *1aiqd-2*, *iqd22.23.24.25.27*, and *proIQD26:IQD26-YFP/1aiqd-2* plants. Meristems were harvested from 5-week-old plants, at the stage shown in fig. 37a,b. Five meristems were analysed per genotype. (a) Angle between wall and main axis (where values closer to zero indicate more transversely oriented walls, (see fig. 13)). Each point represents the angle of an individual wall and each set of points represents the walls of an individual meristem. (b) Density plot of the same data shown in (a). Each line represents an individual meristem. Black dots and whiskers show median and IQR. (**c**) The proportion of wall angles > 45° in each meristem. Data were analysed using a Poisson model. Black dots and whiskers show back-transformed estimates for the rates and asymptotic upper and lower confidence levels (conceptually equivalent to mean and 95% CI). Different letters indicate genotypes that are statistically significantly different ($p<0.05$).

It has previously been noted that *1aiqd-2* plants have visibly flatter and rounder-looking rosette leaves compared to the wild type (Chapter 1 fig. 5, (Mckechnie-Welsh 2021)). The *iqd22.23.24.25.27* plants and *proIQD26:IQD26-YFP/1aiqd-2 #5* had rosette leaves that look intermediate between *1aiqd-2* and wild type plants, but overall, the complementation effect is subtle. *proIQD26:IQD26-YFP/1aiqd-2 #46* had leaves that were visibly narrower and more curled than in *1aiqd-2* plants.

Although there were differences between the leaf and stem phenotypes of the two *proIQD26:IQD26-YFP/1aiqd-2* lines, these are differences of magnitude, rather than direction (both lines generate narrower stems and leaves, relative to the mutant) indicating that they may derive from varying levels of IQD26-YFP expression.

3.2.6.2 Microscopic phenotypes

The distributions of new cell wall angles in the rib meristems of *iqd22.23.24.25.27* and *proIQD26:IQD26-YFP/1aiqd-2* plants were similar to those of the wild type (**fig. 38, 39**). *iqd22.23.24.25.27* and *proIQD26:IQD26-YFP/1aiqd-2* meristems had only 2 or fewer new walls with an angle of 60° of higher (most meristems analysed have none), whereas *1aiqd-2* meristems possessed several. The proportions of angles > 45° in *iqd22.23.24.25.27* and *proIQD26:IQD26-YFP/1aiqd-2* plants were not significantly different to the wild type (**fig. 39c**).

To determine whether there were corresponding effects on growth in the rib meristem, rib meristem area and cell number where quantified at 60 µm and 100 µm vertical distance from the meristem apex. At 60 µm from the apex, the rib meristems of all lines occupied a similar area, although *1aiqd-2* plants had a larger range of values (**fig. 40e**). The number of cells in this region of the rib meristem was also similar between lines (**fig. 40a**). At 100 µm from the meristem, the area and number of cells in the rib meristem in *proIQD26:IQD26-YFP/1aiqd-2* and *iqd.22.23.24.25.27* were similar to the wild type and much smaller than the *1aiqd-2* (**fig. 40b, f**). All genotypes saw an increase in cell number and area from 60 µm to 100 µm. The rib meristems of *proIQD26:IQD26-YFP/1aiqd-2* had a mean increase of

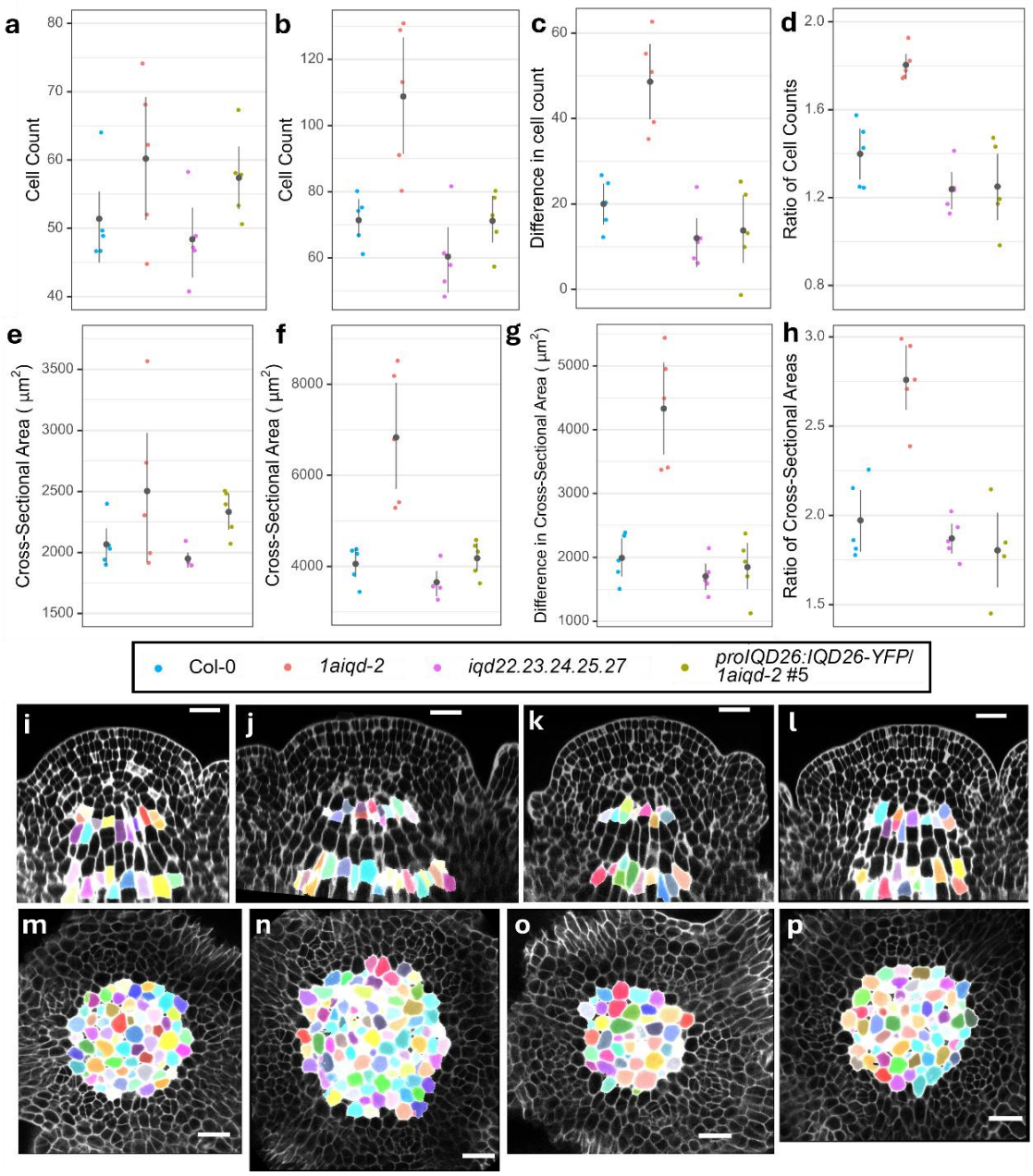

Figure 40 (previous page): Native and transgenic *IQD26* restore wild type cell numbers in the rib meristem. Quantification of rib meristem cell number and cross-sectional area as measured in fixed PI-stained SAMs from wild type Col-0, *1aiqd-2*, *iqd 22.23.24.25.27*, and *proIQD26:IQD26-YFP/1aiqd-2* plants. Meristems were harvested from 5-week-old plants, at the stage shown in fig. 37a,b. Five meristems were analysed per genotype. **(a,b)** The number of rib meristem cells in cross-sections 60 µm (a) and 100 µm (b) from the meristem apex. **(c,d)** Difference in cell number between the 100 µm and 60 µm cross-sections, expressed as an absolute difference (number of cells at 100 µm - number of cells at 60 µm) (c), and as a ratio (number of cells at 100 µm ÷ number of cells at 60 µm) (d). **(e, f)** Area occupied by the rib zone in cross-sections 60 µm (e) and 100 µm (f) from the meristem apex. **(g,h)** difference area between the 100 µm and 60 µm cross-sections, expressed as an absolute difference (area at 100 µm - area at 60 µm) (g), and as a ratio (area at 100 µm ÷ area at 60 µm) (h). **(i-p)** single optical sections of PI-stained SAMs from Col-0 (i, m), *1aiqd-2* (j, n), *iqd 22.23.24.25.27* (k, o), and *proIQD26:IQD26-YFP/1aiqd-2* #5 (l, p) plants. Longitudinal sections from the centre of the meristem (i-l) and transversal sections 100 µm from the meristem apex (m-p) are shown. Cells in the rib meristem at 60 µm and 100 µm from the meristem apex are highlighted in colour. Scale bar: 20 µm

13.8 cells (25%) and 1850 µm^2 (80%) area, while for *iqd.22.23.24.25.27* the mean increases of 12 cells (24%) and 1700 µm^2 (87%) area. These increases are similar, although slightly lower than, the wild type, which increased by 20 (40%) cells, and 1990µm^2 (97%) area, and much lower than the *1aiqd-2* mutant, which had a mean increase of 48.5 cells (80%) and 4331 µm^2 (176%) area. As noted previously when comparing the wild type and *1aiqd-2* lines (Chapter 2, fig. 17), the distribution of cell sizes varied between plants and there were no consistent, observable difference between genotypes.

In summary, native *IQD26* and *proIQD26:IQD26-YFP* can fully complement the stem thickness and cell division phenotypes of the *1aiqd-2* mutant. The cell cycle-related expression of *IQD26,* and its localisation to the PPB during cell division, suggest that *IQD26* has a direct role in regulating division plane placement. This supports the hypothesis that the aberrant cell division orientation observed in the *1aiqd-2* mutant is a direct consequence of *IQD26* loss-of-function (and possibly other 1A *iqd* alleles operating redundantly) rather than a secondary consequence of changes in growth. However, since

IQD26 is expressed in all tissue layers of the meristem (**fig. 29**), these data cannot rule out the possibility that complementation of stem thickness derives from some function of *IQD26* in the epidermal layers.

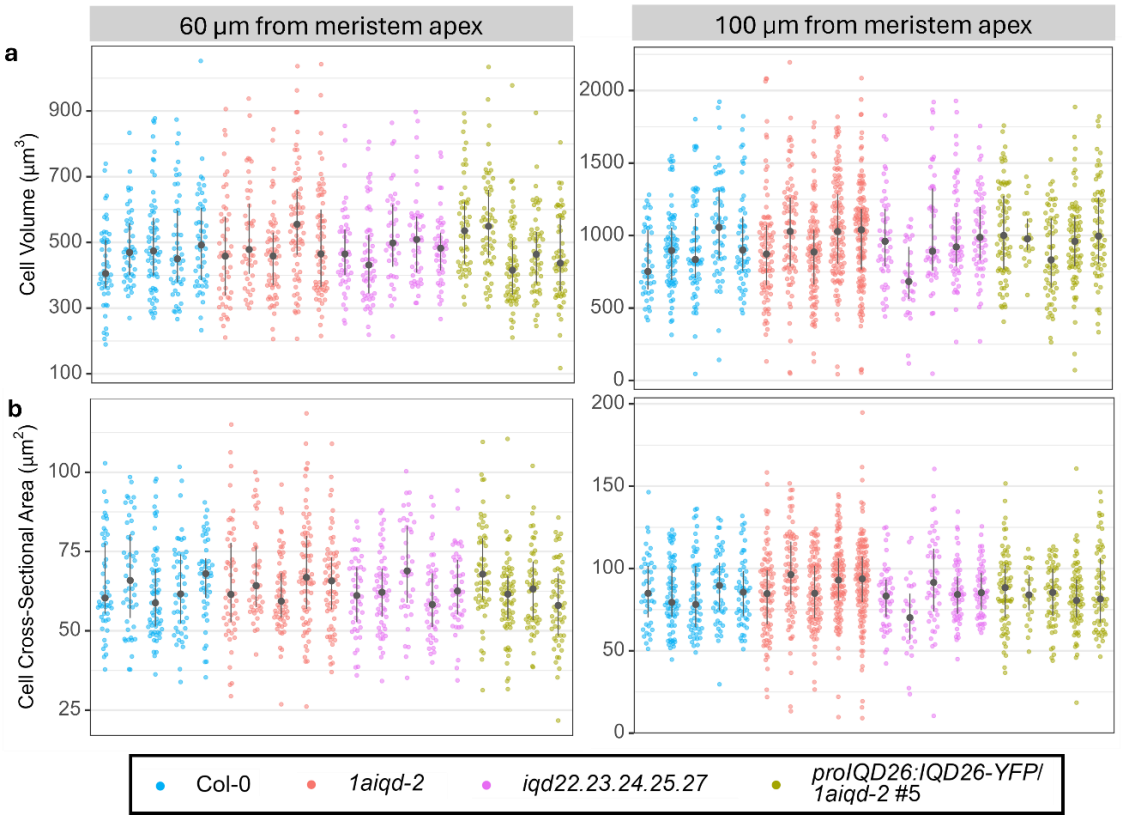

Figure 41: *proIQD26:IQD26-YFP* does not affect cell size. Quantification of rib meristem cell volume (a) and cell cross-sectional area (b) as measured in fixed PI-stained SAMs from wild type Col-0, *1aiqd-2*, *iqd22.23.24.25.27*, and *proIQD26:IQD26-YFP/1aiqd-2* plants. Cell cross-sectional area was measured as shown in Chapter 2, fig. 16. Each point represents the measurement for an individual cell and each set of points represents the cells of an individual meristem. Meristems were harvested from 5-week-old plants, at the stage shown in fig. 37a,b. Five meristems were analysed per genotype.

3.2.7 Complementation of the *1aiqd-2* phenotype by transgene expression in the stem interior

To test whether the complementation of the *1aiqd-2* stem phenotype can be achieved by replacing *IQD26* function in the internal tissues only, I took advantage of the expression pattern of *IQD27*. Expressing *IQD26-YFP* using the *IQD27* promoter yielded an expression pattern similar to *proIQD27:IQD27-YFP* (**fig. 30**), with *IQD26-YFP* expressed in the interior of the meristem (**fig. 42**). I tested whether *proIQD27:IQD26-YFP* could complement the *1aiqd-2* phenotype. Since *IQD27* is natively expressed in the stem interior, and appears to

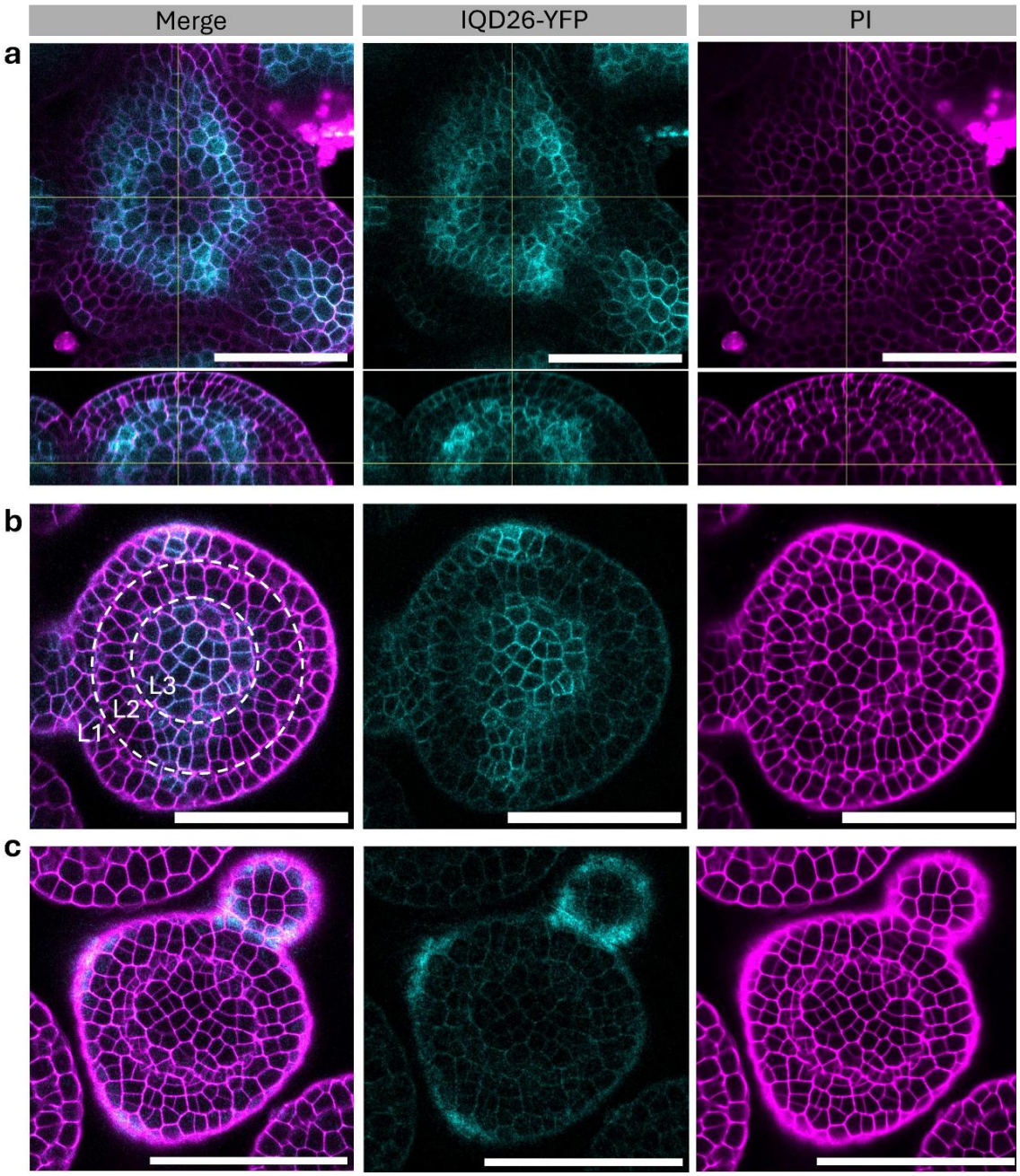

Figure 42: Expressing IQD26-YFP under the *IQD27* promoter restricts IQD26 -YFP expression to the inner inner tissues of the shoot apical meristem. (a, b) Localisation of IQD26-YFP in shoot apical meristem of a flowering *proIQD27:IQD26/1aiqd-2* plants. Single optical sections of IQD26-YFP (cyan, centre), PI-stained cell walls (magenta, right) and merged signal (left) are shown. Transverse sections (a,b) longitudinal sections (a) are shown. Cells inside the L1, L2 and L3 layers are indicated in (b). Images are representative of three independent transgenic lines. **(c)** Single optical sections of a PI-stained meristem from the *1aiqd-2* line, showing the level of background signal in the YFP (cyan) channel. PI (magenta) and YFP (cyan) channels were obtained with the same settings as the images in (a) and (b). Scale bar: 50 µm

have a similar localisation to *IQD26* (**fig. 30**), I tested whether it too could complement the phenotype.

Three independent lines each of *proIQD27:IQD27-YFP* and pro*IQD27:IQD26-YFP* had significantly narrower stems when compared *1aiqd-2* but were not significantly different from the wild type (**fig. 43b,c**). The distributions of new cell wall angles in the rib meristems of *proIQD27:IQD27-YFP/1aiqd-2* and pro*IQD27:IQD26-YFP/1aiqd-2* plants

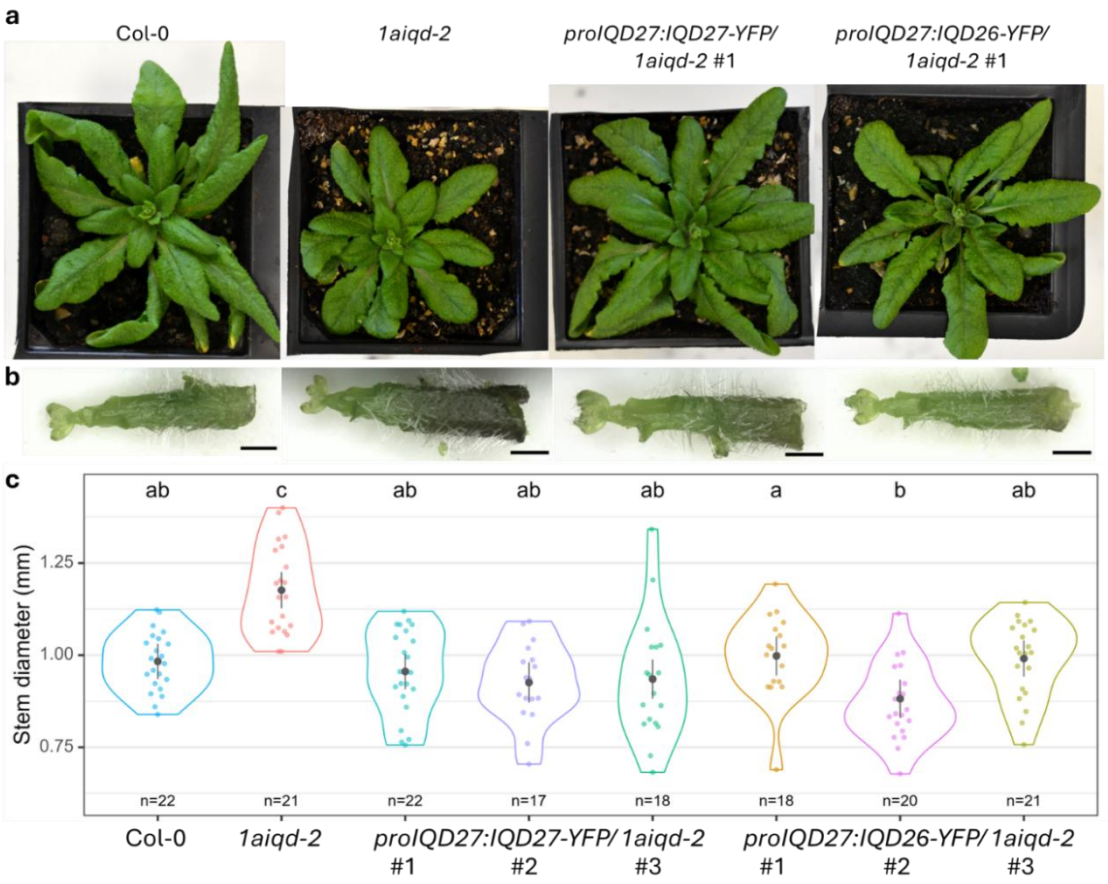

Figure 43: **Expressing *IQD26* or *IQD27* using the *IQD27* promoter fully complements the *1aiqd-2* stem phenotype. (a)** Photographs showing rosette leaves of approx. 5-week-old plants. Left to right: wild type Col-0, *1aiqd-2*, *proIQD27:IQD27-YFP/1aiqd-2, proIQD27:IQD26-YFP/1aiqd-2*. **(b)** Stereomicrographs showing ~5 mm tall stems, of the same genotypes as (a). **(c)** Stem diameters measured 3 mm from the stem apex. Statistical significance was determined by One-Way ANOVA. Post-hoc pairwise comparisons were computed using the Tukey Honestly Significant Difference (HSD) test, with a significance level of 0.05. Different letters indicate groups with significantly different means. Grey dots and whiskers indicate mean and 95% CI of the mean. Scale bar: 1mm.

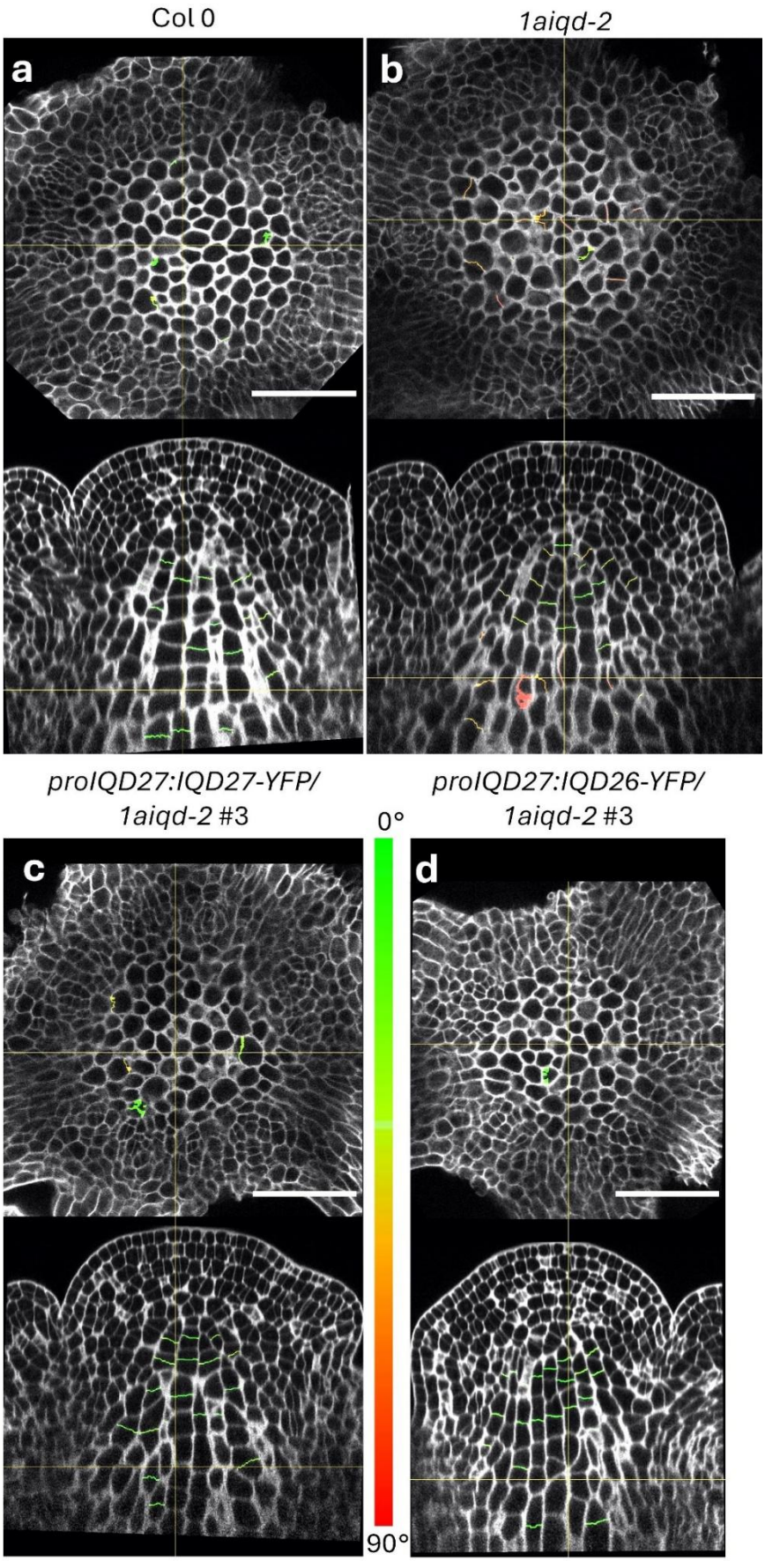
Col 0
1aiqd-2
a
b
proIQD27:IQD27-YFP/
1aiqd-2 #3
proIQD27:IQD26-YFP/
1aiqd-2 #3
0°
90°
c
d

Figure 44 (previous page): Expressing *IQD26* or *IQD27* using the *IQD27* promoter restores wild type cell division orientation in the rib meristem. (a-e) Single optical sections of fixed PI-stained SAMs from wild type Col-0 (a), *1aiqd-2* (b), *proIQD27:IQD27-YFP/1aiqd-2* (c) and *proIQD27:IQD26-YFP/1aiqd-2* (d) plants. Meristems were harvested from 5-week-old plants, at the stage shown in fig. 43. Transverse sections approx. 110 µm from the meristem apex (upper panels) and longitudinal sections through the centre of the meristem (lower panels) are shown. Recently formed cell walls in the rib meristem are coloured on a scale of green to red where green walls are more transversely oriented and red wall are more longitudinal (see Chapter 2, fig. 13). See fig. 45 for quantification. Scale bars: 50 µm

were similar to those of the wild type (**fig. 44, 45**). Wild type, *proIQD27:IQD27-YFP/1aiqd-* and pro*IQD27:IQD26-YFP/1aiqd-2* meristems had only 2 or fewer new walls with an angle of 60° of higher (most meristems analysed have none), whereas *1aiqd-2* meristems had several. The proportions of angles > 45° in *proIQD27:IQD27-YFP/1aiqd-2* and pro*IQD27:IQD26-YFP/1aiqd-2* plants were not significantly different to the wild type (**fig. 45c**). Within the rib meristem, the increase in area and cell number between 60 µm from the apex and 100 µm from the apex, was also similar between *proIQD27:IQD27-YFP/1aiqd-2* and pro*IQD27:IQD26-YFP/1aiqd-2* and the wild type (**fig. 46**). The rib meristems of *proIQD27:IQD27-YFP/1aiqd-2* had a mean increase of 19.2 cells (34%) and 2150 µm^2 (97%) area, while *proIQD27:IQD26-YFP/1aiqd-2* had mean increases of 19.2 cells (38%) and 1980 µm^2 (103%) area. These increases are similar, although slightly lower than, the wild type, which increased by 28 (47%) cells, and 2790 µm^2 (112%) area – and much lower than the *1aiqd-2* mutant, which had a mean increase of 59.2 cells (76%) and 5371 µm^2 (173%) area.

The distribution of cell cross-sectional areas were similar between wild type, *1aiqd-2* and *proIQD27:IQD27-YFP/1aiqd-2* (**fig. 47b-d**). The distribution of *proIQD27:IQD26-YFP/1aiqd-2* cell areas was shifted slightly smaller than the other genotypes at 100 µm from the meristem apex (**fig. 47c, d**). IQD27 is expressed more strongly than IQD26 in the rib meristem (**fig. 29,30**), and therefore *proIQD27:IQD26-YFP* likely causes stronger IQD26 expression in this region relative to normal physiological levels. Smaller cell areas could therefore be a phenotype of subtle IQD26 overexpression.

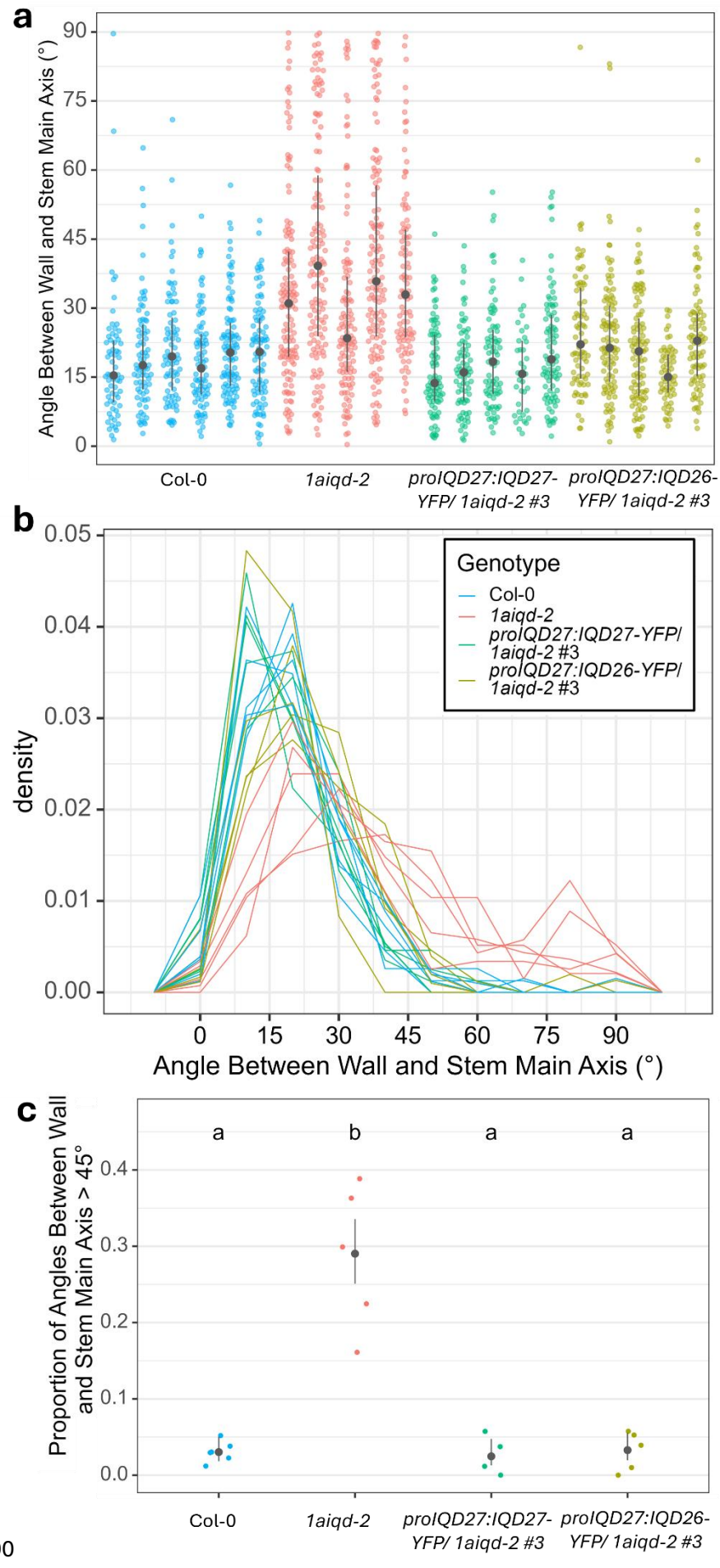
a
Angle Between Wall and Stem Main Axis (°)
90
75
60
45
30
15
0
Col-0
1aiqd-2
proIQD27:IQD27-YFP/ 1aiqd-2 #3
proIQD27:IQD26-YFP/ 1aiqd-2 #3
b
density
0.05
0.04
0.03
0.02
0.01
0.00
Genotype
Col-0
1aiqd-2
proIQD27:IQD27-YFP/ 1aiqd-2 #3
proIQD27:IQD26-YFP/ 1aiqd-2 #3
0
15
30
45
60
75
90
Angle Between Wall and Stem Main Axis (°)
c
Proportion of Angles Between Wall and Stem Main Axis > 45°
0.4
0.3
0.2
0.1
0.0
a
b
a
a
Col-0
1aiqd-2
proIQD27:IQD27-YFP/ 1aiqd-2 #3
proIQD27:IQD26-YFP/ 1aiqd-2 #3

Figure 45 (previous page): Expressing *IQD26* or *IQD27* using the *IQD27* promoter restores wild type cell division orientation in the rib meristem. Quantification of new cell wall orientation in the rib meristem as measured in fixed PI-stained SAMs from wild type Col-0, *1aiqd-2*, *proIQD27:IQD27-YFP/1aiqd-2* and *proIQD27:IQD26-YFP/1aiqd-2* plants. Meristems were harvested from 5-week-old plants, at the stage shown in fig. 43. Five or six meristems were analysed per genotype. **(a)** Angle between wall and main axis, where values closer to zero indicate more transversely oriented walls, (see Chapter 2, fig. 13). Black dots and whiskers show median and IQR. **(b)** Density plot of the same data shown in (a). Each line represents an individual meristem. (**c**) The proportion of wall angles > 45° in each meristem. Data were analysed using a Poisson model. Black dots and whiskers show back-transformed estimates for the rates and asymptotic upper and lower confidence levels (conceptually equivalent to mean and 95% CI). Different letters indicate genotypes that are statistically significantly different ($p<0.05$).

3.3 Discussion

Based on the data presented in this chapter, I propose that *IQD26* and *IQD27* directly regulate cell division orientation in the rib meristem. IQD26 localises to the PPB, CDZ and cell plate - mitotic structures that are required for robust orientation of the new cell wall – and expression of IQD26 (or IQD27) in the internal stem tissues recovers wild-type like cell division orientation and stem thickness. The major contribution of *IQD26* to stem growth is consistent with the statistically significant increase in stem thickness observed in single mutant *iqd26-3* plants (Mckechnie-Welsh 2021). The expression profile and subcellular localisation of IQD26 bear strong similarity to IQD8, which regulates cell division orientation in the root epidermis (Kumari et al. 2021). Moreover, the disruption of cell division orientation *1aiqd-2* is strikingly similar to the *iqd678* mutants, albeit in different tissues. It is, therefore, likely that IQD26 (and IQD27) play a similar role to IQD8 in the regulation of cell division orientation. Further work is required to determine if the specific molecular mechanism by which IQD8 and IQD26 regulate cell division orientation is also similar. This is a focus of the following chapter.

Although there are similarities between the cellular *iqd678* and *1aiqd-2* mutant phenotypes, the mutations do have contrasting effects on organ growth: *iqd678* does not conspicuously affect radial growth of the root meristem but the roots are slightly shorter (Kumari et al. 2021). However, this is consistent with its most severe cell division phenotype occurring in the outer cell layers (lateral root cap and epidermis), which

control longitudinal growth (Kumari et al. 2021; Fridman et al. 2021). In contrast, the radial growth of the root meristem is associated with increase in the number of inner tissue (stele and pericycle) cell files (Miyashima et al. 2019; Fridman et al. 2021), and neither cell division defects or IQD8 expression in these tissues were reported (Kumari et al. 2021).

proIQD24:GUS and *proIQD23:GUS* were not expressed in the SAM, suggesting that *IQD24* and *IQD23* contribute little to the regulation of stem development in the wild-type plants. It is not unusual for gene expression to change when paralogous genes are mutated, but

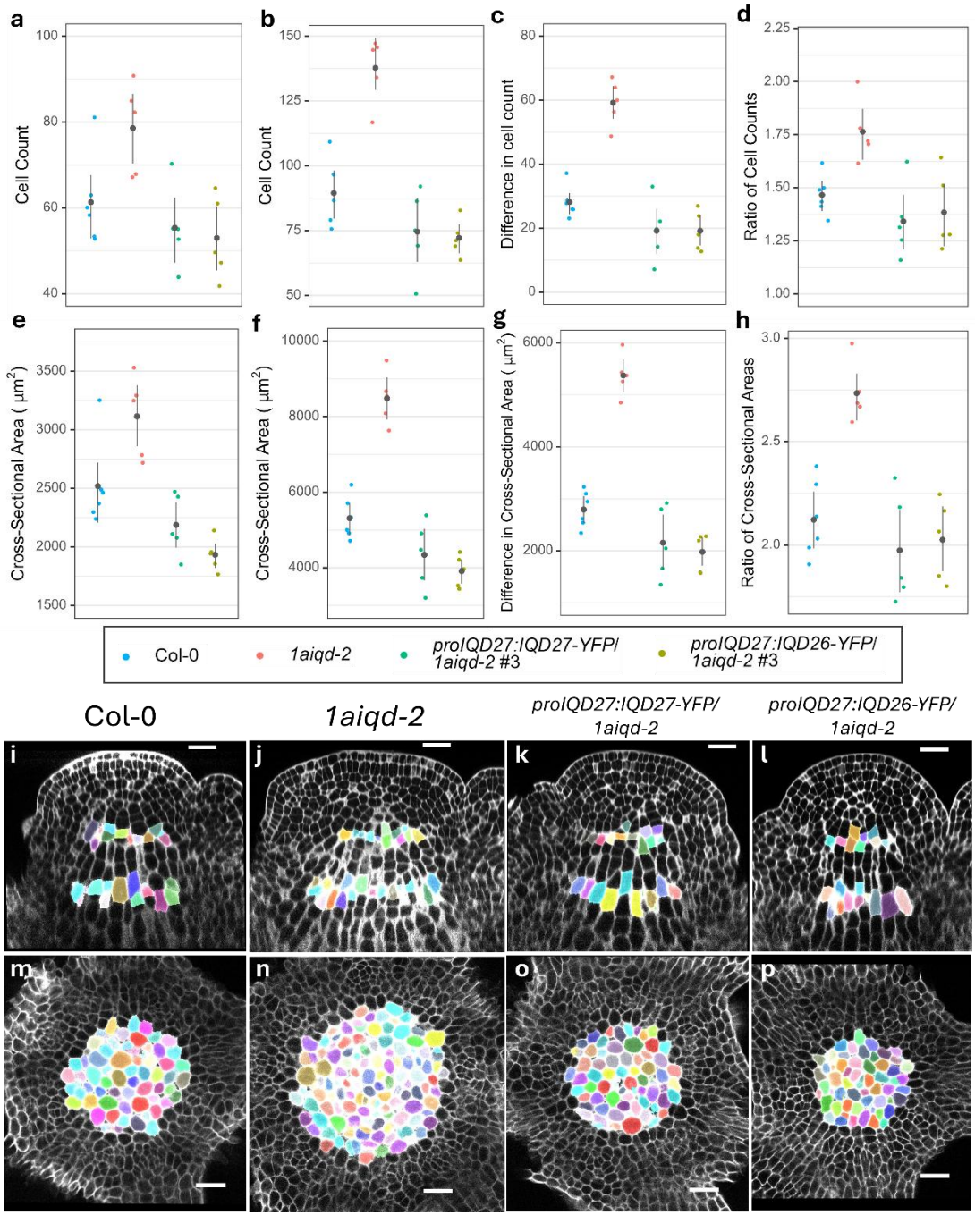

Figure 46 (previous page): Expressing *IQD26* or *IQD27* using the *IQD27* promoter restores wild type cell numbers in the rib meristem. Quantification of rib meristem cell number and cross-sectional area as measured in fixed PI-stained SAMs from wild type Col-0, *1aiqd-2*, *proIQD27:IQD27-YFP/1aiqd-2* and *proIQD27:IQD26-YFP/1aiqd-2* plants. Meristems were harvested from 5-week-old plants, at the stage shown in fig. 43. Five meristems were analysed per genotype. **(a, b)** The number of rib meristem cells in cross-sections 60 µm (a) and 100 µm (b) from the meristem apex. **(c,d)** Difference in cell number between the 100 µm and 60 µm cross-sections, expressed as an absolute difference (number of cells at 100 µm - number of cells at 60 µm) (c), and as a ratio (number of cells at 100 µm ÷ number of cells at 60 µm) (d). **(e, f)** Area occupied by the rib zone in cross-sections 60 µm (e) and 100 µm (f) from the meristem apex. **(g,h)** difference area between the 100 µm and 60 µm cross-sections, expressed as an absolute difference (area at 100 µm - area at 60 µm) (g), and as a ratio (area at 100 µm ÷ area at 60 µm) (h). **(i-p)** single optical sections of PI-stained SAMs from Col-0 (i, m), *1aiqd-2* (j, n), *proIQD27:IQD27-YFP/1aiqd-2* (k, o), and *proIQD27:IQD26-YFP/1aiqd-2* (l, p) plants. Longitudinal sections from the centre of the meristem (i-l) and transversal sections 100 µm from the meristem apex (m-p) are shown. Cells in the rib meristem at 60 µm and 100 µm from the meristem apex are highlighted in colour. Scale bar: 20 µm

even in the *1aiqd-2* background, *proIQD24:IQD24-YFP* and *proIQD23:IQD23-YFP* could not be detected in the SAM, suggesting that *iqd24* and *iqd23* contribute little to the *1aiqd-2* phenotype. This contrasts with prior work, which suggested that *iqd23* and *iqd24* make additive contributions to the stem thickness phenotype: *iqd24.25.26.27* had a larger increase in stem diameter than *iqd25.26.27,* and *1aiqd*-2 had a larger increase than both (Mckechnie-Welsh 2021). However, these three mutant lines were compared to the wild type control in three separate experiments, rather than being grown together, and there was significant difference in the wild-type stem thickness between experiments. To accurately assess the quantitative contribution of different mutations to the *1aiqd-2* stem phenotype, it would be helpful to compare different mutant combinations directly to each other, especially the six pentuple mutants, the six single mutants and *iqd26iqd27*. I was unable to experimentally determine whether *IQD22* is expressed in the SAM and in which cell layers, however publicly available expression data suggests it is expressed there. IQD22 has previously been shown to localise to interphase MT arrays (Matthes et al. 2022; Bürstenbinder, Möller, et al. 2017). Future work could establish whether IQD22 also localises to the PPB/CDZ and can complement the stem phenotype, like IQD26 and IQD27.

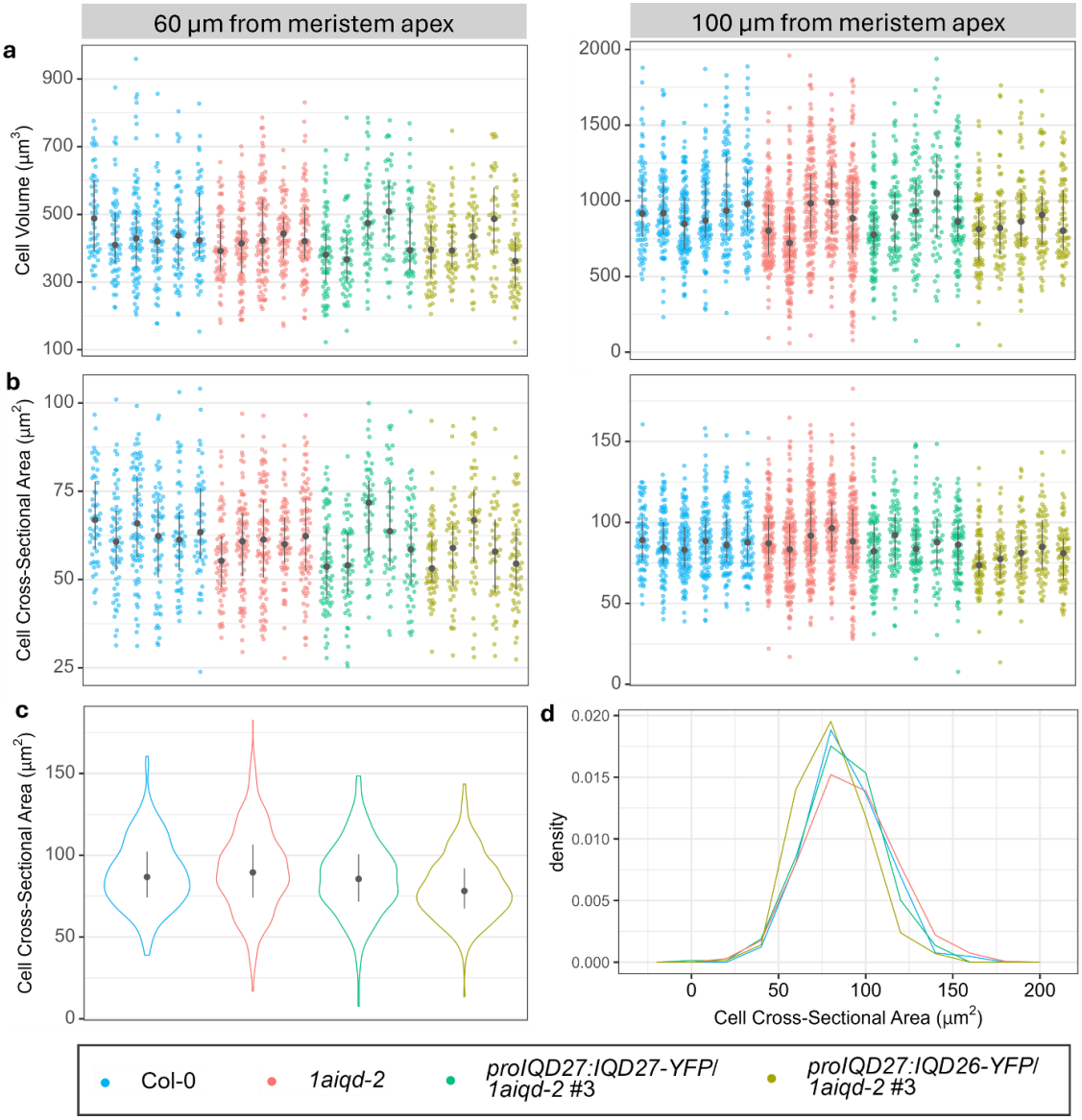

Figure 47: Expressing *IQD26* or *IQD27* using the *IQD27* promoter minimally affects cell size. Quantification of rib meristem cell volume (**a**) and cross-sectional area **(b)** as measured in fixed PI-stained SAMs from wild type Col-0, *1aiqd-2*, *proIQD27:IQD26-YFP/1aiqd-2*, and *proIQD27:IQD26-YFP/1aiqd-2* plants. Cell cross-sectional area was measured as described in chapter 2, fig. 16. Each point represents the measurement for an individual cell and each set of points represents the cells of an individual meristem. Meristems were harvested from 5-week-old plants, at the stage shown in fig. 43. 5-6 meristems were analysed per genotype. **(c, d)** Cell cross sectional area of cells within 100 µm of the meristem apex (i.e. the same data as shown in the right-hand panel of b). Here the data from separate meristems of the same genotype are pooled. The data are displayed as a violin plot (c) and frequency polygon (d).

Expression of IQD26 and IQD27 overlaps in the inner stem tissues and restricting expression of either gene to the inner stem tissues complements both the cell division and stem thickness phenotypes of the *1aiqd-2* mutant. These observations support the hypothesis that the cell division defects of the *1aiqd-2* mutant underpin the mutant's increased stem thickness. However, we cannot rule out that the IQDs secondarily function as cell cycle inhibitors, and it is this functionality that regulates rib meristem cell number and overall stem thickness. Notably, *IQD26* is co-expressed with cell-cycle related genes and loss of cell cycle inhibitors has previously been shown to increase rib meristem cell number (Serrano-Mislata et al. 2017). Furthermore, several core cell cycle proteins localise to the PPB, including Cyclin A1, KIP-RELATED PROTEIN 4, and CYCLIN-DEPENDENT KINASE 1 (Boruc et al. 2010). It has not been determined whether there are overall changes in cell proliferation in the *1aiqd-2* mutant and this would need to be established before the stem thickness phenotype can be confidently attributed to a change in division orientation alone.

4 FURTHER EXPLORATION OF 1A IQD FUNCTION

4.1 INTRODUCTION

IQD proteins are hypothesised to operate as molecular scaffolds that recruit proteins to specific subcellular locations and facilitate localised protein-protein interactions (Bürstenbinder, Mitra, et al. 2017; Abel et al. 2013). IQDs emerged in the algal ancestors of land plants as novel CaM- and MT-binding proteins and may even have facilitated the transition from ancestral cleavage-based cell division to the PPB/phragmoplast mechanism that operates in all extant land plants (Dahiya et al. 2023). In the previous chapter I showed that IQD26 localises to the PPB, CDZ and cell plate. This chapter explores the possible mechanisms through which IQD26 regulates cell division at these sites.

4.1.1 The molecular regulation of plant cell division orientation, from PPB to phragmoplast

PPB formation and the downstream steps of cell division require the temporal and spatial coordination of many different protein factors (Bouchez et al. 2024). In late G2, the cell's interphasic cytoskeletal arrays reorganise to form the PPB. Early-stage PPBs occupy a broad cortical domain and contain short, single actin microfilaments. These microfilaments bridge adjacent MTs and facilitate MT bundling, narrowing the PPB so that by later prophase it precisely marks the future cell division site (Takeuchi et al. 2016). Although the precise mechanisms that underpins PPB formation remain unclear, several key regulators and activities have been identified (Bouchez et al. 2024). One of the best characterised is a complex of TONNEAU1 (TON1), TON1 RECRUITING MOTIF (TRM), and protein phosphatase 2A (PP2A) (abbreviated to TTP), which regulates the spatial organisation of cMTs throughout the cell cycle and is required for PPB formation and division plane positioning (Spinner et al. 2013). The TRM component supports the assembly of the complex, recruits it to MTs, and contributes to the functional specialisation of different TTP isoforms (Drevensek et al. 2012). The TRMs are a large family and different family members support different aspects of MT organisation, with TRM6-8 being specifically required for PPB formation (Schaefer et al. 2017). Precisely how the TTP complex regulates MT organisation remains poorly characterised, since few PP2A targets have been identified. PPB formation likely relies on localised MT bundling, severing, nucleation and actin-MT cross-linking (Bouchez et al. 2024). Several MAPs that

regulate these activities occupy the PPB, including the MT-severing enzyme KTN1, and MAP65, which promotes MT stability via bundling (Smertenko et al. 2004; Panteris et al. 2011; Li et al. 2015). The TTP complex has also been shown to spatially regulate MT nucleation (Kirik et al. 2012).

From approximately late G2 to cell plate completion, the CDZ marks the region where the cell plate will ultimately fuse with the parent's cell walls. The CDZ is distinguished by a specific and evolving set of proteins and the distinct molecular identity of the CDZ may be maintained, in part, by heightened clathrin-mediated endocytic activity in the region (Karahara et al. 2009). The PPB and associated proteins occupy the CDZ from late G2, but the CDZ maintains a distinct identity and protein composition even after the PPB disassembles at metaphase (Smertenko et al. 2017). CDZ formation does not absolutely require the PPB, but the recruitment of key CDZ proteins is partially impaired in cells that lack PPBs (Schaefer et al. 2017; Kumari et al. 2021; Livanos et al. 2025). Several CDZ-resident proteins have been identified, including POK 1 and 2, TANGLED (TAN), RAN GTPase ACTIVATING PROTEIN 1 (RanGAP1), PHGAPs and AUXIN INDUCED IN ROOTS 9 (AIR9) (Walker et al. 2007; Xu et al. 2008; Buschmann et al. 2006; Stöckle et al. 2016). These proteins mutually regulate their recruitment and retention at the CDZ via a complex network of protein-protein interactions and this activity is required to accurately position the new cell wall (Dahiya and Bürstenbinder 2023). Cell cycle regulators also localise to the PPB and CDZ (Boruc et al. 2010), but it is unclear how these mediate the observed effects of cell cycle progression on cell division orientation (Bouchez et al. 2024).

After the PPB breaks down, subsequent mitotic structures orient relative to the future division plane, as marked by the CDZ. Metaphase chromosomes typically line up along the future division plane and at anaphase, the spindle MTs pull the sister chromatids to opposite poles of the cell, in a direction approximately orthogonal to the division plane (Smertenko et al. 2017). Crucially, the phragmoplast forms along the future division plane, scaffolding the new cell plate as it expands centrifugally towards the cell cortex and ultimately fuses with the CDZ. Several CDZ-localised proteins also associate with the phragmoplast and contribute to accurate cell wall placement by regulating phragmoplast orientation, positioning and stability (Livanos et al. 2025; Lipka et al. 2014; Kumari et al. 2021; Mir et al. 2018)

4.1.2 IQDs and cell division

The only other *IQD* mutant (aside from *1aiqd-2*) that has been shown to disrupt division-plane orientation is *iqd678* and this mutant has provided significant insight into the role of

IQDs in cell division. The embryos of triple mutant *iqd678* plants have defects in division plane orientation (Vaddepalli et al. 2021) and *iqd678* roots plants have an increased frequency of oblique cell walls, especially in the root cap and epidermis (a subtler phenotype is observed in the respective single mutants, with the strongest single mutant phenotype observed in *iqd8*) (Kumari et al. 2021). The PPB is tilted, sparse or absent in a high percentage of *iqd678* root epidermal cells (all are very rare occurrences in the wild type) and the phragmoplast is also frequently misoriented. IQD6-GFP and IQD8-GFP localise to the PPB, a polarized cortical domain that encompasses the CDZ (but also extends beyond it), and the cell plate, much like IQD26-YFP. IQD8 interacts with POK1, POK2, PHGAP1 and PHGAP2 through conserved motifs in its C terminus. In *iqd678* mutants, recruitment of POK1 to the site of future cell division is delayed, while PHGAP2 recruitment is reduced and fails in about 25% of cells (Kumari et al. 2021). The authors of this study proposed the following model: IQD8 accumulates at the site of the PPB during prophase; when the PPB disassembles, IQD8 spreads out to occupy a polarized cortical domain that encompasses the CDZ and POKs are recruited to the CDZ; IQD8 and POKs then recruit the PHGAPs; this ensures correct phragmoplast orientation, and subsequently correct cell wall placement. In summary the authors propose “IQD8 and related proteins act as cellular scaffolds during PPB formation and CDZ set up that regulate microtubule organization and macromolecular complex assembly” (Kumari et al. 2021). Research into IQDs from algae and bryophytes suggests that the ancestor of all IQDs could interact with MTs and POK1, while the IQD-PHGAP interaction arose early in land plant evolution (Dahiya et al. 2023). Furthermore, expression of an IQD from moss partially rescues the cell division plane defects in *atiqd678* root epidermis, implying that the role of IQDs in division plane coordination is an ancient one (Dahiya et al. 2023).

While division plane orientation, POK-binding and PHGAP-binding may be ancient functions, they are not necessarily conserved across the IQD family. Indeed, the 33 members of the *Arabidopsis* IQD family differ significantly in the presence and arrangement of different conserved sequence motifs that likely confer protein-binding (Abel et al. 2005). Less than half of the AtIQDs interact with POK1 in yeast, and only 5 or 6 IQDs interact with each of POK2, PHGAP1 and PHGAP2 (Dahiya et al. 2023). Furthermore, one might expect the 1A IQDs to display some significant functional divergence from the ancestral IQD state, since phylogenetic analyses place *IQD22-27* in a separate subfamily from *IQD6-8* (Abel et al. 2005; Dahiya et al. 2023).

Other interaction partners of IQDs have been identified that could plausibly link IQDs with cell division orientation. KTN1 directly interacts with IQD21 to regulate cMT organisation (Feng et al. 2023). *ktn1* mutants have defects in cell division orientation (of a similar degree to *iqd678*) and their PPBs, spindles and phragmoplasts are frequently misoriented and/or misshapen (Panteris et al. 2011). IQD1, IQD2 and IQD9 directly interact with KLCR1. KLCR1 supports cMT-directed cellulose deposition and interacts with the kinesin family of microtubular motor proteins, to which POK1 and POK2 belong (Bürstenbinder et al. 2013; Zang et al. 2021; Yang et al. 2021; Ganguly et al. 2020). All IQDs interact with CaM and CML proteins, which bind free Ca^{2+} and thereby decode cellular Ca^{2+} signals. There is copious evidence that IQDs bind directly to CaMs and CMLs, via their IQ67 domain, and they do so in a selective manner (i.e. a single IQD might bind with some CaMs/ CMLs but not others) (Dahiya et al. 2023; Bürstenbinder, Möller, et al. 2017; Zhao et al. 2025; Levy et al. 2005; Bürstenbinder et al. 2013; Abel et al. 2005; Kumari et al. 2021; Wendrich et al. 2018). Some functions of IQDs are Ca^{2+}/CaM-dependent (Zhao et al. 2025), but for most IQD functions that have been characterised thus far, the link to Ca^{2+} signalling remains elusive. Even so, the conservation of the IQ67 domain and its CaM-binding functionality across the IQD family, imply that it must play a significant role. Identifying additional interactors of IQDs will be key to understanding how IQDs function in such a wide range of cell signalling and developmental processes.

4.1.3 Chapter aims

In this chapter I further explore the role of IQD26-YFP in the regulation of cell division orientation. I investigate how IQD26-YFP localisation is affected by perturbing PPB formation, test candidate protein interactions and examine the developmental effects of IQD26 overexpression. In addition, I explore the effects of an independent cell division orientation mutant on stem development.

4.2 Results

4.2.1 Investigating the effects of *1aiqd-2* on the PPB

To determine whether the *1aiqd-2* mutations affect PPB formation I tried to introduce a MT reporter into the *1aiqd-2* background. I first tried crossing the RFP-TUA5 marker into the *1aiqd-2* background, however after repeated generations of back-crossing, the marker was silenced. I then tried to introduce an MT marker via transformation. I cloned a translational fusion of the mCherry fluorescent protein with the MAP4 MT-binding domain

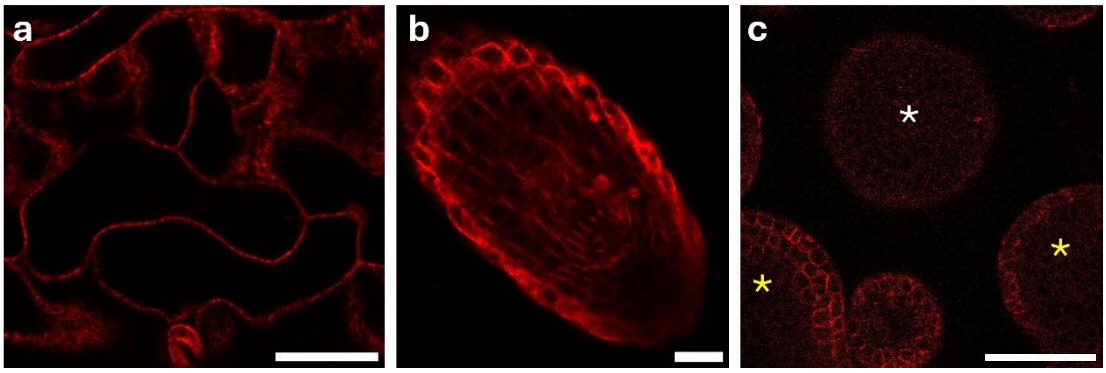

Figure 48: Expression of mCherry-MBD in different tissues. Single optical sections showing proUBQ10:mCherry-MBD in *1aiqd-2* cotyledon pavement cells **(a)**, root meristem **(b)** and SAM **(c)**. White asterisk marks the shoot apical meristem; yellow asterisks mark floral buds. Scale bars: (a,c) 50 µm; (b) 20 µm.

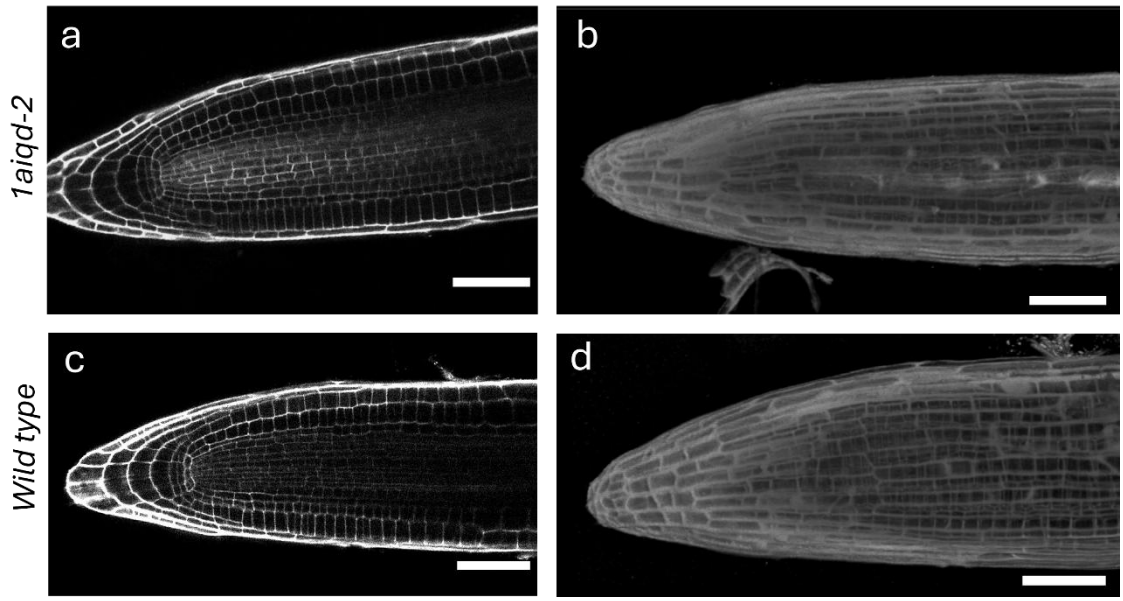

Figure 49: The roots of *1aiqd-2* plants do not have defects in cell division orientation. PI-stained roots from 7-day old *1aiqd-2* **(a,b)** and wild type col-0 **(c,d)** seedlings. The panels show single optical sections (a,c) and z-stacks displayed in the Fiji 3DViewer plugin (b,d). Images shown are representative of 7 seedlings imaged per genotype. Scale bar: 50 µm

(Marc et al. 1998) and transformed it into col-0 and *1aiqd-2*. This expressed well in the root meristem and cotyledons of seedlings but was mostly silenced in the SAM (**fig. 48**). Many transformants displayed developmental defects and died before flowering, probably because high expression of the MT marker affected normal MT organisation and, subsequently, growth. Therefore, the fact that I observed silencing in the SAM is probably

because only the low-expressing or silenced lines were able to grow normally enough to produce SAMs.

Since the marker expressed well in the roots of seedlings, I explored whether I could use the root meristem to investigate the effects of *1aiqd-2* on the PPB. I stained roots with PI and inspected cell wall orientation. Even though *IQD26* is strongly expressed in the root meristem (Chapter 3, fig. 24, 34), there were no conspicuous cell division orientation defects in any of the root meristem cell layers (**fig. 49**). This is likely due to genetic redundancy: *IQD26* is the only 1A *IQD* that is substantially expressed in the root meristem (Chapter 3, figs. 23-28) and so it may operate redundantly with other *IQDs* outside of the 1A subfamily. Indeed, genetic redundancy is common within the *IQD* family (Kumari et al. 2021). Since the root cells divided normally in the *1aiqd-2* mutant, I could not use roots to test how loss of 1A IQD function might affect PPB formation.

4.2.2 IQD26-YFP localisation in *trm678*

I previously showed that in wild type roots, IQD26-YFP accumulates broadly at opposite cell walls, narrows to occupy the CDZ (in parallel with MTs narrowing to form the PPB), remains at the CDZ when the PPB breaks down and then, once the phragmoplast has formed, localises to the cell plate (Chapter 3, fig. 35). Since I was unable to visualise the PPB during aberrant cell divisions in the *1aiqd-2* mutant, I decided to explore how loss of the PPB impacts IQD26-YFP localisation. The *trm678* mutant has significant defects in PPB formation: over 75% of cells at the G2/M stage lack PPBs, and the remaining cells have abnormal PPBs with only sparse MTs at the cell cortex (Schaefer et al. 2017). However, unlike other mutants with defective PPBs, *trm678* has normal interphase and non-cortical MT arrays (Schaefer et al. 2017). The mutant therefore provides a useful tool to explore whether IQD26 operates upstream of the PPB to guide its formation/ positioning or is later recruited to the already-formed PPB, where it may play a role recruiting or retaining proteins at the CDZ. If the former case is true, IQD26 localisation could be largely independent of PPB formation, whereas the latter predicts that disruption of the PPB would also disrupt IQD26 localisation.

I transformed *proIQD26:IQD26-YFP* and *mCherry-MBD* into the *trm678* mutant. To generate a wild-type line with equivalent levels of IQD26-YFP and mCherry-MBD expression, I crossed *proIQD26:IQD26-YFP mCherry-MBD trm678* to wild-type Col-0. I used the progeny of the cross (which had a heterozygous *trm678(+/-)* background) as the wild type control since it has normal cell division orientation and PPB formation (**fig. 50b,d**).

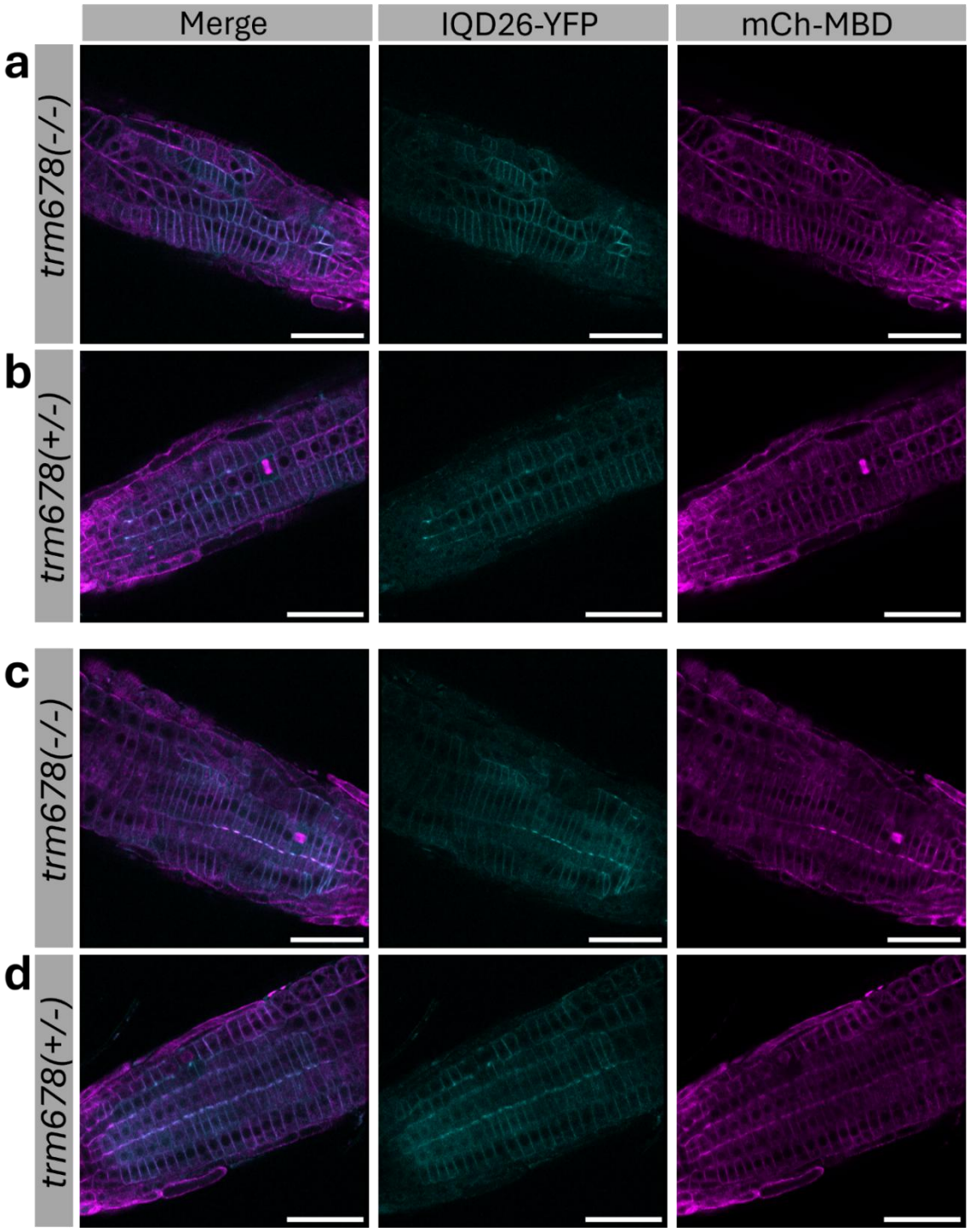

Figure 50: Interphase localisation of IQD26-YFP is similar in the *trm678* mutant. Localisation of IQD26-YFP and mCherry-MBD in the root tips of 6-day-old *trm678* (a,c) and wild-type-like *trm678*(+/-) (b,d) seedlings. Single optical sections of IQD26-YFP (cyan, centre), mCherry-MBD (magenta, right) and merged signal (left) are shown. (a,c) and (b,d) show different optical sections of the same root. **(a,b)** Root epidermis, **(c,d)** cortical and epidermal cell files. Scale bar: 50 µm

At a glance, the distribution of IQD26-YFP in the root meristem was similar in both the *trm678* and wild type backgrounds (**fig. 50**). In the epidermis, IQD26-YFP localised fairly uniformly to the plasma membrane (**fig. 50a**), while in the root cortex it accumulated more on the longitudinal cell walls, overlapping with the transversal cMT arrays (**fig. 50c**). IQD26-YFP also consistently localised to the cell plate in phragmoplast stage *trm678* cells (**fig. 51a-c**). In contrast, IQD26-YFP localisation to the CDZ was often disrupted. In a subset of mitotic cells, IQD26-YFP localised fairly precisely to the CDZ (**fig. 51a**). This pattern of IQD26-YFP accumulation was always accompanied by a sparse accumulation of MTs near the cortical division site, which might be a sparse PPB or the interphasic cMT arrays (**fig. 51a**). Other cells had broad, loosely-defined regions of IQD26-YFP immediately prior to metaphase or lacked any conspicuous IQD26-YFP accumulation at the future division site (**fig. 51b,c**). In these cells, IQD26-YFP also localised with broad domains of MT accumulation at the plasma membrane. In *trm678*, the localisation of the CDZ protein POK2 depends on the organisation of the prophase MT arrays (Livanos et al. 2025). IQD26 might have a similar dependence: in cells with highly anisotropic, transversal MT arrays, IQD26 is recruited to the CDZ fairly efficiently, but in cells where the cMT array organisation is more disorganised or isotropic, IQD26 is recruited to wherever the arrays are dense. Whatever the precise underlying mechanism, these data demonstrate that the efficient and robust localisation of IQD26 to the CDZ depends on the organisation of MTs into the PPB. This implies that IQD26 does not position that PPB but rather functions downstream of PPB formation. This is consistent with static imaging of IQD26-YFP and RFP-TUA5 in the shoot apical meristem, where IQD26-YFP signal at the CDZ was weak or absent in cells at early stages of PPB formation (Chapter 3, fig. 32)

4.2.3 The protein structure of 1A IQDs

The Arabidopsis IQDs are characterised by the presence of short, conserved amino acid motifs, interspersed by regions of intrinsic disorder (Abel et al. 2005). The occurrence and spacing of these motifs vary considerably between family members, and likely underpin their different protein-binding properties and subcellular localisation (Abel et al. 2005; 2013; Bürstenbinder, Möller, et al. 2017). Motif analysis of 1A IQDs reveals four amino acid sequence motifs that are conserved across all six proteins, and three that are present in only a subset (**fig. 52**). The two most statistically significant motifs correspond to previously characterised domains: the IQ67 domain, which binds CaMs, and DUF4005, which confers MT-binding (Abel et al. 2005; Levy et al. 2005; Yan Li et al. 2021; Bürstenbinder et al. 2013). The third most statistically significant motif overlaps with a highly-conserved alanine-rich domain, which has no known function (**fig. 52, 53**).

IQD22, IQD25, IQD26 and IQD27 share a short motif (motif 4) at or near their N-termini (**fig. 52**). Although this motif was not identified in IQD23 or IQD24, multiple sequence alignment shows that these proteins do share a portion of the motif (**fig. 53a**). Motif 4 might mediate the interaction of 1A IQDs with the PM. In IQD21, a 30-aa domain at the protein's N-terminus is necessary and sufficient for localisation to the PM and there is

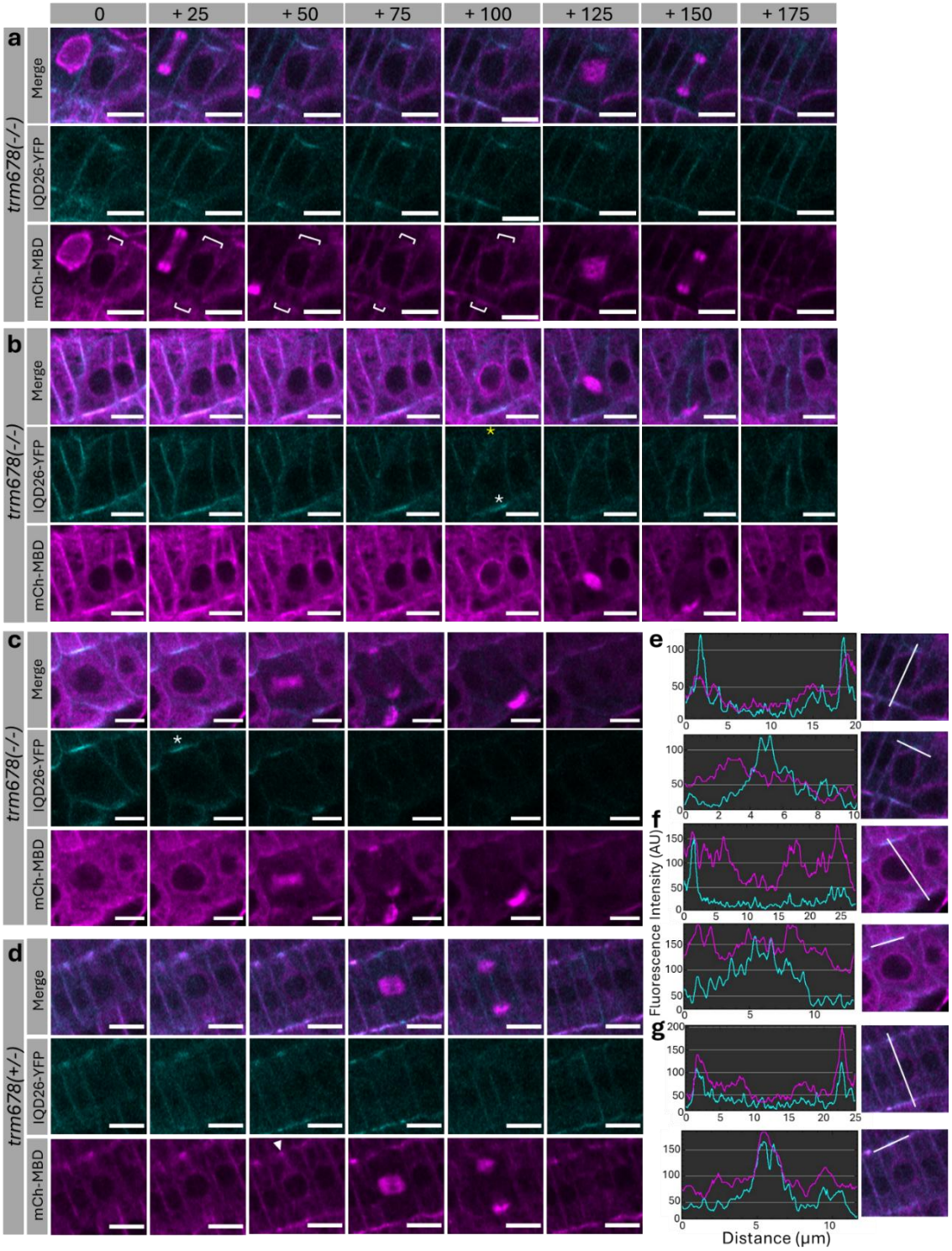

Figure 51 (previous page): Robust localisation of IQD26 to the CDZ requires the PPB. **(a-d)** Subcellular localisation of IQD26-YFP relative to mCherry-MBD during root cell division in *trm678* (a-c) and the heterozygous complemented background (d). Single optical sections of IQD26-YFP (cyan, middle panels), mCherry-MBD (magenta, lower panels) and merged signal (upper panels) are shown. Time elapsed in minutes since the initial image acquisition is shown above the corresponding panels. **(e-g)** Fluorescence intensity profiles of mCherry-MBD (magenta) and IQD26-YFP (cyan) analysed along the white lines. Cells shown in e,f, and g are the same as those shown in a, c and d, respectively, at the PPB stage. White brackets indicate sparse accumulations of microtubules near the cortical division site, white asterisks indicate loosely defined regions of IQD26-YFP accumulation, yellow asterisk indicates the absence of IQD26-YFP at a future division site, white arrowhead marks a typical PPB. Scale bar: 10 µm

some sequence similarity between this IQD21 domain and motif 4: it contains conserved MG and WF sequence elements, and 1-3 lysine residues (**fig. 52, 53**) (Feng et al. 2023). Therefore, this motif might underpin the observed PM-localisation of several 1A IQDs (Chapter 2, figs. 29-31) (Bürstenbinder, Möller, et al. 2017). It might also contribute to the recruitment or retention of IQD26 at the CDZ, since the recruitment and retention of cell division regulator POK2 at the CDZ relies on both direct MT-binding and interaction with PM phospholipids (Livanos et al. 2025). The remaining motifs sit C-terminally of the IQ67 domain and have lower levels of sequence conservation than the other identified motifs. Motifs 6 and 7 are only found in paralogous sister gene pairs (Levy et al. 2005): motif 6 is present in IQD26 and IQD27; motif 7 is present in IQD23 and IQD24.

Few of the sequence motifs identified in 1A IQDs were also identified in IQD8. This is surprising, since IQD8 and IQD26 have strikingly similar subcellular localisation and gene expression, and the *iqd678* and *1aiqd-2* mutants have similar phenotypes (Kumari et al. 2021). It suggests that, while IQD8 and IQD26 may operate as part of a similar pathway, it is likely that they have different interaction partners. Indeed, it has previously been shown that IQD8 interacts with POKs and PHGAPs, whereas IQD26 does not interact with either (although this has only been tested in yeast) (Dahiya et al. 2023).

To explore how the IQD26 protein motifs correspond to structural elements, I inspected its predicted protein structure. The structure was generated by AlphaFold2, an artificial intelligence (AI) program that performs protein structure predictions (Jumper et al. 2021; Fleming et al. 2025). The predicted protein structure of IQD26 comprises alpha helices joined by long regions of intrinsic disorder (**fig. 53**), which is very similar to structural

predictions for other IQDs and the inferred IQD ancestral state (Dahiya et al. 2023; Dahiya and Bürstenbinder 2023). The predicted structure of IQD26 contains two long alpha helices, which correspond to the regions of highest sequence conservation within the 1A IQD subfamily (**fig. 53a,b**). The more N-terminal helix overlaps with the alanine-rich motif that is shared by all 1A IQDs but absent from IQD8. The other encompasses the IQ67 domain (**fig. 52,53**). Additionally, a short region containing the putative MT-binding domain is predicted to form a string of short helices, although this structure

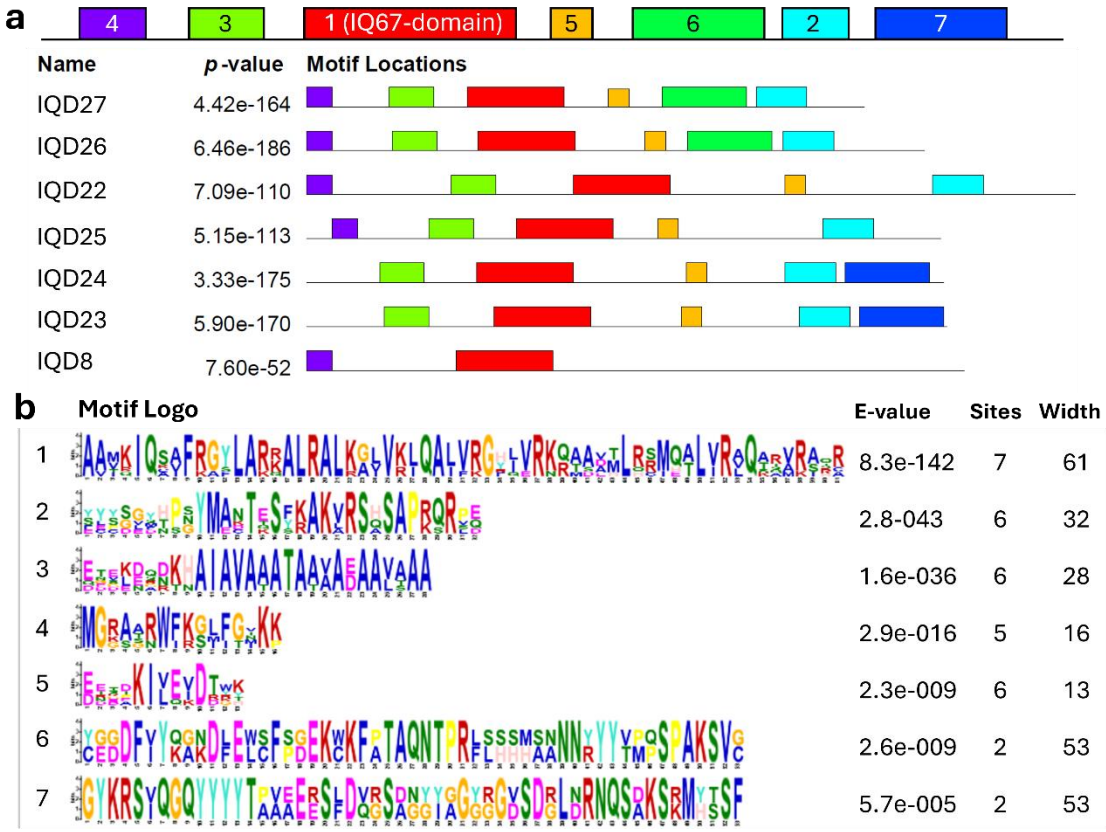

Figure 52: The motif patterns of 1A IQDs differ from IQD8. (a) Organisation of conserved amino acid sequence motifs in the 1A IQDs, compared with IQD8. Coloured boxes indicate the presence and position of different motifs. Combined match *p*-values for each motif arrangement are shown. (b) Motif logos, corresponding to the motifs shown in (a). For each motif, the E-value (statistical significance), width (in amino acids) and number of sites used for its to construction are shown. Motifs were predicted using Multiple Em for Motif Elicitation (MEME), using the amino acid sequences of IQD22-26 and IQD8 as input. This means that motifs that are present in IQD8 but absent from the 1A IQDs (e.g. as identified by Dahiya et al. 2023, Abel et al. 2005) were not identified and are therefore not shown here. Motif identification and generation of the motif diagram and logos were carried out using https://memesuite.org/meme/tools/meme

has a low model confidence (predicted local distance difference test (pLDDT) score <70) (**fig. 53b,c**). A similar structure is predicted for the other 1A IQDs: mostly disordered, with two alpha helices corresponding to the IQ67 domain and alanine-rich domain, although for IQD24 these domains are predicted to form a single long helix (**fig. 54**).

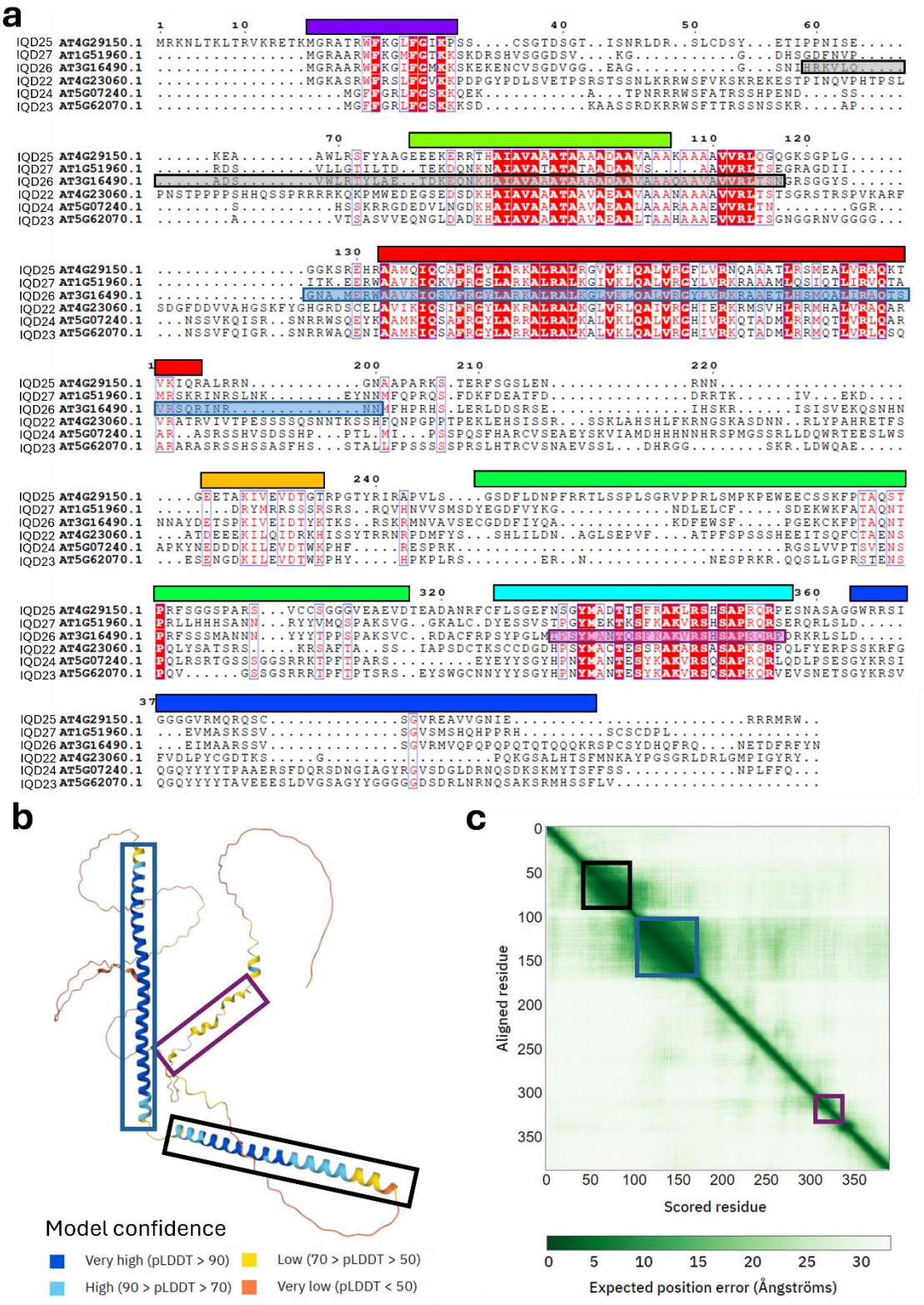

Figure 53 (previous page): IQD26 is predicted to have two alpha helices, interspersed with large regions of intrinsic disorder. **(a)** Multiple protein sequence alignment of the 1A IQD subfamily. The position of meme motifs identified in figure 52 are indicated by coloured boxes above the corresponding sequences. Coloured, shaded boxes overlaying the IQD26 amino acid sequence indicate the position of specific domains within the protein structure that are indicated in (b) and (c). **(b)** AlphaFold2 predicted structure of IQD26. Colour scale indicates predicted local distance difference test score (pLDDT), indicating confidence in the local structure. **(c)** Predicted aligned error (PAE) plot for the predicted structure shown in (a). This measures confidence in the relative position of two residues within the predicted structure. (b) and (c) were accessed from the AlphaFold Protein Structure Database (https://alphafold.ebi.ac.uk/) and shown here under a CC-BY-4.0 license.

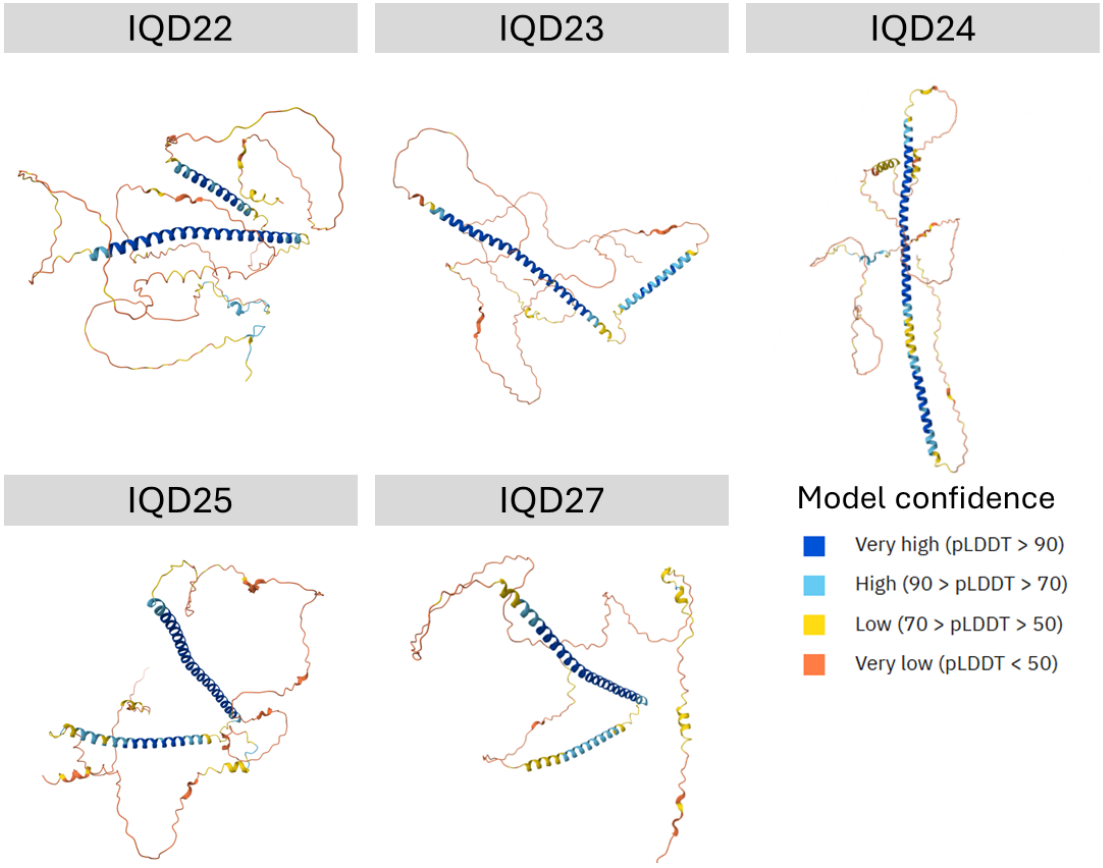

Figure 54: All 1A IQD proteins are predicted to share a similar, largely disordered, structure. AlphaFold2-predicted structures of IQD22, IQD23, IQD24, IQD25 and IQD27. Colour scale indicates the pLDDT score, which measures confidence in the local structure. Structures were accessed from the AlphaFold Protein Structure Database (https://alphafold.ebi.ac.uk/) and shown here under a CC-BY-4.0 license .

4.2.4 AI-facilitated prediction of IQD26 protein interaction partners

Many proteins localise to the PPB and cell plate, making the list of possible IQD26 interactors rather long. To screen for likely candidates, I used AlphaFold2 Multimer to predict the structure of IQD26-protein complexes and assess the likelihood of each complex forming in a biological system. To test the suitability of this approach, I initially modelled known interactions and non-interactions. Because the only known interactors of IQD26 are CaM2 and CaM7 (Dahiya et al. 2023), I included the interactions of IQD8 with CaMs, POKs and PHGAPs as additional positive controls. For negative controls, I included the interactions of IQD26 with POKs and PHGAPs, IQD7 (there is no evidence that IQDs interact with each other), and two randomly selected small proteins (MYB3R-3 and AT4G32100). Because previous studies did not report which splice variants were used to test protein-protein interactions, I queried all CAM2/7, POK1/2 and PHGAP1/2 variants with available protein sequences.

AlphaFold2 Multimer generates two metrics to assess the accuracy of the predicted structure. The predicted template modelling (pTM) score measures the accuracy of the structure of the whole complex (Jumper et al. 2021). A commonly used pTM threshold is 0.5, where a pTM<0.5 indicates that the structure is likely to be wrong (Xu and Zhang 2010). However, because pTM assesses the structure of the whole complex, it is affected by factors like the relative sizes of the candidate interacting partners (i.e. the pTM of the larger partner can dominate the pTM of the complex) and large regions of intrinsic disorder (which lower the overall pTM). The second metric is the interface predicted template modelling (ipTM) score. This measures the accuracy of the protein-protein interface (Evans et al. 2022). An ipTM >0.8 indicates a high quality prediction, ipTM< 0.6 implies an incorrect prediction (indicating the protein-protein interaction is unlikely) and intermediate values are more uncertain (EMBL-EBI, n.d.). ipTM is also reduced by the presence of disordered protein regions, as demonstrated by large discrepancies in ipTM scores when only protein-protein interaction domains are modelled vs the full-length proteins, including the disordered regions (Dunbrack 2025). ipTM thresholds as low as 0.3 have been used for initial screening of protein pairs, but this is only appropriate when candidate protein pairs are subjected to further analysis (Weeratunga et al. 2024).

All the models produced by my query had very low pTM (<0.33) and ipTM (<0.5) scores (**fig. 55a**). However, the highest ipTM scores corresponded to experimentally-confirmed

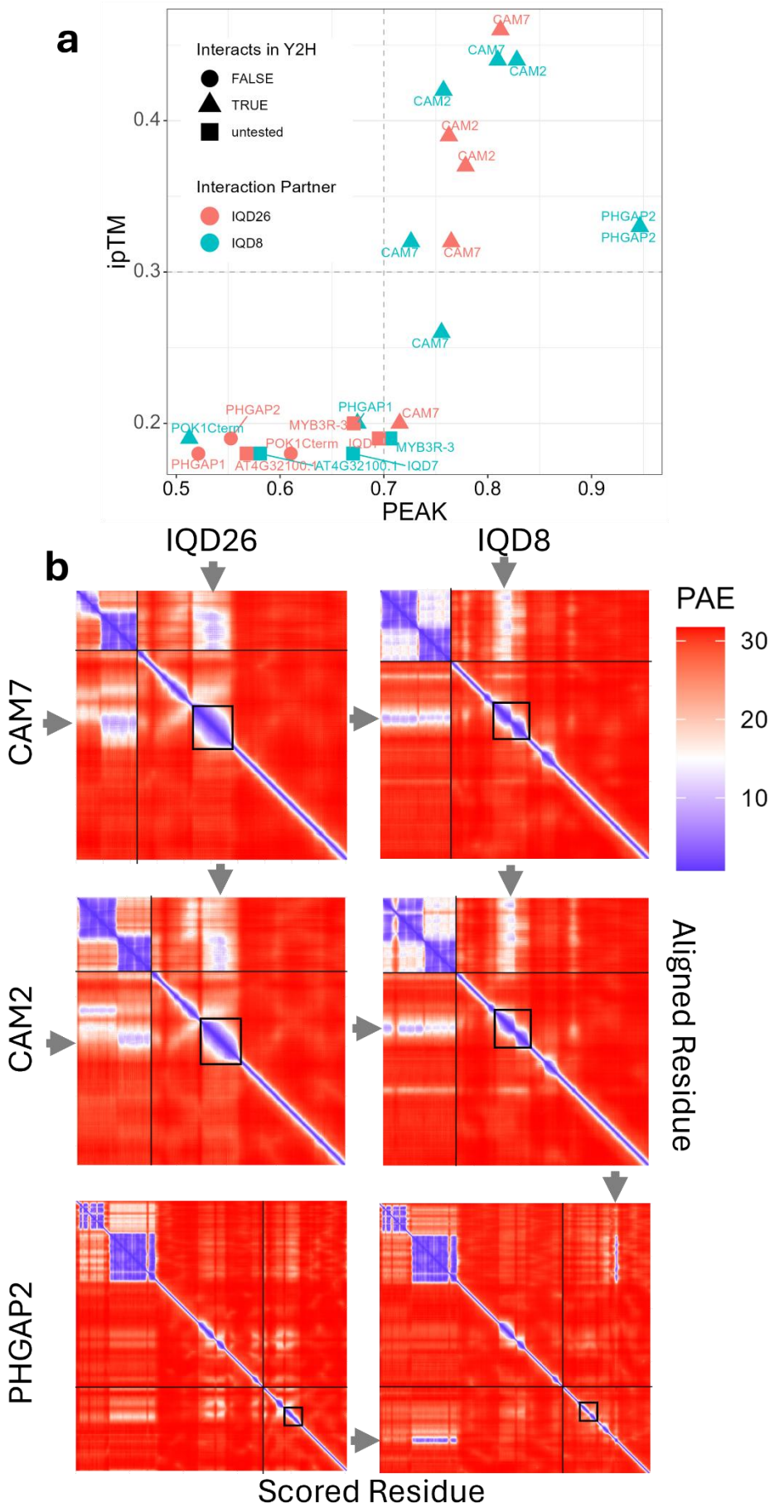
a
Interacts in Y2H
FALSE
TRUE
untested
Interaction Partner
IQD26
IQD8
ipTM
PEAK
0.2
0.3
0.4
0.5
0.6
0.7
0.8
0.9
CAM7
CAM2
PHGAP2
PHGAP1
MYB3R-3
POK1Cterm
IQD7
AT4G32100.1
b
IQD26
IQD8
CAM7
CAM2
PHGAP2
PAE
30
20
10
Aligned Residue
Scored Residue

Figure 55: AlphaFold2 Multimer correctly predicts some IQD interaction partners and their interaction interfaces. **(a)** AlphaFold2 Multimer ipTM scores vs. PEAK score for interactions of IQD26 and IQD8. Whether the interaction was detected in a previously published yeast-2-hybrid (Y2H) screens is indicated. If an interaction has been tested in Y2H and the specific isoform used was not indicated, all splice isoforms of the protein are labelled according to the result of the Y2H interaction. **(b)** PAE plot for interactions of IQD8 and IQD26 with CAM2, CAM7 and PHGAP2. PAE measures the model's confidence in the relative position of two residues within the predicted structure. Red indicates low confidence; blue indicates high confidence. Upper left quadrants indicate within-protein PAE for CAM7, CAM2 and PHGAP2; lower right quadrants indicate within-protein PAE for IQD26 and IQD8; lower left and upper right quadrants indicate inter-molecular PAE. High PAE (dark blue) in the lower left and upper right quadrants indicates likely interaction between the proteins at the corresponding domains. Grey arrows point to interacting regions modelled with high confidence. Black boxes indicate the IQ67 domain.

Interactions indicating that, while ipTM was overall low, it could discriminate between real and not real interactions. To improve confidence in the protein-protein interaction predictions, I calculated an additional metric. AlphaFold2 calculates predicted alignment error (PAE), which measures the model's confidence in the relative position of two residues within the predicted structure (**fig. 53c, 55b**). Scaling and inverting the minimum intermolecular PAE of the whole complex generates the PEAK score (Wallner et al. 2024). This essentially measures the model's maximum confidence at the protein-protein interface. For interaction models with high levels of intrinsic disorder and low ipTM values, combining ipTM and PEAK improves confidence in the modelled protein interface and provides better discrimination between good and poor models (Wallner et al. 2024).

All non-interacting pairs were excluded with an ipTM cut-off of 0.3 and a PEAK cut-off of 0.7 (**fig. 55a**). All but two of the CaM interactions exceeded the cut-off and those that did not could plausibly reflect genuine isoform specific differences in IQD-binding. The ipTM and PEAK metrics effectively discriminated between the interaction of IQD8 with PHGAP2 and the non-interaction of IQD26 with PHGAP2 (**fig. 55a**) (Kumari et al. 2021; Dahiya et al. 2023). However, the interactions of IQD8 with the POK1 C-terminus and PHGAP1 scored similarly to non-interacting protein pairs, indicating that this method is prone to false negatives.

Inspection of the PAE plots for IQD-CaM and IQD-PHGAP2 interactions suggest that AlphaFold2 can predict the correct binding interfaces with reasonable accuracy. IQD8

and IQD26 were predicted to interact with CaMs via their IQ67 domain, as indicated by high intermolecular PAE scores for this domain (**fig. 55b**). IQD8 was predicted to interact with PHGAP2 via a motif situated C-terminally of the IQ67 domain, which is consistent with published data (**fig. 55b**) (Kumari et al. 2021). Together these results suggested that AlphaFold2 Multimer predictions may be useful as a crude screen for IQD protein-protein

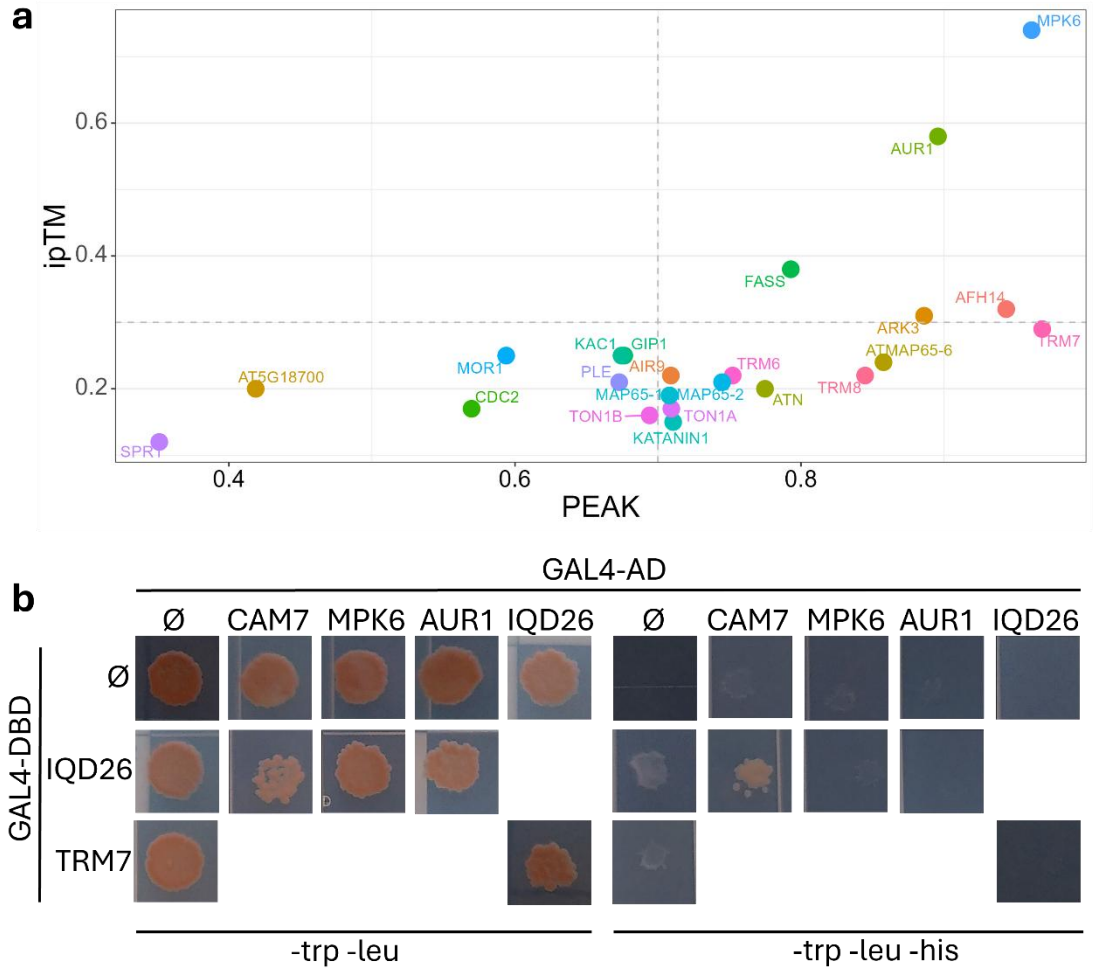

Figure 56: AlphaFold2 Multimer predicts IQD interactors but these were not validated in Y2H assay. (a) AlphaFold Multimer ipTM scores vs. PEAK score for interactions of IQD26 with PPB-related proteins **(b)** Yeast cells containing the indicated combinations of IQD26, CAM7, MPK6, AUR1 cDNAs fused to the GAL4 activation domain (AD) and IQD26 and TRM7 cDNAs fused to the GAL4 DNA binding domain (DBD). Each cDNA-GAL4-DBD/ cDNA-GAL4-AD fusion was transformed alongside the GAL4-DBD or GAL4-AD alone (indicated by Ø) to test for auto-activity. The TRM7-DBD fusion was used to test the IQD26-TRM7 interaction because the TRM7-AD fusion was auto-active. Yeast were grown on vector-selective (-trp -leu) and interaction selective (-trp -leu -his) media. Colonies shown are representative of 3 biological replicates.

interactions and that cut-offs of ipTM>0.3 and PEAK>0.7 are suitable for selecting candidate interaction partners.

To identify proteins that might interact with IQD26 at the PPB, I selected proteins that were associated with the GO terms GO:0009574 preprophase band or GO:0000913 preprophase band assembly, or which otherwise have evidence for PPB localisation/ regulation in the literature. From this list I excluded the POKs and PHGAPs, since I had already tested these, and IQD6-8. This left 23 proteins. I used AlphaFold2 Multimer to model the structure of IQD26 interacting with each of the proteins.

Two proteins stood out from the screen, having higher ipTM scores than any of the previously tested interactions: IQD26-MITOGEN-ACTIVATED PROTEIN KINASE 6 (MPK6) had an ipTM of 0.74 and IQD26-AURORA 1 (AUR1) had an ipTM of 0.58 (**fig. 56a**). Both complexes also had PEAK scores >=0.85. MPK6 and AUR1 are plausible interactors of IQD26. MPK6 localises to the PPB and cell plate and *mpk6* roots haver defects in cell division orientation (Müller et al. 2010). AURORA1 is a Ser/Thr kinase that expresses strongly in dividing cells (similar to IQD26) and localises to mitotic MTs and the cell plate (Boruc et al. 2017). *aur1 aur2* mutants have cell division orientation defects in the lateral root primordia (Van Damme et al. 2011). I therefore selected these proteins for further investigation. I also selected TRM7, since the IQD26-TRM7 complex had the highest PEAK score (0.97) of any complex tested and I have previously shown that IQD26 localisation is disrupted in *trm678* mutants. This complex did have a low ipTM score, however this will have been impacted by the large regions of intrinsic disorder in the TRM7 protein structure.

To test the interaction of IQD26 with MPK6, AUR1 and TRM7 in vivo, I performed a yeast-2-hybrid (Y2H) assay, including CAM7 as a positive interaction control. The assay detected the control CAM7-IQD26 interaction, but did not detect any interactions with MPK6, AUR1 or TRM7 (**fig. 56b**). These could be due to genuine non-interaction, weak interaction or steric hindrance caused by fusion with the GAL4 activation domain (AD) or DNA-binding domain. Further approaches to test these interactions are required to determine if these are true negatives and thereby test the validity of the AlphaFold2 screen.

4.2.5 Additional insights from the *trm678* mutant

While growing *trm678* plants to explore the dynamics of IQD26-YFP in the PPB-less background, I observed that their stems and leaves resembled those of the *1aiqd-2* mutant. Their rosette leaves were thicker and more rounded, and their stems were fatter

than wild type plants (**fig. 57a,b**). The leaf shape phenotype was more extreme than that of *1aiqd-2*: the leaves were conspicuously rounder and thicker, and the leaves also had noticeable craters and wrinkles, which were absent from *1aiqd-2* leaves. This phenotype is similar to that of the *pok1pok2* mutant, albeit in a milder form (Müller et al. 2006; Lipka et al. 2014). This is consistent with *trm678* having a milder cell division phenotype than *pok1pok2* (Schaefer et al. 2017).

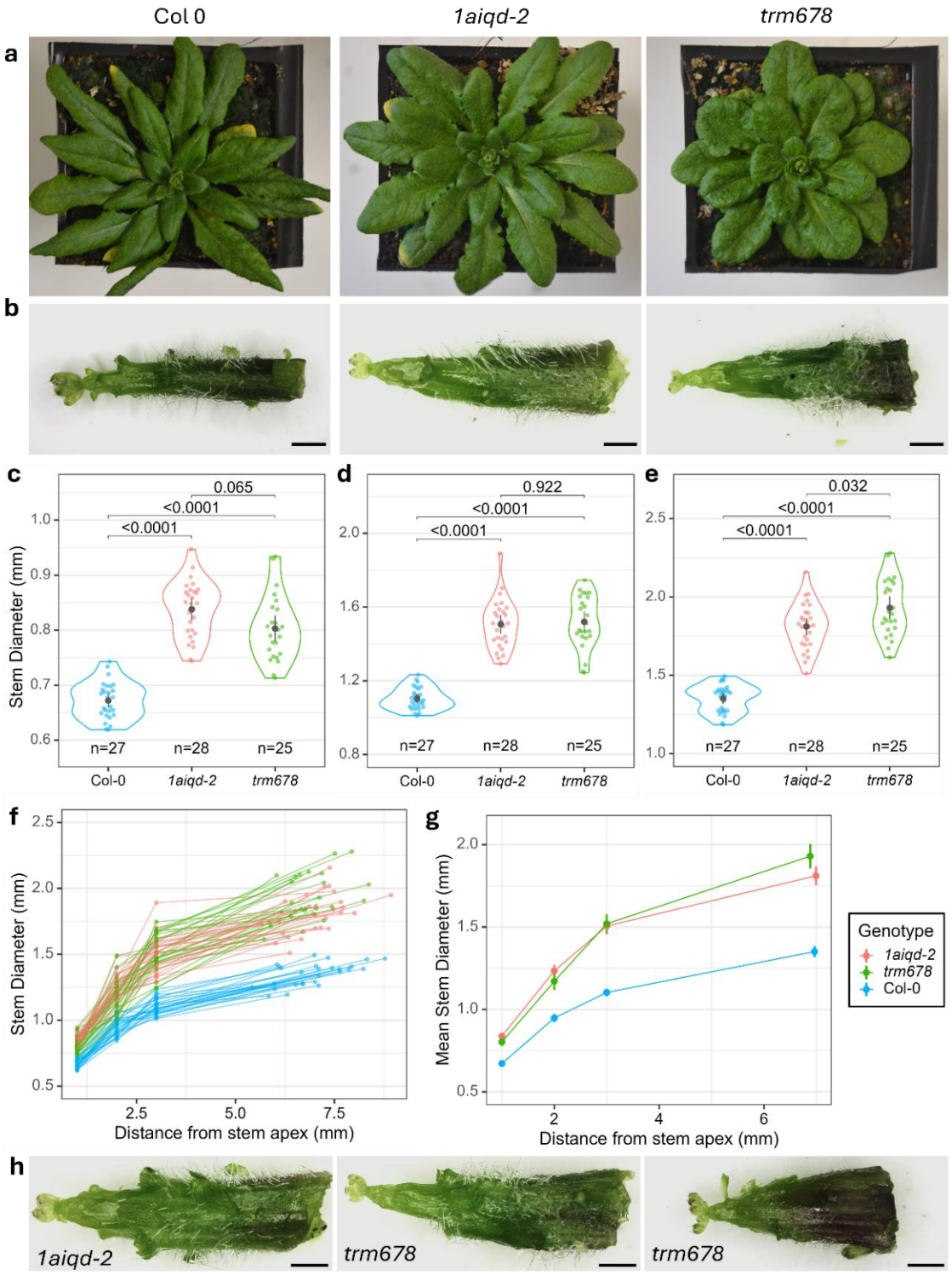

Figure 57: The stems of *trm678* mutants are thicker than wild type plants and are shaped differently to *1aiqd-2* mutants. (a) Rosettes of approx. 5-week-old plants. Left to right: wild type Col-0, *1aiqd-2*, *trm678*. **(b)** Stereomicrographs showing ~6.5 mm tall stems, of the same genotypes as (a). **(c-e)** Stem diameters measured 1 mm (c) and 3 mm (d) from the stem apex and at the stem base (e). Statistical significance was determined by Welch's ANOVA and then post-hoc pairwise comparisons were computed using the Games Howell test. Grey dots and whiskers indicate mean and 95% CI of the mean. **(f)** Stem diameter plotted against vertical distance from the stem apex. Each line represents an individual plant. **(g)** Mean and 95% CI of the data shown in (f). Mean plant height was used as the x coordinate for the mean diameter of the stem base. **(h)** Stereomicrographs of *1aiqd-2* and *trm678* stems with diameters at the upper extreme of the distribution for each genotype. Scale bar: 1mm.

Quantification of stem thickness revealed that *trm678* stems were indeed significantly thicker than wild type stems (**fig. 57c-e**) and this derived from an increase in pith tissue (**fig. 58**). *1aiqd-2* and *trm678* plants were significantly thicker than wild type plants at all positions measured. At 3 mm from the meristem, *1aiqd-2* and *trm678* plants were both around 37% thicker than wild type plants (**fig. 57d**). Further away from the meristem, the *trm678* plants were even slightly thicker than *1aiqd-2* (**fig. 57c,e**). Between the 3 mm point and the stem base, *1aiqd-2* stems increased in diameter more gradually than *trm678* and to a similar degree as wild type stems: note how the slopes of the rightmost line segments in **fig. 57g** are almost identical in *1aiqd-2* and wild type. This is consistent with observation

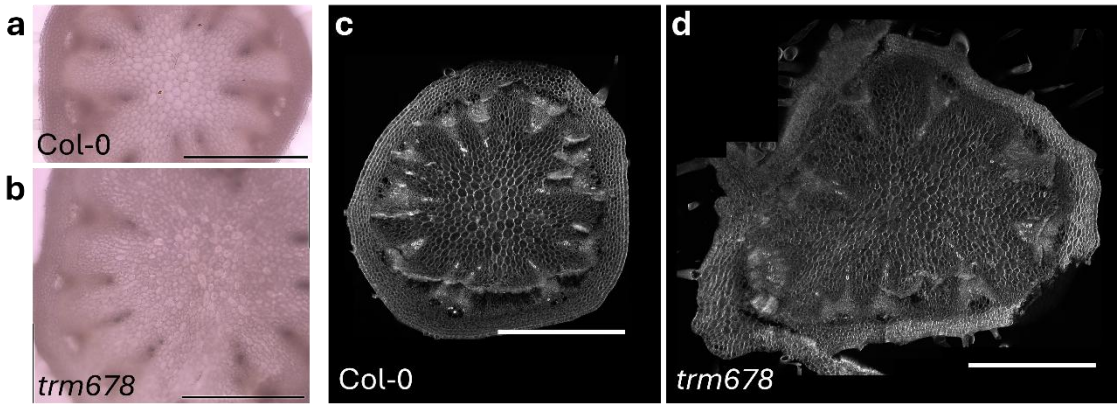

Figure 58: *trm678* stems have more pith cells than wild type plants. Transverse stem sections from col-0 (a,c) and *trm678* (b,d) stems. 6 mm-tall plants (e.g. as shown in fig. 57b) were fixed in EtOH and hand sections were cut approx. 4 mm from the stem apex and stained with calcofluor white. Sections were viewed under brightfield illumination (a,b) and confocal microscopy (c,d). Scale bar: 50 µm

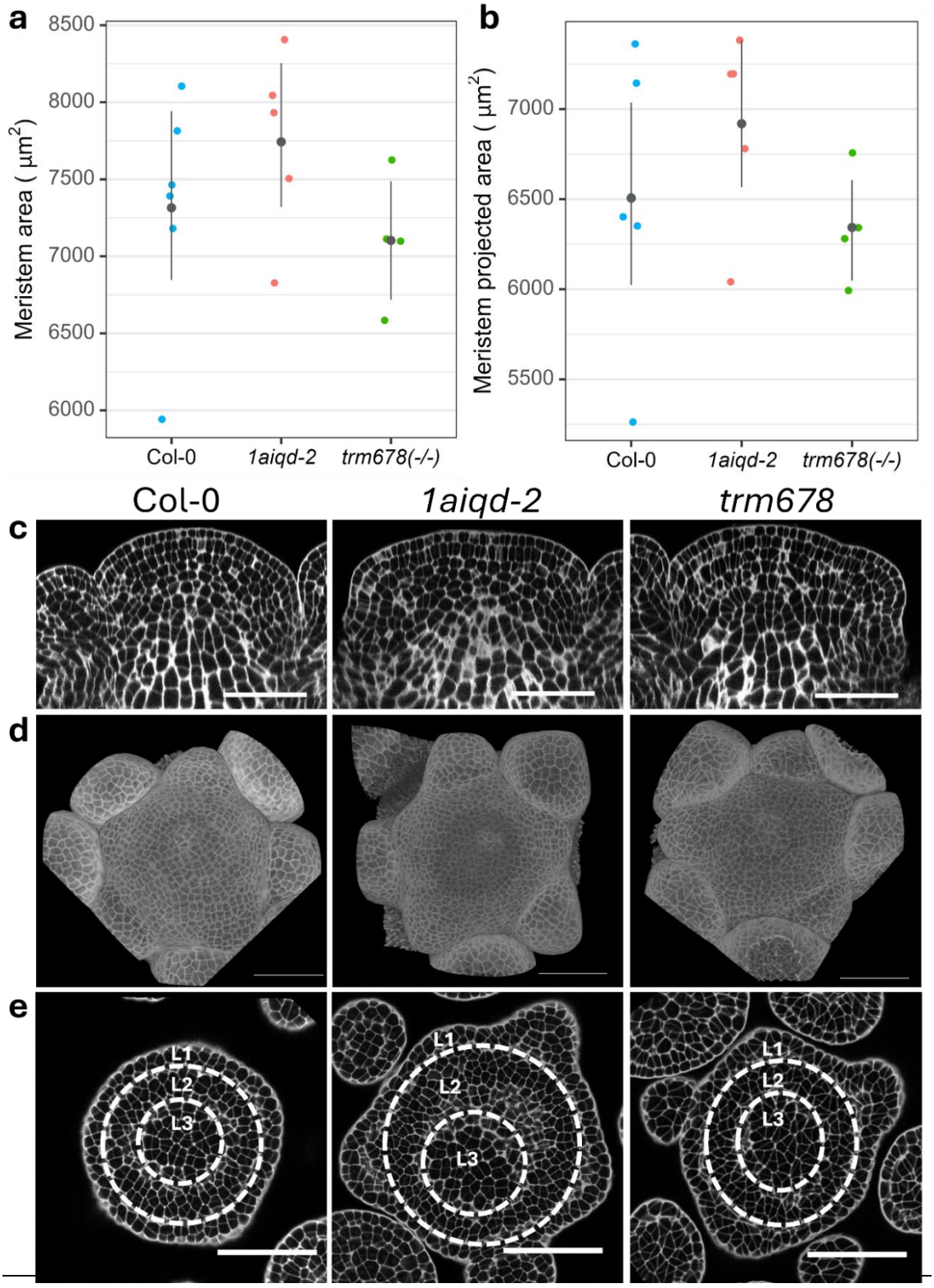
a
Meristem area (µm²)
8500
8000
7500
7000
6500
6000
Col-0
1aiqd-2
trm678(-/-)
b
Meristem projected area (µm²)
7000
6500
6000
5500
Col-0
1aiqd-2
trm678(-/-)
Col-0
1aiqd-2
trm678
c
d
e
L1
L2
L3

Figure 59 (previous page): The *trm678* mutations affect cell division orientation in the SAM but do not affect meristem size or morphology. **(a, b)** Quantification of meristem area (a) and projected area (b) of wild type Col-0, *1aiqd-2* and *trm678* meristems. Area is the total surface area of the meristem; projected area is the area of the 2D shape generated by projecting the meristem surface onto the plane perpendicular to the stem's vertical axis. **(c-e)** PI-stained wild type (left), *1aiqd-2* (middle) and *trm678* (right) meristems. Longitudinal optical sections (c), 3D volumetric projections (d) and transversal optical sections through the L1-L3 layers (e) are shown. Points and whiskers indicate bootstrapped mean and 95% confidence interval of the mean. All plants analysed were approx. 5 weeks old and 6 (+/- 2) mm tall. Four to six meristems were analysed per genotype. Scale bars: 50 µm

that *1aiqd-2* and wild type plants undergo similar amounts of radial growth in this stem region (Chapter 2, figs. 7,10). *trm678* stems, on the other hand, increased in diameter more steeply than *1aiqd-2* plants in the region > 3mm from the meristem (**fig. 57f, g**). This difference was most obvious in the thickest plants from each genotype: the *trm678* mutants had a more conical shape, starting narrower at the apex and then widening substantially (**fig. 57h**). The altered shape of *trm678* plants might originate from a faster radial growth rate or a reduced elongation rate relative to *1aiqd-2* and wild type plants.

trm678 meristems were a similar size to wild type meristems, and their overall morphology was normal (**fig. 59a-d**). However, *trm678* mutants did have striking differences in cell division orientation (**fig. 59d,e**). The organisation of the meristem was normal, with proper specification of the L1, L2 and L3 layers, and no conspicuous layer invasion (**fig. 59c**), however the divisions within layers, though still periclinal, otherwise deviated significantly from their typical orientation. As a result, many cells in the L1, L2 and upper L3 layers were shaped like triangular wedges (**fig. 59d,e**). Previous work on the *trm678* mutant confirmed that PPBs are largely absent in the meristem epidermis but the cell division orientation in these cells was not reported (Schaefer et al. 2017). The cell division phenotype in the SAM is similar to that previously described in the outer layers of the root: cell division orientation within layers is disrupted, but overall meristem organisation is largely unperturbed.

Based on the observation that *trm678* plants have a thick stems and perturbed cell division orientation in the SAM, I quantified cell division orientation in the rib meristem. In *trm678* rib meristems, most new cell walls were oriented near-transversally, but the

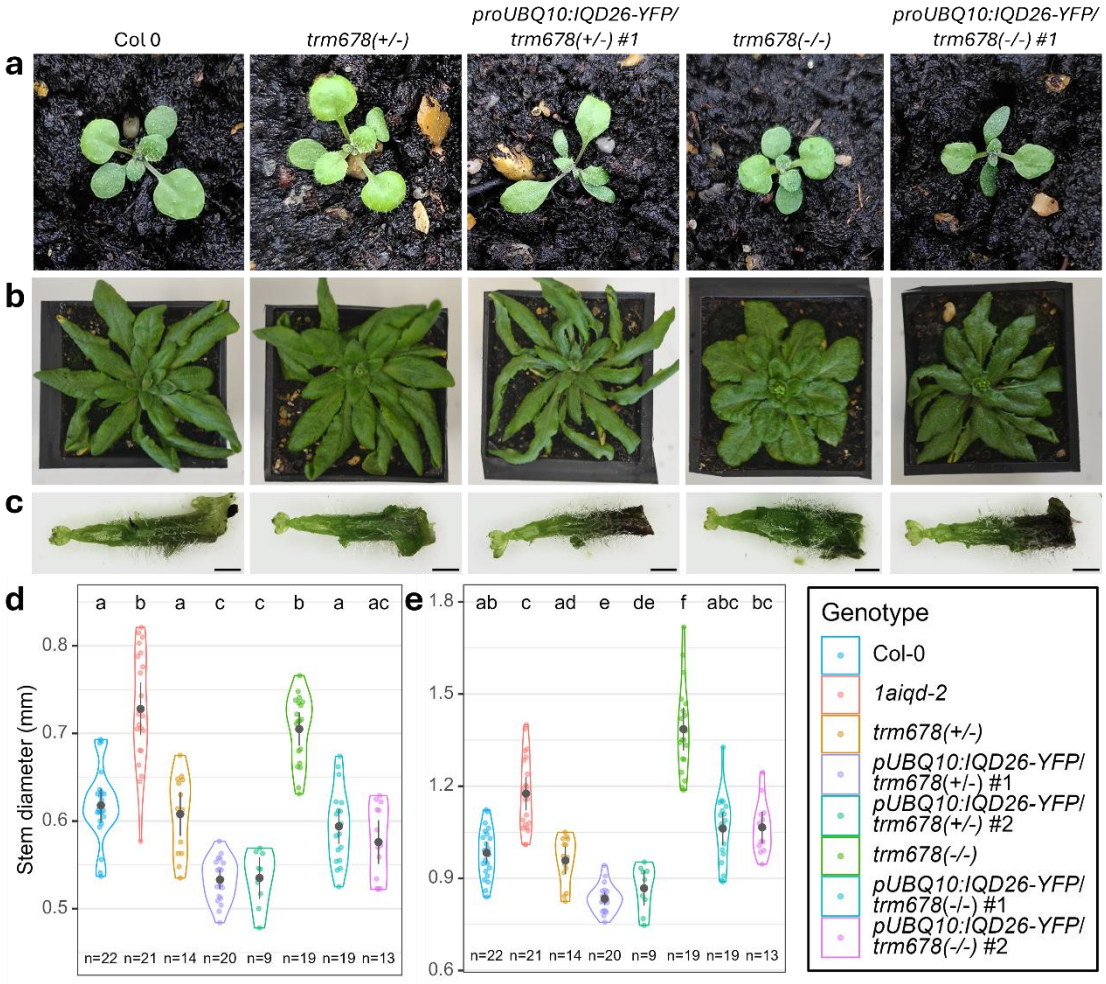

Figure 60: Overexpression of *IQD26* causes stem narrowing in wild type and *trm678* backgrounds. (a) 2-week-old seedlings. Left to right: wild type Col-0, *trm678(+/-)* (heterozygous complemented line), *proUBQ10:IQD26-YFP/ trm678(+/-)*, *trm678*, *proUBQ10:IQD26-YFP/trm678*. **(b)** Rosettes of approx. 5-week-old plants. (b) Stereomicrographs showing ~5.7 mm-tall stems. **(c,d)** Stem diameters measured 1 mm (c) and 3 mm (d) from the stem apex. Statistical significance was determined by Welch's ANOVA and then post-hoc pairwise comparisons were computed using the Games Howell test. Grey dots and whiskers indicate mean and 95% CI of the mean. *proUBQ10:IQD26-YFP/trm678* (+/-) #1 and #2 contain the same *proUBQ10:IQD26-YFP* transgene insertion as *proUBQ10:IQD26-YFP/trm678* (-/-) lines #1 and #2, respectively. Scale bar: 1mm.

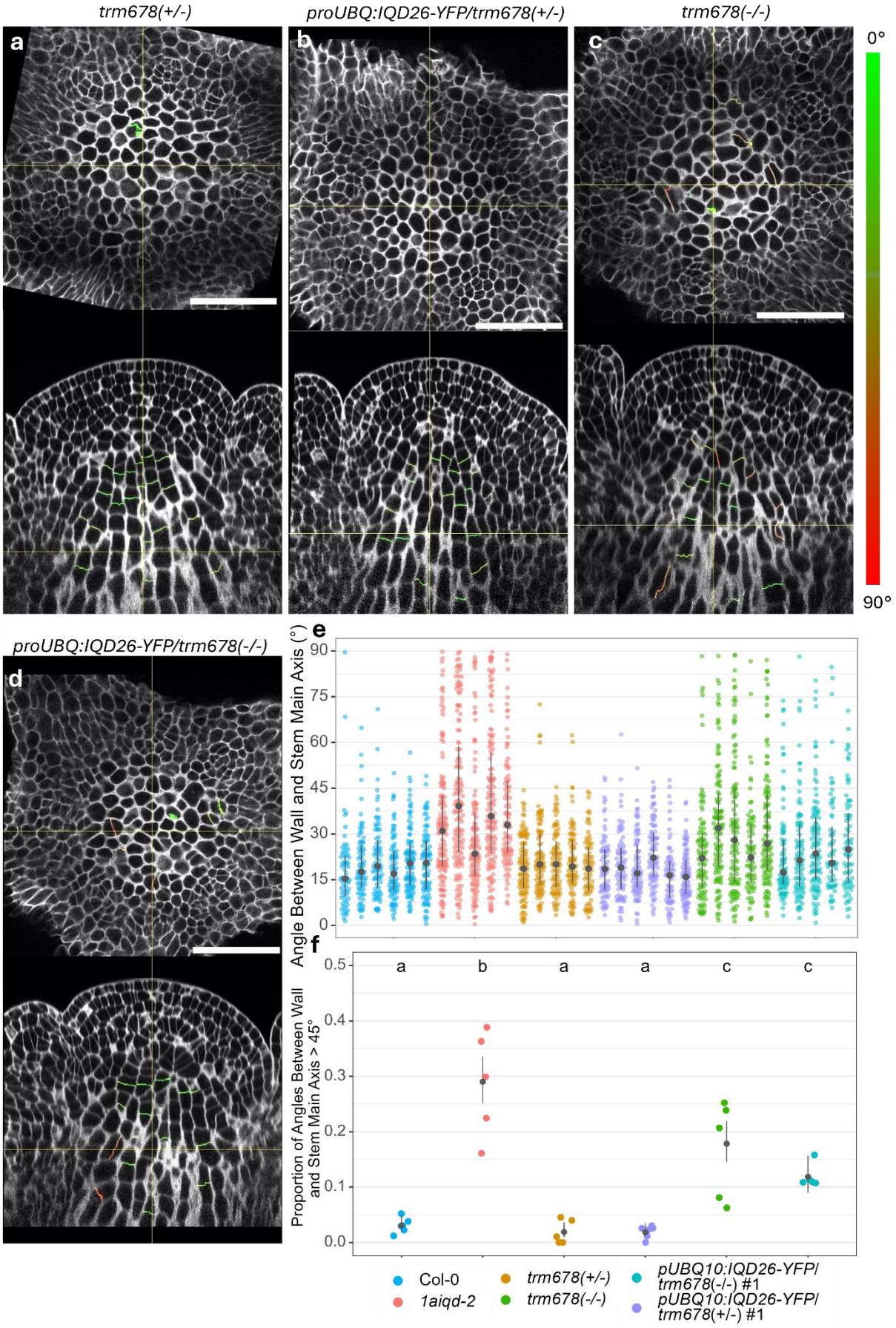
trm678(+/-)
proUBQ:IQD26-YFP/trm678(+/-)
trm678(-/-)
a
b
c
0°
90°
proUBQ:IQD26-YFP/trm678(-/-)
d
e
Angle Between Wall and Stem Main Axis (°)
90
75
60
45
30
15
0
f
Proportion of Angles Between Wall and Stem Main Axis > 45°
0.5
0.4
0.3
0.2
0.1
0.0
a
b
a
a
c
c
Col-0
1aiqd-2
trm678(+/-)
trm678(-/-)
pUBQ10:IQD26-YFP/ trm678(-/-) #1
pUBQ10:IQD26-YFP/ trm678(+/-) #1

Figure 61 (previous page): *trm678* affects division orientation in the rib meristem and this is unaffected by overexpression of *IQD26*. (a-d) Single optical sections of fixed PI-stained SAMs from *trm678(+/-)* (heterozygous complemented line), *proUBQ10:IQD26-YFP/ trm678(+/-)*, *trm678* and *proUBQ10:IQD26-YFP/trm678(-/-)*. Meristems were harvested from 5-week-old plants, at the stage shown in fig. 60. Transverse sections approx. 110 µm from the meristem apex (upper panels) and longitudinal sections through the centre of the meristem (lower panels) are shown. Recently formed cell walls in the rib meristem are coloured on a scale of green to red where green walls are more transversely oriented and red wall are more longitudinal (see Chapter 2, fig. 13). **(e)** Angle between wall and main axis (where values closer to zero indicate more transversely oriented walls). Each point represents the angle of an individual wall and each set of points represents the walls of an individual meristem. Black dots and whiskers show median and IQR. **(f)** The proportion of wall angles > 45° in each meristem. Data were analysed using a Poisson model. Black dots and whiskers show back-transformed estimates for the rates and asymptotic upper and lower confidence levels (conceptually equivalent to mean and 95% CI). Different letters indicate genotypes that are statistically significantly different ($p<0.05$). Data presented for Col-0 and *1aiqd-2* are the same as shown in fig. 45, since both experiments were conducted in parallel using the same control plants. Scale bars: 50 µm.

angles were much more variable than the wild type and a sizeable minority were extremely misoriented (**fig. 61c,e,f**). The distribution of new wall angles was significantly different from both wild type Col-0 and *1aiqd-2*, the latter having an even higher proportion of non-transversal walls (**fig. 61f**). However, the number of cells in the *trm678* rib meristem was similar to wild type plants, and the increase in cell number between 60 µm and 100 µm of the meristem was the same (**fig. 63**). This suggests that the processes responsible for the increase in pith tissue occur further down the stem.

While the disruption of cell division orientation in *trm678* resembled the *1aiqd-2* mutant, the geometry of the rib meristem cells did not. Cell geometry in *1aiqd-2* was fairly uniform within an individual plant and similar to wild type plants (Chapter 2, fig. 15, 17). In transverse sections, all cells look approximately circular unless they have undergone a very recent longitudinal cell division. In contrast, *trm678* rib meristem cells were variable in shape and size. Average cell cross-sectional area was the same as the wild type, but it is more variable, with more very large and very small cell areas (**fig. 62a-g**). The larger cells were also more variable in shape (**fig. 62g**).

4.2.6 The phenotypes of IQD26 overexpression

I previously observed a mild slender organ phenotype in one of the *proIQD26:IQD26-YFP/1aiqd*-2 lines, which might have been the result of mild *IQD26* overexpression (Chapter 3, fig. 37). To confirm this and gain further insight into the function of IQD26, I generated *proUBQ10:IQD26-YFP* lines. I wanted to simultaneously test whether any

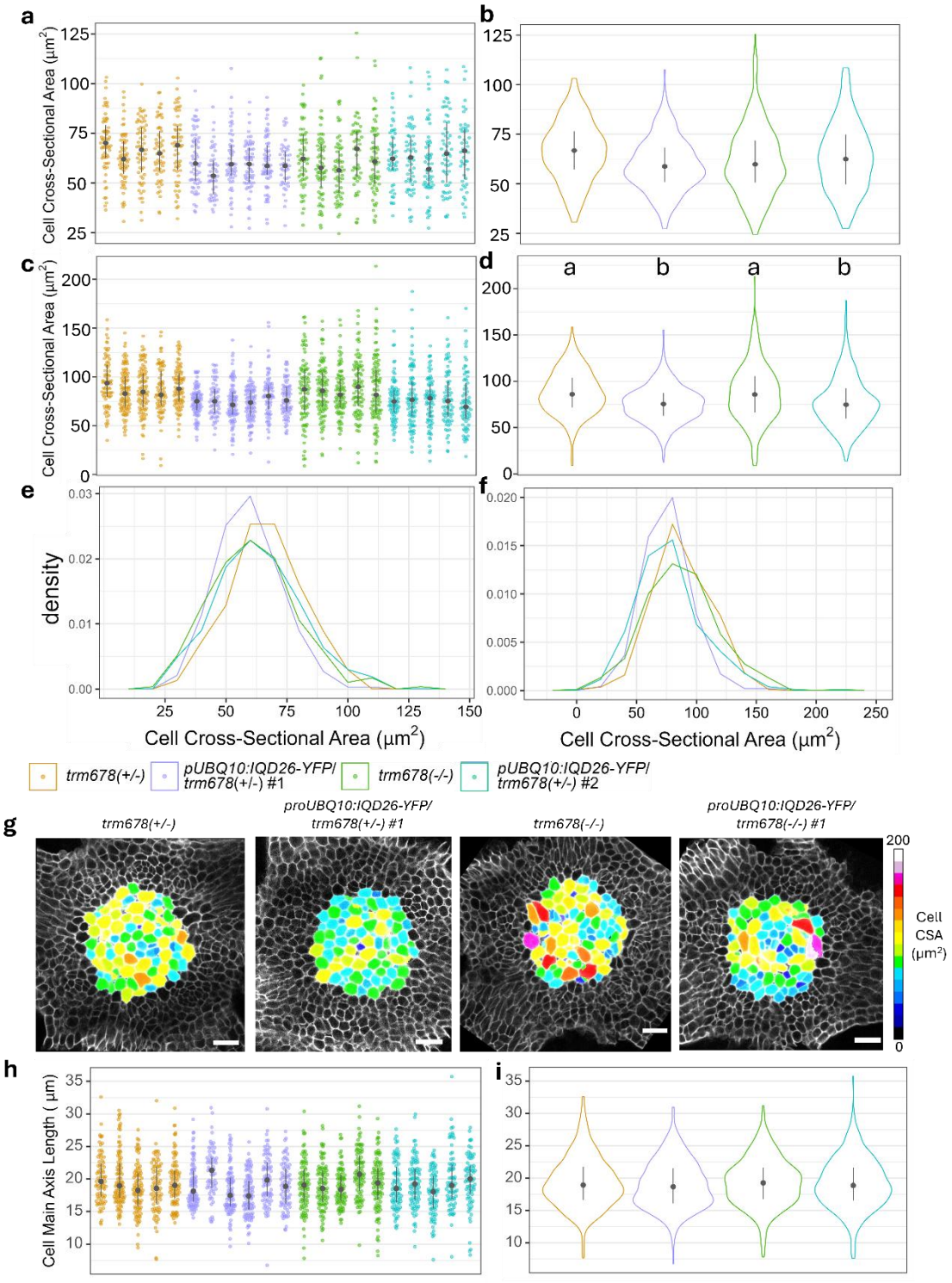

Figure 62 (previous page): *trm678* and overexpression of *IQD26* affect cell area in different, independent ways. Quantification of rib meristem cell cross-sectional area **(a-g)** and main axis length **(h-i)** as measured in fixed PI-stained SAMs from *trm678(+/-)* (wild type-like heterozygous complemented line), *proUBQ10:IQD26-YFP/ trm678(+/-)*, *trm678* and *proUBQ10:IQD26-YFP/trm678(-/-)*. Cell cross-sectional area was measured as described in Chapter 2, fig. 16. Meristems were harvested from 5-week-old plants, at the stage shown in fig. 60. 5-6 meristems were analysed per genotype. Cells within 60 µm (a,b,e) and 100 µm (c,d,f,h,i) of the meristem apex were measured. For (a,c,h)**,** each point represents the measurement for an individual cell and each set of points represents the cells of an individual meristem. (b,d,e,f,i) show the same data, but with data from separate meristems of the same genotype pooled together. The pooled data are displayed as violin plots (b,d, i) and frequency polygons (e,f). In (d), different letters indicate groups with statistically different medians as determined by pairwise Wilcoxon tests, adj. p value >0.05. **(g)** single optical transverse sections of PI-stained meristems, 100 µm vertical distance from the meristem apex. Cells in the rib meristem are coloured according to their cross-sectional area. Scale bar: 20 µm. Black dots and whiskers show median and IQR.

overexpression phenotypes require the PPB, and so I introduced *proUBQ10:IQD26-YFP* into the *trm678* background. To ensure I compared the same overexpression alleles, I crossed *proUBQ10:IQD26-YFP*/*trm678* with wild type col-0 to generate heterozygous *proUBQ10:IQD26-YFP*/*trm678(+/-)* plants. *trm678*(+/-) was phenotypically indistinguishable from wild type col-0 (**fig. 57**), making it a suitable background for measuring the effects of *proUBQ10:IQD26-YFP* on wild type plants.

Wild type plants overexpressing *IQD26* had narrow, slightly twisted cotyledons and rosette leaves as well as narrow stems (**fig. 60**). Overexpressing *IQD26* in the trm678 background partially suppressed the leaf and stem morphology phenotypes of *trm678* (**fig. 60**). *proUBQ10:IQD26-YFP*/*trm678* leaves were more similar in shape to wild type plants, although they were thick like *trm678* leaves (**fig. 60a,b**) and the overall size of the rosette was also small, like *trm678*. Stem diameter was also reduced in *proUBQ10:IQD26-YFP*/*trm678* lines and was similar to wild type plants (**fig. 60c,e**).

To determine whether the effect of *IQD26* overexpression (OE) on stem diameter was due to a complementation of cell division orientation or other changes to growth, I quantified cell division orientation and cell geometry in the rib meristem. *IQD26* OE in the wild-type background did not affect the distribution of new cell wall angles (**fig. 61**). In the *trm678* background, *IQD26 OE* did not significantly reduce the proportion of new cell wall angles

>45° (**fig. 61d,f**). Consistently, the number of cells in the rib meristem was similar across all genotypes (**fig. 63**). Therefore, the narrow stems of *IQD26* overexpressors may not be due to changes to cell division orientation or cell number, although I cannot exclude changes to cell number further down the stem – quantification of pith cell numbers and pith diameter in transverse stem sections from mature stems is required to establish this. It is notable that IQD26-OE did not reduce the cell number in the rib meristem, as this suggests that IQD26 does not repress cell proliferation. This supports the hypothesis that the increased rib meristem/ pith cell number *1aiqd-2* mutants derives from changes to cell division orientation rather than proliferation, although a role for IQD26 in cell cycle regulation remains to be explicitly tested.

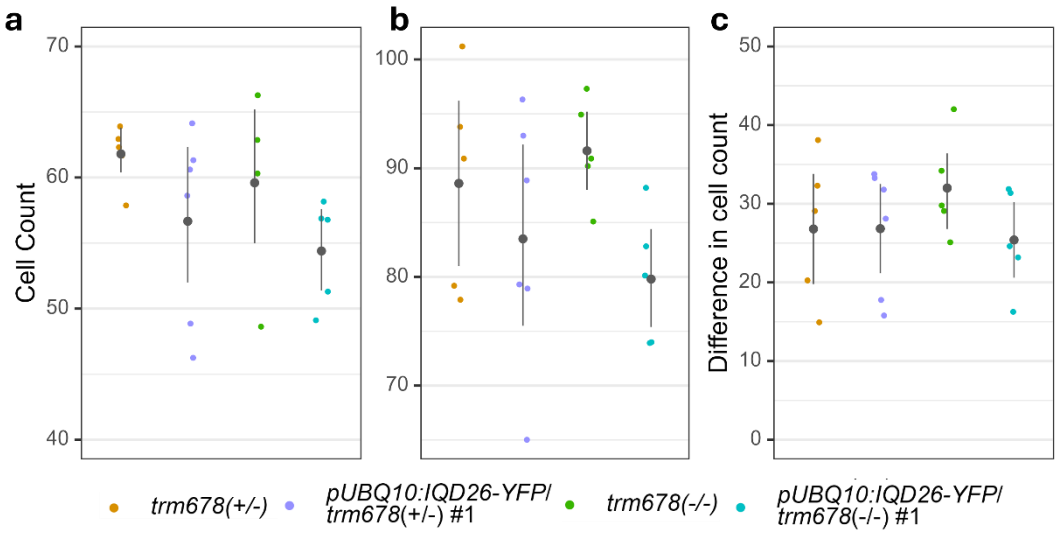

Figure 63: *trm678* and *IQD26-OE* do not affect rib meristem cell number. Quantification of rib meristem cell number as measured in fixed PI-stained SAMs from *trm678(+/-)* (wild type-like heterozygous complemented line), *proUBQ10:IQD26-YFP/ trm678(+/-)*, *trm678* and *proUBQ10:IQD26-YFP/trm678(-/-)*.Five meristems were analysed per genotype. **(a, b)** The number of rib meristem cells in cross-sections 60 µm (a) and 100 µm (b) from the meristem apex. **(c)** Difference in cell number between the 100 µm and 60 µm cross-sections, expressed as an absolute difference (number of cells at 100 µm - number of cells at 60 µm).

IQD26 OE did alter cell shape, reducing the cross-sectional area of rib meristem cells in both the wild-type and *trm678* background, similar to *proIQD27:IQD26* (**fig. 62e,** Chapter 3, **47c,d**). For cells situated 100 µm from the meristem, median wild type and *trm678* cell areas were 88 µm^2 and 87 µm^2, respectively, and overexpressing *IQD26* in these backgrounds reduced the medians to 76 µm^2 and 77 µm^2. These differences were highly

statistically significant (pairwise Wilcoxon, W = 73639.5, p adj $<10^{-15}$; W = 70891, p adj $<10^{-6}$). The cells were not more elongated, however, with similar main axis lengths across the genotypes (Kruskal-Wallace, $\chi^2(3, n=1780)$, p = 0.2607) (**fig. 62h,i**). This indicates that the narrow organ phenotypes of *IQD26* overexpressors likely derive from changes to cell shape, rather than cell division orientation, which is consistent with other *IQD* OE lines (Bürstenbinder, Möller, et al. 2017; Yuanfeng Li et al. 2021; Lee et al. 2006; Drevensek et al. 2012). Therefore, the apparent partial complementation of *trm678* by *IQD26* OE may derive from a small effect on division orientation (**fig. 61e,f**), but likely more from changes in cell shape and therefore is not a true complementation at the mechanistic level.

4.3 Discussion

4.3.1 Regulation of cell division by IQD26

Although the precise molecular role of IQD26 in cell division regulation remains to be discovered, the data presented here significantly narrow down the possibilities and have generated new testable hypotheses. Since reliable localisation of IQD26 to the CDZ requires PPB formation, IQD26 likely functions in the later stages of PPB formation and/or recruits proteins to the CDZ. IQD26 overexpression lines also provide promising insight into IQD26 function. IQD26 OE plants have narrow, slightly twisted cotyledons and leaves, which is strikingly similar to plants that overexpress *IQD11, IQD16, IQD18*, *IQD21* and *LONGIFOLIA1/ TRM2* (Bürstenbinder, Möller, et al. 2017; Yuanfeng Li et al. 2021; Wendrich et al. 2018; Lee et al. 2006). These five proteins localise to cMTs and their overexpression is associated with increased cell elongation and the reorganisation of the cMTs into ordered, directional arrays (Bürstenbinder, Möller, et al. 2017; Yuanfeng Li et al. 2021; Lee et al. 2006; Drevensek et al. 2012). For *IQD21* and *IQD16*, these effects depend on the MT-severing enzyme KTN1 (Feng et al. 2023; Yuanfeng Li et al. 2021). The phenotypic similarities suggest that ectopic IQD26 might similarly bind and organise cMTs, thereby inducing changes to cell shape. Indeed, rib meristem cell geometry was altered in IQD26 OE plants, suggesting that cell geometry changes do underpin the elongated organ phenotype. When expressed under its native promoter, IQD26-YFP did not display a distinctly filamentous localisation pattern that would indicate binding to interphasic cMTs (Chapter 3, figs. 29, 32-34). However, *proIQD26:IQD26* was expressed at lower levels in interphasic cells (fig. 32), which could make detection of cMT-localised IQD26-YFP difficult. Indeed, transiently expressed IQD26-GFP in *N. benthamiana* did have a somewhat filamentous localisation (Bürstenbinder, Möller, et al. 2017). Inspection of

cell geometry, cMT organisation and IQD26-YFP localisation in IQD26 OE leaves will be necessary to test whether ectopic IQD26 does indeed alter cMT organisation and cell shape in leaves, or whether the growth phenotype relates to changes in cell division orientation. Interestingly, overexpression of *IQD22* or *IQD25* does not cause leaf narrowing, which indicates a substantial degree of functional specialisation and divergence within the 1A IQD subfamily (Zhao et al. 2025; Bürstenbinder, Möller, et al. 2017)

A shared mechanism could explain the cell division orientation phenotype of the *1aiqd-2* mutant and the cell shape phenotype of IQD26 OE plants. This is because many of the same proteins that bundle, sever or cross-link MTs during the rearrangement of interphase cMTs also support the rearrangement of MTs into mitotic structures (Bouchez et al. 2024). For example, *ktn1* mutants have cell division orientation defects due of misshapen/ misoriented mitotic MT structures whereas increased KTN1 activity alters cell growth anisotropy by affecting cMT organisation (Feng et al. 2023; Yuanfeng Li et al. 2021; Panteris et al. 2011). Given that IQD26 has a MT-binding domain, it is plausible that IQD26 recruits or retains MT-processing proteins to the CDZ to support local MT organisation in the later stages of PPB formation or during PPB maintenance. One of these could plausibly be KTN1, since it directly binds IQD16 and IQD21, and IQD26 has a very similar motif structure to IQD21 (Abel et al. 2005). Ectopic expression of IQD26 at high levels during interphase might therefore cause artefactual changes in cMT organisation, even if IQD26 does not participate in cMT organisation when expressed at wild-type levels. Visualisation of MTs in the *1aiqd-2* rib meristem (via tubulin immunolocalization or successful introduction of a MT reporter) will be necessary to detect any effects of the *1aiqd-2* mutations on the orientation or structure of the PPB or phragmoplast and therefore establish whether IQD26 is indeed required for the MT organisation in these structures.

4.3.2 The usefulness of AI modelling to predict interaction partners of IQD26

AI-based protein structure prediction programmes are revolutionising structural biology and offer a powerful tool for screening and modelling protein-protein interactions (Yang et al. 2023; Jumper et al. 2021). However modelling proteins with high levels of intrinsic disorder remains a challenge (Bret et al. 2024; Dunbrack 2025). Assessing the ability of AlphaFold2 to predict the interactions of IQDs is particularly challenging because there are few confirmed interactions and no experimentally determined protein complex structures to use for benchmarking. AlphaFold2 Multimer shows potential for screening

IQD interactors, but further work is needed to confirm the accuracy of its predictions. I have generated lines for TurboID-based proximity labelling to detect interactors (including weak ones) of IQD26, and cloned plasmids for testing the interaction MPK6, AUR1 and TRM7 *in planta* via split-luciferase assay. In time, these will reveal the interaction partners of IQD26 and validate or invalidate the usefulness of the AlphaFold screening process.

There is considerable scope for improving AI-based screening of IQD interactors: improved programs and metrics for screening AlphaFold predictions have recently been developed (Mischley et al. 2024; Dunbrack 2025) and, in 2024, Google DeepMind launched AlphaFold3, which can prediction structures with higher accuracy than the previous iteration (Abramson et al. 2024). These technologies will only improve with time. The total IQD interactome is likely vast - the IQD families of every angiosperm characterised so far number several tens of proteins, each of which likely interacts with multiple protein partners. AI programmes make it possible to screen large numbers of possible interactions quickly and cheaply and therefore developing an effective pipeline for IQDs could considerably accelerate research into IQD function.

4.3.3 Further insights into how division orientation regulates stem growth

trm678 and *1aiqd-2* are independent examples of mutants that have misoriented cell divisions and increased radial stem growth. However, they differ in many aspects of their development. Most notably, misoriented cell divisions in the rib meristem of *1aiqd-2* plants are associated with an increase in rib meristem cell number, but in *trm678* they are not. On the one hand, this calls into question the hypothesis that altered division orientation drives radial growth. On the other hand, there are several possible explanations for this discrepancy that do not invalidate this hypothesis.

Firstly, the *trm678* differs from *1aiqd-2* in that the misorientation of cell divisions is not restricted to the rib meristem, occurring in different cell layers. Under normal growth conditions, radial divisions in the periphery of the rib zone contribute cells to the rib meristem (Bencivenga et al. 2016). If the number of these radial divisions were reduced by *trm678*, this might counteract the increase cell numbers from misoriented divisions in the core rib meristem. Secondly, *trm678* rib meristem cells have more irregular size and shape than *1aqid-2* and this could affect the ability of radially adjacent daughter cells to establish new cell files. Finally, tissue-level mechanical effects, arising from the disruption of cell division orientation in the outer cell layers of *trm678*, might somehow restrict the insertion of new cell files. Careful study of the growth dynamics of *trm678*, clonal analysis, and tissue-specific expression of *TRM7* (which complements the

phenotype under its native promoter (Schaefer et al. 2017)) could be used to test these hypotheses. Furthermore, my analysis does not rule out a possible contribution for cell division orientation in radial growth further down the stem, where most radial growth occurs in the *trm678* mutant. This would require quantification of pith cell number and cell division orientation in stem regions >1 mm from the stem apex. Since *trm678* does not affect interphase MTs (Schaefer et al. 2017), it provides an exciting opportunity for assessing the specific role of cell division orientation in morphogenesis in different organs and tissues.

5 General Discussion

In recent years, IQD proteins have emerged as important regulators of plant form, cell division and stress responses (Abel et al. 2013; Dahiya and Bürstenbinder 2023; Bürstenbinder, Mitra, et al. 2017). However, our understating of how IQDs regulate these processes is very limited, and only a handful of IQD proteins having been characterised in detail. IQDs are an exciting and promising research area, with potential to reveal fundamental aspects of plant biology and practical applications for crop improvement (Levy et al. 2005; Matthes et al. 2022; Xiao et al. 2008; Bi et al. 2018). This thesis has made several new contributions to our understanding of the IQDs by characterising a poorly studied IQD subfamily and identifying novel functions in cell division and organ growth.

5.1 The 1A IQD Subfamily

The 33-member AtIQD family is divided into different, phylogenetically-related subfamilies (Abel et al. 2005). Most of these subfamilies have been scarcely studied, so their biological functions are largely unknown. Furthermore, while some closely-related IQD clades share similar expression patterns and functions (Kumari et al. 2021; Vaddepalli et al. 2021; Wendrich et al. 2018), it is unclear how common this is across the IQD family. This thesis and preceding work (Mckechnie-Welsh 2021) are the first to knock-out an entire IQD subfamily to examine the functionality of its members. We have found that knocking out six closely related genes has subtle effects on overall plant growth but nonetheless causes reproducible developmental phenotypes, particularly in leaf and stem morphogenesis (Chapter 2). The 1A IQDs share a similar motif architecture and protein structure, but their divergent expression patterns and differing subcellular localisation suggest a fair degree of functional specialisation within the subfamily (Chapters 3 and 4).

I characterised IQD26 in greater detail and identified it as a novel PPB/ CDZ-localised protein that regulates cell division orientation and has cell-cycle-linked expression (Chapter 3). The subcellular localisation of IQD26 and the disruption of division orientation in mutants is similar to IQD6-8, which function to recruit cell division regulators to the CDZ (Kumari et al. 2021; Vaddepalli et al. 2021). The overexpression phenotype of IQD26, with elongated organs and altered cell shape, is shared by different members of the IQD subfamily, which regulate cell growth anisotropy via cMT organisation (Bürstenbinder, Möller, et al. 2017; Yuanfeng Li et al. 2021; Feng et al. 2023;

Wendrich et al. 2018). IQD26 is the first identified IQD that combines both aspects of IQD function. This may reflect two separate functions of IQD26 – one in cell division regulation, another in cMT organisation. More likely, it reflects a single role of IQD26 in mitotic MT regulation, that leads to cMT organisation defects when IQD26 is ectopically expressed in interphase cells. Further work is required to establish whether the phenotype of IQD26 overexpressors does indeed derive from changes to cMT organisation and to identify the interaction partners through which IQDs regulate cell division orientation.

It is unclear where the 1A IQDs sit within the bigger picture of developmental regulation. IQDs are proposed to act as signalling hubs that integrate the many different pathways that regulate cell growth and division (Bürstenbinder, Mitra, et al. 2017; Kölling et al. 2019). However, so far, few links to these broader regulatory pathways have been identified. The two pathways that have been most strongly linked to IQDs are auxin and Ca^{2+} signalling, both of which have numerous, widespread biological effects. The hormone auxin affects almost every aspect of plant development, including cell division, cell growth, and cell fate specification, while Ca^{2+} is a ubiquitous secondary messenger that transmits, amplifies and integrates upstream signalling pathways to coordinate adaptive cellular responses (Lavy and Estelle 2016; Martin-Arevalillo and Vernoux 2023; Kudla et al. 2010).

Ca^{2+} signals are decoded by Ca^{2+}-binding CaMs and CMLs, to which all IQDs are expected to bind (Dahiya et al. 2023; Bürstenbinder, Möller, et al. 2017). Several IQDs have experimentally-verified CaM-binding and can recruit CaMs to specific cellular locations, which suggests that IQDs may coordinate downstream responses to Ca^{2+}signalling (Mitra et al. 2019; Bürstenbinder, Möller, et al. 2017; Zhao et al. 2025). A link to auxin signalling is probably less universal, since only a subset of IQDs are transcriptionally-regulated by auxin (Möller et al. 2017; Wendrich et al. 2018). Of these, several have been proposed to mediate the effects of auxin on MT organisation (Vaddepalli et al. 2021) and integrate the transcriptional auxin response with cellular Ca^{2+} signalling (Wendrich et al. 2018). IQD26 expression is also auxin-responsive (although this has only been shown for embryos), and binds to Ca^{2+}-binding CaM proteins in yeast (Wendrich et al. 2018; Möller et al. 2017; Dahiya et al. 2023). Therefore, IQD26 might be another link between auxin, Ca^{2+} and the regulation of cell division and MT organisation. IQD27, which seems to have a similar function to IQD26 (Chapter 3), also has auxin-responsive gene expression (Wendrich et al. 2018; Möller et al. 2017). Notably, IQD27 is expressed in the SAM bud primordia but otherwise excluded from the meristem surface and peripheral zone (Chapter 3).

Primordium formation is triggered by local accumulation of auxin (Pernisová and Vernoux 2021), so this might reflect auxin-induced expression of IQD27 and suggests that IQD27 may regulate cell division during primordium outgrowth. The specific CaM/CMLs that interact with IQD26 and IQD27 *in planta* must be identified to elucidate the link the Ca^{2+}-signalling, while further work is needed to establish how auxin affects 1A IQD transcription in different tissues.

5.2 IQDs, Cell Division and Growth

Changes to organ morphology have been widely reported in crops with IQD misexpression (Xiao et al. 2008; Dou et al. 2018; Pan et al. 2017). In some cases, these phenotypes derive from changes to MT organisation and cell growth anisotropy (Bao et al. 2023). However, others are associated with directional changes in cell division driven by some unknown mechanism (Wu et al. 2011). Genetic redundancy within the IQD family, and the paucity of transgenic tools and imaging protocols available for non-model species, make determining the mechanistic basis of these phenotypes challenging. Therefore, *Arabidopsis* models with related phenotypes provide a valuable opportunity to investigate the regulation of morphogenesis by IQDs.

Previous work generated the *1aiqd* mutant, which had thick stems, increased pith cell number and perturbed rib meristem cell division orientation (Mckechnie-Welsh 2021). This thesis builds on this prior work by thoroughly characterising the growth and cell phenotypes of an equivalent mutant to draw stronger causal link between the cell division and growth phenotypes. The increased radial growth of the *1aiqd-2* mutant is restricted to the apical region of the stem, where cells are actively dividing, and misoriented cell divisions generate additional pith cell files that contribute to radial growth (Chapter 2). Moreover, the cell division and stem phenotypes are both complemented by *IQD26* or *IQD27* expression in the inner stem only and the subcellular localisation of these proteins implies that they directly regulate cell division orientation at the PPB or later mitotic stages (Chapter 3). I therefore propose that *IQD26* and *IQD27* regulate cell division in the rib meristem and that disrupted division orientation in the *1aiqd-2* mutant increases stem diameter, via the insertion of new pith cell files.

5.2.1 Implications for organ-level growth control

This hypothesis challenges long-held assumptions about the regulation of stem growth. As far back as the mid-19th century, authors have been theorising how stem growth might be governed by organ-level mechanical forces (Kutschera and Niklas 2007; Thompson

2009). In the stem, the inner tissue layers are predicted to be softer and more extensible than the stiffer outer tissue layers. Since the inner and outer tissues must grow at the same rate, despite differences in extensibility, the outer tissues are placed under tension, while the softer inner tissues are compressed (or, more realistically, less stressed) (Kutschera and Niklas 2007; Thompson 2009). In support of this model, the outer epidermal wall of some plants is substantially thicker (and so probably stiffer) than the internal cell wall (Kutschera and Niklas 2007). More direct evidence comes from computational simulations of growth (Beauzamy et al. 2015; Kierzkowski et al. 2012) and genetic work, where expressing a functional gene copy solely in the epidermis of mutant lines is sufficient to restore wild-type-like growth (Savaldi-Goldstein et al. 2007; Lan et al. 2025).

My results conflict with the theory of epidermal growth control. Expression of *IQD26* or *IQD27* in only the inner tissues of *1aiqd-2* mutants was sufficient to complement the stem growth defects (Chapter 3), implying that the inner tissues can also regulate growth. This conflict might derive in part from the epidermal theory's focus on stem elongation rather than radial growth (Kutschera and Niklas 2007). Furthermore, the validity of epidermal growth control is debated (Peters 2009; Peters and Tomos 2000) and others have argued that there is a theoretical basis for inner tissue cell mechanics having some influence on growth (Thompson 2009). In highlighting the importance of internal tissues for regulating organ growth, my results are consistent with a recent study of anther development (Silveira et al. 2025). Using a combination of experimental and modelling approaches, the authors found that the early stages of anther growth are driven by soft-walled, rapidly expanding inner tissue and that the outward mechanical pressure applied by the inner tissues controls the growth and shape of epidermal cells (Silveira et al. 2025).

Tissue- and cell-layer-specific gene expression have revealed the importance of specific cell layers for regulating growth, cell division and cell signalling in roots and SAMs (Lan et al. 2025; Fridman et al. 2021; Savaldi-Goldstein et al. 2007; Hacham et al. 2011; Ackerman-Lavert et al. 2021). I have identified a suite of promoters that express only in specific stem tissues: *proIQD26* expresses in all tissues except the vascular bundles, *proIQD27* is pith-specific, *proIQD25* is excluded from the epidermis and cortex and *proIQD24* is only expressed in the vascular bundles (Chapter 3). These could be used to drive layer-specific expression of different genes to investigate the relative importance of different stem layers on morphogenesis. To specifically investigate cell division orientation, the *trm678* mutant background could be used (Schaefer et al. 2017), since I

have shown that it has altered stem morphogenesis and cell division orientation defects in all layers of the stem and SAM. Cell-layer specific expression of *TRM7* in *trm678* could reveal the effects of restoring cell division orientation in specific tissues and cell layers.

5.2.2 Implications for growth mechanics

While my model of cell division-driven stem growth is consistent with the data, it raises questions about the mechanics of growth in the *1aiqd-2* mutant. Plant cell growth is the increase in volume that occurs when the cell's walls deform irreversibly due to mechanical stress. The rate at which cell walls deform, where they deform (in the spatial context of an individual cell, a tissue or an organism) and in what direction they deform largely underpins the diversity of plant growth and form. By extension, tissue and organ growth are also an increase in volume – the sum of the volume increases in individual cells. If we consider the plant as a purely mechanical system, subdividing that organ volume more in one direction by inserting cell walls does not drive growth. In fact, it might be expected to decrease growth in that direction because there will be more wall area to mechanically resist growth. Therefore, in a scenario of increased directional cell divisions, like the *1aiqd-2* rib meristem, there needs to be some factor that is driving the growth.

The primary mechanical properties of a cell wall are its stiffness (resistance to mechanical forces) and extensibility (the ability of the wall to deform) (Cosgrove 2016; 2024). These properties determine how cell wall growth responds to mechanical stress. Computational modelling in the root meristem indicates that tissue-specific cell wall stiffening regulates radial growth (Fridman et al. 2021). Therefore, could the *1aiqd-2* mutant have altered cell wall stiffness in the pith cells? Connections between IQDs and cell wall structure have been found: IQDs regulate cMT organisation, which affects the direction and efficiency of cellulose microfibril deposition (Yang et al. 2021). Cellulose is the stiffest of the cell wall polysaccharides and so the amount of cellulose deposition and the orientation of the microfibrils affects both wall stiffness and extensibility (Cosgrove 2024). No links between IQDs and de novo cell wall biosynthesis have yet been identified, although several, including IQD26, localise to the cell plate (Kumari et al. 2021) and mutations in de novo wall biosynthesis affect whole organ mechanics, size and shape (Lan et al. 2025). It's therefore plausible that the 1A IQDs could directly regulate wall composition and biomechanics.

Alternatively, changes to cell wall biomechanics could derive from the changes in cell division orientation. There is some evidence to suggest that new cell walls have different mechanical properties than older walls (Bonfanti et al. 2023), although it is unclear how

widespread this phenomenon is across different tissue types. The rib meristem of *1aiqd-2* must be enriched in young radial cell walls, whereas in the wild type, most radial walls are old since new cell walls are almost always places transversely. If the young walls are less stiff or more extensible, or if radial cell divisions trigger cMT rearrangements that affect remodelling of all the radial walls, this could explain the increased growth.

Cell wall mechanics are very difficult to measure in internal tissues, although differences in cell wall geometry and chemical composition could be measured to infer some mechanical properties. Therefore, studies that explore the mechanical interactions between cell layers rely on computational modelling – by fitting a model to experimental data, one can make inferences about cell and layer mechanical properties. (Fridman et al. 2021; Silveira et al. 2025). A model of the growing rib meristem could be used to simulate how changes in division orientation might drive growth and test how this depends on the mechanical properties of rib meristem cell walls.

5.3 Conclusion

It takes a web of interconnected biological processes to build an organism. I have demonstrated the IQD26 is one node in that web, regulating growth through cell division orientation. How exactly IQD26 fits into this web, and how it is connected to other morphogenetic processes like hormone signalling and mechanics, remains to be discovered. Further work on IQD26 and its relatives will uncover the precise roles they play and thereby shed light on some of the remaining mysteries in morphogenesis.

6 MATERIALS AND METHODS

6.1 GROWTH CONDITIONS

Plants were grown on Levington F2 compost with 10% grit and grown under long day illumination (16 hr light: 8 hr dark) at 20 °C. If no screening or selection steps were required, seeds were stratified on damp filter paper, in the dark at 4 °C for 2-4 d, then transferred to compost. If prior screening was required, the seeds were first sterilised. If seeds had been collected following floral dip, they were treated with 70% EtOH for 1-2 mins, then 5 mins in 5% sodium hypochlorite soln., followed by 3 washes in dH_2O. Otherwise, seeds were treated with 70% EtOH for 5 mins and then deposited on sterile filter paper inside a laminar flow hood, to allow the residual EtOH to evaporate. Seeds were then plated on half-strength Murashige and Skoog medium (Duchefa Biochemie) with 0.9% agarose (Melford Biolaboratories Ltd). Plates were stratified in the dark at 4 °C for 2-4 d and then transferred to 16 h light: 8 h dark, 20 °C. If required, hygromycin selection was carried out according to a published protocol (Harrison et al. 2006). Seedlings were grown on plates for 1-2 w before transfer to compost. FASTred seeds and seedlings expressing fluorescent proteins were screened using a Leica MZFLIII stereo microscope with coolLED illumination system before being sown or transferred to compost, respectively.

6.2 PLANT MATERIAL

Arabidopsis thaliana Columbia-0 (Col-0) was used as the wild type and all transgenic lines were constructed in the Col-0 ecotype. The RFP-TUA5 line was obtained from Dr Jordi Chan, John Innes Centre, originally received from Dr David Ehrhardt (Gutierrez et al. 2009). The *trm678* mutant (Schaefer et al. 2017) was received from Martine Pastuglia and David Bouchez (Université Paris-Saclay, INRAE, Institute Jean-Pierre Bourgin for Plant Sciences, Versailles, France). The original *iqd222324252627* sextuple mutant (*1aiqd)* was provided by Emma Mckechnie-Welsh (previously of the Sablowski lab, John Innes Centre) and contained the following alleles: *iqd22-1* (SALK 103903.55.75.x), *iqd23-2* (SALK_073090), *iqd25-1* (SALK_058876.25.70.x), *iqd26-3* (GK-728F02) and *iqd27-2* (SALK_103602.28.55.X) (lines originally supplied by Katharina Bürstenbinder, Leibniz Institute for Plant Biochemistry, Halle) and an *iqd24* mutation generated by CRISPR-Cas9 mutagenesis (Mckechnie-Welsh 2021). The new *iqd22.23.24.25.26.27* sextuple mutant (*1aiqd-2)* was generated by CRISPR Cas-9 mutagenesis of *IQD22* and *IQD26* in the *iqd23.24.27*

background (see Section 2.2.1). This was crossed to the *1aiqd* mutant to introduce the *iqd25-1* allele. The final homozygous *1aiqd-2* genotype (*iqd23-2, iqd25-1, iqd27-2, iqd24, iqd22-5, iqd26-4*) was obtained following several rounds of selfing and genotyping.

6.3 Cloning and Plant Transformation

DNA fragments for cloning were amplified by PCR using Q5 Polymerase (NEB) or Phusion HF Polymerase (NEB), according to the manufacturer's instructions. PCR bands were analysed by gel electrophoresis, cut out and purified using the NucleoSpin Gel and PCR Clean-up kit (Macherey-Nagel). The purified fragments were used in plasmid assembly reactions as described below. Gene identifiers, templates and other clone information are listed in Appendix 2,

Table 3. Primer sequences are listed in Appendix 2, **Table 5**.

6.3.1 CRISPR-Cas9 mutagenesis

Construction of binary T-DNAs for CRISPR-Cas9-induced gene editing of *IQD26* and *IQD22* was carried out by adapting a published protocol (Castel et al. 2019). Guide RNAs were designed to target sequences in variable (i.e. not evolutionary conserved) N-terminal regions of the IQD gene sequences, upstream of the IQ67-domain. This was to minimise the risk of off-target edits of other IQD genes, and to maximise disruption of the protein sequence. A pair of gRNAs targeting exon 1 of *IQD26* were designed using an online gRNA design tool (https://www.atum.bio/eCommerce/cas9/input). This tool gives gRNAs a score based on predicted off-target effects. The gRNAs selected has scores of 100 (the best possible score), indicating low off-target activity. Each sgRNA was introduced into an sgRNA scaffold, flanked by *Bsa*I restriction sites, by amplifying vector piCSL70001 (Addgene #46966) using Phusion HF Polymerase (New England Biosciences, NEB) and the following primers:

IQD26 Target site #1

Forward: tgtggtctcaATTGACAGAACAAACACGCGATTGgttttagagctagaaatagcaag

IQD26 Target site #2

Forward: tgtggtctcaATTGTGAGCCAGACGGAGTCAGCTgttttagagctagaaatagcaag

The gRNAs targeting *IQD22* were designed, cloned and transformed into *Arabidopsis* by Emma Mckechnie-Welsh. To check for possible off-target effects, I queried the target sequences against the TAIR10 *Arabidopsis* genome using https://beta.ensembl.org/blast/.

In both cases, only the target sites had an exact matching sequence (E-values of 0.02) . For target site #1, all other hits matched a maximum of 17 nucleotides out of 20 and had E-values >=0.3, indicating much low similarity overall. Target site #2 had a strong match to a region on chromosome 4 (matched 17 out of 18 nucleotides, E-value < 0.09). This site is situated within the first intron of *MYB3R2* on chromosome 4, approximately 11.8 Mb upstream of *IQD22*. Since only one of the gRNAs might target this region, and it is a non-coding region, any off-target effects would be unlikely to have phenotypic consequences. Furthermore, the CRISPR-edited plant line was crossed to the *1aiqd-1* mutant (to introduce the *iqd25* mutation into the line), meaning that off-target mutations would likely have been segregated out (note that the distance between the loci is approximately 59 cMs (Copenhaver et al. 1998), so the two loci are not genetically linked).

IQD22 Target site #1

Forward: tgtggtctcaATTGGACGATTGGTGGTGAGACGGgttttagagctagaaatagcaag

IQD22 Target site #2

Forward: tgtggtctcaATTGGCCGATGTGGGAGGATGAgttttagagctagaaatagcaag

Reverse primer for all target sites: tgtggtctcaAGCGTAATGCCAACTTTGTAC

Key: *Bsa*I recognition sequence *Bsa*I cut site sgRNA target

The sgRNAs were designed so that successful CRISPR-Cas9 editing at both target sites could cause a deletion for 40-60 bp that would be easily detectable by gel electrophoresis.

sgRNA expression cassettes were generated by level 1 Golden Gate assembly. Each sgRNA was combined with the AtU6-26 promoter (carried by vector pICSL90002 (Castel et al. 2019)) in a Level 1 acceptor plasmid (piCH47751, AddGene #48002 and piCH47761 AddGene #48003) via restriction-ligation reaction with *Bsa*I-HF (NEB). The resulting plasmids were combined in a level 2 Golden Gate assembly reaction (using *Bpi*I, Thermo Scientific) with the following modules: FASTred Selection marker (Shimada et al. 2010) (pOLE1:OLE1-RFP:OLE1t, vector pICSL11015), Cas9 (proYAO:Cas9:E9, vector BCJJ345 (Castel et al. 2019)), end-linker (pICH50900, AddGene #48047) and the accepting vector (pAGM8031, AddGene #48037). The plasmids were stably transformed into *A. thaliana* by floral dip (Clough and Bent 1998).

FASTred-positive T1 plants were screened for the presence of CRISPR-Cas9-induced indels and selfed. Two approaches were used for screening. The first involved amplifying a region containing the gRNA target sites and detecting indels by band separation in gel electrophoresis, however this approach was too low resolution detect small CRISPR-Cas9 edits in *IQD26*. To detect these alleles, Derived Cleaved Amplified Polymorphic Sequences (dCAPS) was used. PCR products were amplified using a reverse primer that introduced a single base mutation, generating a *Hinf*I recognition site in target site #2. An existing a *Hinf*I site was present in target site #1. After the initial PCR reaction was complete, 2 µL of *Hinf*I enzyme (Invitrogen) was added to each 25 µL reaction and the reactions were incubated at 37 °C for 2 h and then analysed by agarose gel electrophoresis using a 2.5% (w/v) agarose gel. This identified several small deletions in *IQD26* at target site #1 only. No alleles with edits at target site #2 were recovered.

The *iqd22/ iqd26* alleles of T2 progeny that were FASTred negative (i.e. lacking Cas9) were amplified and sequenced by sanger sequencing. Cas9 was segregated out at the earliest opportunity to minimise the risk of off-target edits.

The following plasmids were supplied by The Sainsbury Laboratory (TSL) Synthetic Biology Service: piCH47751, piCH47761, pICSL90002, pICSL11015, pAGM8031

6.3.2 Heat shock-inducible GFP

proAtHSP18.2:Cre recombinase:terNOS and *pro35S*:lox*P:CFP*:lox*P:GFP:terActin* were amplified from published constructs (Sieburth et al. 1998; Bencivenga et al. 2016) and inserted into level 1 Golden Gate vectors (pICH47751, AddGene #48002 and pICH47742 , AddGene #48001, respectively) using a restriction-ligation reaction containing *Bsa*I-HF (NEB). The 140bp second intron of the *AtHSP101* gene was PCR amplified from Col-0 gDNA and inserted between base 432 and 433 of the Cre recombinase CDS using NEBuilder® HiFi DNA Assembly (NEB). This prevented Cre recombinase expression and *lox*P recombination occurring in *E. coli* during the next cloning step. The level 1 constructs were assembled into a level 2 Golden Gate vector (pICL4723, AddGene #48015) with a FASTred plant selection cassette (pICSL11015), and end linker (pICH41766, pELE-3 AddGene #48018) using a restriction-ligation reaction, containing *Bpi*I (Thermo Scientific). Transgenic plants were generated by floral dip into Col-0 and *1aiqd-2*. Hemizygous stock was maintained by back-crossing to the parental line.

The following plasmids were supplied by TSL Synthetic Biology Service: pICH47751, pICH47742, pICL4723, pICSL11015

6.3.3 proIQD:IQD-YFP, proIQD:GUS and proUBQ10:IQD26-YFP

The promoters and full-length coding regions (i.e. from the start codon, up to but excluding the stop codon and including introns) of *IQD23, IQD25, IQD26,* and *IQD27* were amplified from Col-0 gDNA. For *proIQD23* and *proIQD27*, the genomic region between start codon of the *IQD* gene and the stop (or start, if oppositely oriented) codon of the upstream gene was amplified. For *IQD25* and *IQD26*, this region was impractically large so a 1.4 kb region upstream of *IQD25* (note this is a slightly larger region than a *proIQD25* used previously (Bürstenbinder, Möller, et al. 2017)) and a 2.03 kb region upstream of *IQD26* were amplified. *proIQD23*, *IQD25* full-length gene, *IQD26* full-length gene and *proIQD27* were assembled into Level 0 Golden Gate vectors using NEBuilder® HiFi DNA Assembly (NEB) to remove *Bsa*I restriction enzyme recognition sites. Note that *Bpi*I recognition sites were not removed because level 2 Golden Gate assembly was not required. The level 0 vectors used were pICH41295 (AddGene #47997) for promoters and pICSL01005 (published as pAGM1287, AddGene #47996) for the coding genes. The *IQD24* promoter and CDS were amplified from an existing proIQD24:IQD24-YFP construct generated by Emma Mckechnie-Welsh (Mckechnie-Welsh 2021).

For each fluorescent reporter, the promoter (native or *pUBQ10* (pICSL12015)), gene sequence, C-terminal *YFP* tag (pICSL50005) and *AtHSP18.2* terminator (pICSL60008) were assembled into the level 1 Golden Gate vector (pICSL86944OD), containing a FASTred plant selection cassette. For the GUS reporters, the promoter, *GUS* gene (with two introns) (pICH7511, AddGene #50327), and AtHSP18.2 terminator were similarly assembled into pICSL86944OD. The components were assembled using a restriction-ligation reaction, containing *Bsa*I-HF (NEB).

Transgenic plants were generated by floral dip into Col-0, *1aiqd-2* and *trm678*. T1 seed was screened for FASTred fluorescence. Mature plant tissues were screened for YFP fluorescence or GUS expression. A minimum of 5 independent primary transformants (T1 generation) were screened for GUS expression/ fluorescence and selfed to generate T2 segregating seed. In all cases, patterns of expression were broadly consistent among independent T1 plants, with differences only in the level of GUS/ YFP expression. If there were conspicuous differences in expression levels, lines representative of this variation were selected for detailed experimentation. To generate lines that were used for phenotyping (*proIQD26:IQD26-YFP/1aiqd-2*, *proIQD27:IQD26-YFP/1aiqd-2, proIQD27:IQD27-YFP/1aiqd-2* and *proUBQ10:IQD26-YFP/trm678*), a minimum of three T1 plants were crossed to the untransformed parent line to generate hemizygous lines.

Single T-DNA copy number was determined by an approximately 50:50 ratio of FASTred segregation in the progeny of the cross. This approach was used because it generated lines with consistent T-DNA copy number in fewer generations that it took to generate homozygous T3 lines.

The level 1 *proIQD26:IQD26-YFP* module generated as described above, was not compatible with assembly into a level 2 vector because it contained three *Bpi*I recognition sites. To make a level 2 plasmid containing *proIQD26:IQD26-YFP* and mCherry-MBD, *proIQD26:IQD26-YFP:terHSP18.2* was first amplified from the Level 1 plasmid in four fragments to remove the *Bpi*I sites. These were assembled with a hygromycin-resistance selection cassette (pICSL11059), mCherry-MBD and an end-linker (pICH41766, pELE-3 AddGene #48018) into the level 2 vector pICSL4723 (AddGene #48015) via restriction-ligation using *Bpi*I. Transgenic plants were generated by floral dip into *trm678*.

The following plasmids were supplied by TSL Synthetic Biology Service: pICH41295, pICSL01005, pICSL12015, pICSL50005, pICSL60008, pICSL86944OD, pICH751, pICSL11059, pICH41766, pICSL4723.

6.3.4 Microtubule reporter

The MAP4 MBD was amplified from plasmid DNA. It was amplified in two fragments to remove a *Bsa*I recognition site. These fragments were assembled with the UBQ10 promoter (pICSL13005), N-terminal mCherry tag (pICSL30003, AddGene #50304), and AtHSP18.2 terminator (pICSL60008) into the level 1 Golden Gate vector (pICH47811, AddGene #48008. The resulting level 1 module was assembled with a gentamycin-resistance selection cassette and end linker (pICH41744, pELE-2 AddGene #48017) into the level 2 vector pICSL4723 (AddGene #48015). Transgenic plants were generated by floral dip into Col-0 and *1aiqd-2*.

The following plasmids were supplied by TSL Synthetic Biology Service: pICSL30003, pICH47811, pICH41744, pICSL4723 and pICSL60008

6.3.5 Yeast-2-Hybrid

The CDSs of *IQD26*, *MPK6*, *AUR1*, *TRM7* and *CAM7* were amplified from col-0 cDNA and assembled into the level 1 Golden Gate vectors pGADT7-ΔBsa1 and pGBKT7-ΔBsa1 via a restriction-ligation reaction. This generated GAL4 AD and GAL4 DBD fusions, respectively. pGADT7-ΔBsa1 and pGBKT7-ΔBsa1 were supplied by TSL Synthetic Biology Service

6.4 GENOTYPING

6.4.1 gDNA extraction

gDNA extraction protocol was adapted from a published protocol (Edwards et al. 1991). Tissue approximately equivalent to a 5 mm-diameter leaf disk was harvested into a 2 mL microfuge tube containing a ~2.5 mm metal ball. Tissue was ground by shaking the tubes for 1 min at 50 oscillations/s in a TissueLyser LT (QIAGEN). 400 µL of extraction buffer (200 mM Tris-HCl pH 8.0, 250 mM NaCl, 25 mM EDTA pH 8.0, 0.5 % SDS) was added to each tube and they were then centrifuged at 4000 g for 15 min. 250 µL of supernatant was mixed with 250 µL isopropanol in a fresh tube and the tubes were then chilled at -20 °C for 20-60 min. The precipitated DNA was pelleted by centrifugation at 4000 g for 10 min and the supernatant removed. Pellets were washed with 70 % EtOH and centrifuged at 4000 g for 5 min. The EtOH was removed and the pellets left to air dry for 30 min. The pellets were resuspended in 50-100 µL diH_2O.

6.4.2 Taq PCR for genotyping

T-DNA insertions and CRISPR-Cas9-induced mutations were genotyped using Taq DNA Polymerase (Qiagen). Reactions were carried out according to the manufacturer's instructions. Thermocycling conditions were adapted to each reaction, following manufacturer's recommendations, and annealing temperatures were calculated using the NEB Tm Calculator (https://tmcalculator.neb.com/#!/main). Products of the PCRs were analysed by agarose gel electrophoresis on a 1% (w/v) agarose gel. Primer combinations used for genotyping are listed in Appendix 2, **Table 4** and primer sequences are listed in Appendix 2, **Table 5**.

To genotype the very small deletion mutations of the *iqd22-5* and *iqd26-4,* restriction digestion was used. The *iqd22-5* mutation interrupts a *Bts*CI restriction site. This allele was genotyped by amplifying a 315 bp amplicon in a 25 µL reaction and then incubating with 6.7 units *Bts*CI (NEB) at 50 °C for at least 1 hr (the *Bts*CI enzyme was added directly to PCR reaction mixture without clean-up). The amplicon generated from the *iqd22-5* allele resisted digestion, whereas the wild type amplicon was digested into a 140bp product and a 175bp product. Products of the restriction digest were analysed by agarose gel electrophoresis on a 1% (w/v) agarose gel.

To genotype *iqd26-4,* a dCAPS approach was used. The reverse primer was designed to introduce a *Sac*I restriction site in amplicons generated from the *iqd26-4* allele but not the wild type allele. Following PCR amplification in a 25 µL reaction, 6.7 units *Sac*I-HF (NEB)

were added directly to the reaction mixture and this was incubated at 37 °C for at least 1 hr. The product amplified from the *iqd26-4* allele was digested into two products of sizes 21 bp and 205 bp. The products of the restriction digest were analysed by agarose gel electrophoresis. A 2.5% (w/v) agarose gel was used to enable discrimination of the 226 bp wild type and 205 *iqd26-4* bands.

6.4.3 DNA sequencing

High fidelity (HF) polymerases were used to amplify sequences for sanger sequencing. Q5 Polymerase (NEB) or Phusion HF Polymerase (NEB) were used according to the manufacturer's instructions. Reactions were run on an agarose gel and the DNA was extracted using the NucleoSpin Gel and PCR Clean-up kit (Macherey-Nagel). For plasmid sequencing, plasmid DNA was purified from 4 mL of overnight culture using the Nucleospin Plasmid kit (Macherey-Nagel). Sanger sequencing was carried out by Source BioScience. Whole plasmid sequencing was carried out by Plasmidsaurus Inc.

6.5 Stem Growth Phenotyping

For all phenotyping experiments, different genotypes were systematically distributed across all trays. Plants were labelled with unique numbers to avoid bias in data collection and downstream image analysis.

6.5.1 Measurement of growth post-flowering

Col-0 and *1aiqd-2* plants and were grown in 8 cm pots. On the day when the first floral organ abscission was observed, ink marks were placed on the stem at 2 mm intervals and the plant was photographed next to a ruler using a Nikon D3100 DSLR camera. Three stem positions (the stem base, where first silique pedicel and first branch meet the stem) were also imaged using a Leica S8AP0 stereo microscope with GXCAM LITE camera. Plants were returned to the controlled environment room for 4 d and then re-photographed. Manual land marking of the stem ink marks was performed using the Point Picker plugin of Fiji (Schindelin et al., 2012). Stem width was measured manually in Fiji. Length of segments and vertical growth were calculated using Python 3.11. Additional data processing, statistical tests and plotting were carried out in RStudio using R version 4.3.2 and the tidyverse (https://www.tidyverse.org/) and rstatix packages. Because the data were not normally distributed, non-parametric Mann-Whitney U tests were calculated using wilcox_test (rstatix package). To reduce the false discovery rate, given the large number of individual pairwise comparisons that were performed, all p values were subsequently corrected using the Benjamini-Hochberg correction (Benjamini and

Hochberg 1995). 95 % confidence intervals for the means of each genotype and the difference between the means were calculated using bootstrapping (MeanCI and MeanDiffCI functions, from the DescTools package)

6.5.2 Measurement of growth pre-flowering

Col-0 and *1aiqd-2* plants and were grown in 8 cm pots. When a stem was approx. 6-7 mm tall (plants were checked twice daily), ink marks were placed on the stem at 1 mm intervals using a uni PIN 0.03 Line Drawing Pen. The plant was photographed and the stem was imaged at all marked positions using the same equipment as described above. This was repeated twice at 2 d intervals. At each time point (day 0, 2, and 4), a portion of stems were cut from their base and dehydrated in an EtOH series (15, 30, 50, 70, 85, 95, 100% EtOH, 15 mins per treatment) for long-term storage and subsequent imaging. Stem measurements, data analysis and plotting were carried out as described above.

6.5.3 Other stem measurements

For static measurement of stem thickness, plants were grown in 15-cell trays. When a stem was approximately 5-6 mm tall, it was excised from the rosette, imaged using a Leica SP8AP0 stereo microscope with GXCAM LITE camera and dehydrated through the EtOH series (as described above). The rosette was also photographed. Stem diameter at set positions from the stem apex was measured manually in Fiji. Statistical analysis and plotting were carried out in RStudio using R version 4.3.2, tidyverse and rstatix packages. Homogeneity of variance was tested with Levene's test and normality was tested with the Shapiro-Wilk test. If the assumptions of homogeneity of variance and normality were both met, one-way ANOVA was used to calculate statistical significance and Tukey HSD post-hoc tests were used for pairwise comparisons if the ANOVA result was statistically significant. If only the assumption of normality was met, Welch's ANOVA was used and post-hoc pairwise comparisons were carried out using the Games Howell test.

6.6 Preparation of Material for Confocal Imaging

Microscope settings are detailed in Appendix 2, **Table 2**.

6.6.1 Imaging of Cre-*lox* sectors

5–6-week-old plants hemizygous for *proHSP18.2:Cre* and *pro35S:loxP:CFP:loxGFP* were heat-shocked by immersing their inflorescence apices in a bath of dH_2O supplemented with 0.05% (v/v) Silwet l-77 (De Sangosse Ltd) at 38.5°C for 75 s. The plants were then returned to standard growth conditions for 10 days. Before imaging, flowers and floral

buds were first removed with fine forceps. The top 1.5 cm was of the stem was excised, immersed in dH_2O, and longitudinal sections were cut with a razor. The sections were mounted as follows. Two 25 mm x 2 mm strips of 0.5 mm-thick polytetrafluoroethylene (PTFE) sheet were stuck (using double-sided tape) across the width of a microscope slide, approximately 15 mm apart. Between the PTFE strips, a small well was made using dimethylsiloxane gum (Gelest), and this was filled with perfluorodecalin (Molekula). The sections were placed inside the well and a cover slip was placed over the top. The sections were imaged immediately.

6.6.2 Modified pseudo-Schiff-propidium iodide staining of stem apices

For measurement of cell wall orientation and SAM morphology, modified pseudo-Schiff-propidium iodide (mPS-PI) staining was used. In preparation for mPS-PI staining, shoot primary apices were dissected by eye, using fine forceps to remove buds larger than 0.5 mm. The top 1 cm of the dissected stem was excised and deposited in 15% EtOH. The apices were dehydrated by successive 15 min treatments in 15%, 30%, 50%, 70%, 85%, 95%, and 100% EtOH. Apices were stored in 100% EtOH at -20 °C at least overnight, and up to a few months. The apices were partially rehydrated through the same EtOH series until 70% EtOH. The apices were then further dissected in 70% EtOH using a 0.33 mm (29 G) insulin needle to remove as many buds as possible without damaging the meristem. The top 2-3 mm of each apex was excised, further rehydrated through 15 min treatments of 50%, 30% and 15% EtOH and then washed twice with diH_2O. mPS-PI staining and specimen mounting was then carried out as described previously (Schiessl et al. 2012). The specimens were imaged 1-7 d after mounting.

6.6.3 Imaging of IQD-YFP reporters in the SAM

Primary inflorescence apices of 5-6-week-old plants were dissected by eye, using fine forceps to remove buds larger than 0.5 mm. The top 1 cm of the dissected stem was excised ~1.5cm below the meristem and transferred to a 5 cm diameter petri dish containing solidified 2% (w/v) agarose gel and immersed in diH_2O. Further dissection was carried out using a 0.33 mm (29 G) insulin needle until the meristem surface was fully exposed. If PI staining was used, the meristems were stained in 25 µg/mL PI solution (Merck Life Science UK Ltd) for ~45 mins then washed in diH_2O. The stem apices were transferred back to the 2% agarose gel, immersed in diH_2O and imaged. Following image acquisition, fluorescence intensity profiles were generated in Fiji using the Multi-channel Plot Tool from the Visualization Toolset (https://github.com/kwolbachia/Visualization_toolset).

6.6.4 PI-stained root meristems

Seeds were sterilised and sown on growth medium as described in section 6.1. 7 d after germination, the seedlings were stained in 10 µg/mL PI solution (Merck Life Science UK Ltd) for 10 mins then washed twice in diH_2O. The seedlings were mounted on slides in diH_2O and a coverslip placed over the top, attached by four dots of vacuum grease (DuPont).

6.6.5 Time-lapse imaging of root meristem cells

Seeds were sterilised and sown on growth medium as described in section 6.1. 6-7 d after germination, seedlings were transferred to imaging chambers. The chambers were constructed as previously described (Kirchhelle and Moore 2017), although using strips of 1.5 mm PTFE as spacers (rather than strips of glass microscope slide). The chambers were stored horizontally to limit spreading of dimethylsiloxane gum (Gelest) and flipped every ~30 mins to prevent gravitropic bending of the roots. Imaging commenced approximately 2 hrs after the seedlings were transferred to the chambers and the roots were imaged at approx. 25 min intervals. Following image acquisition, fluorescence intensity profiles were generated in Fiji using the Multi-channel Plot Tool from the Visualization Toolset (https://github.com/kwolbachia/Visualization_toolset).

6.6.6 Calcofluor-white staining of leaf and stem tissue

Fully expanded rosette leaves of ~6-week-old plants were hand-sectioned in diH_2O using a razor blade. Plant stems (prepared as described in section 6.5.2) were hand-sectioned in 70% EtOH approx. 4 mm from the stem apex and then rehydrated through an EtOH series and washed twice in diH_2O. The sections were stained in a 0.02% solution of calcofluor white (fluorescent brightener 28, Sigma-Aldrich) for 5 mins, washed twice with diH_2O. The sections were mounted in diH_2O and imaged.

6.7 GUS STAINING

GUS staining was carried out as previously described (Sieburth et al. 1998) with slight modifications. Sample tissues were fixed by incubation in 90% acetone, on ice, for 15 to 20 min. The acetone was replaced with washing buffer (50 mM $NaPO_4$ pH 7, 2 mM $K_3Fe(CN)_6$, and 2 mM $K_4Fe(CN)_6.3H_2O$, 0.2% Triton X-100) and the tissues were vacuum infiltrated or 2-5 mins. The wash buffer was replaced with GUS staining buffer (the washing buffer supplemented with 1 mM X-GlcA (5-Bromo-4-chloro-3-indolyl-β-D-glucuronic acid), Melford Biolaboratories Ltd). The tissues were incubated in the dark at 37 °C for 4 hrs, 6 hrs or overnight. After staining, the tissue was processed through an

ethanol series (15, 30, 50, 70, 85, 95, and 100%) and left in 100% EtOH overnight. The tissues were then rehydrated through the reverse EtOH series up to 70% EtOH for imaging and long-term storage. Imaging of GUS staining patterns was performed using a Leica MZFLIII stereo microscope with GXCAM LITE camera or Nikon Eclipse E600 microscope with a GXCAM HiChrome-HR4 HS camera

6.8 Yeast-2-Hybrid Assay

Yeast (*Saccharomyces cerevisiae*) was co-transformed with bait and prey vectors using the LiAc method (Gietz et al. 1992). The yeast colonies were preselected on vector-selective media (-tryptophan, -leucine). For the interaction assays, yeast cultures were spotted on interaction-selective media (-tryptophan/−histidine/-leucine) and interaction was estimated after 3 d incubation at 30 °C. As a control, the same colonies were spotted onto vector-selective media. Three independent colonies were used to test each interaction.

6.9 Motif Prediction, Multiple Sequence Alignment and In Silico Expression Analysis

Protein sequence motifs were detected using Multiple Em for motif elucidation (https://memesuite.org/meme/tools/meme) (Bailey and Elkan 1994), using the following parameters: Motif Site Distribution, ANR: Any number of sites per sequence; Objective Function, E-value of product of p-values; Starting Point Function, E-value of product of p-values; Site Strand Handling, This alphabet only has one strand; Maximum Number of Motifs, 7; Motif E-value Threshold, no limit; Minimum Motif Width, 6; Maximum Motif Width, 70; Minimum Sites per Motif, 2; Maximum Sites per Motif, 35. The analysed protein sequences were AT1G51960.1, AT3G16490.1, AT4G23060.1, AT4G29150.1, AT5G07240.1, AT5G62070.1, AT1G72670.1 obtained from https://www.arabidopsis.org/.

The multiple sequence alignment (MSA) was performed on Clustal Omega program (Clustal O(1.2.4)) at https://www.ebi.ac.uk/Tools/msa/clustalo/, using the default parameters (Sievers et al. 2011; Madeira et al. 2024; Goujon et al. 2010). The analysed protein sequences were AT1G51960.1, AT3G16490.1, AT4G23060.1, AT4G29150.1, AT5G07240.1, AT5G62070.1 obtained from https://www.arabidopsis.org/. The default parameters for MSA were used. They were as follows: Output format, ClustalW with character counts; Dealign input, no; MBED-like Clustering guide-tree, yes; MBED-like clustering iteration, yes; Combined iterations, default(0); Max guide tree, default; Max

HMM iterations, default; order, aligned; distance matrix, no; output guide tree, yes. A color-coded figure of protein sequence alignment was generated with ESPript 3.0 (https://espript.ibcp.fr/ESPript/cgi-bin/ESPript.cgi) (Robert and Gouet 2014).

In silico expression analysis of *IQD26* was carried out using the Arabidopsis Coexpression Tool (ACT) Version 2.6 (https://www.michalopoulos.net/act2.6/) (Zogopoulos et al. 2025). The full list of genes significantly co-expressed with IQD26 is given in Appendix 1, **Table 1**.

6.10 Protein Structure Prediction

Protein structure predictions for IQD22-26 were accessed from the AlphaFold protein database (https://alphafold.ebi.ac.uk/) (Fleming et al. 2025; Jumper et al. 2021). Modelling of IQD26-protein complexes was carried out using the AlphaFold2_batch notebook from ColabFold v1.5.5 (Mirdita et al. 2022). The number of recycles used was 12 or 24, but otherwise the default settings were used. Plotting was carried out using RStudio and R version 4.3.2

6.11 Quantification of Meristem Size, Division Plane Orientation and Cell Geometry

Quantification of meristem size, division plane orientation and cell geometry was carried out using custom python scripts and Fiji macros that were adapted and extended from previously published analysis pipelines (Bencivenga et al. 2016; Serrano-Mislata et al. 2017). Fiji was used to visualise and interact with processed images. The landmarks_3D.ijm macro (Serrano-Mislata et al. 2017) was used to select landmarks for meristem size.

6.11.1 Extraction of geometric properties using python

Python scripts were executed in Python 3.11. The scripts had the following dependencies: Numerical Python (http://www.numpy.org), Scientific Python (http://www.scipy.org), matplotlib (http://matplotlib.org) and SimpleITK (http://www.simpleitk.org) and napari (https://napari.org/).

The following scripts were used as previously described, with minor changes (including updating them to Python 3): double_watershed_segmentation.py, cell_data_table.py, cell_layers.py, cell_layers.py, meristem_area.py, rib_zone.py, new_walls.py, cell_wall_orientation.py, bud_analysis_lib.py (Serrano-Mislata et al. 2017; Bencivenga et

al. 2016). Additional scripts developed specifically for this analysis are summarised below:

select_conical_ROI.py Defines a conical region centered on the image's main axis and selects objects which have their centre of mass inside this region. The conical region is defined by the following parameters: starting and ending distance to meristem apex, starting radius, rate of radius increase as a function of distance to apex. The script's outputs include two labelled 3D image stacks: one of the new cell walls that fall inside the conical ROI and one of the segmented cells within the ROI. The parameters that define the region are modified to optimally capture the rib meristem region. Subsequent manual correction steps ensure accuracy. A companion Fiji macro *check_rz_roi.ijm* can be used to rapidly check how effectively the rib meristem was captured by displaying the original confocal image merged with the image of segmented cells within the ROI.

correct_new_wall_identification.py Opens a napari image viewer that displays the original 3D confocal image, labelled cell walls image, and the rib meristem new cell walls image (output of select_conical_ROI.py). The user can manually add, merge and delete rib meristem new cell walls to correct errors in the automatic wall detection (output of *new_walls.py*) or errors in rib meristem boundary selection (output of *select_conical_ROI.py*) and save the corrected image.

correct_new_wall_identification_partII.py Quantifies the properties of the rib meristem new cell walls. Calculates the orientation of each new wall in relation to the image main axis: the angle between the given vector for the image main axis and the vector normal to plane best fitting the wall. Heat map images are produced in which the new walls are given values proportional to the angles to the main axis. Adapted from *cell_wall_orientation.py* (Bencivenga et al. 2016).

select_RZ_slices.py Rotates and centres the segmented cell image so that the main axis of the meristem is aligned with the z axis and positioned at the centre of the 3D image stack. It then isolates the xy slice of the array that is situated a specified vertical distance (60 µm and 100 µm were used in this study) from the meristem apex. It identifies all the cells that both overlap this slice and have centroids situated within a specified radius of the main axis (to capture only the rib meristem cells). A 3D image array is produced containing only these cells.

correct_RZ_slices.py Opens a napari image viewer that displays the centred, rotated confocal image, segmented cell images, and the image of rib meristem cells that are

situated a specified distance from the apex. The user can manually add, merge and delete rib meristem cells to correct segmentation errors or errors in rib meristem boundary selection (i.e. if the radius set in *select_RZ_slices.py* was too broad or narrow). The corrected image is saved.

RZ_slice_quantification.py From the corrected image of RZ cells (outputted by *correct_RZ_slices.py*), calculates the area occupied by the RZ, the number of cells and quantifies the geometric properties of the cells (as described in Chapter 2, fig. 16).

cell_geometry_heat_maps.py Produces heat map images in which the segmented cells are given values proportional to geometric properties

6.11.2 Statistical analysis and plotting using R

Statistical analysis and graph plotting was carried out in RStudio using R version 4.3.2 and the tidyverse package. Meristem sizes were compared using the Mann Whitney U test (using wilcox_test from the rstatix package). Means and 95% CIs for meristem size, rib meristem cell number and rib meristem cell area were calculated using the bootstrap method (using MeanCI from the DescTools package). To compare the distributions of cell geometric properties, the Anderson-Darling test was performed (using ad.test from the kSamples package). If this was statistically significant and more than two groups were being compared, an Anderson-Darling all pairs comparison test was performed (using adAllPairsTest from the PMCMRplus package). To statistically compare average cell geometric characteristics, Kruskal_Wallace tests were performed (using kruskal.test from the stats package). If this was statistically significant, post-hoc pairwise Wilcox tests were performed (pairwise_wilcox_test from the rstatix package) using the Holm method for p value adjustment. To statistically compare cell wall angle deviation, cell wall angles > 45° were counted for each meristem. These data were then fitted to a Poisson generalised linear model, with genotype as the predictor, using the glm() function in R. The fitted rates and asymptotic upper and lower confidence levels were back-transformed to derive means and confidence intervals for plotting. In all cases genotype was found to significantly predict the proportion of cell wall angles >45. If more than one genotype was significantly different from the wild type , a Tukey post hoc test was performed using pairs() and emmeans() from the emmeans package.

BIBLIOGRAPHY

Abel, Steffen, Katharina Bürstenbinder, and Jens Müller. 2013. “The Emerging Function of IQD Proteins as Scaffolds in Cellular Signaling and Trafficking.” *Plant Signaling & Behavior* 8 (6): e24369. https://doi.org/10.4161/psb.24369.

Abel, Steffen, Tatyana Savchenko, and Maggie Levy. 2005. “Genome-Wide Comparative Analysis of the IQD Gene Families in Arabidopsis Thaliana and Oryza Sativa.” *BMC Evolutionary Biology* 5 (1): 72. https://doi.org/10.1186/1471-2148-5-72.

Abramson, Josh, Jonas Adler, Jack Dunger, et al. 2024. “Accurate Structure Prediction of Biomolecular Interactions with AlphaFold 3.” *Nature* 630 (8016): 493–500. https://doi.org/10.1038/s41586-024-07487-w.

Ackerman-Lavert, M., Y. Fridman, R. Matosevich, et al. 2021. “Auxin Requirements for a Meristematic State in Roots Depend on a Dual Brassinosteroid Function.” *Current Biology* 31 (20): 4462-4472.e6. https://doi.org/10.1016/j.cub.2021.07.075.

Aichinger, Ernst, Noortje Kornet, Thomas Friedrich, and Thomas Laux. 2012. “Plant Stem Cell Niches.” *Annual Review of Plant Biology* 63 (Volume 63, 2012): 615–36. https://doi.org/10.1146/annurev-arplant-042811-105555.

Ambrose, J. Christian, and Richard Cyr. 2008. “Mitotic Spindle Organization by the Preprophase Band.” *Molecular Plant* 1 (6): 950–60. https://doi.org/10.1093/mp/ssn054.

Asada, Tetsuhiro. 2019. “Preprophase-Band Positioning in Isolated Tobacco BY-2 Cells: Evidence for a Principal Role of Nucleus-Cell Cortex Interaction in Default Division-Plane Selection.” *Protoplasma* 256 (3): 721–29. https://doi.org/10.1007/s00709-018-01331-5.

Badmi, Raghuram, Raja S. Payyavula, Garima Bali, et al. 2018. “A New Calmodulin-Binding Protein Expresses in the Context of Secondary Cell Wall Biosynthesis and Impacts Biomass Properties in Populus.” *Frontiers in Plant Science* 9. https://www.frontiersin.org/article/10.3389/fpls.2018.01669.

Bailey, T. L., and C. Elkan. 1994. “Fitting a Mixture Model by Expectation Maximization to Discover Motifs in Biopolymers.” *Proceedings. International Conference on Intelligent Systems for Molecular Biology* 2: 28–36.

Bao, Zhiru, Ye Guo, Yaling Deng, et al. 2023. “Microtubule-Associated Protein SlMAP70 Interacts with IQ67-Domain Protein SlIQD21a to Regulate Fruit Shape in Tomato.” *The Plant Cell* 35 (12): 4266–83. https://doi.org/10.1093/plcell/koad231.

Barton, M. K. 2010. “Twenty Years on: The Inner Workings of the Shoot Apical Meristem, a Developmental Dynamo.” *Developmental Biology*, Special Section: Morphogenesis, vol. 341 (1): 95–113. https://doi.org/10.1016/j.ydbio.2009.11.029.

Bayer, Emmanuelle M, Imogen Sparkes, Steffen Vanneste, and Abel Rosado. 2017. “From Shaping Organelles to Signalling Platforms: The Emerging Functions of Plant ER–PM Contact Sites.” *Current Opinion in Plant Biology*, 40 Cell Biology 2017, vol. 40 (December): 89–96. https://doi.org/10.1016/j.pbi.2017.08.006.

Beauzamy, Léna, Marion Louveaux, Olivier Hamant, and Arezki Boudaoud. 2015. "Mechanically, the Shoot Apical Meristem of Arabidopsis Behaves like a Shell Inflated by a Pressure of About 1 MPa." *Frontiers in Plant Science* 6 (November). https://doi.org/10.3389/fpls.2015.01038.

Bencivenga, Stefano, Antonio Serrano-Mislata, Max Bush, Samantha Fox, and Robert Sablowski. 2016. "Control of Oriented Tissue Growth through Repression of Organ Boundary Genes Promotes Stem Morphogenesis." *Developmental Cell* 39 (2): 198–208. https://doi.org/10.1016/j.devcel.2016.08.013.

Benjamini, Yoav, and Yosef Hochberg. 1995. "Controlling the False Discovery Rate: A Practical and Powerful Approach to Multiple Testing." *Journal of the Royal Statistical Society. Series B (Methodological)* 57 (1): 289–300.

Besson, Sébastien, and Jacques Dumais. 2011. "Universal Rule for the Symmetric Division of Plant Cells." *Proceedings of the National Academy of Sciences* 108 (15): 6294–99. https://doi.org/10.1073/pnas.1011866108.

Bi, Lulu, Lin Weng, Zhuyan Jiang, and Han Xiao. 2018. "The Tomato IQD Gene SUN24 Regulates Seed Germination through ABA Signaling Pathway." *Planta* 248 (4): 919–31. https://doi.org/10.1007/s00425-018-2950-6.

Boardman, N. K. 1977. "Comparative Photosynthesis of Sun and Shade Plants." *Annual Review of Plant Biology* 28 (Volume 28, 1977): 355–77. https://doi.org/10.1146/annurev.pp.28.060177.002035.

Bonfanti, Alessandra, Euan Thomas Smithers, Matthieu Bourdon, et al. 2023. "Stiffness Transitions in New Walls Post-Cell Division Differ between Marchantia Polymorpha Gemmae and Arabidopsis Thaliana Leaves." *Proceedings of the National Academy of Sciences* 120 (41): e2302985120. https://doi.org/10.1073/pnas.2302985120.

Boruc, Joanna, Evelien Mylle, Maria Duda, et al. 2010. "Systematic Localization of the Arabidopsis Core Cell Cycle Proteins Reveals Novel Cell Division Complexes." *Plant Physiology* 152 (2): 553–65. https://doi.org/10.1104/pp.109.148643.

Boruc, Joanna, Annika K. Weimer, Virginie Stoppin-Mellet, et al. 2017. "Phosphorylation of MAP65-1 by Arabidopsis Aurora Kinases Is Required for Efficient Cell Cycle Progression." *Plant Physiology* 173 (1): 582–99. https://doi.org/10.1104/pp.16.01602.

Bouchez, David, Magalie Uyttewaal, and Martine Pastuglia. 2024. "Spatiotemporal Regulation of Plant Cell Division." *Current Opinion in Plant Biology* 79 (June): 102530. https://doi.org/10.1016/j.pbi.2024.102530.

Bret, Hélène, Jinmei Gao, Diego Javier Zea, Jessica Andreani, and Raphaël Guerois. 2024. "From Interaction Networks to Interfaces, Scanning Intrinsically Disordered Regions Using AlphaFold2." *Nature Communications* 15 (1): 597. https://doi.org/10.1038/s41467-023-44288-7.

Burda, Isabella, Fridtjof Brauns, Frances K. Clark, Chun-Biu Li, and Adrienne H. K. Roeder. 2024. "Robust Organ Size in Arabidopsis Is Primarily Governed by Cell Growth

Rather than Cell Division Patterns." *Development* 151 (19): dev202531. https://doi.org/10.1242/dev.202531.

Bürstenbinder, Katharina, Dipannita Mitra, and Jakob Quegwer. 2017. "Functions of IQD Proteins as Hubs in Cellular Calcium and Auxin Signaling: A Toolbox for Shape Formation and Tissue-Specification in Plants?" *Plant Signaling & Behavior* 12 (6): e1331198. https://doi.org/10.1080/15592324.2017.1331198.

Bürstenbinder, Katharina, Birgit Möller, Romina Plötner, et al. 2017. "The IQD Family of Calmodulin-Binding Proteins Links Calcium Signaling to Microtubules, Membrane Subdomains, and the Nucleus." *Plant Physiology* 173 (3): 1692–708. https://doi.org/10.1104/pp.16.01743.

Bürstenbinder, Katharina, Tatyana Savchenko, Jens Müller, et al. 2013. "Arabidopsis Calmodulin-Binding Protein IQ67-Domain 1 Localizes to Microtubules and Interacts with Kinesin Light Chain-Related Protein-1 *." *Journal of Biological Chemistry* 288 (3): 1871–82. https://doi.org/10.1074/jbc.M112.396200.

Buschmann, Henrik, Jordi Chan, Luis Sanchez-Pulido, Miguel A. Andrade-Navarro, John H. Doonan, and Clive W. Lloyd. 2006. "Microtubule-Associated AIR9 Recognizes the Cortical Division Site at Preprophase and Cell-Plate Insertion." *Current Biology* 16 (19): 1938–43. https://doi.org/10.1016/j.cub.2006.08.028.

Bush, Max, Vishmita Sethi, and Robert Sablowski. 2022. "A Phloem-Expressed PECTATE LYASE-LIKE Gene Promotes Cambium and Xylem Development." *Frontiers in Plant Science* 13 (April). https://doi.org/10.3389/fpls.2022.888201.

Castel, Baptiste, Laurence Tomlinson, Federica Locci, Ying Yang, and Jonathan D. G. Jones. 2019. "Optimization of T-DNA Architecture for Cas9-Mediated Mutagenesis in Arabidopsis." *PLOS ONE* 14 (1): e0204778. https://doi.org/10.1371/journal.pone.0204778.

Chakrabortty, Bandan, Ikram Blilou, Ben Scheres, and Bela M. Mulder. 2018. "A Computational Framework for Cortical Microtubule Dynamics in Realistically Shaped Plant Cells." *PLOS Computational Biology* 14 (2): e1005959. https://doi.org/10.1371/journal.pcbi.1005959.

Clough, Steven J., and Andrew F. Bent. 1998. "Floral Dip: A Simplified Method for Agrobacterium -Mediated Transformation of Arabidopsis Thaliana." *The Plant Journal* 16 (6): 735–43. https://doi.org/10.1046/j.1365-313x.1998.00343.x.

Coen, Enrico, and Daniel J. Cosgrove. 2023. "The Mechanics of Plant Morphogenesis." *Science* 379 (6631): eade8055. https://doi.org/10.1126/science.ade8055.

Colón-Carmona, Adán, Ratha You, Tal Haimovitch-Gal, and Peter Doerner. 1999. "Spatio-Temporal Analysis of Mitotic Activity with a Labile Cyclin–GUS Fusion Protein." *The Plant Journal* 20 (4): 503–8. https://doi.org/10.1046/j.1365-313x.1999.00620.x.

Copenhaver, Gregory P., William E. Browne, and Daphne Preuss. 1998. "Assaying Genome-Wide Recombination and Centromere Functions with Arabidopsis Tetrads." *Proceedings of the National Academy of Sciences* 95 (1): 247–52. https://doi.org/10.1073/pnas.95.1.247.

Cosgrove, Daniel J. 2016. “Plant Cell Wall Extensibility: Connecting Plant Cell Growth with Cell Wall Structure, Mechanics, and the Action of Wall-Modifying Enzymes.” *Journal of Experimental Botany* 67 (2): 463–76. https://doi.org/10.1093/jxb/erv511.

Cosgrove, Daniel J. 2024. “Structure and Growth of Plant Cell Walls.” *Nature Reviews Molecular Cell Biology* 25 (5): 340–58. https://doi.org/10.1038/s41580-023-00691-y.

Dahiya, Pradeep, and Katharina Bürstenbinder. 2023. “The Making of a Ring: Assembly and Regulation of Microtubule-Associated Proteins during Preprophase Band Formation and Division Plane Set-Up.” *Current Opinion in Plant Biology* 73 (June): 102366. https://doi.org/10.1016/j.pbi.2023.102366.

Dahiya, Pradeep, Samuel Haluška, Jonas Buhl, et al. 2023. “Origin and Evolution of IQD Scaffolds and Assembled Protein Complexes in Plant Cell Division.” SSRN Scholarly Paper No. 4655235. Rochester, NY, December 6. https://doi.org/10.2139/ssrn.4655235.

Davière, Jean-Michel, Michael Wild, Thomas Regnault, et al. 2014. “Class I TCP-DELLA Interactions in Inflorescence Shoot Apex Determine Plant Height.” *Current Biology* 24 (16): 1923–28. https://doi.org/10.1016/j.cub.2014.07.012.

Daxinger, Lucia, Ben Hunter, Mazhar Sheikh, et al. 2008. “Unexpected Silencing Effects from T-DNA Tags in *Arabidopsis*.” *Trends in Plant Science* 13 (1): 4–6. https://doi.org/10.1016/j.tplants.2007.10.007.

Dou, Junling, Shixiang Duan, Muhammad Jawad Umer, et al. 2022. “Genome-Wide Analysis of IQD Proteins and Ectopic Expression of Watermelon ClIQD24 in Tomato Suggests Its Important Role in Regulating Fruit Shape.” *Frontiers in Genetics* 13 (September). https://doi.org/10.3389/fgene.2022.993218.

Dou, Junling, Shengjie Zhao, Xuqiang Lu, et al. 2018. “Genetic Mapping Reveals a Candidate Gene (ClFS1) for Fruit Shape in Watermelon (Citrullus Lanatus L.).” *Theoretical and Applied Genetics* 131 (4): 947–58. https://doi.org/10.1007/s00122-018-3050-5.

Drevensek, Stéphanie, Magali Goussot, Yann Duroc, et al. 2012. “The Arabidopsis TRM1–TON1 Interaction Reveals a Recruitment Network Common to Plant Cortical Microtubule Arrays and Eukaryotic Centrosomes.” *The Plant Cell* 24 (1): 178–91. https://doi.org/10.1105/tpc.111.089748.

Dunbrack, Roland L. 2025. “Rēs ipSAE Loquunt: What’s Wrong with AlphaFold’s ipTM Score and How to Fix It.” *bioRxiv*, February 14, 2025.02.10.637595. https://doi.org/10.1101/2025.02.10.637595.

Durand-Smet, Pauline, Tamsin A. Spelman, Elliot M. Meyerowitz, and Henrik Jönsson. 2020. “Cytoskeletal Organization in Isolated Plant Cells under Geometry Control.” *Proceedings of the National Academy of Sciences* 117 (29): 17399–408. https://doi.org/10.1073/pnas.2003184117.

Edwards, K., C. Johnstone, and C. Thompson. 1991. “A Simple and Rapid Method for the Preparation of Plant Genomic DNA for PCR Analysis.” *Nucleic Acids Research* 19 (6): 1349. https://doi.org/10.1093/nar/19.6.1349.

Ejaz, Mahwish, Stefano Bencivenga, Rafael Tavares, Max Bush, and Robert Sablowski. 2021. “ARABIDOPSIS THALIANA HOMEOBOX GENE 1 Controls Plant Architecture by Locally Restricting Environmental Responses.” *Proceedings of the National Academy of Sciences* 118 (17): e2018615118. https://doi.org/10.1073/pnas.2018615118.

Elliott, L., and C. Kirchhelle. 2020. “The Importance of Being Edgy: Cell Geometric Edges as an Emerging Polar Domain in Plant Cells.” *Journal of Microscopy* 278 (3): 123–31. https://doi.org/10.1111/jmi.12847.

EMBL-EBI. n.d. *Confidence Scores in AlphaFold-Multimer | AlphaFold*. Accessed September 8, 2025. https://www.ebi.ac.uk/training/online/courses/alphafold/inputs-and-outputs/evaluating-alphafolds-predicted-structures-using-confidence-scores/confidence-scores-in-alphafold-multimer/.

Evans, Richard, Michael O’Neill, Alexander Pritzel, et al. 2022. “Protein Complex Prediction with AlphaFold-Multimer.” Preprint, bioRxiv, March 10. https://doi.org/10.1101/2021.10.04.463034.

Feng, Lin, Zhu Chen, Hui Ma, et al. 2014. “The IQD Gene Family in Soybean: Structure, Phylogeny, Evolution and Expression.” *PLOS ONE* 9 (10): e110896. https://doi.org/10.1371/journal.pone.0110896.

Feng, Xinhua, Shujuan Pan, Haifu Tu, et al. 2023. “IQ67 DOMAIN Protein 21 Is Critical for Indentation Formation in Pavement Cell Morphogenesis.” *Journal of Integrative Plant Biology* 65 (3): 721–38. https://doi.org/10.1111/jipb.13393.

Ferrero-Serrano, Ángel, Christian Cantos, and Sarah M. Assmann. 2019. “The Role of Dwarfing Traits in Historical and Modern Agriculture with a Focus on Rice.” *Cold Spring Harbor Perspectives in Biology* 11 (11): a034645. https://doi.org/10.1101/cshperspect.a034645.

Fleming, Jennifer, Paulyna Magana, Sreenath Nair, et al. 2025. “AlphaFold Protein Structure Database and 3D-Beacons: New Data and Capabilities.” *Journal of Molecular Biology*, Computation Resources for Molecular Biology, vol. 437 (15): 168967. https://doi.org/10.1016/j.jmb.2025.168967.

Fletcher, Jennifer C. 2002. “Shoot and Floral Meristem Maintenance in Arabidopsis.” *Annual Review of Plant Biology* 53 (Volume 53, 2002): 45–66. https://doi.org/10.1146/annurev.arplant.53.092701.143332.

Fridman, Y., S. Strauss, G. Horev, et al. 2021. “The Root Meristem Is Shaped by Brassinosteroid Control of Cell Geometry.” *Nature Plants* 7 (11): 11. https://doi.org/10.1038/s41477-021-01014-9.

Fu, F. Q., W. H. Mao, K. Shi, Y. H. Zhou, and J. Q. Yu. 2010. “Spatio-Temporal Changes in Cell Division, Endoreduplication and Expression of Cell Cycle-Related Genes in Pollinated and Plant Growth Substances-Treated Ovaries of Cucumber.” *Plant Biology* 12 (1): 98–107. https://doi.org/10.1111/j.1438-8677.2009.00203.x.

Gallois, Jean-Luc, Fabiana R. Nora, Yukiko Mizukami, and Robert Sablowski. 2004. “WUSCHEL Induces Shoot Stem Cell Activity and Developmental Plasticity in the

Root Meristem." *Genes & Development* 18 (4): 375–80. https://doi.org/10.1101/gad.291204.

Gallois, Jean-Luc, Claire Woodward, G. Venugopala Reddy, and Robert Sablowski. 2002. "Combined SHOOT MERISTEMLESS and WUSCHEL Trigger Ectopic Organogenesis in Arabidopsis." *Development* 129 (13): 3207–17. https://doi.org/10.1242/dev.129.13.3207.

Ganguly, Anindya, Chuanmei Zhu, Weizu Chen, and Ram Dixit. 2020. "FRA1 Kinesin Modulates the Lateral Stability of Cortical Microtubules through Cellulose Synthase–Microtubule Uncoupling Proteins." *The Plant Cell* 32 (8): 2508–24. https://doi.org/10.1105/tpc.19.00700.

Giannoutsou, Eleni, Basil Galatis, Michael Zachariadis, and Panagiotis Apostolakos. 2012. "Formation of an Endoplasmic Reticulum Ring Associated with Acetylated Microtubules in the Angiosperm Preprophase Band." *Cytoskeleton* 69 (4): 252–65. https://doi.org/10.1002/cm.21020.

Gietz, Daniel, Andrew St. Jean, Robin A. Woods, and Robert H. Schiestl. 1992. "Improved Method for High Efficiency Transformation of Intact Yeast Cells." *Nucleic Acids Research* 20 (6): 1425. https://doi.org/10.1093/nar/20.6.1425.

Gorelova, Vera, Joris Sprakel, and Dolf Weijers. 2021. "Plant Cell Polarity as the Nexus of Tissue Mechanics and Morphogenesis." *Nature Plants* 7 (12): 1548–59. https://doi.org/10.1038/s41477-021-01021-w.

Goujon, Mickael, Hamish McWilliam, Weizhong Li, et al. 2010. "A New Bioinformatics Analysis Tools Framework at EMBL–EBI." *Nucleic Acids Research* 38 (suppl_2): W695–99. https://doi.org/10.1093/nar/gkq313.

Gutierrez, Ryan, Jelmer J. Lindeboom, Alex R. Paredez, Anne Mie C. Emons, and David W. Ehrhardt. 2009. "Arabidopsis Cortical Microtubules Position Cellulose Synthase Delivery to the Plasma Membrane and Interact with Cellulose Synthase Trafficking Compartments." *Nature Cell Biology* 11 (7): 797–806. https://doi.org/10.1038/ncb1886.

Hacham, Yael, Neta Holland, Cristina Butterfield, et al. 2011. "Brassinosteroid Perception in the Epidermis Controls Root Meristem Size." *Development* 138 (5): 839–48. https://doi.org/10.1242/dev.061804.

Hall, Hardy, and Brian Ellis. 2012. "Developmentally Equivalent Tissue Sampling Based on Growth Kinematic Profiling of Arabidopsis Inflorescence Stems." *New Phytologist* 194 (1): 287–96. https://doi.org/10.1111/j.1469-8137.2012.04060.x.

Harashima, Hirofumi, Nico Dissmeyer, and Arp Schnittger. 2013. "Cell Cycle Control across the Eukaryotic Kingdom." *Trends in Cell Biology* 23 (7): 345–56. https://doi.org/10.1016/j.tcb.2013.03.002.

Harrison, Samuel J., Ellie K. Mott, Kate Parsley, Sue Aspinall, John C. Gray, and Amanda Cottage. 2006. "A Rapid and Robust Method of Identifying Transformed Arabidopsis Thaliana Seedlings Following Floral Dip Transformation." *Plant Methods* 2 (1): 19. https://doi.org/10.1186/1746-4811-2-19.

Hedden, Peter. 2003. “The Genes of the Green Revolution.” *Trends in Genetics* 19 (1): 5–9. https://doi.org/10.1016/S0168-9525(02)00009-4.

Hoermayer, Lukas, Juan Carlos Montesinos, Nicola Trozzi, et al. 2024. “Mechanical Forces in Plant Tissue Matrix Orient Cell Divisions via Microtubule Stabilization.” *Developmental Cell*, ahead of print, April 4. https://doi.org/10.1016/j.devcel.2024.03.009.

Hwang, Jae-Ung, Guang Wu, An Yan, Yong-Jik Lee, Claire S. Grierson, and Zhenbiao Yang. 2010. “Pollen-Tube Tip Growth Requires a Balance of Lateral Propagation and Global Inhibition of Rho-Family GTPase Activity.” *Journal of Cell Science* 123 (3): 340–50. https://doi.org/10.1242/jcs.039180.

Ishikawa, Masaki, Ayaka Fujiwara, Ken Kosetsu, et al. 2023. “GRAS Transcription Factors Regulate Cell Division Planes in Moss Overriding the Default Rule.” *Proceedings of the National Academy of Sciences* 120 (4): e2210632120. https://doi.org/10.1073/pnas.2210632120.

Jarsch, Iris K., Sebastian S.A. Konrad, Thomas F. Stratil, et al. 2014. “Plasma Membranes Are Subcompartmentalized into a Plethora of Coexisting and Diverse Microdomains in Arabidopsis and Nicotiana Benthamiana.” *The Plant Cell* 26 (4): 1698–711. https://doi.org/10.1105/tpc.114.124446.

Jarvis, M. C., S. P. H. Briggs, and J. P. Knox. 2003. “Intercellular Adhesion and Cell Separation in Plants.” *Plant, Cell & Environment* 26 (7): 977–89. https://doi.org/10.1046/j.1365-3040.2003.01034.x.

Jumper, John, Richard Evans, Alexander Pritzel, et al. 2021. “Highly Accurate Protein Structure Prediction with AlphaFold.” *Nature* 596 (7873): 583–89. https://doi.org/10.1038/s41586-021-03819-2.

Karahara, Ichirou, Jinsuke Suda, Hiroshi Tahara, et al. 2009. “The Preprophase Band Is a Localized Center of Clathrin-Mediated Endocytosis in Late Prophase Cells of the Onion Cotyledon Epidermis.” *The Plant Journal* 57 (5): 819–31. https://doi.org/10.1111/j.1365-313X.2008.03725.x.

Ke, Qinglin, Huifan Sun, Minqiang Tang, et al. 2022. “Genome-Wide Identification, Expression Analysis and Evolutionary Relationships of the IQ67-Domain Gene Family in Common Wheat (Triticum Aestivum L.) and Its Progenitors.” *BMC Genomics* 23 (1): 264. https://doi.org/10.1186/s12864-022-08520-w.

Kierzkowski, Daniel, Naomi Nakayama, Anne-Lise Routier-Kierzkowska, et al. 2012. “Elastic Domains Regulate Growth and Organogenesis in the Plant Shoot Apical Meristem.” *Science* 335 (6072): 1096–99. https://doi.org/10.1126/science.1213100.

Kilian, Joachim, Dion Whitehead, Jakub Horak, et al. 2007. “The AtGenExpress Global Stress Expression Data Set: Protocols, Evaluation and Model Data Analysis of UV-B Light, Drought and Cold Stress Responses.” *The Plant Journal* 50 (2): 347–63. https://doi.org/10.1111/j.1365-313X.2007.03052.x.

Kirchhelle, Charlotte, Cheung-Ming Chow, Camille Foucart, et al. 2016. “The Specification of Geometric Edges by a Plant Rab GTPase Is an Essential Cell-Patterning

Principle During Organogenesis in *Arabidopsis*." *Developmental Cell* 36 (4): 386–400. https://doi.org/10.1016/j.devcel.2016.01.020.

Kirchhelle, Charlotte, and Ian Moore. 2017. "A Simple Chamber for Long-Term Confocal Imaging of Root and Hypocotyl Development." *Journal of Visualized Experiments (JoVE)*, no. 123 (May): e55331. https://doi.org/10.3791/55331.

Kirik, Angela, David W. Ehrhardt, and Viktor Kirik. 2012. "TONNEAU2/FASS Regulates the Geometry of Microtubule Nucleation and Cortical Array Organization in Interphase Arabidopsis Cells." *The Plant Cell* 24 (3): 1158–70. https://doi.org/10.1105/tpc.111.094367.

Kleinboelting, Nils, Gunnar Huep, Andreas Kloetgen, Prisca Viehoever, and Bernd Weisshaar. 2012. "GABI-Kat SimpleSearch: New Features of the Arabidopsis Thaliana T-DNA Mutant Database." *Nucleic Acids Research* 40 (D1): D1211–15. https://doi.org/10.1093/nar/gkr1047.

Kölling, Malte, Pratibha Kumari, and Katharina Bürstenbinder. 2019. "Calcium- and Calmodulin-Regulated Microtubule-Associated Proteins as Signal-Integration Hubs at the Plasma Membrane–Cytoskeleton Nexus." *Journal of Experimental Botany* 70 (2): 387–96. https://doi.org/10.1093/jxb/ery397.

Kudla, Jörg, Oliver Batistič, and Kenji Hashimoto. 2010. "Calcium Signals: The Lead Currency of Plant Information Processing." *The Plant Cell* 22 (3): 541–63. https://doi.org/10.1105/tpc.109.072686.

Kumari, Pratibha, Pradeep Dahiya, Pantelis Livanos, et al. 2021. "IQ67 DOMAIN Proteins Facilitate Preprophase Band Formation and Division-Plane Orientation." *Nature Plants* 7 (6): 6. https://doi.org/10.1038/s41477-021-00923-z.

Kutschera, U., and K. J. Niklas. 2007. "The Epidermal-Growth-Control Theory of Stem Elongation: An Old and a New Perspective." *Journal of Plant Physiology* 164 (11): 1395–409. https://doi.org/10.1016/j.jplph.2007.08.002.

Lan, Miao, Yimin Zhu, Alexis Peaucelle, et al. 2025. "CSLD5-Mediated Cell Wall Remodelling Regulates Tissue Mechanics and Shoot Meristem Growth." *Nature Communications* 16 (1): 7229. https://doi.org/10.1038/s41467-025-62651-8.

Lavy, Meirav, and Mark Estelle. 2016. "Mechanisms of Auxin Signaling." *Development* 143 (18): 3226–29. https://doi.org/10.1242/dev.131870.

Lee, Young Koung, Gyung-Tae Kim, In-Jung Kim, et al. 2006. "LONGIFOLIA1 and LONGIFOLIA2, Two Homologous Genes,Regulate Longitudinal Cell Elongation in Arabidopsis." *Development* 133 (21): 4305–14. https://doi.org/10.1242/dev.02604.

Levy, Maggie, Qiaomei Wang, Roy Kaspi, Michael P. Parrella, and Steffen Abel. 2005. "Arabidopsis IQD1, a Novel Calmodulin-Binding Nuclear Protein, Stimulates Glucosinolate Accumulation and Plant Defense." *The Plant Journal* 43 (1): 79–96. https://doi.org/10.1111/j.1365-313X.2005.02435.x.

Leyser, Ottoline. 2011. "Auxin, Self-Organisation, and the Colonial Nature of Plants." *Current Biology* 21 (9): R331–37. https://doi.org/10.1016/j.cub.2011.02.031.

Li, Shanwei, Tiantian Sun, and Haiyun Ren. 2015. “The Functions of the Cytoskeleton and Associated Proteins during Mitosis and Cytokinesis in Plant Cells.” *Frontiers in Plant Science* 6 (April). https://doi.org/10.3389/fpls.2015.00282.

Li, Shundai, Lei Lei, Chris R. Somerville, and Ying Gu. 2012. “Cellulose Synthase Interactive Protein 1 (CSI1) Links Microtubules and Cellulose Synthase Complexes.” *Proceedings of the National Academy of Sciences* 109 (1): 185–90. https://doi.org/10.1073/pnas.1118560109.

Li, Xing, Li Wang, Yupeng Cui, et al. 2023. “The Cotton Protein GhIQD21 Interacts with GhCaM7 and Modulates Organ Morphogenesis in Arabidopsis by Influencing Microtubule Stability.” *Plant Cell Reports* 42 (6): 1025–38. https://doi.org/10.1007/s00299-023-03010-z.

Li, Yan, Yujia Huang, Yunze Wen, et al. 2021. “The Domain of Unknown Function 4005 (DUF4005) in an *Arabidopsis* IQD Protein Functions in Microtubule Binding.” *Journal of Biological Chemistry* 297 (1): 100849. https://doi.org/10.1016/j.jbc.2021.100849.

Li, Yuanfeng, Meng Deng, Haofeng Liu, et al. 2021. “ABNORMAL SHOOT 6 Interacts with KATANIN 1 and SHADE AVOIDANCE 4 to Promote Cortical Microtubule Severing and Ordering in Arabidopsis.” *Journal of Integrative Plant Biology* 63 (4): 646–61. https://doi.org/10.1111/jipb.13003.

Liang, Hong, Yi Zhang, Pablo Martinez, Carolyn G. Rasmussen, Tongda Xu, and Zhenbiao Yang. 2018. “The Microtubule-Associated Protein IQ67 DOMAIN5 Modulates Microtubule Dynamics and Pavement Cell Shape.” *Plant Physiology* 177 (4): 1555–68. https://doi.org/10.1104/pp.18.00558.

Lin, Deshu, Shingo Nagawa, Jisheng Chen, et al. 2012. “A ROP GTPase-Dependent Auxin Signaling Pathway Regulates the Subcellular Distribution of PIN2 in *Arabidopsis* Roots.” *Current Biology* 22 (14): 1319–25. https://doi.org/10.1016/j.cub.2012.05.019.

Lindeboom, Jelmer J., Masayoshi Nakamura, Anneke Hibbel, et al. 2013. “A Mechanism for Reorientation of Cortical Microtubule Arrays Driven by Microtubule Severing.” *Science* 342 (6163): 1245533. https://doi.org/10.1126/science.1245533.

Lipka, Elisabeth, Astrid Gadeyne, Dorothee Stöckle, et al. 2014. “The Phragmoplast-Orienting Kinesin-12 Class Proteins Translate the Positional Information of the Preprophase Band to Establish the Cortical Division Zone in Arabidopsis Thaliana.” *The Plant Cell* 26 (6): 2617–32. https://doi.org/10.1105/tpc.114.124933.

Liu, Jie, Alisdair R. Fernie, and Jianbing Yan. 2020. “The Past, Present, and Future of Maize Improvement: Domestication, Genomics, and Functional Genomic Routes toward Crop Enhancement.” *Plant Communications* 1 (1): 100010. https://doi.org/10.1016/j.xplc.2019.100010.

Livanos, Pantelis, Choy Kriechbaum, Sophia Remers, Arvid Herrmann, and Sabine Müller. 2025. “Kinesin-12 POK2 Polarization Is a Prerequisite for a Fully Functional Division Site and Aids Cell Plate Positioning.” *Nature Communications* 16 (1): 4464. https://doi.org/10.1038/s41467-025-58852-w.

Livanos, Pantelis, and Sabine Müller. 2019. “Division Plane Establishment and Cytokinesis.” *Annual Review of Plant Biology* 70 (Volume 70, 2019): 239–67. https://doi.org/10.1146/annurev-arplant-050718-100444.

Lloyd, Clive W. 1991. “How Does the Cytoskeleton Read the Laws of Geometry in Aligning the Division Plane of Plant Cells?” *Development* 113 (Supplement_1): 55–65. https://doi.org/10.1242/dev.113.Supplement_1.55.

Lloyd, Clive W., Catharina J. Venverloo, Kim C. Goodbody, and Peter J. Shaw. 1992. “Confocal Laser Microscopy and Three-Dimensional Reconstruction of Nucleus-Associated Microtubules in the Division Plane of Vacuolated Plant Cells.” *Journal of Microscopy* 166 (1): 99–109. https://doi.org/10.1111/j.1365-2818.1992.tb01509.x.

Louveaux, Marion, Jean-Daniel Julien, Vincent Mirabet, Arezki Boudaoud, and Olivier Hamant. 2016. “Cell Division Plane Orientation Based on Tensile Stress in Arabidopsis Thaliana.” *Proceedings of the National Academy of Sciences* 113 (30): E4294–303. https://doi.org/10.1073/pnas.1600677113.

Madeira, Fábio, Nandana Madhusoodanan, Joonheung Lee, et al. 2024. “The EMBL-EBI Job Dispatcher Sequence Analysis Tools Framework in 2024.” *Nucleic Acids Research* 52 (W1): W521–25. https://doi.org/10.1093/nar/gkae241.

Marc, Jan, Cheryl L. Granger, Jennifer Brincat, et al. 1998. “A GFP–MAP4 Reporter Gene for Visualizing Cortical Microtubule Rearrangements in Living Epidermal Cells.” *The Plant Cell* 10 (11): 1927–39. https://doi.org/10.1105/tpc.10.11.1927.

Martin-Arevalillo, Raquel, and Teva Vernoux. 2023. “Decoding the Auxin Matrix: Auxin Biology Through the Eye of the Computer.” *Annual Review of Plant Biology* 74 (Volume 74, 2023): 387–413. https://doi.org/10.1146/annurev-arplant-102720-033523.

Matthes, Michaela C., Joao P. Pennacchi, Johnathan A. Napier, and Smita Kurup. 2022. “The Palisade-Specific Gene IQD22 Enhances Photosynthetic Capacity by Phenocopying ‘Sun Leaf’ Architecture.” Preprint, bioRxiv, August 28. https://doi.org/10.1101/2022.08.27.505449.

Mckechnie-Welsh, Emma. 2021. “Function of IQD Proteins in Shoot Organ Growth.” University of East Anglia.

Mei, Chao, Yuwei Liu, Xue Dong, et al. 2021. “Genome-Wide Identification and Characterization of the Potato IQD Family During Development and Stress.” *Frontiers in Genetics* 12 (July). https://doi.org/10.3389/fgene.2021.693936.

Melogno, Isaty, Shogo Takatani, Paula Llanos, et al. 2024. “A Transient Radial Cortical Microtubule Array Primes Cell Division in Arabidopsis.” *Proceedings of the National Academy of Sciences* 121 (29): e2320470121. https://doi.org/10.1073/pnas.2320470121.

Mills, Alison M, Victoria H Morris, and Carolyn G Rasmussen. 2022. “The Localization of PHRAGMOPLAST ORIENTING KINESIN1 at the Division Site Depends on the Microtubule-Binding Proteins TANGLED1 and AUXIN-INDUCED IN ROOT

CULTURES9 in Arabidopsis." *The Plant Cell* 34 (11): 4583–99. https://doi.org/10.1093/plcell/koac266.

Mir, Ricardo, Victoria H. Morris, Henrik Buschmann, and Carolyn G. Rasmussen. 2018. "Division Plane Orientation Defects Revealed by a Synthetic Double Mutant Phenotype." *Plant Physiology* 176 (1): 418–31. https://doi.org/10.1104/pp.17.01075.

Mirabet, Vincent, Pawel Krupinski, Olivier Hamant, Elliot M. Meyerowitz, Henrik Jönsson, and Arezki Boudaoud. 2018. "The Self-Organization of Plant Microtubules inside the Cell Volume Yields Their Cortical Localization, Stable Alignment, and Sensitivity to External Cues." *PLOS Computational Biology* 14 (2): e1006011. https://doi.org/10.1371/journal.pcbi.1006011.

Mirdita, Milot, Konstantin Schütze, Yoshitaka Moriwaki, Lim Heo, Sergey Ovchinnikov, and Martin Steinegger. 2022. "ColabFold: Making Protein Folding Accessible to All." *Nature Methods* 19 (6): 679–82. https://doi.org/10.1038/s41592-022-01488-1.

Mischley, Victoria, Johannes Maier, Jesse Chen, and John Karanicolas. 2024. "PPIscreenML: Structure-Based Screening for Protein-Protein Interactions Using AlphaFold." *bioRxiv*, April 30, 2024.03.16.585347. https://doi.org/10.1101/2024.03.16.585347.

Mitra, Dipannita, Sandra Klemm, Pratibha Kumari, et al. 2019. "Microtubule-Associated Protein IQ67 DOMAIN5 Regulates Morphogenesis of Leaf Pavement Cells in Arabidopsis Thaliana." *Journal of Experimental Botany* 70 (2): 529–43. https://doi.org/10.1093/jxb/ery395.

Miyashima, Shunsuke, Pawel Roszak, Iris Sevilem, et al. 2019. "Mobile PEAR Transcription Factors Integrate Positional Cues to Prime Cambial Growth." *Nature* 565 (7740): 490–94. https://doi.org/10.1038/s41586-018-0839-y.

Mlotshwa, Sizolwenkosi, Gail J. Pruss, Zhihuan Gao, et al. 2010. "Transcriptional Silencing Induced by Arabidopsis T-DNA Mutants Is Associated with 35S Promoter siRNAs and Requires Genes Involved in siRNA-Mediated Chromatin Silencing." *The Plant Journal* 64 (4): 699–704. https://doi.org/10.1111/j.1365-313X.2010.04358.x.

Möller, Barbara K., Colette A. ten Hove, Daoquan Xiang, et al. 2017. "Auxin Response Cell-Autonomously Controls Ground Tissue Initiation in the Early Arabidopsis Embryo." *Proceedings of the National Academy of Sciences* 114 (12): E2533–39. https://doi.org/10.1073/pnas.1616493114.

Müller, Jens, Martina Beck, Ursula Mettbach, et al. 2010. "Arabidopsis MPK6 Is Involved in Cell Division Plane Control during Early Root Development, and Localizes to the Pre-Prophase Band, Phragmoplast, Trans-Golgi Network and Plasma Membrane." *The Plant Journal* 61 (2): 234–48. https://doi.org/10.1111/j.1365-313X.2009.04046.x.

Müller, Sabine, Shengcheng Han, and Laurie G. Smith. 2006. "Two Kinesins Are Involved in the Spatial Control of Cytokinesis in *Arabidopsis Thaliana*." *Current Biology* 16 (9): 888–94. https://doi.org/10.1016/j.cub.2006.03.034.

Mulvey, Hugh, and Liam Dolan. 2023. “RHO GTPase of Plants Regulates Polarized Cell Growth and Cell Division Orientation during Morphogenesis.” *Current Biology* 33 (14): 2897-2911.e6. https://doi.org/10.1016/j.cub.2023.06.015.

Muroyama, Andrew, Yan Gong, and Dominique C. Bergmann. 2020. “Opposing, Polarity-Driven Nuclear Migrations Underpin Asymmetric Divisions to Pattern Arabidopsis Stomata.” *Current Biology* 30 (22): 4467-4475.e4. https://doi.org/10.1016/j.cub.2020.08.100.

Nagawa, Shingo, Tongda Xu, Deshu Lin, et al. 2012. “ROP GTPase-Dependent Actin Microfilaments Promote PIN1 Polarization by Localized Inhibition of Clathrin-Dependent Endocytosis.” *PLOS Biology* 10 (4): e1001299. https://doi.org/10.1371/journal.pbio.1001299.

Oda, Yoshihisa, and Hiroo Fukuda. 2012. “Initiation of Cell Wall Pattern by a Rho- and Microtubule-Driven Symmetry Breaking.” *Science* 337 (6100): 1333–36. https://doi.org/10.1126/science.1222597.

Pan, Yupeng, Xinjing Liang, Meiling Gao, et al. 2017. “Round Fruit Shape in WI7239 Cucumber Is Controlled by Two Interacting Quantitative Trait Loci with One Putatively Encoding a Tomato SUN Homolog.” *Theoretical and Applied Genetics* 130 (3): 573–86. https://doi.org/10.1007/s00122-016-2836-6.

Panteris, Emmanuel, Ioannis-Dimosthenis S. Adamakis, Georgia Voulgari, and Galini Papadopoulou. 2011. “A Role for Katanin in Plant Cell Division: Microtubule Organization in Dividing Root Cells of Fra2 and lue1Arabidopsis Thaliana Mutants.” *Cytoskeleton* 68 (7): 401–13. https://doi.org/10.1002/cm.20522.

Paredez, Alexander R., Christopher R. Somerville, and David W. Ehrhardt. 2006. “Visualization of Cellulose Synthase Demonstrates Functional Association with Microtubules.” *Science* 312 (5779): 1491–95. https://doi.org/10.1126/science.1126551.

Pernisová, Markéta, and Teva Vernoux. 2021. “Auxin Does the SAMba: Auxin Signaling in the Shoot Apical Meristem.” *Cold Spring Harbor Perspectives in Biology* 13 (12): a039925. https://doi.org/10.1101/cshperspect.a039925.

Peters, Winfried S. 2009. “My Embarrassment at Not Knowing Heinich.” *Journal of Plant Physiology* 166 (16): 1713–16. https://doi.org/doi:10.1016/j.jplph.2009.08.004.

Peters, Winfried S., and A. Deri Tomos. 2000. “The Mechanic State of ‘Inner Tissue’ in the Growing Zone of Sunflower Hypocotyls and the Regulation of Its Growth Rate Following Excision1.” *Plant Physiology* 123 (2): 605–12. https://doi.org/10.1104/pp.123.2.605.

Procko, Carl, Travis Lee, Aleca Borsuk, et al. 2022. “Leaf Cell-Specific and Single-Cell Transcriptional Profiling Reveals a Role for the Palisade Layer in UV Light Protection.” *The Plant Cell* 34 (9): 3261–79. https://doi.org/10.1093/plcell/koac167.

Rashotte, Aaron M., Susan D. B. Carson, Jennifer P. C. To, and Joseph J. Kieber. 2003. “Expression Profiling of Cytokinin Action in Arabidopsis.” *Plant Physiology* 132 (4): 1998–2011. https://doi.org/10.1104/pp.103.021436.

Rehman, Abdul, Zhen Peng, Hongge Li, et al. 2021. “Genome Wide Analysis of IQD Gene Family in Diploid and Tetraploid Species of Cotton (*Gossypium* Spp.).” *International Journal of Biological Macromolecules* 184 (August): 1035–61. https://doi.org/10.1016/j.ijbiomac.2021.06.115.

Reinhardt, Didier. 2004. “Regulation of Phyllotaxis.” *International Journal of Developmental Biology* 49 (5–6): 5–6. https://doi.org/10.1387/ijdb.041922dr.

Rhoads, Allen R., and Felix Friedberg. 1997. “Sequence Motifs for Calmodulin Recognition.” *The FASEB Journal* 11 (5): 331–40. https://doi.org/10.1096/fasebj.11.5.9141499.

Robert, Xavier, and Patrice Gouet. 2014. “Deciphering Key Features in Protein Structures with the New ENDscript Server.” *Nucleic Acids Research* 42 (W1): W320–24. https://doi.org/10.1093/nar/gku316.

Robinson, Sarah. 2021. “Mechanobiology of Cell Division in Plant Growth.” *New Phytologist* 231 (2): 559–64. https://doi.org/10.1111/nph.17369.

Robinson, Sarah, and Cris Kuhlemeier. 2018. “Global Compression Reorients Cortical Microtubules in Arabidopsis Hypocotyl Epidermis and Promotes Growth.” *Current Biology* 28 (11): 1794-1802.e2. https://doi.org/10.1016/j.cub.2018.04.028.

Sachs, Julius. 2011 [1875]. *A Text-Book of Botany: Morphological and Physiological*. Edited and translated by Alfred W. Bennett. Cambridge Library Collection - Botany and Horticulture. Cambridge University Press. https://doi.org/10.1017/CBO9781139105231.

Sachs, R M. 1965. “Stem Elongation.” *Annual Review of Plant Physiology* 16 (1): 73–96. https://doi.org/10.1146/annurev.pp.16.060165.000445.

Sambade, Adrian, Amitesh Pratap, Henrik Buschmann, Richard J. Morris, and Clive Lloyd. 2012. “The Influence of Light on Microtubule Dynamics and Alignment in the Arabidopsis Hypocotyl.” *The Plant Cell* 24 (1): 192–201. https://doi.org/10.1105/tpc.111.093849.

Savaldi-Goldstein, Sigal, Charles Peto, and Joanne Chory. 2007. “The Epidermis Both Drives and Restricts Plant Shoot Growth.” *Nature* 446 (7132): 199–202. https://doi.org/10.1038/nature05618.

Schaefer, Estelle, Katia Belcram, Magalie Uyttewaal, et al. 2017. “The Preprophase Band of Microtubules Controls the Robustness of Division Orientation in Plants.” *Science* 356 (6334): 186–89. https://doi.org/10.1126/science.aal3016.

Schiessl, Katharina, Swathi Kausika, Paul Southam, Max Bush, and Robert Sablowski. 2012. “JAGGED Controls Growth Anisotropy and Coordination between Cell Size and Cell Cycle during Plant Organogenesis.” *Current Biology* 22 (19): 1739–46. https://doi.org/10.1016/j.cub.2012.07.020.

Schmid, Markus, Timothy S. Davison, Stefan R. Henz, et al. 2005. “A Gene Expression Map of Arabidopsis Thaliana Development.” *Nature Genetics* 37 (5): 5. https://doi.org/10.1038/ng1543.

Schoof, Heiko, Michael Lenhard, Achim Haecker, Klaus F. X. Mayer, Gerd Jürgens, and Thomas Laux. 2000. “The Stem Cell Population of Arabidopsis Shoot Meristems Is Maintained by a Regulatory Loop between the CLAVATA and WUSCHEL Genes.” *Cell* 100 (6): 635–44. https://doi.org/10.1016/S0092-8674(00)80700-X.

Serrano-Mislata, Antonio, Stefano Bencivenga, Max Bush, Katharina Schiessl, Scott Boden, and Robert Sablowski. 2017. “DELLA Genes Restrict Inflorescence Meristem Function Independently of Plant Height.” *Nature Plants* 3 (9): 9. https://doi.org/10.1038/s41477-017-0003-y.

Serrano-Mislata, Antonio, and Robert Sablowski. 2018. “The Pillars of Land Plants: New Insights into Stem Development.” *Current Opinion in Plant Biology*, Cell signalling and gene regulation, vol. 45 (October): 11–17. https://doi.org/10.1016/j.pbi.2018.04.016.

Serrano-Mislata, Antonio, Katharina Schiessl, and Robert Sablowski. 2015. “Active Control of Cell Size Generates Spatial Detail during Plant Organogenesis.” *Current Biology* 25 (22): 2991–96. https://doi.org/10.1016/j.cub.2015.10.008.

Shi, Dongbo, Virginie Jouannet, Javier Agustí, et al. 2021. “Tissue-Specific Transcriptome Profiling of the Arabidopsis Inflorescence Stem Reveals Local Cellular Signatures.” *The Plant Cell* 33 (2): 200–223. https://doi.org/10.1093/plcell/koaa019.

Shimada, Takashi L., Tomoo Shimada, and Ikuko Hara-Nishimura. 2010. “A Rapid and Non-Destructive Screenable Marker, FAST, for Identifying Transformed Seeds of Arabidopsis Thaliana.” *The Plant Journal* 61 (3): 519–28. https://doi.org/10.1111/j.1365-313X.2009.04060.x.

Sieburth, Leslie E., Gary N. Drews, and Elliot M. Meyerowitz. 1998. “Non-Autonomy of AGAMOUS Function in Flower Development: Use of a Cre/loxP Method for Mosaic Analysis in Arabidopsis.” *Development* 125 (21): 4303–12. https://doi.org/10.1242/dev.125.21.4303.

Sievers, Fabian, Andreas Wilm, David Dineen, et al. 2011. “Fast, Scalable Generation of High-quality Protein Multiple Sequence Alignments Using Clustal Omega.” *Molecular Systems Biology* 7 (1): 539. https://doi.org/10.1038/msb.2011.75.

Silveira, Sylvia R., Loann Collet, Sahil M. Haque, et al. 2025. “Mechanical Interactions between Tissue Layers Underlie Plant Morphogenesis.” *Nature Plants* 11 (4): 909–23. https://doi.org/10.1038/s41477-025-01944-8.

Smertenko, Andrei, Farhah Assaad, František Baluška, et al. 2017. “Plant Cytokinesis: Terminology for Structures and Processes.” *Trends in Cell Biology* 27 (12): 885–94. https://doi.org/10.1016/j.tcb.2017.08.008.

Smertenko, Andrei P., Hsin-Yu Chang, Vera Wagner, et al. 2004. “The Arabidopsis Microtubule-Associated Protein AtMAP65-1: Molecular Analysis of Its Microtubule Bundling Activity.” *The Plant Cell* 16 (8): 2035–47. https://doi.org/10.1105/tpc.104.023937.

Smith, Harley M. S., and Sarah Hake. 2003. “The Interaction of Two Homeobox Genes, BREVIPEDICELLUS and PENNYWISE, Regulates Internode Patterning in the

Arabidopsis Inflorescence." *The Plant Cell* 15 (8): 1717–27. https://doi.org/10.1105/tpc.012856.

Smith, Laurie G. 2001. "Plant Cell Division: Building Walls in the Right Places." *Nature Reviews Molecular Cell Biology* 2 (1): 33–39. https://doi.org/10.1038/35048050.

Spinner, Lara, Astrid Gadeyne, Katia Belcram, et al. 2013. "A Protein Phosphatase 2A Complex Spatially Controls Plant Cell Division." *Nature Communications* 4 (1): 1863. https://doi.org/10.1038/ncomms2831.

Stöckle, Dorothee, Arvid Herrmann, Elisabeth Lipka, et al. 2016. "Putative RopGAPs Impact Division Plane Selection and Interact with Kinesin-12 POK1." *Nature Plants* 2 (9): 16120. https://doi.org/10.1038/nplants.2016.120.

Sugiyama, Yuki, Mayumi Wakazaki, Kiminori Toyooka, Hiroo Fukuda, and Yoshihisa Oda. 2017. "A Novel Plasma Membrane-Anchored Protein Regulates Xylem Cell-Wall Deposition through Microtubule-Dependent Lateral Inhibition of Rho GTPase Domains." *Current Biology* 27 (16): 2522-2528.e4. https://doi.org/10.1016/j.cub.2017.06.059.

Takeuchi, Miyuki, Ichirou Karahara, Naoko Kajimura, et al. 2016. "Single Microfilaments Mediate the Early Steps of Microtubule Bundling during Preprophase Band Formation in Onion Cotyledon Epidermal Cells." *Molecular Biology of the Cell* 27 (11): 1809–20. https://doi.org/10.1091/mbc.e15-12-0820.

Thompson, David. 2009. "Untangling Tensions: A Consideration of the Epidermal-Growth-Control and Developmental-Hydraulic Interpretations of Tissue Tension." *Journal of Plant Physiology* 166 (16): 1717–19. https://doi.org/10.1016/j.jplph.2009.08.005.

Uyttewaal, Magalie, Agata Burian, Karen Alim, et al. 2012. "Mechanical Stress Acts via Katanin to Amplify Differences in Growth Rate between Adjacent Cells in Arabidopsis." *Cell* 149 (2): 439–51. https://doi.org/10.1016/j.cell.2012.02.048.

Vaddepalli, Prasad, Thijs de Zeeuw, Sören Strauss, et al. 2021. "Auxin-Dependent Control of Cytoskeleton and Cell Shape Regulates Division Orientation in the Arabidopsis Embryo." *Current Biology* 31 (22): 4946-4955.e4. https://doi.org/10.1016/j.cub.2021.09.019.

Van Damme, Daniël, Bert De Rybel, Gustavo Gudesblat, et al. 2011. "Arabidopsis α Aurora Kinases Function in Formative Cell Division Plane Orientation." *The Plant Cell* 23 (11): 4013–24. https://doi.org/10.1105/tpc.111.089565.

Verger, Stéphane, Yuchen Long, Arezki Boudaoud, and Olivier Hamant. 2018. "A Tension-Adhesion Feedback Loop in Plant Epidermis." *eLife* 7 (April): e34460. https://doi.org/10.7554/eLife.34460.

Vineyard, Laura, Andrew Elliott, Sonia Dhingra, Jessica R. Lucas, and Sidney L. Shaw. 2013. "Progressive Transverse Microtubule Array Organization in Hormone-Induced Arabidopsis Hypocotyl Cells." *The Plant Cell* 25 (2): 662–76. https://doi.org/10.1105/tpc.112.107326.

Walker, Keely L., Sabine Müller, Dorianne Moss, David W. Ehrhardt, and Laurie G. Smith. 2007. "*Arabidopsis* TANGLED Identifies the Division Plane throughout Mitosis and

Cytokinesis." *Current Biology* 17 (21): 1827–36. https://doi.org/10.1016/j.cub.2007.09.063.

Wallner, Eva-Sophie, Andrea Mair, Dominik Handler, et al. 2024. "Spatially Resolved Proteomics of the *Arabidopsis* Stomatal Lineage Identifies Polarity Complexes for Cell Divisions and Stomatal Pores." *Developmental Cell* 59 (9): 1096-1109.e5. https://doi.org/10.1016/j.devcel.2024.03.001.

Wang, Bing, Steven M. Smith, and Jiayang Li. 2018. "Genetic Regulation of Shoot Architecture." *Annual Review of Plant Biology* 69 (April): 437–68. https://doi.org/10.1146/annurev-arplant-042817-040422.

Wang, Yixin, Shijie Ma, Xiaomeng Cao, et al. 2024. "Morphological, Histological and Transcriptomic Mechanisms Underlying Different Fruit Shapes in Capsicum Spp." *PeerJ* 12 (September): e17909. https://doi.org/10.7717/peerj.17909.

Weeratunga, Saroja, Rachel S. Gormal, Meihan Liu, et al. 2024. "Interrogation and Validation of the Interactome of Neuronal Munc18-Interacting Mint Proteins with AlphaFold2." *Journal of Biological Chemistry* 300 (1): 105541. https://doi.org/10.1016/j.jbc.2023.105541.

Wendrich, Jos R., Barbara K. Möller, Song Li, et al. 2017. "Framework for Gradual Progression of Cell Ontogeny in the Arabidopsis Root Meristem." *Proceedings of the National Academy of Sciences* 114 (42): E8922–29. https://doi.org/10.1073/pnas.1707400114.

Wendrich, Jos R., Bao-Jun Yang, Pieter Mijnhout, Hong-Wei Xue, Bert De Rybel, and Dolf Weijers. 2018. "IQD Proteins Integrate Auxin and Calcium Signaling to Regulate Microtubule Dynamics during Arabidopsis Development." Preprint, bioRxiv, March 2. https://doi.org/10.1101/275560.

Weston, Emma, Keira Thorogood, Giovanna Vinti, and Enrique López-Juez. 2000. "Light Quantity Controls Leaf-Cell and Chloroplast Development in Arabidopsis Thaliana Wild Type and Blue-Light-Perception Mutants." *Planta* 211 (6): 807–15. https://doi.org/10.1007/s004250000392.

Wilson, Thomas H, Manoj Kumar, and Simon R Turner. 2021. "The Molecular Basis of Plant Cellulose Synthase Complex Organisation and Assembly." *Biochemical Society Transactions* 49 (1): 379–91. https://doi.org/10.1042/BST20200697.

Winter, Debbie, Ben Vinegar, Hardeep Nahal, Ron Ammar, Greg V. Wilson, and Nicholas J. Provart. 2007. "An 'Electronic Fluorescent Pictograph' Browser for Exploring and Analyzing Large-Scale Biological Data Sets." *PLOS ONE* 2 (8): e718. https://doi.org/10.1371/journal.pone.0000718.

Wu, Min, Yuan Li, Danmei Chen, Huanlong Liu, Dongyue Zhu, and Yan Xiang. 2016. "Genome-Wide Identification and Expression Analysis of the IQD Gene Family in Moso Bamboo (Phyllostachys Edulis)." *Scientific Reports* 6 (1): 1. https://doi.org/10.1038/srep24520.

Wu, Shan, Han Xiao, Antonio Cabrera, Tea Meulia, and Esther van der Knaap. 2011. "SUN Regulates Vegetative and Reproductive Organ Shape by Changing Cell Division

Patterns." *Plant Physiology* 157 (3): 1175–86. https://doi.org/10.1104/pp.111.181065.

Xiao, Han, Ning Jiang, Erin Schaffner, Eric J. Stockinger, and Esther van der Knaap. 2008. "A Retrotransposon-Mediated Gene Duplication Underlies Morphological Variation of Tomato Fruit." *Science* 319 (5869): 1527–30. https://doi.org/10.1126/science.1153040.

Xu, Jinrui, and Yang Zhang. 2010. "How Significant Is a Protein Structure Similarity with TM-Score = 0.5?" *Bioinformatics* 26 (7): 889–95. https://doi.org/10.1093/bioinformatics/btq066.

Xu, Xianfeng Morgan, Qiao Zhao, Thushani Rodrigo-Peiris, et al. 2008. "RanGAP1 Is a Continuous Marker of the Arabidopsis Cell Division Plane." *Proceedings of the National Academy of Sciences* 105 (47): 18637–42. https://doi.org/10.1073/pnas.0806157105.

Yang, Bo, Gina Stamm, Katharina Bürstenbinder, and Cătălin Voiniciuc. 2021. "Microtubule-Associated IQD9 Guides Cellulose Synthase Velocity to Shape Seed Mucilage." Preprint, bioRxiv, December 12. https://doi.org/10.1101/2021.12.11.472226.

Yang, Zhenbiao, and Irene Lavagi. 2012. "Spatial Control of Plasma Membrane Domains: ROP GTPase-Based Symmetry Breaking." *Current Opinion in Plant Biology* 15 (6): 601–7. https://doi.org/10.1016/j.pbi.2012.10.004.

Yang, Zhenyu, Xiaoxi Zeng, Yi Zhao, and Runsheng Chen. 2023. "AlphaFold2 and Its Applications in the Fields of Biology and Medicine." *Signal Transduction and Targeted Therapy* 8 (1): 115. https://doi.org/10.1038/s41392-023-01381-z.

Yoshida, Saiko, Pierre Barbier de Reuille, Brendan Lane, et al. 2014. "Genetic Control of Plant Development by Overriding a Geometric Division Rule." *Developmental Cell* 29 (1): 75–87. https://doi.org/10.1016/j.devcel.2014.02.002.

Yuan, J., Z. Yu, Y. Li, et al. 2022. "Ectopic Expression of BrIQD35 Promotes Drought Stress Tolerance in Nicotiana Benthamiana." *Plant Biology* 24 (5): 887–96. https://doi.org/10.1111/plb.13425.

Yuan, Jingping, Tongkun Liu, Zhanghong Yu, et al. 2019. "Genome-Wide Analysis of the Chinese Cabbage IQD Gene Family and the Response of BrIQD5 in Drought Resistance." *Plant Molecular Biology* 99 (6): 603–20. https://doi.org/10.1007/s11103-019-00839-5.

Zachariadis, M., H. Quader, B. Galatis, and P. Apostolakos. 2001. "Endoplasmic Reticulum Preprophase Band in Dividing Root-Tip Cells of Pinus Brutia." *Planta* 213 (5): 824–27. https://doi.org/10.1007/s004250100563.

Zang, Jingze, Sandra Klemm, Charlotte Pain, et al. 2021. "A Novel Plant Actin-Microtubule Bridging Complex Regulates Cytoskeletal and ER Structure at ER-PM Contact Sites." *Current Biology* 31 (6): 1251-1260.e4. https://doi.org/10.1016/j.cub.2020.12.009.

Zentella, Rodolfo, Zhong-Lin Zhang, Mehea Park, et al. 2007. “Global Analysis of DELLA Direct Targets in Early Gibberellin Signaling in Arabidopsis.” *The Plant Cell* 19 (10): 3037–57. https://doi.org/10.1105/tpc.107.054999.

Zhang, Yu, Shengjie Wang, Chaochao Zhang, et al. 2024. “Genome-Wide Characterization of IQD Family Proteins in Apple and Functional Analysis of the Microtubule-Regulating Abilities of MdIQD17 and MdIQD28 under Cold Stress.” *Plants* 13 (17): 2532. https://doi.org/10.3390/plants13172532.

Zhao, Shanshan, Qin-Fang Chen, Li Chen, et al. 2025. “The Plant-Specific Protein IQD22 Interacts with Calcium Sensors to Activate Anaerobic Respiration during Hypoxia in *Arabidopsis*.” *Molecular Plant* 18 (8): 1330–50. https://doi.org/10.1016/j.molp.2025.07.005.

Zogopoulos, Vasileios L., Konstantinos Papadopoulos, Apostolos Malatras, Vassiliki A. Iconomidou, and Ioannis Michalopoulos. 2025. “ACT2.6: Global Gene Coexpression Network in Arabidopsis Thaliana Using WGCNA.” *Genes* 16 (3): 3. https://doi.org/10.3390/genes16030258.

APPENDICES

APPENDIX 1: SUPPLEMENTARY DATA

Table 1: Genes Co-expressed with IQD26 The list was generated using the Arabidopsis Coexpression Tool (ACT) Version 2.6 (https://www.michalopoulos.net/act2.6/) (Zogopoulos et al. 2025)

Probe Set	Symbol	Name	Description
AT4G03270_at	CYCD6;1	Cyclin D6;1	Cyclin D6;1
AT2G45870_at	AT2G45870		Bestrophin-like protein
AT1G65470_at	FAS1	FASCIATA 1	chromatin assembly factor-1 (FASCIATA1) (FAS1)
AT2G44440_at	EML4	EMSY-like 4	Emsy N Terminus (ENT) domain-containing protein
AT1G07880_at	ATMPK13		Protein kinase superfamily protein
AT3G56810_at	AT3G56810		hypothetical protein
AT1G46264_at	HSFB4	heat shock transcription factor B4	heat shock transcription factor B4
AT2G13690_at	AT2G13690		PRLI-interacting factor
AT4G35880_at	AT4G35880		Eukaryotic aspartyl protease family protein
AT3G07540_at	AT3G07540		Actin-binding FH2 (formin homology 2) family protein
AT4G13710_at	AT4G13710		Pectin lyase-like superfamily protein
AT4G15140_at	AT4G15140		hypothetical protein
AT1G32190_at	AT1G32190		alpha/beta-Hydrolases superfamily protein
AT2G38720_at	MAP65-5	microtubule-associated protein 65-5	microtubule-associated protein 65-5
AT2G23380_at	CLF	CURLY LEAF	SET domain-containing protein
AT1G79820_at	SGB1	SUPPRESSOR OF G PROTEIN BETA1	Major facilitator superfamily protein
AT2G38370_at	AT2G38370		weak chloroplast movement under blue light protein (DUF827)

AT1G47230_at	CYCA3;4	CYCLIN A3;4	CYCLIN A3;4
AT5G57410_at	AT5G57410		Afadin/alpha-actinin-binding protein
AT3G43610_at	AT3G43610		Spc97 / Spc98 family of spindle pole body (SBP) component
AT2G21050_at	LAX2	like AUXIN RESISTANT 2	like AUXIN RESISTANT 2
AT5G59020_at	AT5G59020		hepatocyte growth factor activator, putative (DUF3527)
AT4G37740_at	GRF2	growth-regulating factor 2	growth-regulating factor 2
AT4G37110_at	AT4G37110		Zinc-finger domain of monoamine-oxidase A repressor R1
AT4G31890_at	AT4G31890		ARM repeat superfamily protein
AT3G50870_at	MNP	MONOPOLE	GATA type zinc finger transcription factor family protein
AT3G06840_at	AT3G06840		hypothetical protein
AT5G67460_at	AT5G67460		O-Glycosyl hydrolases family 17 protein
AT3G48490_at	AT3G48490		hypothetical protein
AT3G19300_at	AT3G19300		Protein kinase superfamily protein
AT1G80280_at	AT1G80280		alpha/beta-Hydrolases superfamily protein
AT1G53070_at	AT1G53070		Legume lectin family protein
AT2G24440_at	AT2G24440		selenium binding protein
AT5G65420_at	CYCD4;1	CYCLIN D4;1	CYCLIN D4;1
AT1G02110_at	AT1G02110		bZIP domain class transcription factor (DUF630 and DUF632)
AT3G48210_at	AT3G48210		kinetochore protein
AT3G49250_at	DMS3	DEFECTIVE IN MERISTEM SILENCING 3	defective in meristem silencing 3
AT3G53380_at	AT3G53380		Concanavalin A-like lectin protein kinase family protein
AT3G09070_at	OPS	OCTOPUS	LOW protein: UPF0503-like protein, putative (DUF740)
AT4G32840_at	PFK6	phosphofructokinase 6	phosphofructokinase 6
AT5G41060_at	AT5G41060		DHHC-type zinc finger family protein
AT5G57130_at	AT5G57130		Clp amino terminal domain-containing protein
AT5G04320_at	AT5G04320		Shugoshin C terminus
AT4G33130_at	AT4G33130		rho GTPase-activating protein

AT1G67040_at	TRM22	TON1 Recruiting Motif 22	DnaA initiator-associating protein
AT2G37300_at	ABCI16	ATP-binding cassette I16	transmembrane protein
AT5G43020_at	AT5G43020		Leucine-rich repeat protein kinase family protein
AT5G48360_at	AT5G48360		Actin-binding FH2 (formin homology 2) family protein
AT2G37080_at	RIP2	ROP interactive partner 2	ROP interactive partner 3
AT5G60210_at	RIP5	ROP interactive partner 5	ROP interactive partner 5
AT5G26850_at	AT5G26850		Uncharacterized protein
AT1G10850_at	AT1G10850		Leucine-rich repeat protein kinase family protein
AT3G08680_at	AT3G08680		Leucine-rich repeat protein kinase family protein
AT3G12170_at	AT3G12170		Chaperone DnaJ-domain superfamily protein
AT5G18620_at	CHR17	chromatin remodeling factor17	chromatin remodeling factor17
AT4G17610_at	AT4G17610		tRNA/rRNA methyltransferase (SpoU) family protein
AT2G23700_at	AT2G23700		Itga6 (Protein of unknown function, DUF547)
AT1G21740_at	AT1G21740		DUF630 family protein, putative (DUF630 and DUF632)
AT1G19950_at	HVA22H	HVA22-like protein H (ATHVA22H)	HVA22-like protein H (ATHVA22H)
AT1G49910_at	BUB3.2	BUB (BUDDING UNINHIBITED BY BENZYMIDAZOL) 3.2	Transducin/WD40 repeat-like superfamily protein
AT5G38690_at	AT5G38690		Zinc-finger domain of monoamine-oxidase A repressor R1 protein
AT5G04620_at	BIOF	biotin F	biotin F
AT1G67690_at	AT1G67690		Zincin-like metalloproteases family protein
AT5G17620_at	39295	augmin subunit 7	nuclear matrix protein
AT1G32930_at	AT1G32930		Galactosyltransferase family protein
AT2G44690_at	ARAC9	Arabidopsis RAC-like 9	RAC-like 9
AT2G24230_at	AT2G24230		Leucine-rich repeat protein kinase family protein
AT1G54960_at	NP2	NPK1-related protein kinase 2	NPK1-related protein kinase 2
AT2G37390_at	NAKR2	SODIUM POTASSIUM ROOT DEFECTIVE 2	Chloroplast-targeted copper chaperone protein

AT3G18000_at	XPL1	XIPOTL 1	S-adenosyl-L-methionine-dependent methyltransferases superfamily protein
AT5G08580_at	AT5G08580		Calcium-binding EF hand family protein
AT1G55130_at	TMN6	transmembrane nine 6	Endomembrane protein 70 protein family
AT4G17190_at	FPS2	farnesyl diphosphate synthase 2	farnesyl diphosphate synthase 2
AT2G43800_at	AT2G43800		Actin-binding FH2 (formin homology 2) family protein
AT4G02290_at	GH9B13	glycosyl hydrolase 9B13	glycosyl hydrolase 9B13
AT1G71830_at	SERK1	somatic embryogenesis receptor-like kinase 1	somatic embryogenesis receptor-like kinase 1
AT5G54670_at	ATK3	kinesin 3	kinesin 3
AT1G70710_at	GH9B1	glycosyl hydrolase 9B1	glycosyl hydrolase 9B1
AT5G01890_at	AT5G01890		Leucine-rich receptor-like protein kinase family protein
AT1G44780_at	AT1G44780		translation initiation factor
AT1G66250_at	AT1G66250		O-Glycosyl hydrolases family 17 protein
AT1G19850_at	MP	MONOPTEROS	Transcriptional factor B3 family protein / auxin-responsive factor AUX/IAA-like protein
AT3G13190_at	AT3G13190		WEB family protein (DUF827)
AT2G24970_at	AT2G24970		spindle/kinetochore-associated protein
AT5G13290_at	CRN	CORYNE	Protein kinase superfamily protein
AT1G35780_at	AT1G35780		N-lysine methyltransferase
AT3G14890_at	AT3G14890		phosphoesterase
AT1G73590_at	PIN1	PIN-FORMED 1	Auxin efflux carrier family protein
AT1G25510_at	AT1G25510		Eukaryotic aspartyl protease family protein
AT4G28190_at	ULT1	ULTRAPETALA1	Developmental regulator, ULTRAPETALA
AT1G28110_at	SCPL45	serine carboxypeptidase-like 45	serine carboxypeptidase-like 45
AT5G25475_at	AT5G25475		AP2/B3-like transcriptional factor family protein
AT3G56640_at	SEC15A	exocyst complex component sec15A	exocyst complex component sec15A
AT5G23420_at	HMGB6	high-mobility group box 6	high-mobility group box 6

AT1G23000_at	AT1G23000		Heavy metal transport/detoxification superfamily protein
AT4G00020_at	BRCA2(IV)	BREAST CANCER 2 like 2A	BREAST CANCER 2 like 2A
AT5G48820_at	ICK6	inhibitor/interactor with cyclin-dependent kinase	inhibitor/interactor with cyclin-dependent kinase
AT3G24660_at	TMKL1	transmembrane kinase-like 1	transmembrane kinase-like 1
AT2G27040_at	AGO4	ARGONAUTE 4	Argonaute family protein
AT3G17160_at	AT3G17160		hypothetical protein
AT4G00480_at	ATMYC1		basic helix-loop-helix (bHLH) DNA-binding superfamily protein
AT2G44830_at	AT2G44830		Protein kinase superfamily protein
AT3G50070_at	CYCD3;3	CYCLIN D3;3	CYCLIN D3;3
AT2G37560_at	ORC2	origin recognition complex second largest subunit 2	origin recognition complex second largest subunit 2
AT5G05180_at	AT5G05180		myosin heavy chain, striated protein
AT4G15890_at	AT4G15890		binding protein
AT4G24610_at	AT4G24610		pesticidal crystal cry8Ba protein
AT3G53320_at	AT3G53320		mediator of RNA polymerase II transcription subunit-like protein
AT1G11130_at	SUB	STRUBBELIG	Leucine-rich repeat protein kinase family protein
AT3G02920_at	RPA32B		Replication protein A, subunit RPA32
AT1G14180_at	AT1G14180		RING/U-box superfamily protein
AT3G18524_at	MSH2	MUTS homolog 2	MUTS homolog 2
AT3G06740_at	GATA15	GATA transcription factor 15	GATA transcription factor 15
AT5G23400_at	AT5G23400		Leucine-rich repeat (LRR) family protein
AT4G37750_at	ANT	AINTEGUMENTA	Integrase-type DNA-binding superfamily protein
AT4G28950_at	ROP9	RHO-related protein from plants 9	RHO-related protein from plants 9
AT3G53760_at	GCP4	GAMMA-TUBULIN COMPLEX PROTEIN 4	GAMMA-TUBULIN COMPLEX PROTEIN 4
AT4G24710_at	AT4G24710		pachytene checkpoint-like protein
AT1G63480_at	AT1G63480		AT hook motif DNA-binding family protein
AT4G25240_at	SKS1	SKU5 similar 1	SKU5 similar 1

AT1G63650_at	EGL3	ENHANCER OF GLABRA 3	basic helix-loop-helix (bHLH) DNA-binding superfamily protein
AT3G09730_at	AT3G09730		POLAR LOCALIZATION DURING ASYMMETRIC DIVISION AND protein
AT1G08260_at	TIL1	TILTED 1	DNA polymerase epsilon catalytic subunit
AT1G77720_at	PPK1	putative protein kinase 1	putative protein kinase 1
AT3G48425_at	AT3G48425		DNAse I-like superfamily protein
AT3G48540_at	AT3G48540		Cytidine/deoxycytidylate deaminase family protein
AT5G52950_at	AT5G52950		LIM domain protein
AT1G03830_at	AT1G03830		guanylate-binding family protein
AT1G05950_at	AT1G05950		hypothetical protein
AT1G18040_at	CDKD1;3	cyclin-dependent kinase D1;3	cyclin-dependent kinase D1;3
AT3G14740_at	AT3G14740		RING/FYVE/PHD zinc finger superfamily protein
AT3G29280_at	AT3G29280		hypothetical protein
AT3G63300_at	FKD1	FORKED 1	FORKED 1
AT5G06590_at	AT5G06590		hypothetical protein
AT2G01630_at	AT2G01630		O-Glycosyl hydrolases family 17 protein
AT1G04730_at	CTF18	CHROMOSOME TRANSMISSION FIDELITY 18	P-loop containing nucleoside triphosphate hydrolases superfamily protein
AT5G46740_at	UBP21	ubiquitin-specific protease 21	ubiquitin-specific protease 21
AT1G67320_at	EMB2813	EMBRYO DEFECTIVE 2813	DNA primase, large subunit family
AT2G36010_at	E2F3	E2F transcription factor 3	E2F transcription factor 3
AT1G78650_at	POLD3		DNA-directed DNA polymerase
AT5G63960_at	AT5G63960		DNA polymerase delta subunit 1
AT1G08130_at	LIG1	DNA ligase 1	DNA ligase 1
AT5G56740_at	HAG2	histone acetyltransferase of the GNAT family 2	histone acetyltransferase of the GNAT family 2
AT5G25590_at	AT5G25590		DNA ligase (DUF630 and DUF632)
AT5G01370_at	ACI1	ALC-interacting protein 1	ALC-interacting protein 1
AT5G57590_at	BIO1	biotin auxotroph 1	adenosylmethionine-8-amino-7-oxononanoate transaminase

AT2G01120_at	ORC4	origin recognition complex subunit 4	origin recognition complex subunit 4
AT3G05740_at	RECQI1	RECQ helicase l1	RECQ helicase l1
AT5G51590_at	AT5G51590		AT hook motif DNA-binding family protein
AT4G34160_at	CYCD3;1	CYCLIN D3;1	CYCLIN D3;1
AT2G01210_at	AT2G01210		Leucine-rich repeat protein kinase family protein
AT4G24790_at	AT4G24790		AAA-type ATPase family protein
AT5G26670_at	AT5G26670		Pectinacetylesterase family protein
AT5G06050_at	AT5G06050		Putative methyltransferase family protein
AT3G22880_at	DMC1	DISRUPTION OF MEIOTIC CONTROL 1	DNA repair (Rad51) family protein
AT2G38810_at	HTA8	histone H2A 8	histone H2A 8
AT1G17560_at	HLL	HUELLENLOS	Ribosomal protein L14p/L23e family protein
AT5G38110_at	ASF1B	anti- silencing function 1b	anti- silencing function 1b
AT5G13960_at	SUVH4	SU(VAR)3-9 homolog 4	histone-lysine N-methyltransferase, H3 lysine-9 specific SUVH4-like protein
AT1G69770_at	CMT3	chromomethylase 3	chromomethylase 3
AT4G02150_at	MOS6	MODIFIER OF SNC1, 6	ARM repeat superfamily protein
AT1G44900_at	MCM2	MINICHROMOSOME MAINTENANCE 2	minichromosome maintenance (MCM2/3/5) family protein
AT2G16780_at	MSI2	MULTICOPY SUPPRESSOR OF IRA1 2	Transducin family protein / WD-40 repeat family protein
AT5G02370_at	AT5G02370		ATP binding microtubule motor family protein
AT5G67200_at	AT5G67200		Leucine-rich repeat protein kinase family protein
AT3G47460_at	ATSMC2		Structural maintenance of chromosomes (SMC) family protein
AT5G63950_at	CHR24	chromatin remodeling 24	chromatin remodeling 24
AT3G61610_at	AT3G61610		Galactose mutarotase-like superfamily protein
AT5G14610_at	AT5G14610		DEAD box RNA helicase family protein
AT3G58100_at	PDCB5	plasmodesmata callose-binding protein 5	plasmodesmata callose-binding protein 5
AT1G50110_at	AT1G50110		D-aminoacid aminotransferase-like PLP-dependent enzymes superfamily protein

AT2G25880_at	AUR2	ataurora2	ataurora2
AT5G33300_at	AT5G33300		chromosome-associated kinesin-like protein
AT4G26760_at	MAP65-2	microtubule-associated protein 65-2	microtubule-associated protein 65-2
AT3G22780_at	TSO1	CHINESE FOR 'UGLY'	Tesmin/TSO1-like CXC domain-containing protein
AT3G62300_at	DUF7	DOMAIN OF UNKNOWN FUNCTION 724 7	agenet domain protein (DOMAIN OF UNKNOWN FUNCTION 724 7)
AT5G62710_at	AT5G62710		Leucine-rich repeat protein kinase family protein
AT4G29360_at	AT4G29360		O-Glycosyl hydrolases family 17 protein
AT1G02970_at	WEE1	WEE1 kinase homolog	WEE1-like kinase
AT4G28430_at	AT4G28430		Reticulon family protein
AT4G14200_at	AT4G14200		Pentatricopeptide repeat (PPR) superfamily protein
AT1G16520_at	AT1G16520		interactor of constitutive active ROPs protein
AT4G20430_at	AT4G20430		Subtilase family protein
AT2G31270_at	CDT1A	homolog of yeast CDT1 A	CDT1-like protein A
AT1G75640_at	AT1G75640		Leucine-rich receptor-like protein kinase family protein
AT4G39860_at	AT4G39860		hematological/neurological-like protein
AT2G24490_at	RPA2	replicon protein A2	replicon protein A2
AT3G25100_at	CDC45	cell division cycle 45	cell division cycle 45
AT5G49010_at	SLD5	SYNTHETIC LETHALITY WITH DPB11-1 5	DNA replication protein-like protein
AT2G42120_at	POLD2	DNA polymerase delta small subunit	DNA polymerase delta small subunit
AT3G02820_at	AT3G02820		zinc knuckle (CCHC-type) family protein
AT5G08020_at	RPA70B	RPA70-kDa subunit B	RPA70-kDa subunit B
AT1G61450_at	AT1G61450		CAP-gly domain linker
AT4G35730_at	AT4G35730		Regulator of Vps4 activity in the MVB pathway protein
AT2G42110_at	AT2G42110		hypothetical protein
AT1G04020_at	BARD1	breast cancer associated RING 1	breast cancer associated RING 1
AT3G24495_at	MSH7	MUTS homolog 7	MUTS homolog 7
AT5G43080_at	CYCA3;1	Cyclin A3;1	Cyclin A3;1

AT3G17680_at	AT3G17680		Kinase interacting (KIP1-like) family protein
AT3G54750_at	AT3G54750		downstream neighbor of Son
AT3G53190_at	AT3G53190		Pectin lyase-like superfamily protein
AT1G18250_at	ATLP-1		Pathogenesis-related thaumatin superfamily protein
AT3G19590_at	BUB3.1	BUB (BUDDING UNINHIBITED BY BENZYMIDAZOL) 3.1	Transducin/WD40 repeat-like superfamily protein
AT4G31840_at	ENODL15	early nodulin-like protein 15	early nodulin-like protein 15
AT4G02800_at	AT4G02800		GRIP/coiled-coil protein
AT5G16250_at	AT5G16250		transmembrane protein
AT1G02730_at	CSLD5	cellulose synthase-like D5	cellulose synthase-like D5
AT2G25060_at	ENODL14	early nodulin-like protein 14	early nodulin-like protein 14
AT3G02640_at	AT3G02640		transmembrane protein
AT3G54560_at	HTA11	histone H2A 11	histone H2A 11
AT1G07370_at	PCNA1	proliferating cellular nuclear antigen 1	proliferating cellular nuclear antigen 1
AT2G29570_at	PCNA2	proliferating cell nuclear antigen 2	proliferating cell nuclear antigen 2
AT1G57820_at	VIM1	VARIANT IN METHYLATION 1	Zinc finger (C3HC4-type RING finger) family protein
AT5G49160_at	MET1	methyltransferase 1	methyltransferase 1
AT1G63470_at	AT1G63470		AT hook motif DNA-binding family protein
AT5G45700_at	AT5G45700		Haloacid dehalogenase-like hydrolase (HAD) superfamily protein
AT2G17620_at	CYCB2;1	Cyclin B2;1	Cyclin B2;1
AT3G62060_at	AT3G62060		Pectinacetylesterase family protein
AT3G42660_at	AT3G42660		transducin family protein / WD-40 repeat family protein
AT5G48600_at	SMC3	structural maintenance of chromosome 3	structural maintenance of chromosome 3
AT4G31360_at	AT4G31360		selenium binding protein
AT2G29890_at	VLN1	villin 1	villin-like 1
AT4G14770_at	TCX2	TESMIN/TSO1-like CXC 2	TESMIN/TSO1-like CXC 2
AT3G57860_at	UVI4-LIKE	UV-B-insensitive 4-like	UV-B-insensitive 4-like protein

AT4G28230_at	AT4G28230		hypothetical protein
AT1G30600_at	AT1G30600		Subtilase family protein
AT1G50490_at	UBC20	ubiquitin-conjugating enzyme 20	ubiquitin-conjugating enzyme 20
AT4G32830_at	AUR1	ataurora1	ataurora1
AT2G34190_at	AT2G34190		Xanthine/uracil permease family protein
AT3G20260_at	AT3G20260		DUF1666 family protein (DUF1666)
AT1G49870_at	AT1G49870		myosin-2 heavy chain-like protein
AT2G38160_at	AT2G38160		hypothetical protein
AT3G22790_at	NET1A	Networked 1A	Kinase interacting (KIP1-like) family protein
AT1G15660_at	CENP-C	centromere protein C	centromere protein C
AT1G09470_at	AT1G09470		myosin heavy chain, cardiac protein
AT1G78430_at	RIP4	ROP interactive partner 4	ROP interactive partner 2
AT3G60840_at	MAP65-4	microtubule-associated protein 65-4	microtubule-associated protein 65-4
AT1G67630_at	POLA2	DNA polymerase alpha 2	DNA polymerase alpha 2
AT2G40550_at	ETG1	E2F target gene 1	E2F target protein 1 (ETG1)
AT4G02060_at	PRL	PROLIFERA	Minichromosome maintenance (MCM2/3/5) family protein
AT5G46280_at	MCM3	MINICHROMOSOME MAINTENANCE 3	Minichromosome maintenance (MCM2/3/5) family protein
AT5G67100_at	ICU2	INCURVATA2	DNA-directed DNA polymerase
AT2G07690_at	MCM5	MINICHROMOSOME MAINTENANCE 5	Minichromosome maintenance (MCM2/3/5) family protein
AT2G16440_at	MCM4	MINICHROMOSOME MAINTENANCE 4	Minichromosome maintenance (MCM2/3/5) family protein
AT2G25270_at	AT2G25270		transmembrane protein
AT3G54630_at	AT3G54630		kinetochore protein
AT5G66750_at	CHR1	chromatin remodeling 1	chromatin remodeling 1
AT1G78770_at	APC6	anaphase promoting complex 6	anaphase promoting complex 6
AT5G56580_at	MKK6	MAP kinase kinase 6	MAP kinase kinase 6
AT1G01370_at	HTR12		Histone superfamily protein
AT1G16070_at	TLP8	tubby like protein 8	tubby like protein 8

AT5G38300_at	AT5G38300		homeobox Hox-B3-like protein
AT5G13520_at	AT5G13520		peptidase M1 family protein
AT3G56100_at	MRLK	meristematic receptor-like kinase	meristematic receptor-like kinase
AT4G05520_at	EHD2	EPS15 homology domain 2	EPS15 homology domain 2
AT4G26660_at	AT4G26660		kinesin-like protein
AT5G60930_at	AT5G60930		P-loop containing nucleoside triphosphate hydrolases superfamily protein
AT5G62410_at	SMC2	structural maintenance of chromosomes 2	structural maintenance of chromosomes 2
AT2G37420_at	AT2G37420		ATP binding microtubule motor family protein
AT1G15570_at	CYCA2;3	CYCLIN A2;3	CYCLIN A2;3
AT4G11080_at	3xHMG-box1	3xHigh Mobility Group-box1	HMG (high mobility group) box protein
AT1G80370_at	CYCA2;4	Cyclin A2;4	Cyclin A2;4
AT4G36180_at	AT4G36180		Leucine-rich receptor-like protein kinase family protein
AT1G02690_at	IMPA-6	importin alpha isoform 6	importin alpha isoform 6
AT2G07170_at	AT2G07170		ARM repeat superfamily protein
AT3G57060_at	AT3G57060		binding protein
AT4G37490_at	CYCB1;1	CYCLIN B1;1	CYCLIN B1;1
AT3G01410_at	AT3G01410		Polynucleotidyl transferase, ribonuclease H-like superfamily protein
AT4G01730_at	AT4G01730		DHHC-type zinc finger family protein
AT2G28620_at	AT2G28620		P-loop containing nucleoside triphosphate hydrolases superfamily protein
AT3G27330_at	AT3G27330		zinc finger (C3HC4-type RING finger) family protein
AT4G39630_at	AT4G39630		translation initiation factor
AT3G11520_at	CYCB1;3	CYCLIN B1;3	CYCLIN B1;3
AT2G26180_at	IQD6	IQ-domain 6	IQ-domain 6
AT5G55820_at	WYR	WYRD	inner centromere protein, ARK-binding region protein
AT1G34355_at	PS1	PARALLEL SPINDLE 1	forkhead-associated (FHA) domain-containing protein
AT5G62550_at	AT5G62550		microtubule-associated futsch-like protein
AT3G03130_at	AT3G03130		lisH domain-like protein

AT5G03870_at	AT5G03870		Glutaredoxin family protein
AT3G25980_at	MAD2	MITOTIC ARREST-DEFICIENT 2	DNA-binding HORMA family protein
AT3G51720_at	AT3G51720		WEB family protein (DUF827)
AT5G25090_at	ENODL13	early nodulin-like protein 13	early nodulin-like protein 13
AT5G37010_at	AT5G37010		rho GTPase-activating protein
AT1G72670_at	iqd8	IQ-domain 8	IQ-domain 8
AT1G20930_at	CDKB2;2	cyclin-dependent kinase B2;2	cyclin-dependent kinase B2;2
AT4G33400_at	AT4G33400		Vacuolar import/degradation, Vid27-related protein
AT3G44050_at	AT3G44050		P-loop containing nucleoside triphosphate hydrolases superfamily protein
AT4G03100_at	AT4G03100		Rho GTPase activating protein with PAK-box/P21-Rho-binding domain-containing protein
AT1G23790_at	AT1G23790		dicer-like protein (DUF936)
AT3G52110_at	AT3G52110		interferon-activable protein
AT4G21820_at	AT4G21820		binding / calmodulin binding protein
AT5G17160_at	AT5G17160		aspartic/glutamic acid-rich protein
AT3G05330_at	ATN	TANGLED	cyclin family
AT5G11510_at	MYB3R-4	myb domain protein 3r-4	myb domain protein 3r-4
AT1G10780_at	AT1G10780		F-box/RNI-like superfamily protein
AT4G21270_at	ATK1	kinesin 1	kinesin 1
AT5G66230_at	AT5G66230		Chalcone-flavanone isomerase family protein
AT2G33560_at	BUBR1	BUB1-related (BUB1: budding uninhibited by benzymidazol 1)	BUB1-related (BUB1: budding uninhibited by benzymidazol 1)
AT4G35620_at	CYCB2;2	Cyclin B2;2	Cyclin B2;2
AT5G13840_at	FZR3	FIZZY-related 3	FIZZY-related 3
AT1G63100_at	AT1G63100		GRAS family transcription factor
AT5G67270_at	EB1C	end binding protein 1C	end binding protein 1C
AT4G23800_at	3xHMG-box2	3xHigh Mobility Group-box2	HMG (high mobility group) box protein
AT2G26760_at	CYCB1;4	Cyclin B1;4	Cyclin B1;4

AT5G48310_at	AT5G48310		portal protein
AT1G76540_at	CDKB2;1	cyclin-dependent kinase B2;1	cyclin-dependent kinase B2;1
AT3G12870_at	AT3G12870		transmembrane protein
AT5G01910_at	AT5G01910		myelin transcription factor
AT2G36200_at	AT2G36200		P-loop containing nucleoside triphosphate hydrolases superfamily protein
AT5G51600_at	PLE	PLEIADE	Microtubule associated protein (MAP65/ASE1) family protein
AT5G15510_at	AT5G15510		TPX2 (targeting protein for Xklp2) protein family
AT2G22610_at	AT2G22610		Di-glucose binding protein with Kinesin motor domain-containing protein
AT1G59540_at	ZCF125		P-loop containing nucleoside triphosphate hydrolases superfamily protein
AT2G16270_at	AT2G16270		transmembrane protein
AT3G20150_at	AT3G20150		Kinesin motor family protein
AT3G02120_at	AT3G02120		hydroxyproline-rich glycoprotein family protein
AT4G15830_at	AT4G15830		ARM repeat superfamily protein
AT3G55660_at	ROPGEF6	ROP (rho of plants) guanine nucleotide exchange factor 6	ROP (rho of plants) guanine nucleotide exchange factor 6
AT1G72250_at	AT1G72250		Di-glucose binding protein with Kinesin motor domain-containing protein
AT1G53140_at	DRP5A	Dynamin related protein 5A	Dynamin related protein 5A
AT3G14190_at	AT3G14190		hypothetical protein
AT1G76310_at	CYCB2;4	CYCLIN B2;4	CYCLIN B2;4
AT3G06030_at	NP3	NPK1-related protein kinase 3	NPK1-related protein kinase 3
AT1G44110_at	CYCA1;1	Cyclin A1;1	Cyclin A1;1
AT5G55520_at	AT5G55520		kinesin-like protein
AT3G51280_at	AT3G51280		Tetratricopeptide repeat (TPR)-like superfamily protein
AT3G23890_at	TOPII	topoisomerase II	topoisomerase II
AT1G03780_at	TPX2	targeting protein for XKLP2	targeting protein for XKLP2
AT1G18370_at	HIK	HINKEL	ATP binding microtubule motor family protein
AT1G08560_at	SYP111	syntaxin of plants 111	syntaxin of plants 111
AT4G05190_at	ATK5	kinesin 5	kinesin 5

AT5G63920_at	TOP3A	topoisomerase 3alpha	topoisomerase 3alpha
AT1G50240_at	FU	FUSED	kinase family with ARM repeat domain-containing protein
AT1G09450_at	Haspin	Haspin-related gene	Protein kinase superfamily protein
AT5G23910_at	AT5G23910		ATP binding microtubule motor family protein
AT3G10310_at	AT3G10310		P-loop nucleoside triphosphate hydrolases superfamily protein with CH (Calponin Homology) domain-containing protein
AT3G15550_at	AT3G15550		trichohyalin
AT3G51740_at	IMK2	inflorescence meristem receptor-like kinase 2	inflorescence meristem receptor-like kinase 2
AT4G14330_at	AT4G14330		P-loop containing nucleoside triphosphate hydrolases superfamily protein
AT3G58650_at	TRM7	TON1 Recruiting Motif 7	GPI-anchored adhesin-like protein
AT2G32590_at	EMB2795	EMBRYO DEFECTIVE 2795	condensin complex subunit
AT3G23670_at	KINESIN-12B		phragmoplast-associated kinesin-related protein

APPENDIX 2: SUPPLEMENTARY METHODS

Table 2: Settings Used for Confocal Imaging

Experiment	Figures	System	Imaging Mode	Lens	Excitation	Emission	Laser power	Gain	Z step size
mPS-PI-stained meristems	12, 13, 15, 38, 40, 44, 46, 59, 61, 63,	Zeiss LSM 880	Airyscan Fast	40x/1.3 oil immersion	488 nm	BP 495-550 + LP 570 filters	6 %	675 – 750 V	0.334/ 0.25 µm
Cre-*lox*P GFP sectors	21	Zeiss LSM 980	LSM	10x/0.45 or 20x/0.8 air	488 nm	490-552 nm	2-4.5%	790-810 V	2.2-4.5 µm
PI-stained meristems with IQD-YFP reporters	29, 30, 31	Zeiss LSM880	Airyscan Fast	40x/1.0 X water dipping	561 nm; 514 nm	SBS SP 615; SBS SP 615 and BP 420-280 + BP 495-550	9%; 12%	800 V; 950 V	0.334 µm
PI-stained roots	49	Zeiss LSM 880	Airyscan Fast	40x/1.1 water immersion	488 nm	BP 495-550 + LP 570	6-8 %	900 V	0.576 µm
RFP-TUA5 with IQD26-YFP	32, 33, 34	Zeiss LSM880	LSM	40x/1.0 water dipping (SAM); 25x/0.8 multi-	594; 514 nm	597–654; 516 – 574 nm	9 % ; 10 %	800 V; 950 – 1000 V	n/a

				immersion (seedlings)					
RFP-TUA5 with IQD26-YFP time course in roots	35	Zeiss LSM980	Airyscan	40x/1.1 water immersion	594 nm; 514 nm	570-630 nm (SBS LP 525 and BP 420-480 + BP 570-630); 499-557 nm (SBS SP 615 and BP 495-555 + LP 660)	10 % ;10 %	800 V; 850 V	1.38 µm
mCherry-MAP4MBD	48	Zeiss LSM880	LSM	40x/1.1 water immersion (root and leaf); 40x/1.0 water dipping (SAM)	561 nm	578-641 nm	8 %	850 V	n/a
mCherry-MAP4MBD and IQD26-YFP time course in roots	51	Zeiss LSM980	Airyscan	25x/0.8 multi-immersion	594 nm; 514 nm	570-630 nm (SBS LP 525 and BP 420-480 + BP 570-630); 499-557 nm (SBS SP 615 and BP 495-555 + LP 660)	7 %; 10 %	900 V	1.38 µm
Calcofluor-white-stained sections	6, 58	Zeiss LSM880	LSM	10X/0.45 air	405 nm	410-523 nm	5 %	450 – 600 V	2 µm

Table 3: Gene identifiers and additional clone information. Abbreviations: FL = full length coding region i.e. genomic region from the start codon to the stop codon (unless otherwise specified) including introns; GG = Golden Gate (cloning)

Gene Name	Gene Model	Primer Orientation		Template	Position relative to ATG in gDNA/ cDNA			Notes
		Fwd	Rev		Start	Stop	Introduced mutations	
proIQD22	AT4G23060.1	P275	P276	Col-0 gDNA	-3574	-1		Amplification was unsuccessful
IQD22 FL (no stop codon)	AT4G23060.1	P277	P278	Col-0 gDNA	+1	+3124		
proIQD23	AT5G62070.1	P281	P282	Col-0 gDNA	-1345	-1		
IQD23 FL (no stop codon, no *Bsa*I)	AT5G62070.1	P283	P284	Col-0 gDNA	+1	+2392	+2209G>A +2220G>A	IQD26 was amplified in two fragments. Level 0 GG vector was amplified as one fragment. All fragments were assembled together
		P285	P286	Col-0 gDNA				
		P287	P288	Level 0 GG plasmid pICL01005				

								using NEBbuilder® HiFi DNA Assembly
proIQD24	AT5G07240.2	P423	P424	proIQD24:IQD24-YFP plasmid (Mckechnie-Welsh 2021)	-617	-2		
IQD24 CDS (no stop codon, no *Bsa*I)	AT5G07240.2	P425	P426		+1	+3435	+307TCT>AGC	
proIQD25	AT4G29150.1	P291	P292	Col-0 gDNA	-1422	-1		
IQD25 FL (no stop codon, no *Bsa*I)	AT4G29150.1	P293	P294	Col-0 gDNA	+1	+1568	+1265G>C, +1433G>A	IQD25 was amplified in three fragments. Level 0 GG vector was amplified as one fragment. All fragments were assembled together using NEBbuilder® HiFi DNA Assembly
		P295	P296	Col-0 gDNA				
		P297	P298	Col-0 gDNA				
		P299	P400	Level 0 GG plasmid pICL01005				
proIQD26	AT3G16490.1	P403	P404	Col-0 gDNA	-2057	-1		
IQD26 FL (no stop codon, no *Bsa*I)	AT3G16490.1	P405	P406	Col-0 gDNA	+1	+1525	+1000G>A	IQD26 was amplified in three fragments. Level 0 GG vector was amplified as one
		P407	P408	Col-0 gDNA				
		P409	P410	Level 0 GG plasmid pICL01005				

								fragment. All fragments were assembled together using NEBbuilder® HiFi DNA Assembly
proIQD26:IQD26-YFP:terHSP18.2 no *Bsa*I, no *Bpi*I	AT3G16490.1	P634	P635	proIQD26:IQD26-YFP:terHSP18.2 Level 1 GG plasmid			-1061T>C -149T>C +348T>C +1000G>A	
		P636	P637					
		P642	P639					
		P640	P641					
IQD26 CDS (for Y2H)	AT3G16490.1	P601	P602	Col-0 cDNA	+1	+640	+642G>A	
		P603	P604	Col-0 cDNA	+641	+1170		
proIQD27 (no *Bsa*I)	AT1G51960.1	P413	P414	Col-0 gDNA	-3224	-1	-2365C>G	3224bp proIQD26 was amplified in two fragments. Level 0 GG vector was amplified as one fragment. All fragments were assembled together using NEBbuilder® HiFi DNA Assembly
		P415	P416	Col-0 gDNA				
		P417	P418	Level 0 GG plasmid pICL01005				

IQD27 FL (no stop codon)	AT1G51960.1	P419	P420	Col-0 gDNA	+1	+1508		
MPK6 CDS (for Y2H)	AT2G43790.1	P607	P608	Col-0 cDNA	+1	+1188		
CAM7 CDS (for Y2H)	AT3G43810.3	P605	P606	Col-0 cDNA	+1	+342		
TRM7 CDS (for Y2H)	AT3G58650.1	P611	P612	Col-0 cDNA	+1	+2463		
AUR1 CDS (for Y2H)	AT4G32830.1	P609	P610	Col-0 cDNA	+1	+885		
MAP4-MBD		P618	P619	plasmid DNA	+1	+1281	1119C>T	
		P620	P621	plasmid DNA	+1117	+1278		
proHSP18:Cre:tNOS		P482	P483	proHSP18:Cre:tNOS in pCGN1547 plasmid				
proHSP18:Cre:AtHSP101intron: Cre:tNOS		P488	P489	proHSP18:Cre:tNOS Level1 GG plasmid				
	AT1G74310.1	P490	P491	Col-0 gDNA	+1417	+1556		
		P492	P493	proHSP18:Cre:tNOS Lv1 GG plasmid				

		P494	P495	proHSP18:Cre:tNOS Lv1 GG plasmid				
pro35S:*loxP*:CFP:*lox*P: GFP:tActin		P477	P478	pro35S:*loxP*:CFP:*lox*P: GFP:tActin plasmid				

Table 4: Primer combinations used for genotyping.

Purpose	Allele	Primer Orientation		Position relative to ATG in gDNA		Amplicon Length
		Fwd	Rev			
Genotyping *iqd22-5*	WT allele	P209	P210	+101	+415	*Bts*CI digests 315 bp amplicon into two products of 140 bp and 175 bp.
	iqd22-5	P209	P210	+101	+408	298 bp. Resistant to digestion by *Bts*CI
Genotyping *iqd22-1*	WT allele	P238	P239	-567	+430	997 bp
	iqd22-1	P201	P239	SALK LBb1.3	+430	
Genotyping *iqd23-2*	WT allele	P215	P216	-275	+855	1130 bp
	iqd23-2	P201	P216	SALK LBb1.3	+855	
Genotyping *iqd24*	WT allele	P242	P243	-51	+354	405 bp
	iqd24	P242	P243	-51	+292	343 bp

Genotyping *iqd25-1*	WT allele	P234	P235	-622	+537	1159 bp
	iqd25-1	P201	P235	SALK LBb1.3	+537	
Genotyping *iqd27-2*	WT allele	P241	P240	-16	+1107	1123 bp
	iqd27-2	P241	P201	-16	SALK LBb1.3	
Genotyping *iqd26-3*	WT allele	P459	P460	+55	+1122	1068 bp
	iqd26-3	P459	P472	+55	GABI LB	
Genotyping *iqd26-4*	WT allele	P272	P254	+107	+340	234 bp
	Iqd26-5	P272	P254	+107	+332	*Sac*I-HF digests 226bp amplicon into two products of 21 bp and 205 bp
iqd26 CRISPR allele screening		P253	P262	+8	+214	207 bp. Digestion of wild type gDNA with *Hinf*I yields three products of 126 bp, 59bp and 22 bp. If the most 5' *Hinf*I site is disrupted, two products of 185 bp and 22 bp are produced. If the most 3' HinfI site is disrupted, two products of 126 bp and 81 bp are produced
Amplification of *iqd26* CRISPR alleles for sanger sequencing		P255	P254	-152	+340	492 bp
Amplification of *iqd22* CRISPR alleles for sanger sequencing		P231	P210	-255	+415	670 bp

Table 5: Primer sequences. ***Bold italics*** indicates a Type IIS restriction enzyme recognition site; underline only indicates a 4-base pair Golden Gate overhang; red indicates an introduced single base substitution; other lowercase indicates the overlap region of a primer used in NEBuilder® cloning

Primer	Sequence (5'-> 3')	Reference
P201	ATTTTGCCGATTTCGGAAC	SALK LBb1.3 (http://signal.salk.edu/tdnaprimers.2.html)
P209	CCTCTAATCTCAAACGCC	(Mckechnie-Welsh 2021)
P210	GACTTCGAGTCGACCTCC	(Mckechnie-Welsh 2021)
P215	ACTTTAACCGACGCCCTTTAG	(Mckechnie-Welsh 2021)
P216	AACTTGGCCCATCTGACAAC	(Mckechnie-Welsh 2021)
P231	TGACACGGAAATTACACGACG	
P234	GGGACAATTGCATGGGAATG	(Mckechnie-Welsh 2021)
P235	AACGCTTTTCTCGCCTTTTAC	(Mckechnie-Welsh 2021)
P238	GACGAAAAACGGAGTAGGGAC	(Mckechnie-Welsh 2021)
P239	ACCGTGCCTTAACAGGACTTC	(Mckechnie-Welsh 2021)
P240	TCCACCAACACTCTTAGCTGG	(Mckechnie-Welsh 2021)
P241	ATTCTTCCAAATCGAGATGGG	(Mckechnie-Welsh 2021)
P242	CTCAACCGTAGAAAATTCCGACA	(Mckechnie-Welsh 2021)
P243	GCCACGAAAAGCGGATTGAA	(Mckechnie-Welsh 2021)
P253	GAGCTGCGAGATGGTTCAAG	
P254	GAATTTTCACTGCGGCCCA	

P255	TGTCTTCAGTTTCAGTGCCG	
P262	CTGTAGCAGCAGCAACCGgA	
P272	ACATTCACCGGAAAGTTCTCCgAGC	
P275	CT***GGTCTC***CGGAGGAAGGTAAACAGTACATGGTTAAAGG	
P276	CT***GGTCTC***GCATTTGCTGATGAACACTTTGATACG	
P277	TA***GGTCTC***CAATGGGAAAAGCGTCACG	
P278	AT***GGTCTC***CCGAAGAGTACCTATACCCAATTGGCA	
P281	CT***GGTCTC***CGGAGTTAAGCTACGAGTCAATTCCAAG	
P282	AC***GGTCTC***TCATTCTTTCATCGTCGGAAAATCG	
P283	gtctcaaATGGGCTTTTTCGGGAGACTG	
P284	tcattagagactTCAACTCTCTGTTTCGGC	
P285	agagagttgaagtctctaatgaAACCAGTGGCTACAAGAG	
P286	gtctcacgaaGAAACAAGAAACGAAGAATGC	
P287	tcttgtttcTTCGTGAGACCACGAAGTG	
P288	cgaaaaagccCATTTGAGACCACAGAGTG	
P291	CC***GGTCTC***AGGAGCTCTCCAGAAATTTCGTT	
P292	AT***GGTCTC***GCATTAATGGTTTTAGTTTGGTTTCAC	
P293	gtctcaaATGAGAAAGAATCTCACAAAATTGACC	
P294	cgccggagagCCACCAGAAAAACGAGGT	
P295	tttctggtggcTCTCCGGCGAGGAGCGTG	

P296	ctctggtcttTGTCTCGGTGCACTATGCGAC	
P297	caccgagacaaAGACCAGAGAGTAATGCTTCA	
P298	gtctcacgaagACCAACGCATCCTACGC	
P299	gcgttggtcTTCGTGAGACCACGAAGT	
P400	gattctttctCATTTGAGACCACAGAGTG	
P403	GC***GGTCTC***AGGAGCTACTCTGTTAGAACCAAAA	
P404	CGT***GGTCTC***GCATTCTTCTCTTTCAATTCAAATTATAAAG	
P405	gtctcaaatgGGAAGAGCTGCGAGATGG	
P406	gggactggttTCATCGTACGCATTGTTGTTG	
P407	cgtacgatgaaACCAGTCCCAAGATTGTG	
P408	gtctcacgaagAATTATAGAATCTAAAATCAGTCTCGT	
P409	ctataattcttcgTGAGACCACGAAGTGG	
P410	cagctcttcccattTGAGACCACAGAGTGAT	
P413	gtctcaggagAGAAAAAGATCTTTTACAGCTTTTAAAG	
P414	gtaactataacGTCTCATATTGCTGCTTC	
P415	atatgagacgTTATAGTTACTTTTTTCCTTTTGC	
P416	gtctcacattCTCGATTTGGAAGAATCAAG	
P417	ccaaatcgagaatgTGAGACCACGAAGTG	
P418	atctttttctctccTGAGACCACAGAGTG	
P419	GT***GGTCTC***AAATGGGCAGAGCAGCAAGATG	

P420	GT***GGTCTC***ACGAAGAAAGCGGATCACAGGAACAAG	
P423	ATAT***GGTCTC***AGGAGGAACAACATTCAGTTCCGAGG	(Mckechnie-Welsh 2021)
P424	ATAT***GGTCTC***ACATTCTTAGTTCATTGTATGAACTGAAC	(Mckechnie-Welsh 2021)
P425	ATAT***GGTCTC***AAATGGGTTTCTTTGGAAGACTGTTCG	(Mckechnie-Welsh 2021)
P426	ATAT***GGTCTC***ACGAACCTTGAAAGAAAAGAGGATTAGAAC	(Mckechnie-Welsh 2021)
P459	GAGAAAGAGAACTGTGTTTCC	
P460	CTCCATTCGAAATCTTTGGC	
P472	ATAATAACGCTGCGGACATCTACATTTT	GABI o8474 (Kleinboelting et al. 2012)
P477	TA***GGTCTC***TGGAGGTCAACATGGTGGAGCAC	
P478	TA***GGTCTC***G*AGCG*AAATGGTGCGATCTTA	
P482	CC***GGTCTC***AGGAG AAGCTTTTCTCTTCATTTCTC	
P483	GC***GGTCTC***CAGCG TCGATCTAGTAACATAGATG	
P488	accgcagggcACTTATCCCCAGGCTTGTC	
P489	tgtatcatacCTGGTCGAAATCAGTGCG	
P490	tttcgaccagGTATGATACAGCTTTCTTTTC	
P491	gtgaacgaacCTACAGATTCATAGTTTGAGAAAATTATATC	
P492	gaatctgtagGTTCGTTCACTCATGGAAAATAG	
P493	ccgcatcaagTGTTTTGGCTCTCAGGC	
P494	agccaaaacaCTTGATGCGGAAGAAGTCG	
P495	ggggataagtGCCCTGCGGTATTGACAC	

P601	GT***GGTCTC***AAATGGGAAGAGCTGCGAGATGG	
P602	GT***GGTCTC***AGTTTCATCGTACGCATTGTTGTTGTG	
P603	GT***GGTCTC***AAAACCAGTCCCAAGATTGTG	
P604	GT***GGTCTC***AAAGCCTAATTATAGAATCTAAAATCAGTCTCG	
P605	GT***GGTCTC***AAATGAGATCACTTGGGCAGAAC	
P606	GT***GGTCTC***AAAGCTCACTTTGCCATCATGACTTTG	
P607	GT***GGTCTC***AAATGGACGGTGGTTCAGGT	
P608	GT***GGTCTC***AAAGCCTATTGCTGATATTCTGGATTGAAAGC	
P609	GT***GGTCTC***AAATGGCGATCCCTACGGAGAC	
P610	GT***GGTCTC***AAAGCTTAAACTCTGTAGATTCCAGAAGGAT	
P611	GT***GGTCTC***AAATGGACGTCGTTGAGAGAAAAAG	
P612	GT***GGTCTC***AAAGCTTACAACAACGACCGTTTAAGAAC	
P618	GT***GGTCTC***AAATGGCCGCCATGTCCCG	
P619	GC***GGTCTC***AAAACCTTGGATATGTCCACTTTCTTGTTCTG	
P620	GT***GGTCTC***AGTTTCCTCCAAGTGTGGGTCCAAAGC	
P621	GC***GGTCTC***AAAGCTCAGATCCCGGGCCCACC	
P634	TGT***GAAGAC***AAACTAGAATTCG	
P635	GCC***GAAGAC***CGGAGGACGAATATATTAACTATTTTCTACAAATTAAAC	
P636	GGT***GAAGAC***AACCTCATTGTTTGTCTGCAGATCCG	
P637	GCC***GAAGAC***CGTGAGGACACAATGTGATGTTTTGAGAAAG	

P639	GCC***GAAGAC***CGAAACTGATTGAATTTTCACTGCGG	
P640	GGT***GAAGAC***CAGTTTTCAAGGGCTATTTGGTAAATTTC	
P641	GCA***GAAGAC***AA*GTAA*AGCG	
P642	GGT***GAAGAC***GCCTCAGTTTCAGTGCCGTAAATTTTG	